Preface

To facilitate the timely exchange of achievements in accelerator physics within China, gain insights into international frontiers and development trends, and enhance the level of accelerator physics research in the country, the Particle Accelerator Branch of the Chinese Physical Society and the Chinese Nuclear Society hosted the “15th Symposium on Accelerator Physics” (SAP2025) from September 2 to 5, 2025.

This conference presented and discussed recent research achievements in China’s accelerator physics field while introducing and exchanging international cutting-edge advancements. Topics include, but are not limited to: accelerator physics challenges in the operation and enhancement of major accelerator facilities; accelerator physics issues related to new facilities under design and construction, such as novel light sources, colliders, and high-current proton/ion accelerators; novel beam manipulation techniques; nonlinear theory; beam instabilities, beam-beam interactions, novel acceleration principles, accelerating structures, and applications of artificial intelligence methods. It also included accelerator physics issues in applied and small-scale accelerator research.

Table of Contents

ISBN: 978-3-95450-279-0 ISSN: 3043-0208 doi: 10.18429/JACoW-SAP2025-WEMC3

MULTIPLE-ECHO-ENABLED HARMONIC GENERATION METHOD FOR STORAGE RING LIGHT SOURCES

Weihang Liu*, Yu Zhao, Weilun Qin
Institute of High Energy Physics, Chinese Academy of Sciences, Beijing, China
Spallation Neutron Source Science Center, Dongguan, China

Abstract

Storage ring light sources (SRLS) can reuse a single electron beam to serve multiple users, offering high repetition rates and cost efficiency. However, despite the transverse emittance reaching the X-ray diffraction limit in fourth-generation SRLS, the storage ring suffers from limited longitudinal coherence. Enhancing longitudinal coherence has been shown to significantly improve spectral brightness, time resolution, and energy resolution. Laser modulation schemes for SRLS have been explored for their potential to induce strong micro-bunching, thereby enhancing spectral power and coherence. However, these methods modulate each bunch only once per revolution, limiting their application to a single beamline and underutilizing the multi-user capacity of storage rings. To enable coherent radiation delivery to multiple beamlines, we propose a multiple-echo-enabled harmonic generation scheme. This approach modulates the electron beam multiple times, generating coherent pulses at different wavelengths. By leveraging the multi-user capability of storage rings while simultaneously improving longitudinal coherence, our method enhances both spectral and temporal performance.

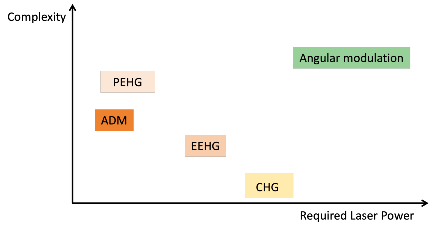

Figure 1: Implementation complexity of seeding methods in storage rings.

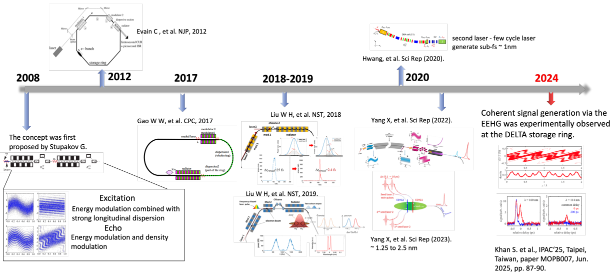

Figure 2: Development of EEHG schemes for storage rings.

INTRODUCTION

Storage ring light sources have been developed from third-generation to fourth-generation, achieving approximately two orders of magnitude improvement in brightness. However, their longitudinal coherence has not been enhanced compared to third-generation sources. Improving longitudinal coherence can enhance the temporal and energy resolution capabilities of the light source, and significant advancements in these areas would provide users with a more advanced photon source. In fact, many experts believe that the next generation of storage ring light sources will possess higher longitudinal coherence.

In storage rings, the interaction between a laser and the electron beam in an undulator enables energy modulation of the beam. This energy modulation can then be converted into density modulation through longitudinal dispersion, thereby achieving micro-bunching. This micro-bunched beam can subsequently generate coherent radiation when passing through a downstream undulator [1–5]. Through this approach, the radiation performance of the light source can be substantially enhanced.

With ongoing research, similar schemes that are more suitable for storage rings and those enabling higher harmonic conversions have been progressively proposed. Figure 1 compares the implementation difficulties of several advanced seeding schemes, including echo-enabled harmonic generation (EEHG) [6–10], phase-merging enhanced harmonic generation (PEHG) [11, 12], angular dispersion-induced microbunching (ADM) [13–15], and angular modulation [12, 16], to illustrate their relative challenges. To mitigate these challenges and reduce the application complexity, the use of higher laser power is necessary. For instance, the EEHG scheme. As shown in Fig. 2, since its proposal, EEHG has been continuously explored for application in storage rings, and numerous schemes tailored for storage rings have been proposed [6–10]. By 2024, EEHG was successfully demonstrated for the first time in a storage ring [17], although the wavelength of the coherent signal obtained in the experiment did not yet meet expectations. Nevertheless, this crucial experimental validation has increased confidence in the feasibility of this approach.

However, the beam modulated by these schemes can only supply coherent radiation to a single beamline. This fundamentally differs from the conventional operation of storage rings, where a single electron bunch routinely serves multiple user beamlines with synchrotron radiation.

To enable a single electron bunch to supply coherent radiation to multiple beamlines, we propose the Multi-stage Echo-Enabled Harmonic Generation (MEEHG) method.

---

* liuwh@ihep.ac.cn

ISBN: 978-3-95450-279-0 ISSN: 3043-0208 doi: 10.18429/JACoW-SAP2025-WEMC3

This scheme achieves the generation of coherent pulses for multiple beamlines by applying multiple modulations to a single bunch.

This paper is organized as follows. In the next section, we will present the theoretical details of MEEHG. Section 3 is devoted to the verification of this theory. Sections 4 and 5 will demonstrate the application of MEEHG in generating radiation at different wavelengths and with different pulse durations, respectively.

MULTIPLE-ECHO-ENABLED HARMONIC GENERATION METHOD

The MEEHG process begins with a complete EEHG process. First, a laser modulation is applied to the beam, which then passes through a strong dispersion section, exciting the first echo. This first echo is realized through a second energy modulation and density modulation of the electron beam. The echo-modulated beam then generates the first coherent radiation through the downstream undulator.

Subsequently, the excitation of the second echo no longer requires laser modulation, but only the action of a strong dispersion section. After this process, coherent radiation is produced at the second radiator. By repeating this procedure, multiple EEHG can be achieved.

To obtain the harmonic bunching factor of MEEHG, we make the following assumption: the perturbation of the beam by coherent radiations are negligible compared to the laser modulation. This allows significant simplification of the analysis. Through analysis, with full details to be published elsewhere, the expression for the nth echo bunching factor can be derived as:

$$
\begin{aligned}
b\left(k_z\right) &= \sum_{m_1,m_2,\cdots m_{n+1}=-\infty}^{+\infty} e^{-\frac{c_2^2}{2}} \prod_{i=1}^{n+1} J_{m_i}\left(A_i \xi_i\right), \\
\xi_1 &= c_1\left(k_z-\sum_{i=2}^{n+1} m_i k_L\right)+\left(c_2+c_3\right)\left(k_z-\sum_{i=3}^{n+1} m_i k_L\right)+\cdots \\
&\quad +\left(c_{2n-2}+c_{2n-1}\right)\left(k_z-m_{n+1} k_L\right)+c_{2n} k_z, \\
\xi_{k+1} &= \xi_k-\left(c_{2k-2}+c_{2k-1}\right)\left(k_z-\sum_{i=k+1}^{n+1} m_i k_L\right).
\end{aligned} \tag{1}
$$

Given the infinite series in Eq. (1), for any given harmonic order, certain terms dominate significantly over others. We may approximate the complex bunching factor by retaining only these dominant terms:

$$
\begin{aligned}
b_{0,0,\ldots,1,N-1} = {} & J_{N-1}\left(A_{n+1} B_{2n} N\right) J_1\left(A_n \xi\right) \ldots \\
& \times J_0\left(A_2 \xi\right) J_0\left(A_1 \xi\right) \exp\left(-\xi^2/2\right),
\end{aligned} \tag{2}
$$

where ξ can be write as

$$
\xi = B_{2n} N+\left(B_{2n-1}+B_{2n-2}\right). \tag{3}
$$

Based on Eqs. (2)–(3), we observe that the bunching factor for the $n-$ echo in MEEHG depends on the amplitudes of all preceding $n+1$ energy modulations. Furthermore, we note that the relationship between the modulation amplitudes of the first n echoes and the resulting bunching factor follows a zero-order Bessel function behavior. Consequently, when none of the preceding $n-1$ echoes are excited, the bunching factor reduces, as expected, to the well-known expression for standard EEHG [18].

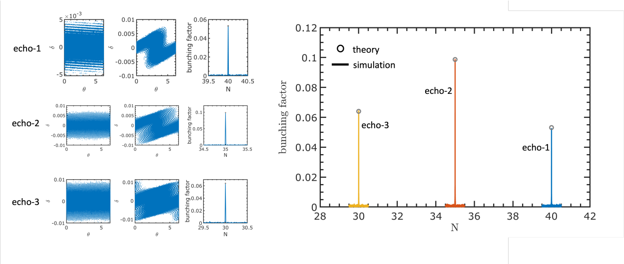

Figure 3: Phase space distributions after three echoes (left) and corresponding bunching factors from simulation and theory (right).

Table 1: Parameters Using in the Simulation

i	A_i	B_i
1	1	−13.9551
2	2.8143	0.3708
3	2.5976	−13.9551
4	2.2628	0.4028
5	–	−13.9551
6	–	0.4639

THEORETICAL VERIFICATION

To validate our theory, we consider a simulation involving a three-echo process. In this simulation, only linear particle dynamics within the dispersive sections are considered. The modulations and radiation processes are simulated using the Genesis code [19]. The parameters employed in the simulation are summarized in Table 1.

The phase-space distributions for the three echoes are shown in Fig. 3. The characteristic phase-space structures associated with each successive EEHG stage are clearly observed. Additionally, the simulated bunching factors are presented alongside their theoretical counterparts in Fig. 3, demonstrating excellent agreement between simulation results and theoretical predictions.

APPLICATION OF MEEHG TO SAPS FOR GENERATING COHERENT RADIATION AT THREE DIFFERENT HARMONICS

We now apply the MEEHG scheme to the Southern Advanced Photon Source (SAPS) storage ring to generate coherent radiation at three distinct wavelengths. SAPS is a planned fourth-generation synchrotron light source currently in the preliminary design phase. Its parameters are still being optimized; the values used in this study are listed in Table 2 [20].

Based on these parameters, we designed three wavelengths corresponding to the 20th, 30th, and 40th harmonic orders.

ISBN: 978-3-95450-279-0 ISSN: 3043-0208 doi: 10.18429/JACoW-SAP2025-WEMC3

Table 2: Main Parameters of SAPS

Parameters	**Values**
Energy	3.5 GeV
Emittance x/y	60 / 6 pm
Energy spread	0.1 %
Peak Current	32 A
Straight section length	6 m

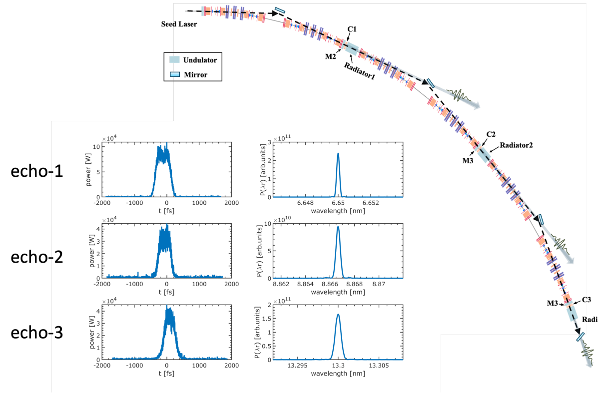

Figure 4: MEEHG Layout in the SAPS storage ring and pulse profiles from different echoes.

To integrate the three-echo scheme into the storage ring, each strong dispersion section is implemented using two connected arcs, as illustrated in Fig. 4. In this layout, the radiator for each echo is placed in a straight section. Additionally, the power of the modulation laser is designed in a decreasing pattern, allowing the same laser to be transported via mirrors to different modulation sections, thereby enabling multiple modulations with a single laser source.

The resulting radiation performance is shown in the inset of Fig. 4. The radiation exhibits a spectral bandwidth of less than 10 meV and a pulse duration of approximately 400 fs. The photon number per pulse reaches the order of 10^9, representing an enhancement of approximately three orders of magnitude compared to the synchrotron radiation.

APPLICATION FOR GENERATING COHERENT RADIATION AT THREE DIFFERENT TIME DURATIONS

In this section, we further apply MEEHG to SAPS to generate three coherent pulses with distinct temporal durations, aiming to cover attosecond, femtosecond, and picosecond timescales.

To generate attosecond pulses, we employ a few-cycle, CEP-stabilized laser pulse to modulate the electron beam [21].

The simulated performance of the three echoes is summarized in Fig. 5. The attosecond pulse duration is about 500 as with a photon number per pulse of approximately 10^5. The femtosecond pulse has a duration of around 290 fs and a photon number of about 2×10^9 per pulse, while the picosecond pulse reaches a duration of 1.4 ps with approximately 7×10^9 photons per pulse.

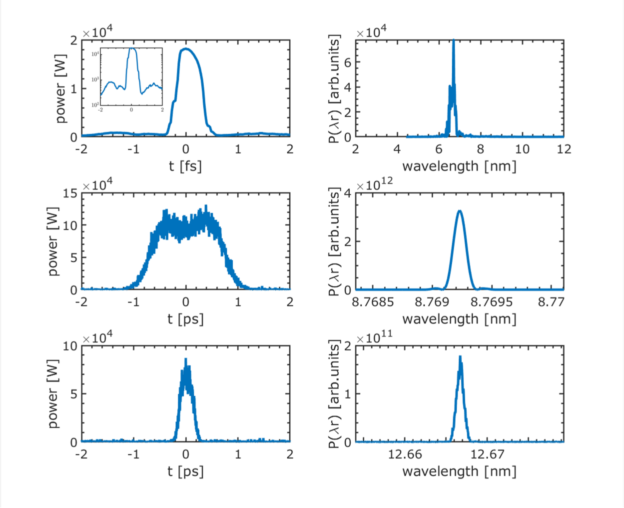

Figure 5: Radiation pulses with different durations from the three-echo process, corresponding to the 1st, 2nd, and 3rd echo results from top to bottom.

CONCLUSION

The Multi-EEHG scheme offers a promising approach for generating multiple coherent radiation pulses within a storage ring, enabling the simultaneous provision of light sources to users with diverse experimental requirements.

In this study, we have demonstrated the versatility of MEEHG through two representative examples: a three-echo configuration producing coherent pulses at three distinct wavelengths, and a temporally structured output covering durations from attoseconds to picoseconds.

Several aspects of the scheme warrant further investigation. These include more detailed design of the radiation spectrum and improved independent control over individual beamlines.

ACKNOWLEDGEMENTS

This work was supported by National Natural Science Foundation of China (No. 12405176).

REFERENCES

[1] B. Girard *et al.*, "Optical frequency multiplication by an optical klystron", *Phys. Rev. Lett.*, vol. 53, no. 25, pp. 2405–2408, Dec. 1984. doi:10.1103/PhysRevLett.53.2405

[2] G. Stupakov, "Using the beam-echo effect for generation of short-wavelength radiation", *Phys. Rev. Lett.*, vol. 102, p. 074801, 2009. doi:10.1103/PhysRevLett.102.074801

[3] D. Xiang and W. Wan, "Generating ultrashort coherent soft X-ray radiation in storage rings using angular-modulated electron beams", *Phys. Rev. Lett.*, vol. 104, p. 084803, 2010. doi:10.1103/PhysRevLett.104.084803

[4] H. Deng and C. Feng, "Using off-resonance laser modulation for beam-energy-spread cooling in generation of short-wavelength radiation", *Phys. Rev. Lett.*, vol. 111, p. 084801,

ISBN: 978-3-95450-279-0 ISSN: 3043-0208 doi: 10.18429/JACoW-SAP2025-WEMC3

2013. doi:10.1103/PhysRevLett.111.084801

[5] C. Feng and Z. Zhao, "A storage ring based free-electron laser for generating ultrashort coherent EUV and X-ray radiation", *Sci. Rep.*, vol. 7, p. 4724, 2017. doi:10.1038/s41598-017-04962-5

[6] C. Evain *et al.*, "Soft x-ray femtosecond coherent undulator radiation in a storage ring", *New J. Phys.*, vol. 14, p. 023003, 2012. doi:10.1088/1367-2630/14/2/023003

[7] W. Liu, G. Zhou, and Y. Jiao, "Generating femtosecond coherent X-ray pulses in a diffraction-limited storage ring with the echo-enabled harmonic generation scheme", *Nucl. Sci. Tech.*, vol. 29, p. 143, 2018. doi:10.1007/s41365-018-0476-z

[8] W. Liu *et al.*, "Generation of two-color polarization-adjustable radiation pulses for storage ring light source", *Nucl. Sci. Tech.*, vol. 30, p. 66, 2019. doi:10.1007/s41365-019-0578-2

[9] J.-G. Hwang *et al.*, "Generation of intense and coherent sub-femtosecond X-ray pulses in electron storage rings", *Sci. Rep.*, vol. 10, p. 10093, 2020. doi:10.1038/s41598-020-67027-0

[10] X. Yang *et al.*, "Optimization of echo-enabled harmonic generation toward coherent EUV and soft X-ray free-electron laser at NSLS-II", *Sci. Rep.*, vol. 12, p. 9437, 2022. doi:10.1038/s41598-022-13702-3

[11] W. Liu, C. Feng, Y. Jiao, and S. Wang, "A coherent harmonic generation method for producing femtosecond coherent radiation in a laser plasma accelerator based light source", *J. Synchrotron Radiat.*, vol. 28, pp. 669–680, 2021. doi:10.1107/S1600577521002745

[12] Y. Lu *et al.*, "Methods for enhancing the steady-state microbunching in storage rings", *Results Phys.*, vol. 40, p. 105849, 2022. doi:10.1016/j.rinp.2022.105849

[13] B. Jiang *et al.*, "A synchrotron-based kilowatt-level radiation source for EUV lithography", *Sci. Rep.*, vol. 12, p. 3325, 2022. doi:10.1038/s41598-022-07323-z

[14] W. Liu *et al.*, "Generating high repetition rate X-ray attosecond pulses in a diffraction limited storage ring", *Sci. Rep.*, vol. 13, p. 14019, 2023. doi:10.1038/s41598-023-41118-0

[15] W. Liu *et al.*, "Method for reversing the laser modulation in a storage ring", *Phys. Rev. Accel. Beams*, vol. 28, no. 6, p. 060703, Jun. 2025. doi:10.1103/PhysRevAccelBeams.28.060703

[16] X. Wang *et al.*, "Angular dispersion enhanced prebunch for seeding ultrashort and coherent EUV and soft X-ray free-electron laser in storage rings", *J. Synchrotron Radiat.*, vol. 26, pp. 677–684, 2019. doi:10.1107/S1600577519002674

[17] S. Khan *et al.*, "Echo-enabled harmonic generation at the DELTA storage ring", presented at IPAC'25, Taipei, Taiwan, Jun. 2025, to be published.

[18] D. Xiang and G. Stupakov, "Echo-enabled harmonic generation free electron laser", *Phys. Rev. ST Accel. Beams*, vol. 12, p. 030702, 2009. doi:10.1103/PhysRevSTAB.12.030702

[19] S. Reiche, "GENESIS 1.3: A fully 3D time-dependent FEL simulation code", *Nucl. Instrum. Methods Phys. Res. A*, vol. 429, pp. 243–248, 1999. doi:10.1016/S0168-9002(99)00114-X

[20] Y. Zhao, Y. Jiao, and S. Wang, "Design study of APS-U-type hybrid-MBA lattice for mid-energy DLSR", *Nucl. Sci. Tech.*, vol. 32, p. 71, 2021. doi:10.1007/s41365-021-00902-1

[21] A. Zholents and G. Penn, "Obtaining two attosecond pulses for X-ray stimulated Raman spectroscopy", *Nucl. Instrum. Methods Phys. Res. A*, vol. 612, pp. 254–259, 2010. doi:10.1016/j.nima.2009.10.063

ISBN: 978-3-95450-279-0 ISSN: 3043-0208 doi: 10.18429/JACoW-SAP2025-WENC5

MODELING OF CSR AND ITS CANCELLATION IN DBA/CHICANE TYPE COMPRESSORS*

Fancong Zeng[1, 2], Yi Jiao[†, 1, 2], Weihang Liu[1, 3], Cheng-Ying Tsai[4]
[1]Institute of High Energy Physics, Chinese Academy of Sciences, Beijing, China
[2]University of Chinese Academy of Sciences, Beijing, China
[3]Spallation Neutron Source Science Center, Dongguan, China
[4]School of Electrical and Electronic Engineering, Huazhong University of Science and Technology, Wuhan, China

Abstract

In advanced accelerator-based light sources and colliders, bunch compressors like arc-type (DBA) and linear-type (chicane) are widely used to generate high-quality electron beams with kiloampere (kA)-level peak currents. However, a serious problem in increasing the peak current even higher is the significant degradation of beam quality caused by the Coherent Synchrotron Radiation (CSR) effect. To tackle this, we develop a new analytical model for CSR that can describe beam transport with varying bunch lengths, establish a practical framework for analyzing CSR in both DBA and chicane-type compressors, and design CSR-suppressed DBA compressors (arc-type) as well as non-symmetric C- and S-shaped chicanes (linear-type). General analytical conditions for CSR cancellation are derived for these designs. Simulations show that, with these new compressors, high beam quality can be maintained even when the peak current is increased up to 10 kA. This work provides important guidance for enhancing the performance of existing accelerator facilities, as well as for the development of next-generation accelerator-based light sources and colliders.

INTRODUCTION

The advent of accelerators and accelerator-based light sources has revolutionized advancements in science, industry, medicine, and materials research. In modern accelerators, electron bunch compressors play a pivotal role, with wide applications in linear colliders, linacs, beam driven plasma-wakefield accelerators, and significant roles in x-ray free electron lasers (FELs) [1]. Combined with the position-energy correlation provided by the rf cavity, the following dispersive element converts the energy difference into a difference in the time of flight of the particles. This effect causes the particles at the head and tail to become closer, enabling beam compression [2].

Currently, symmetric C-chicanes and DBA-based compressors are the most commonly used bunch compressors in linac-based systems and arc systems, respectively. However, due to the high peak current required for FELs, the ability to compress an electron bunch with minimal degradation of beam quality becomes challenging because of the effects of coherent synchrotron radiation (CSR). CSR is emitted for wavelengths longer than or comparable to the length of the electron bunch, and leads to detrimental tail-head inter actions in the bends [3]. The shorter and more intense the bunch is, the stronger the CSR fields produced and the more severe the CSR effects become. The emission of CSR results in projected transverse emittance growth [4]. In the past decades, various efforts have been stimulated to suppress CSR-induced emittance growth in chicane compressors, including analytical, numerical, and experimental studies [5-8]. Among them, the approach of suppressing the deleterious effects of CSR by manipulating beam optics has sparked continuing research interest.

The optical balance method was first proposed by Douglas [9] and was further developed by Courant-Snyder (C-S) formalism analysis [6]. Subsequently, the point-kick model was proposed and works well in transport systems where the bunch length remains constant or changes very little (hereafter referred to as the constant- σ_z point-kick model) [7, 8]. However, for magnetic bunch compressors, this model lacks self-consistency due to significant variations in bunch length within the bends.

To address this issue, in this study, we propose a self-consistent modified CSR point-kick model that accounts for variations in bunch length. Based on this model, we establish a practical framework for analyzing CSR in both DBA and chicane-type compressors, envisaging the potential designs for a CSR-immune DBA and chicane compressors.

Modified CSR Point-Kick Model

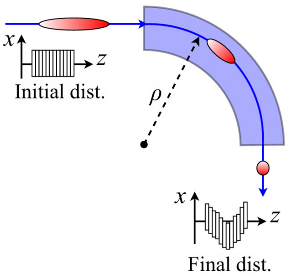

Figure 1: Schematic of the compression process after a bunch passes through a dipole, within sets of the initial and final beam distribution affected by CSR into the $x-z$ phase plane.

---

* Work supported by National Natural Science Foundation of China (No.12275284 and No. 12275094), the Fundamental Research Funds for the Central Universities (HUST) under Project No. 2021GCRC006, and National Key Research and Development Program of China (No.2022YFA1603402).
† jiaoyi@ihep.ac.cn

ISBN: 978-3-95450-279-0 ISSN: 3043-0208 doi: 10.18429/JACoW-SAP2025-WENC5

After a particle passes through a dipole magnet with a bending radius ρ and bending angle θ (see Fig. 1), its horizontal coordinate deviation and energy deviation relative to synchronous particle change under the influence of CSR as follows [10]:

$$\begin{aligned} x_{\mathrm{csr}} &= \int_0^\theta \frac{d\delta_{\mathrm{csr}}(\phi)}{d\phi} R_{16}^{s\to s_f} d\phi, \\ x'_{\mathrm{csr}} &= \int_0^\theta \frac{d\delta_{\mathrm{csr}}(\phi)}{d\phi} R_{26}^{s\to s_f} d\phi, \\ \delta_{\mathrm{csr}} &= \int_0^\theta \frac{d\delta_{\mathrm{csr}}(\phi)}{d\phi} d\phi. \end{aligned} \tag{1}$$

The gradient of the energy deviation due to CSR along the bending angle can be derived based on the 1D CSR model. When considering only the steady state case and assuming the beam distribution in the dipole is Gaussian, it can be expressed as

$$\frac{d\delta_{\mathrm{csr}}}{d\phi} = k\rho^{\frac{1}{3}}\left(\frac{\sigma_{z0}}{\sigma_z(\phi)}\right)^{\frac{4}{3}}. \tag{2}$$

Here σ_{z0} is the bunch length at the entrance of the dipole, $\sigma_z(\phi)$ denotes the bunch length after bending by an angle ϕ, and the CSR strength parameter k corresponds to the initial bunch length and is in the form

$$k = 0.2459\,\frac{N_b r_c}{\gamma\sigma_{z0}^{4/3}} \tag{3}$$

The resulting CSR kick after a particle passes through a dipole magnet is given by (a more detailed analysis can be found in Ref. [11])

$$X_k = \begin{pmatrix} x_k \\ x'_k \end{pmatrix} = \begin{pmatrix} \rho^{4/3}k[g_x\theta\cos(\theta/2) - 2(g_x\cos(\theta/2)^2 + g_{xp}\sin(\theta/2)^2)\sin(\theta/2)] \\ \sin(\theta/2)[2\delta + \rho^{1/3}k(g_x\theta + (g_{xp} - g_x)\sin\theta)] \end{pmatrix}.$$

Here g_x, g_{xp}, and g_δ are the dimensionless correction functions, which can be expressed as

$$\begin{aligned} g_x([a,b],\xi) &= 3\int_0^1 \left[1 + \xi\frac{ax+bx^2+x^3}{a+b+1}\right]^{-\frac{4}{3}}(1-\tau)^2 d\tau \\ g_{xp}([a,b],\xi) &= 2\int_0^1 \left[1 + \xi\frac{ax+bx^2+x^3}{a+b+1}\right]^{-\frac{4}{3}}(1-\tau) d\tau \\ g_\delta([a,b],\xi) &= \int_0^1 [1 + \xi\frac{ax+bx^2+x^3}{a+b+1}]^{-4/3} d\tau \end{aligned} \tag{4}$$

where the variable $\xi \equiv \frac{\sigma_{zf}}{\sigma_{z0}} - 1$ represents the rate of bunch length variation after passing through the dipole, the parameters a and b are related to η_0 and η'_0, respectively, and can be written as

$$a = 6\frac{\eta_0}{\rho\theta^2}, b = 3\frac{\eta'_0}{\theta}. \tag{5}$$

They reflect the impact of the dipole on the dispersion function. By setting all correction functions are equal to 1, the resulting CSR kick after a particle passes through a dipole magnet can be reduced to the constant-length point-kick model:

$$X_k = \begin{pmatrix} x_k \\ x'_k \end{pmatrix} = \begin{pmatrix} \rho^{\frac{4}{3}}k\left[\theta\cos\left(\frac{\theta}{2}\right) - 2\sin\left(\frac{\theta}{2}\right)\right] \\ \sin\left(\frac{\theta}{2}\right)\left[2\delta + k\rho^{\frac{1}{3}}\theta\right] \end{pmatrix} \tag{6}$$

This constant-length model is more appropriate to the transport system where the bunch length has a small variation.

Application to a DBA Compressor

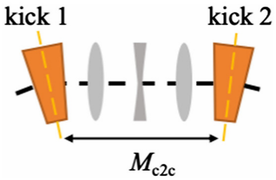

Figure 2: Schematic of a DBA and the physical model for the CSR point-kick analysis in the DBA. The lattice section between two dipoles containing two quadrupoles and one skew quadrupole. The kicks point to the centers of the bends.

Due to the arbitrariness of the parameters a and b in Eq. (5), the correction functions in Eq. (4) generally cannot be expressed in a simple analytical form. However, there are two special cases (see Fig. 2) where the dispersion functions can be well determined. We first consider a dipole with zero entrance dispersion and dispersion gradient (e.g., the dipole in a single dipole system and the first dipole in a multidipole achromat system), where $a = b = 0$. In this case, the correction functions can be expressed in the following analytical form:

$$\begin{aligned} g_x([0,0],\xi) &= 3\,\frac{-1+(1+\xi)^{\frac{1}{3}}-\xi[\,{}_2F_1(\frac{1}{3},1,\frac{5}{3},-\xi)-1]}{\xi(1+\xi)^{\frac{1}{3}}}, \\ g_{xp}([0,0],\xi) &= \frac{2-\,{}_2F_1\left(\frac{1}{3},1,\frac{5}{3},-\xi\right)}{(1+\xi)^{\frac{1}{3}}}, \\ g_\delta([0,0],\xi) &\approx \frac{1}{(1+\xi)^{\frac{1}{3}}}, \end{aligned} \tag{7}$$

where ${}_2F_1$ denotes the standard hypergeometric function.

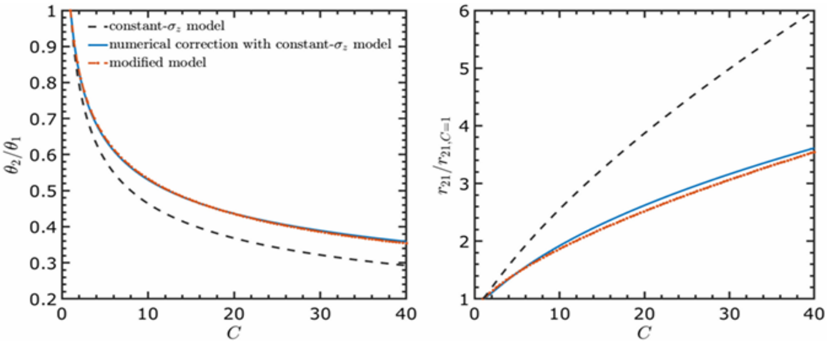

Figure 3: The bending angle ratio and matrix element r_{21} as functions of the total compression ratio C.

ISBN: 978-3-95450-279-0 ISSN: 3043-0208 doi: 10.18429/JACoW-SAP2025-WENC5

Another special case is when both the dispersion and dispersion gradient at the dipole exit are zero (e.g., the last dipole in a multi-dipole achromat system). In this case, $a = 3$ and $b = -3$. The corresponding correction functions can be expressed analytically as

$$\begin{aligned} g_x([3,-3],\xi) &= 3\frac{(1+\xi)^{\frac{1}{3}}-1}{\xi(1+\xi)^{\frac{1}{3}}}, \\ g_{xp}([3,-3],\xi) &\approx \frac{1}{(1+\xi)^{\frac{3}{4}}}, \\ g_{\delta}([3,-3],\xi) &\approx \frac{1}{1+\xi}. \end{aligned} \tag{8}$$

For the g_{xp} and g_δ functions, we utilized approximate forms to avoid overly complex expressions.

We calculate the corresponding θ_2/θ_1 and r_{21} for a given C: (A more detailed analysis can be found in Ref. [11])

$$\begin{aligned} \frac{\theta_2}{\theta_1} \equiv \zeta &= \frac{(3g_{xp1}-2g_{x1})^{\frac{1}{4}}}{(3g_{xp2}-2g_{x2})^{\frac{1}{4}}} C_1^{-\frac{1}{3}}, \\ r_{21} &= \frac{6\zeta\left(2g_{\delta 1}-g_{xp1}+g_{xp2}\zeta C_1^{\frac{4}{3}}\right)}{(3g_{xp1}-2g_{x1})\rho\theta_1}. \end{aligned} \tag{9}$$

We then compare these results with those from the constant$-\sigma_z$ model and the numerical corrections in Eq. (9). As shown in Fig. 3, the discrepancy between the constant$-\sigma_z$ model and the modified model is notable, emphasizing the importance of accounting for the bunch length variation within the dipole. The numerical corrections and the modified model demonstrate excellent agreement for C up to 40, with a relative discrepancy of less than 1.5% in θ_2/θ_1 and less than 4% in r_{21}, respectively. Notably, the numerical fit coefficients used in the numerical corrections were originally derived for C less than 15, which illustrates the strong generalizability of the numerical corrections from Ref. [12].

Application to a Chicane Compressor

We consider a general chicane model consisting of four bends separated by three adjustable drifts (see Fig. 4). The length of each bend is L_B, while the bending angles of the four bends are not subject to a specific constraint.

We derive the analytical expressions of net CSR kick at the chicane exit and further the ss-CSR cancelation conditions using a modified CSR-kick model (see Ref. [13]).

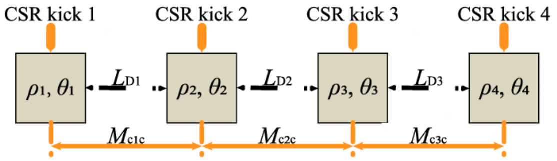

Figure 4: Schematic of the point-kick analysis of the CSR effects.

By setting $L_B = 0$ and assuming that all correction functions are equal to 1, the ss-CSR cancelation conditions can be reduced to the constant-length point-kick model. Using the modified CSR-kick model, the parameters for a ss-CSR-immune chicane are plotted in Fig. 5, compared to the simplified results (dot-dashed curves). It can be observed that these angle parameters (q_3, q_4) exhibit relatively small errors, while there are relatively larger errors in the drift parameters (ℓ_2, ℓ_3).

CONCLUSION

We have proposed a self-consistent modified CSR point-kick model that accounts for variations in bunch length. Then we presented a solvable model of the CSR effects in a generic four-bend chicane and DBA, which provides us insights on CSR compensation during beam compression. The design of the CSR-immune DBA and chicane compressors are successfully completed. For CSR-immune DBA, the discrepancy between the constant$-\sigma_z$ model and the modified model is notable, emphasizing the importance of accounting for the bunch length variation within the dipole. For the CSR-immune chicane, our results demonstrate that the modified model exhibits only minor deviations, with the constant$-\sigma_z$ model yielding better performance.

REFERENCES

[1] W. Ackermann *et al.*, “Operation of a free-electron laser from the extreme ultraviolet to the water window”, *Nat. Photonics*, vol. 1, no. 6, pp. 336-342, Jun. 2007. `doi:10.1038/nphoton.2007.76`

[2] H. Bartosik, Y. Papaphilippou, and A. Wolski, “A first taste of nonlinear beam dynamics”, Jan. 2022, arXiv:2201.01532 [physics.acc-ph]. `doi:10.48550/arXiv.2201.01532`

[3] Y. S. Derbenev *et al.*, “Microbunch radiative tail-head interaction”, Report No. TESLA-FEL 95-05, DESY, 1995.

[4] H. H. Braun *et al.*, “Emittance growth and energy loss due to coherent synchrotron radiation in a bunch compressor”,

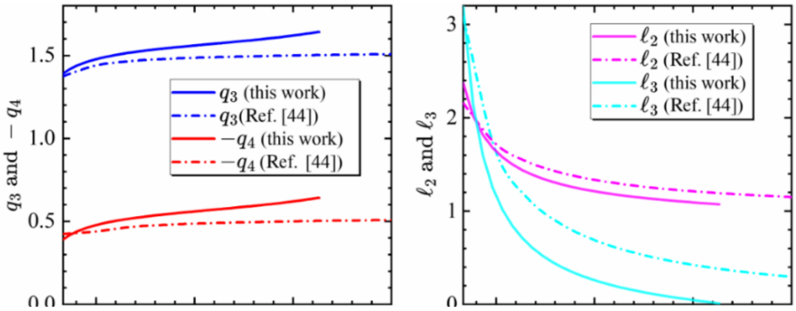

Figure 5: Calculated $(q_3, q_4, \ell_2, \ell_3)$ for $\Lambda = 0.81 : 5$ for a partial-CSR-immune chicane and ss-CSR-immune chicane.

Phys. Rev. ST Accel. Beams, vol. 3, p. 124402, 2000. `doi:10.1103/PhysRevSTAB.3.124402`

[5] C. Mitchell, J. Qiang, and P. Emma, "Longitudinal pulse shaping for the suppression of coherent synchrotron radiation-induced emittance growth", *Phys. Rev. ST Accel. Beams,* vol. 16, p. 060703, 2013. `doi: 10.1103/PhysRevSTAB.16.060703`

[6] S. Di Mitri, M. Cornacchia, and S. Spampinati, "Cancellation of coherent synchrotron radiation kicks with optics balance", *Phys. Rev. Lett.,* vol.110, p. 014801, 2013. `doi:10.1103/PhysRevLett.110.014801`

[7] Y. Jiao, X. Cui, X. Huang, and G. Xu, "Generic conditions for suppressing the coherent synchrotron radiation induced emittance growth in a two-dipoles achromat", *Phys. Rev. ST Accel. Beams,* vol. 17, p. 060701, 2014. `doi:10.1103/PhysRevSTAB.17.060701`

[8] C. Zhang, Y. Jiao, and C.Y. Tsai, "Quasi-isochronous triple bend achromat with periodic stable optics and negligible coherent-synchrotron-radiation effects", *Phys. Rev. Accel. Beams,* vol. 24, p. 060701, 2021. `doi:10.1103/PhysRevAccelBeams.24.060701`

[9] D. Douglas, "Suppression and enhancement of CSR-driven emittance degradation in the IR-FEL driver", Technical Report No. JLAB-TN-98-012, Thomas Jefferson National Accelerator Facility, 1998.

[10] P. Emma and R. Brinkmann, "Emittance Dilution through Coherent Energy Spread Generation in Bending Systems", in *Proc. PAC'97*, Vancouver, Canada, May 1997, paper 5V030, pp. 1679-1681.

[11] W. Liu, F. Zeng, and Y. Jiao, "Modified coherent synchro tron radiation point-kick model with self-consistent con sideration of bunch length varying", *Phys. Rev. Accel. Beams,* vol. 28, p. 024402, 2025. `doi:10.1103/PhysRevAccelBeams.28.024402`

[12] C. Zhang, Y. Jiao, W. Liu, and C.Y. Tsai, "Suppression of the coherent synchrotron radiation induced emittance growth in a double-bend achromat with bunch compression", *Phys. Rev. Accel. Beams,* vol. 26, p. 050701, 2023. `doi:10.1103/PhysRevAccelBeams.26.050701`

[13] F. Zeng, Y. Jiao, W. Liu, and C.Y. Tsai, "Cancelation of coherent synchrotron radiation kicks in chicane bunch compressors", *Phys. Rev. Accel. Beams,* vol. 28, p. 070701, 2025. `doi:10.1103/2vjn-t4qb`

ISBN: 978-3-95450-279-0 ISSN: 3043-0208 doi: 10.18429/JACoW-SAP2025-WEXC6

BEAM EXTRACTION AND DARK CURRENT STUDY OF A C-BAND RF PHOTO GUN

Xingguang Liu*, Shimin Jiang, Shengjin Liu, Junyu Zhu, Hui Zhang, Xiao Li
Institute of High Energy Physics, Beijing, China

Abstract

We report on beam extraction and preliminary dark current studies conducted on a 3.6-cell C-band radio-frequency (RF) photocathode gun, designed for high-brightness electron beam generation. The test programme investigated the gun's performance under varying RF power, measured the resulting dark current and examined the impact of surface preparation on field emission. Particle tracking and multipacting simulations were performed to interpret the measurements. The gun achieved gradients close to 140 MV/m with photo-induced electron extraction, while significant dark current was observed at high fields. Surface analysis after the beam test revealed discharge damage on the cathode surface disk, particularly around the center area. Cleaning method comparisons were conducted, with 'snowflake' cleaning showing no detrimental effects on surface roughness. This work represents the first reported beam test for a C-band RF photocathode gun.

INTRODUCTION

Next-generation light sources and linacs require high-brightness electron beams from the beginning. Increasing the surface field of the cathode is one of the most effective ways to get smaller emittance. In Recent years, C-band RF photo guns have drawn interests among several institutes aiming to work at an extraction field of up to 180 MV/m compared to a conventional S-band gun, which typically works at 80 MV/m and higher in some test. For example, a 3.6-cell C-band RF photo gun at SARI [1] shows that it can work at 180 MV/m in high power test, while a 2.6-cell gun at INFN/PSI [2] have been tested at 160 MV/m at a very low break-down rate. Except for these standing-wave structures, travelling-wave structures have also been designed and tested recently at PSI [3]. We began to develop a 3.6-cell C-band RF gun at IHEP-Dongguan since 2021 [4]. Beam extraction has been conducted since the end of 2024. It is the first reported beam test for a C-band RF photo gun [5] and we observed the dark current is relatively very high in our gun. So we investigated this issue with simulations and surface observations after the test.

C-BAND TEST PLATFORM

The beam tests were carried out at a C-band test platform (CTP) for the development of RF photocathode and high gradient accelerating structures at IHEP-Dongguan, which is shown in Fig. 1. A brief timeline for the development of the 3.6-cell RF photo gun is:

2021.9: initial proposal
2022.1: project start
2022.4: external review
2022.12: prototype Gun-0
2023.4: prototype Gun-1 cold test
2024.7: high power test
2024.10: installation
2024.12: Beam test
2025.4: prototype Gun-2 cold test

We have an initial prototype (Gun-0) to verify the fabrication process and conducted high power test in Jul 2024 and beam test in Dec 2024 for another protoype (Gun-1).

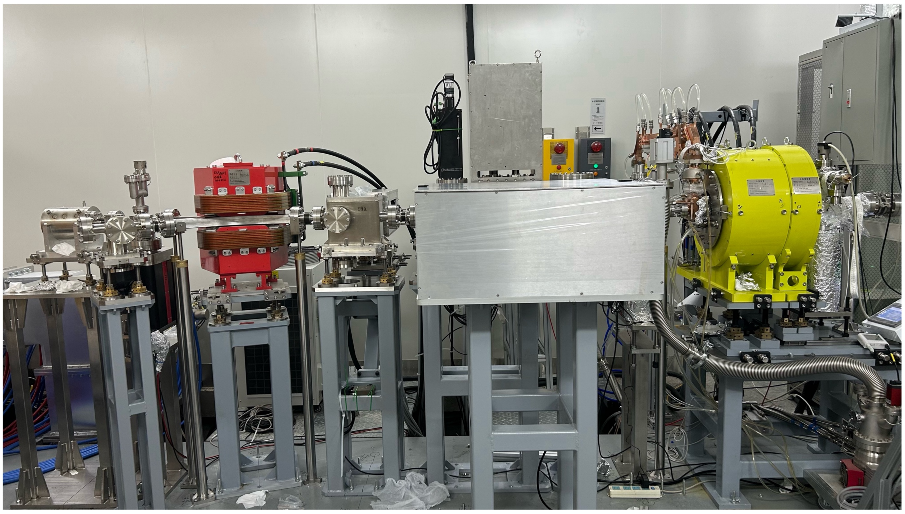

Figure 1: Test platform for the 3.6-cell RF photo gun.

---

* liuxg@ihep.ac.cn

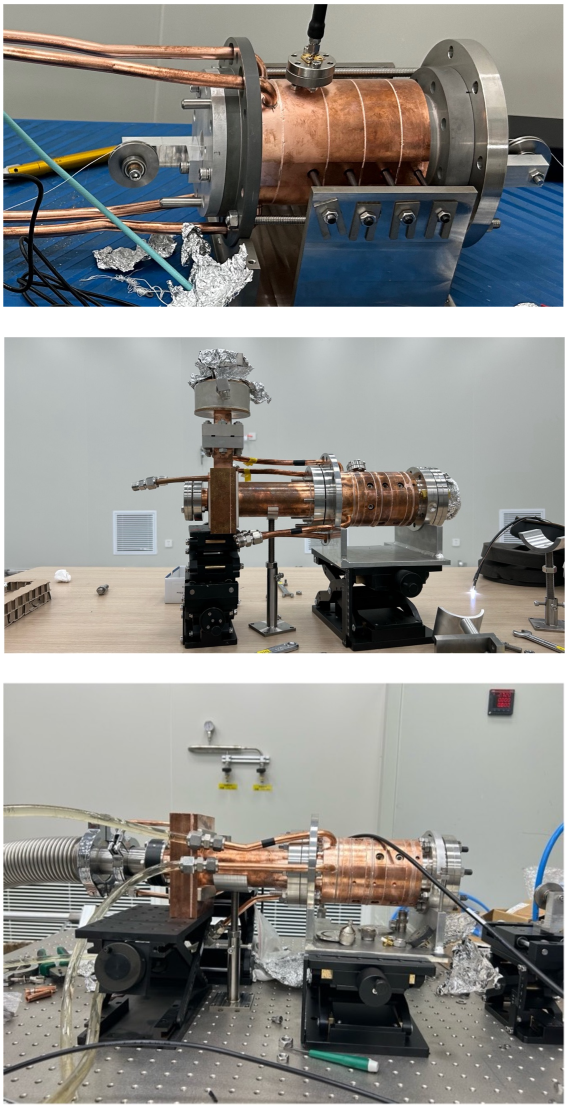

Figure 2: Prototypes for the 3.6-cell RF photo gun (Gun-0, Gun-1, Gun-2 from above.

After the beam test, another prototype with better cleaning method have been prepared for new beam test. In this paper, we focus on the beam test and dark current studies of Gun-1. The RF design and initial test results for Gun-1 can be found at Ref. [6]. Photos of three guns are shown in Fig. 2.

BEAM EXTRACTION AND THE DARK CURRENT

Beam Extraction

As shown in Fig. 3, which is measured with a Farady Cup (FC), dark current is very large in amount and occupies most of the RF pulse duration while photon induced electron beam is narrow and sharp.

Beam extraction test has been done at various RF input power, corresponding to different electric field on the cathode surface. In order to obtain a reliable extraction surface gradient for the experiment, we have used ASTRA simulation to reproduce the same beam energy at various phase and gradient. It shows that the maximum beam energy in this round of test is close to 7 MeV, corresponding to a surface graident of about 140 MV/m. At this gradient, the dark current intensity is above 7 mA.

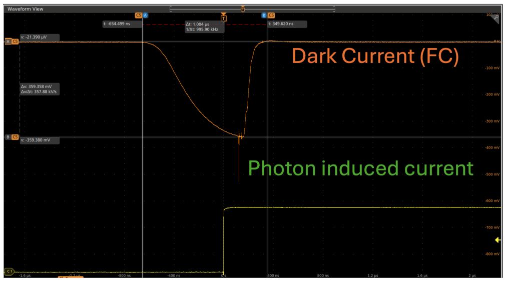

Figure 3: Dark current measurement with the Faraday Cup (FC).

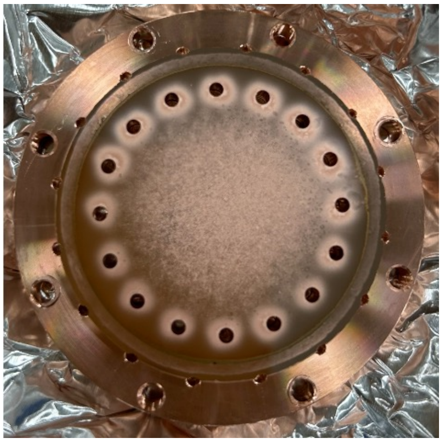

Figure 4: Dark current measurement with the Faraday Cup (FC).

Discharge Observations and Surface Check

After high-power operation, Gun-1 was dismantled into three parts: the surface disk, the standing-wave cavity and the coupler. Discharge tracks are found on the surface disk, also on the area around the cavity disk aperture. Some discharge tracks are found on the surface of ceramic window which is used to separate the vacuum between the coupler and the wave guide. Among those the cathode surface disk suffers from the most serious discharge damage, as shown in Fig. 4. It has been designed to be replaceable, so it could be inspected with surface analysis. The white dots are discharge points where the dark current charges are extracted. With eye observation one can see that the discharge tracks are more serious in the center area and gradually reduce towards outside, due to the fact that the electric field decreases in the radical direction.

Surface analysis revealed that the roughness near the center of the cathode surface is $S_a = 1\,\mu\text{m}$, compared to $S_a = 10\,\text{nm}$ before the test. A crater with a diameter around 200 µm has been observed, which is supposed to be the laser spot which stay the same during the whole test process.

ISBN: 978-3-95450-279-0 ISSN: 3043-0208 doi: 10.18429/JACoW-SAP2025-WEXC6

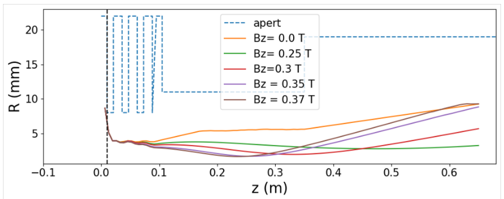

Figure 5: Dark current measurement with the Faraday Cup (FC).

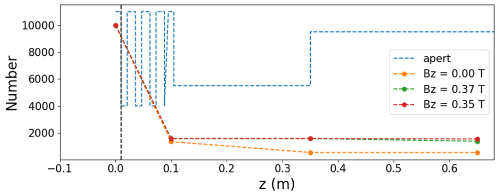

Figure 6: Dark current measurement with the Faraday Cup (FC).

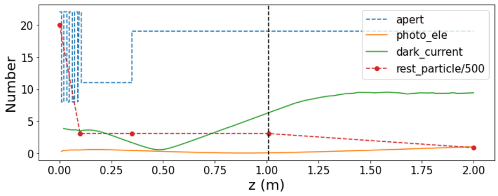

Figure 7: Beam extraction measured with FC and the dark current.

Another important observation is the serious discharge happened in the holes around the surface disk, which are designed to support a better vacuum in the gun. As a result, they should be removed in the future design and new ways to keep a good vacuum is necessary.

Simulation Trials on the Dark Current

Simulation work has been performed in several aspects. Our preliminary study with particle tracking simulation indicates that 80 percent field emitted electrons are stopped at the first disk aperture without solenoid (Fig. 5), while most of the assumed field emitted electrons from the cathode surface can pass through the gun to the downstream (Fig. 6). Also, the dark current have a larger beam size compared with photo induced beam, as shown in Fig. 7. Therefore, as to the dark current, what has been measured at the FC cannot be fully accounted to the surface emission. In this simulation, cathode surface are assumed to be a emission surface while the discharge current density is assumed a radical distribution following the transverse E_z amplitude. Areas near the disk aperture are assumed to be emission surface too, and some energetic particles can fly towards the disk surface.

Preliminary simulation on the multipacting factor, assuming typical secondary electron emission curve of copper surface. It shows that almost all electrons will concentrate near the outer corner of the disk where magnetic field are dominant at this frequency, which suggests that though further confirmation might be needed, multipacting is not a main issue in such a structure.

Cleaning Method

To study how different cleaning methods will affect the roughness of the cathode disk surface, four typical ways of cleaning are compared along with the surface check:(1) ”Ethanol + fine fabric” by hand; (2)”Ultra sonic + Deionized Water/Ethanol” which is common in superconducting structures and also recently used in very-high-frequency structures; (3) Dry ice (CO_2); (4) ”Snowflake” which is also CO_2 but much finer, common in semiconductor cleaning. In our test, only the first and the last method turn out to have no detrimental effects on the surface roughness.

CONCLUSION

A 3.6-cell C-band RF photo gun has been tested at IHEP-Dongguan, the first beam delivery from a C-band RF photogun worldwide. The gun achieved gradients up to 137 MV/m with photo induced electron extraction; however significant dark current was observed at high fields. Surface analysis after the beam test shows that serious discharge happens at the cathode surface disk. Surface cleaning method comparison shows that ‘snowflake’ cleaning will not affect the surface roughness. Some preliminary simulation studies on the dark current have been done while more detailed experimental and simulational studies are expected to understand more about the RF photocathode working at such a high gradient.

ACKNOWLEDGEMENTS

This work has been supported by the Institute of High Energy of China Academy of Science (E3545AU2).

REFERENCES

[1] C Wang *et al.*, “High-power experiment of a C-band photocathode gun”, *J. Phys.: Conf. Ser.*, vol. 2687, p. 032036, 2024. doi:10.1088/1742-6596/2687/3/032036

[2] T. Lucas *et al.*, “Developments and first results from an RF test stand for high brightness C-band photoguns at PSI”, in *Proc. IPAC’24*, Nashville, TN, May 2024, pp. 2133-2136. doi:10.18429/JACoW-IPAC2024-WEPC69

[3] T. Lucas *et al.*, “Toward a brightness upgrade to the SwissFEL: A high gradient traveling-wave RF photogun”, *Phys. Rev. Accel. Beams*, vol. 26, p. 103401, 2023. doi:10.1103/PhysRevAccelBeams.26.103401

[4] X. Liu *et al.*, “A C-band test platform for the development of RF photo cathode and high gradient accelerating structures”, *J. Phys.: Conf. Ser.*, vol. 2687, p. 042001, 2024. doi:10.1088/1742-6596/2687/4/042001

[5] X. Liu, “Initial beam test of a 3.6-cell C-band RF photo gun”, presented at the 16th International Workshop on Breakdown Science and High Gradient Accelerator Technology (HG2025), Mérida, Yucatán, Mexico, Mar. 2025, unpublished.

[6] S. Liu *et al.*, “RF design of C-band photocathode electron gun for Southern Advanced Photon Source”, *High Power Laser Part. Beams*, vol. 37, p. 014005, 2025. doi:10.11884/HPLPB202537.240195

ISBN: 978-3-95450-279-0 ISSN: 3043-0208 doi: 10.18429/JACoW-SAP2025-THNC3

PRELIMINARY DESIGN OF THE BEAM TRANSPORT SYSTEM FOR THE SUPER TAU-CHARM FACILITY*

Ruixuan Huang†,1, Jingyu Tang1, Ze Yu1, Youjin Yuan2
1University of Science and Technology of China, Hefei, China
2Institute of Modern Physics, Chinese Academy of Sciences, Lanzhou, China

Abstract

The injector of the Super Tau-Charm Facility (STCF) should provide high-quality electron and positron beams for the collider ring according to different injection schemes, which is one of the key systems to ensure the high brightness of STCF. This paper presents the preliminary physical design and beam dynamics optimization of the complex beam transport system, which interconnects the main accelerator components over approximately 550 meters. The design encompasses three major segments: the injection line from the positron linac to the damping ring (PL2DR), the extraction and transport line from the damping ring to the main linac (DR2ML), and the final transport lines from the main linac to the collider rings (ML2CR). Each segment addresses unique challenges, including transverse emittance preservation, Twiss parameter matching, sophisticated phase-space manipulation and tight restrictions on the geometrical conditions. Through detailed optics design and particle tracking simulations, these results demonstrate the feasibility of the transport system in maintaining the high beam quality essential for the STCF's physics program.

INTRODUCTION

The Super Tau-Charm Facility (STCF) is new-generation electron-positron collider proposed in China, aimed at in-depth research into tau-charm physics with unprecedented precision [1-3]. It is envisioned to achieve a peak luminosity of 5×10^{34} $\mathrm{cm^{-2}s^{-1}}$ with a center of mass energy of 2-7 GeV [4-6]. STCF will serve as a unique facility for precision measurements in the charm energy region. The injector is a sophisticated accelerator system to provide high-quality, full-energy electron and positron beams for the collider rings, serving as a key component to ensure the realization of high luminosity at STCF.

To improve the robustness of the injection process, an off-axis injection scheme is adopted, in which a schematic layout of the injector is shown as (Fig. 1) [7]. An electron beam with an intensity of 11.6 nC/bunch at 30 Hz is first generated from a thermionic gun, is then accelerated to 1.0 GeV in the first electron linac (EL1), and finally strikes a tungsten target to produce positrons. The positron beam with a bunch charge of 1.0 nC is accelerated to 1.0 GeV in the positron linac (PL) and injected into a damping ring (DR) for emittance reduction. Another electron beam with an intensity of 1.0 nC/bunch at 30 Hz is generated from a photocathode RF gun and accelerated to 1.0 GeV in the second electron linac (EL2). Both the 1.0 nC bunch charge e^-/e^+ beams are transferred to the main linac (ML) and alternately boosted to a maximum energy of 3.5 GeV. Finally, the e-/e+ beams are separated and conveyed to the e-/e+ collider rings, respectively. All the linac sections and a part of transport system are situated in the same tunnel, which will significantly reduce the construction cost.

The transport system connect the above sections and convey the electron and position beams separately from the injector to the collider rings, totally having a length of about 550 m. Optics design and beam tracking are carried out to confirm the optics matching and a sufficiently small emittance of both e-/e+ beams. The main components of the transport system are highlighted in (Fig. 1), including three parts:

(1) Injection line from PL to DR (PL2DR).
(2) Extraction and transport line from DR to ML (DR2ML).
(3) Beam transport lines from ML to CR (ML2CR).

OPTICS DEVELOPMENT

The severely short beam lifetime at STCF presents significant challenges for the injector design. For the transport system, the primary challenges include transverse emittance preservation and Twiss parameters matching. In the PL2DR, an energy-spread compression system (ECS) is carefully designed to match a very limited RF acceptance of the DR. In the DR2ML, a bunch compression system (BCS) is necessary to facilitate the transition to the ML. While in the ML2CR, tight restrictions on the geometrical conditions lead to a large curvature and a multiple horizontal-vertical bending transitions in the beam lines.

Optics of PL2DR

PL2DR is the injection line to the DR, whose length is about 90 m. It consists of a horizontal bending arc with eight 15-degree dipoles, a chicane-based ECS with four 30-degree dipoles and one 1.6-meter accelerating structure, as well as a matching unit with one 10-degree dipole. Standard FODO cells are adopted to focus the beam and realize optics matching throughout the line. As shown in (Fig. 2), the β functions at the exit of injection septum in the DR is adjusted to $\beta_{x/y}$ =9.5/4.1 m, and the dispersion is suppressed to zero, just as the DR required.

---

* Work is supported by the National Key R&D Program of China under Contract No. 2022YFA1602202, the National Natural Science Foundation of China (No.12341501 and 12175224) and the STCF key technology research and development project.

† rxhuang@ustc.edu.cn

ISBN: 978-3-95450-279-0 ISSN: 3043-0208 doi: 10.18429/JACoW-SAP2025-THNC3

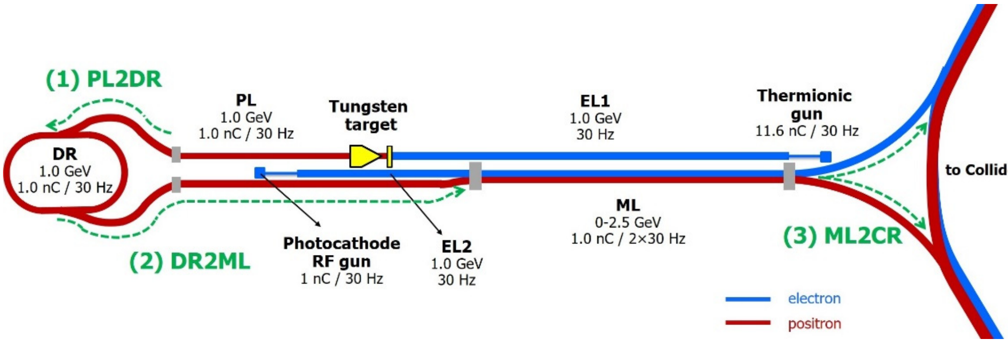

Figure 1: A schematic layout of STCF injector with transport system highlighted in green dashed lines.

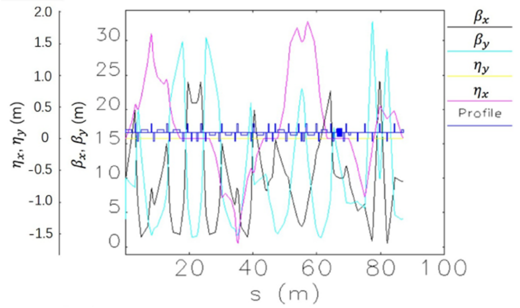

Figure 2: The β and dispersion functions for PL2DR.

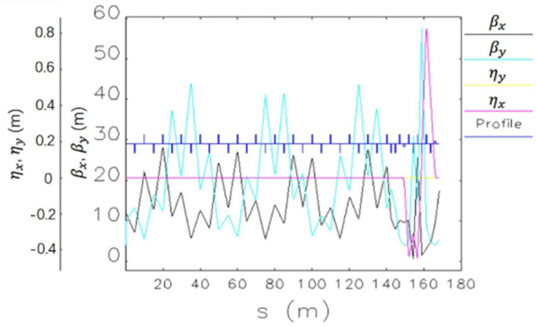

Figure 3: The β and dispersion functions for part of DR2ML.

Optics of ML2CR

The transport lines of ML2CR has the task of separating the e$^-$/e$^+$ beams and injecting them into the CRs. It should be noted that the injector tunnel (including the DR) is located 6.5-meter underground while the collider tunnel is placed on the ground level. Naturally, ML2CR should also deflect the beam vertically to the CRs. Finally, the e$^-$/e$^+$ beams are steered to two different directions and injected into straight sections of the CRs which are symmetrically located on the opposite to the interaction point. The total bending angle required for each line is 60-degree, which is realized by six 10-degree dipoles. In the R&D stage, the coupled optics of the alternating bending lattice are treated by the superposition of separate optics analyses for the horizontal and vertical planes, as shown in (Fig. 4). The β functions at the exit of injection septum in the CR is adjusted to $\beta_{x/y} = 12.9/1.4$ m, and the dispersion is suppressed to zero, just as the CR required.

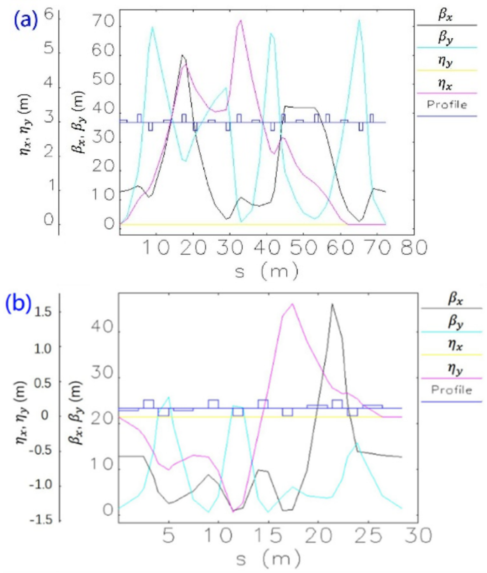

Figure 4: The β and dispersion functions of the horizontal optics (a) and vertical optics (b) for ML2CR.

BEAM DYNAMICS OPTIMIZATION

Table 1: Beam Parameters at Entrance of Each Line

Parameters	PL2DR	DR2ML	ML2CR
$\beta_{x/y}$ (m)	9.9/10.0	9.5/4.1	12.9/1.4
$\alpha_{x/y}$	-1.3/0.2	0/0.1	0/0
$\varepsilon_{nx/ny}$ (μm.rad)	165/75	21.5/0.4	3.0/3.0
dE/E (rms)	0.6%	0.5%	0.2%
σ_s (mm)	1.5	4.5	1.0

To meet the high luminosity requirements, the injector's emittance and energy spread are both crucial parameters, which should be carefully restrained. We used the tracking code Elegant [8] for beam dynamics optimization. Space charge effect and coherent synchrotron radiation in dipoles are considered in simulation. The input beams are modelled as a 3-σ truncated Gaussian distribution with the specific parameters rigorously determined by the upstream sections. Critical beam parameters at the injection point of each transport line are summarized in Table 1. To ensure a consistent comparison, all the emittance discussed in this paper are the normalized RMS values.

Transverse Emittance Control

For the positron beam, it is quite challenging to preserve the emittance because of its large divergence angles due to the target-based production procedure. The evolution of transverse emittance in the PL2DR line is shown in (Fig. 5). Through careful optimization, we achieved a significant reduction in emittance growth, with increasing by only 3.6% and 0.8%, respectively.

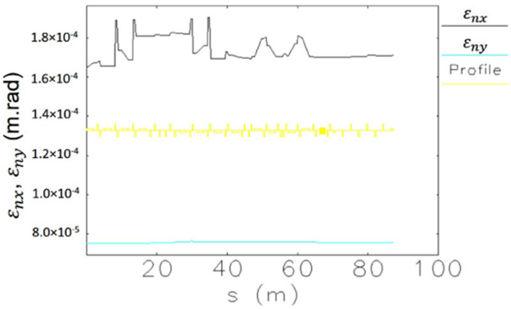

Figure 5: Evolution of transverse emittance in PL2DR.

In the DR2ML line, the emittance growth mainly occurs in curved arcs, as shown in (Fig. 6). Finally, the emittance increase is well controlled within 28%, fully satisfying the requirements for ML injection.

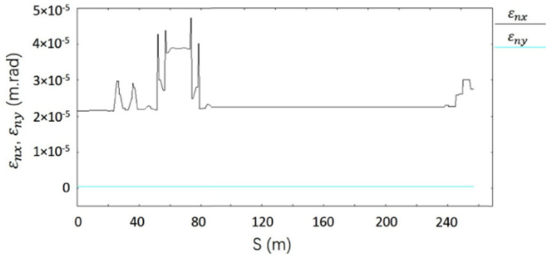

Figure 6: Evolution of transverse emittance in DR2ML.

Likewise, along the ML2CR lines, a measurable increase in the beam emittance is also observed. By optimizing the optics and suppressing the high-order dispersion terms, the emittance growth at the entrance of CR is limited to within 54%. Despite a considerable growth, its value remains within the acceptance limit of the CR.

Energy-Spread and Bunch Compression

Considering the DR momentum acceptance and the CSR effect, a smaller energy spread with a longer bunch length is desirable for the positron beam. The ECS consists of a four-bending C-shape chicane and one 1.6 m-long S-band accelerating tube. Long dipoles and large bending angles can effectively increase R56 with a reduced magnetic field. The RMS energy spread of the positron beam is substantially decreased from 0.6% to 0.2% and the RMS bunch length is increased from 1.5 mm to 4.3 mm.

The beam extracted from the DR are characterized by a long bunch length, which mandates the use of a BCS to facilitate downstream acceleration. The BCS comprises an RF section and a subsequent dispersive section, both of which share the same design as the ECS. Consequently, the RMS bunch length is reduced from 4.5 mm to 1.0% at the expense of increasing the RMS energy spread from 0.05% to 0.55%.

CONCLUSION

The preliminary design of the beam transport system for the STCF injector has been successfully completed, demonstrating its capability to fulfill the stringent beam quality requirements for high-luminosity collision operations. A robust optics design has been developed for the three transport segments (PL2DR, DR2ML and ML2CR), effectively accommodating the distinct challenges of each section, from energy spread and bunch compression to complex geometrical constraints. Through meticulous beam dynamics optimization using the code Elegant, the transverse normalized emittance growth has been constrained to acceptable levels across the entire transport system, ensuring beam quality at the entrances of each section. With the specialized ECS and BCS, successful phase-space manipulation has been performed to better match the RF acceptance of the downstream sections. Future work will focus on further optimization of beam dynamics through detailed technical design, and integration with injection procedures of both the DR and CR.

REFERENCES

[1] Jiancong Bao *et al*, "Conceptual Design Report of Super Tau-Charm Facility: The Accelerator", *Nucl. Sci. Tech.*, vol. 36, pp. 242, Sep. 2025, arXiv: 2509.11522 [physics.acc-ph]. `doi:10.48550/arXiv.2509.11522`

[2] Ye Zou *et al*, "Optics design of the Super Tau-Charm Facility collider rings", Jul. 2025, arXiv: 2507.18924 [physics.acc-ph]. `doi:10.48550/arXiv.2507.18924`

[3] Linhao Zhang *et al*, "Crab-waist interaction region design and integration for the Super Tau-Charm Facility", Oct. 2025, arXiv: 2510.09198 [physics.acc-ph]. `doi:10.48550/arXiv.2510.09198`

[4] K. Oide *et al*, "Design of beam optics for the Future Circular Collider *e*+*e*−-collider rings", *Phys. Rev. Accel. Beams.*, vol. 19, no. 11, Nov. 2016. `doi:10.1103/physrevaccelbeams.19.111005`

[5] H. Peng *et al*, "Super Tau-Charm Facility of China", *Physics,* vol. 49, no. 8, pp.513-524, 2020. `doi:10.7693/wl20200803`

[6] P. Raimondi *et al*, "Application of frequency map analysis to beam-beam effects study in crab waist collision scheme", in *Proc. EPAC'08,* Genoa, Italy, 2008, pp. 2620. `doi:10.1103/PhysRevSTAB.14.014001`

[7] The CEPC Study Group, "CEPC Technical Design Report - Accelerator", *Radiation Detection Technology and Methods,* vol. 8, pp. 1-1105, 2024. `doi:10.1007/s41605-024-00463-y`

[8] M. Borland, "elegant: A Flexible SDDS-Compliant Code for Accelerator Simulation", *Advanced Photon Source,* LS-287, Sep. 2000. `https://www.aps.anl.gov/Accelerator-Operations-Physics/Software`

TRACKING SIMULATION OF LONGITUDINAL BEAM DYNAMICS IN A TRIPLE RF SYSTEM FOR ELECTRON STORAGE RINGS

Jincheng Xiao, Tianlong He*, Weimin Li†
National Synchrotron Radiation Laboratory, USTC, Hefei, China

Abstract

For diffraction-limited storage rings, the triple radio-frequency (RF) system has been proposed to achieve further bunch lengthening or to meet specific requirements for longitudinal injection. The choice of RF cavity parameters for the triple RF system has a significant influence on the longitudinal beam dynamics. Macroparticle tracking simulation is commonly used to accurately analyze this influence. In this paper, we extend the STABLE code to study the dynamics of the triple RF system assumed for the Hefei Advanced Light Facility storage ring. It is found that there are two important factors that possibly limit the bunch lengthening.

INTRODUCTION

The use of a double RF system to lengthen the bunch to mitigate intrabeam scattering (IBS) and Touschek scattering effects has been widely adopted in fourth-generation light sources [1,2]. More recently, a triple RF system has been proposed to further extend the bunch length and meet specific requirements for longitudinal injection. Theoretical analyses suggest that a triple RF system can approximately double the bunch lengthening capability of a double RF system [3]. However, potential instability issues, which could significantly hinder bunch lengthening, cannot be fully explored using analytical formulas.

To study longitudinal beam dynamics in double RF systems, tracking simulations are typically employed, as they provide more comprehensive, realistic, and reliable computational results. Various tracking methods have been developed for double RF systems [4–6], which are good references to implement tracking simulation for triple RF systems. In this work, we extend the STABLE code—a GPU-accelerated multi-particle, multi-bunch tracking method—by incorporating additional functional modules to enable the simulation of triple RF systems [6]. This extended code is then applied to study the assumed triple RF system for the Hefei Advanced Light Facility storage ring (HALF), which includes two HCs of order 3 and 5 (3HC and 5HC).

STABLE FOR THE TRIPLE RF SYSTEM

STABLE is a MATLAB code that comprehensively accounts for the effects of short-range wakefields, as well as the fundamental and higher-order modes of RF cavities on beam dynamics. It is used to simulate the longitudinal motion of bunches in a double RF system under arbitrary filling patterns. To enhance its capability for accurately simulating longitudinal beam dynamics in a triple RF system, relevant functional modules are integrated into the code. The process for running this code is shown in Fig. 1.

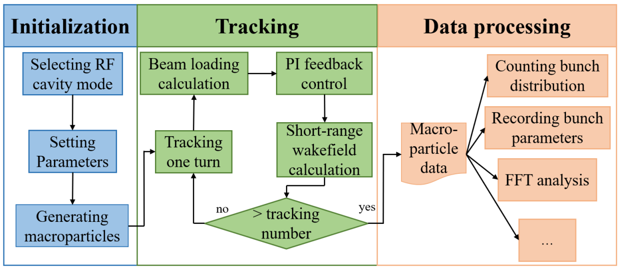

Figure 1: The flowchart of STABLE.

Related Function Modules

PI feedback module To achieve a realistic LLRF feedback for the RF cavities, a PI feedback module has been incorporated. This module first computes the error between the measured and target cavity voltages, then processes it through the PI controller to determine the corrected transmitter current, which is expressed as:

$$\Delta\tilde{I}_g(t) = \frac{\Delta\tilde{V}(t)}{R_L}K_P + \int_0^t \frac{\Delta\tilde{V}(t)}{R_L}K_I dt, \tag{1}$$

where $\Delta\tilde{I}_g$ is the corrected generator current phasor, $\Delta\tilde{V}$ is the error cavity voltage, R_L is the loaded shunt impedance, K_P and K_I are the proportional and integral gains, respectively. Last the generator current phasor is updated with $\Delta\tilde{I}_g + \tilde{I}_{g0}$, where $\tilde{I}_{g0}$ is the initialized generator current phasor, and it is subsequently applied to the cavity voltage after a specified delay d. A detailed flowchart illustrating this process is provided in Fig. 6 of Reference [7].

Initially, this module was implemented to regulate the cavity voltage of the main cavity (MC). It was later integrated into the harmonic cavity (HC) module to enable the simulation of an active HC.

RF cavity module A dedicated higher-order HC module has been integrated into the code. To accurately simulate RF cavity under various conditions, the RF cavity module has been designed to operate in three distinct modes: ideal RF cavity, passive RF cavity, and active RF cavity.

In the ideal cavity mode, the cavity voltage remains fixed at the target voltage. In the passive RF cavity mode, the cavity voltage is determined solely by the beam loading voltage. In the active RF cavity mode, a PI feedback module is incorporated, ensuring that the total cavity voltage is the sum of the beam loading voltage and the transmitter voltage.

---

* htlong@ustc.edu.cn
† lwm@ustc.edu.cn

Parameter Initialization

Before running the STABLE code, it is essential to initialize the relevant parameters. A dedicated initialization section has been implemented in the code, organizing the parameters into a structured variable to prevent data conflicts during computation. The main parameter settings are divided into three categories: storage ring parameters, RF cavity parameters, and PI feedback parameters.

Storage Ring Parameters This study uses the parameters of the HALF for initialization, with detailed values available in Reference [8]. Each bunch is represented by 10,000 macroparticles, and the tracking simulation is performed over 300,000 turns.

RF Cavity Parameters First, the desired operating mode is selected. The specific RF cavity parameters are set according to the system's actual conditions. In the active mode, the target total cavity voltage must be specified. Typically, the required cavity voltages for the target bunch lengthening scheme are precomputed using analytical formulas.

In this study, the parameters are based on the MC and 3HC settings in HALF's double RF system scheme. For the three actively controlled RF cavities in the triple RF system under study, the detuning frequencies are configured to minimize transmitter power. For MC and 5HC, the detuning directions are negative, the loading angle is set to zero, and the detuning frequency Δf is calculated with:

$$\Delta f = \frac{n f_{rf} I_0 F \cos(\phi)}{V_c} \frac{R_L}{Q_L}, \tag{2}$$

where n is the order of RF cavity, f_{rf} is the RF frequency, I_0 is the beam current, F is the bunch form factor of corresponding RF cavity, V_c and ϕ are the cavity voltage amplitude and phase, respectively, Q_L is the loaded quality factor. For 3HC, since the detuning direction is positive, the beam loading voltage in equilibrium should be as close as possible to the target cavity voltage to minimize transmitter power. The detuning frequency Δf and unload impedance R_s are calculated accordingly:

$$R_s = \frac{V_c}{2 I_0 F \cos(\psi)}, \tag{3}$$

$$\Delta f = \frac{n f_{rf} \tan(\psi)}{2 Q_s}, \tag{4}$$

where ψ is the detuning angle and Q_s is the unload quality factor.

PI Feedback Parameters For each actively controlled RF cavity, individual settings are required. In addition to ensuring the physically meaningful configuration of parameters such as the PI delay d, selecting appropriate values for the proportional gain K_P and the integral gain K_I is crucial: If K_P is too large, the system becomes unstable, leading to beam loss. If K_P is too small, the cavity voltage cannot be regulated to the target voltage effectively. If K_I is too large, zero-mode oscillations may be induced, while a very small K_I results in slow convergence of the cavity voltage to the target value.

In this study, K_P is set to 1, while K_I is chosen within the range of 0.01 to 0.1.

APPLICATION TO HALF

Benchmark Test

To verify the accuracy of the modified STABLE code, we computed the steady-state bunch distribution in HALF's triple RF system under optimal bunch stretching conditions using both the semi-analytic algorithm and tracking simulations. We set the test beam current to 50 mA to avoid instability phenomena at low current. The results, displayed in Fig. 2, show the bunch center and bunch length distribution after reaching equilibrium for 4 bunch trains with 80 % filling.

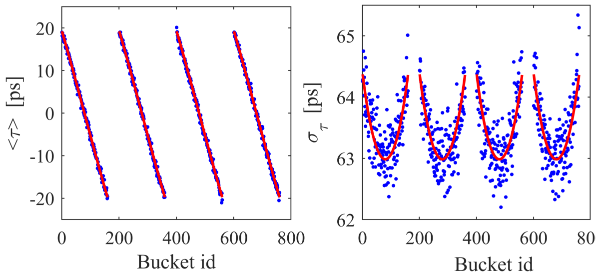

Figure 2: The bunch center (left) and bunch length (right) distribution after reaching equilibrium for 4 bunch trains with 80 % filling. The solid line in red represents the semi-analytical method results, and the scatter points in blue represent the tracing simulation results.

Figure 2 shows that the tracking simulation results closely match those obtained from the semi-analytic calculation, confirming the correctness of the extended STABLE code. All simulations were conducted using a GeForce RTX 4070 GPU, equipped with 5888 CUDA cores. The simulations tracked 2000 turns in just 15 seconds, demonstrating the high efficiency of the STABLE code in simulating the triple RF system.

Periodic Transient Beam Loading

When using the HC to stretch the bunch length, instability may occur, severely hindering the bunch lengthening process. One such instability is the periodic transient beam loading (PTBL) instability, also known as mode-1 instability, which can arise even under uniform filling conditions. The severity of PTBL is positively correlated with both the beam current and the R/Q value of the HC. Therefore, to design the HC parameters of the triple RF system effectively, it is essential to study PTBL using tracking simulations.

It is commonly believed that adding a higher-order HC with an opposite detuning direction can help dampen the

PTBL induced by the lower-order HC. However, our tracking results show that this assumption is incorrect. Figure 3 presents the tracking results of the beam's longitudinal motion after 300,000 turns at standard beam current using STABLE.

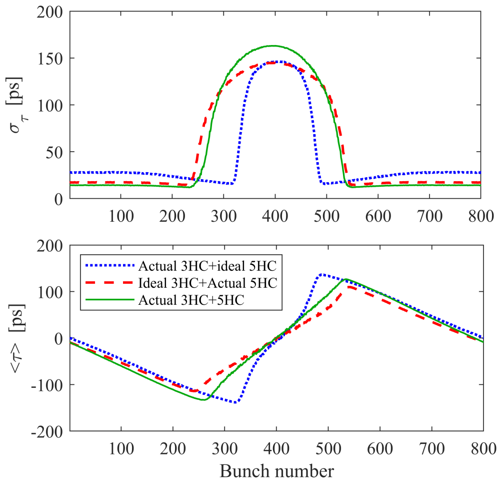

Figure 3: The bunch-by-bunch centers (bottom) and bunch lengths (top) distribution for 800 bunches at beam current of 350 mA, obtained at the end of tracking simulation. For comparison, the distributions are manually shifted so that the maximum bunch length occurs at bunch number 400.

The results show that significant PTBL occurred in all three cases. Furthermore, when considering the beam loading effects of both HCs, the PTBL effect is more pronounced compared to when considering the loading of only one HC. This indicates that the combined effects of the two HCs actually amplify the PTBL effect, rather than mitigating it.

Another Bunch Equilibrium Density Distribution

It is worth mentioning that during the study of the anomalous PTBL phenomenon, an unexpected bunch equilibrium density distribution was observed. When 3HC was set as an ideal cavity and 5HC as a passive cavity (thus no longer providing optimal bunch stretching), the bunch center was found to continuously shift to one side. In the final equilibrium, the bunch was hardly stretched, and the cavity voltage of 5HC deviated from the target value. This instability was later observed in the semi-analytic algorithm as well, with corresponding calculation results shown in Fig. 4.

In Fig. 4, the results from both methods are almost identical, both indicating that after reaching equilibrium, the bunch center is −155 ps, which significantly deviates from the synchronous phase. Moreover, the bunch length becomes 7 ps, much less than expected.

Notably, when the working mode of 5HC was changed to an active cavity, this instability was suppressed under the same target cavity voltage. This demonstrates that controlling the cavity voltage through PI feedback can effectively mitigate the instability. Furthermore, when 5HC remained in passive mode and 3HC was set as a passive cavity, the instability did not occur. However, when the detuning frequency of 3HC was increased (i.e., reducing the load cavity voltage of 3HC), the instability reappeared. This suggests that this phenomenon may be driven by the beam loading of 5HC and damped by 3HC, highlighting a complex interaction that warrants further investigation.

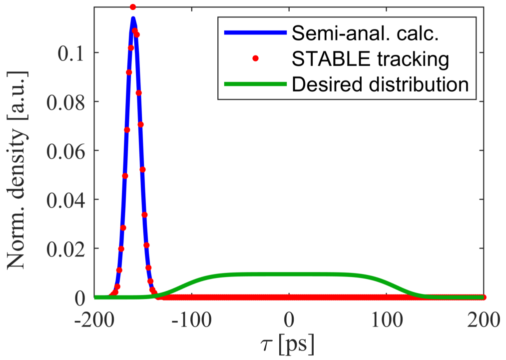

Figure 4: Bunch density distributions obtained by semi-analytical calculation (blue) and tracking simulation (red), compared with desired distribution (green).

CONCLUSION

In this paper, we expanded the STABLE code and modularized it to facilitate and enhance the study of longitudinal beam dynamics in a triple RF system. Benchmark test results indicate that this code is not only accurate, but also efficient. By applying to HALF, it is found that the PTBL effect is jointly enhanced by two HC cavities, making it more intense than in the double RF system. In addition, an unexpected bunch distribution was observed, posing challenges for the use of the passive 5HC scheme. These findings provide key insights for the design of triple RF systems.

To mitigate PTBL, future work will explore how feedforward and feedback techniques affect its threshold. Additionally, the influence of higher-order modes on longitudinal beam motion will be considered in subsequent research.

ACKNOWLEDGEMENTS

This work was supported by the National Natural Science Foundation of China (No.12375324, No.12105284, and No.11475167) and the Fundamental Research Funds for the Central Universities (No.WK2310000127).

REFERENCES

[1] F. J. Cullinan, Å. Andersson, and P. F. Tavares, "Review of harmonic cavities in fourth-generation storage rings", in *Proc. FLS2023*, Luzern, Switzerland, 2023. `doi:10.18429/JACoW-FLS2023-MO2L3`

[2] J. M. Byrd and M. Georgsson, "Lifetime increase using passive harmonic cavities in synchrotron light sources", *Phys. Rev. ST Accel. Beams*, vol. 4, p. 030701, 2001. `doi:10.1103/PhysRevSTAB.4.030701`

[3] G. Bassi, A. Khan, and V. Smaluk, “Bunch lengthening induced by a combination of higher-harmonic cavities of different order in low-emittance rings”, in *Proc. IPAC’24*, Nashville, TN, USA, May 2024, pp. 2952–2955. `doi:10.18429/JACoW-IPAC2024-THBD2`

[4] G. Skripka, R. Nagaoka, M. Klein, F. Cullinan, and P. F. Tavares, “Simultaneous computation of intrabunch and interbunch collective beam motions in storage rings”, *Nucl. Instrum. Methods Phys. Res. Sect. A*, vol. 806, p. 221, 2016. `doi:10.1016/j.nima.2015.10.029`

[5] M. Migliorati and L. Palumbo, “Multibunch and multiparticle simulation code with an alternative approach to wakefield effects”, *Phys. Rev. ST Accel. Beams*, vol. 18, p. 031001, 2015. `doi:10.1103/PhysRevSTAB.18.031001`

[6] T. He and Z. Bai, “Graphics-processing-unit-accelerated simulation for longitudinal beam dynamics of arbitrary bunch trains in electron storage rings”, *Phys. Rev. Accel. Beams*, vol. 24, p. 104401, 2021. `doi:10.1103/PhysRevAccelBeams.24.104401`

[7] T. L. He, W. W. Li, Z. H. Bai, and W. M. Li, “Analytic formulas for the D-mode Robinson instability”, *Phys. Rev. Accel. Beams*, vol. 27, p. 064402, 2024. `doi:10.1103/PhysRevAccelBeams.27.064402`

[8] J. Xiao, T. He, and W. Li, “Periodic transient beam loading effect in triple radio-frequency systems”, *Phys. Rev. Accel. Beams*, vol. 28, p. 104401, 2025. `doi:10.1103/zd54-9t48`

ISBN: 978-3-95450-279-0 ISSN: 3043-0208 doi: 10.18429/JACoW-SAP2025-THP03

A UNIVERSAL NUMERICAL OPTIMIZATION FRAMEWORK FOR STUDYING SEEDED FREE-ELECTRON LASER SCHEMES

Zihan Wang, Zhenghe Bai*, Guangyao Feng†
National Synchrotron Radiation Laboratory, USTC, Hefei, China

Abstract

Seeded free-electron lasers (FELs) have become indispensable tools across numerous scientific fields, owing to their high coherence and stability. To facilitate the discovery and optimization of such FELs, we propose a general-purpose framework utilizing intelligent optimization algorithms for identifying high-performance seeded FELs. In this paper, we demonstrate that our framework can automatically reproduce established seeded FELs, eliminating the need for prior physical analysis. Furthermore, this framework has the potential to discover novel schemes through the systematic incorporation of additional physical elements.

INTRODUCTION

Free-electron lasers (FELs) represent a transformative light source capable of generating high-brightness, megawatt-level pulsed beams with femtosecond-scale duration and exceptional spatial-temporal coherence [1]. A leading approach to generating short-wavelength radiation in the ultraviolet and X-ray regions is self-amplified spontaneous emission (SASE) FELs. However, SASE radiation exhibits low temporal coherence and pronounced shot-to-shot fluctuations, as the amplification process initiates from stochastic shot noise inherent in the electron beam [2].

To overcome these limitations, seeded FELs have been developed as a promising alternative. A seeded FEL operates by imprinting a periodic density modulation onto a relativistic electron beam using external coherent seed lasers and optical components. This pre-bunched beam then traverses an undulator magnet. Within the high-gain FEL regime, the induced micro-bunching is amplified through coherent emission and energy extraction, generating intense, fully coherent radiation at the seed wavelength or its harmonics. Achieving micro-bunching is the most important aspect of seeded FELs. High-gain harmonic generation (HGHG) [3] first initiates energy modulation with an external seed laser, and then converts this modulation into density modulation using a dedicated chicane. While HGHG can generate the high-order harmonic components of the seed laser frequency, its conversion efficiency decreases markedly with increasing harmonic number. Building on HGHG, echo-enabled harmonic generation (EEHG) [4] has been developed, which employs two seed lasers and two chicanes to generate a much higher harmonic density modulation in the beam from a relatively small initial energy modulation.

Different seeded FELs produce distinct micro-bunching patterns due to their unique phase space manipulation mechanisms. In this paper, we propose a general-purpose numerical framework utilizing intelligent optimization algorithms (IOA) for identifying high-performance seeded FELs. We will introduce the main components of this framework and their respective functions. Subsequently, we will illustrate its workflow and demonstrate its effectiveness with an example.

PROPOSED FRAMEWORK

The schematic layout of the optimization framework is shown in Fig. 1. It comprises five key components: (i) element definition layer, (ii) initial beam state, (iii) "black box" layer, (iv) final beam state, and (v) objective layer. The element definition layer specifies all seed lasers and optical elements available for the optimization process, with their parameters treated as variables within this framework. The initial beam state defines critical parameters of the initial beam configuration, including beam energy, relative energy spread, and phase space distribution. The "black box" layer conducts intelligent optimization by randomly selecting elements from the element definition layer along with their corresponding parameters. The final beam state characterizes the information of beam at the entrance of the radiator, which are directly determined by the initial beam state and the "black box" layer. The objective layer represents the key performance indicators for the required seeded FELs and serves as the objective functions for IOA.

First, all available seed lasers, optical elements, and critical parameters of the initial beam configuration are defined in the element definition layer and the initial beam state. These initial conditions are then passed to the "black box" layer for application of IOA. Within this layer, potential schemes are simulated. For each scheme, the resulting beam information is the final beam state at the radiator entrance. Here, by analyzing the information under the given objective functions, the potential schemes are sorted into distinct non-dominated layers. This ranking result is then utilized in the subsequent intelligent optimization cycle. Through multiple iterations of this process, seeded FEL schemes capable of achieving high performance for the specified objectives are identified.

EXAMPLE

We demonstrate our framework with an example, identifying high-performance seeded FELs that use only seed lasers for energy modulation and chicanes for density modulation. For simplicity and generality, we neglect the process in the last radiator. Considering the synchronization challenges inherent in multi-laser systems and the complexity of configuration, we configure the element definition layer with

---

* baizhe@ustc.edu.cn

† fenggy@ustc.edu.cn

ISBN: 978-3-95450-279-0 ISSN: 3043-0208 doi: 10.18429/JACoW-SAP2025-THP03

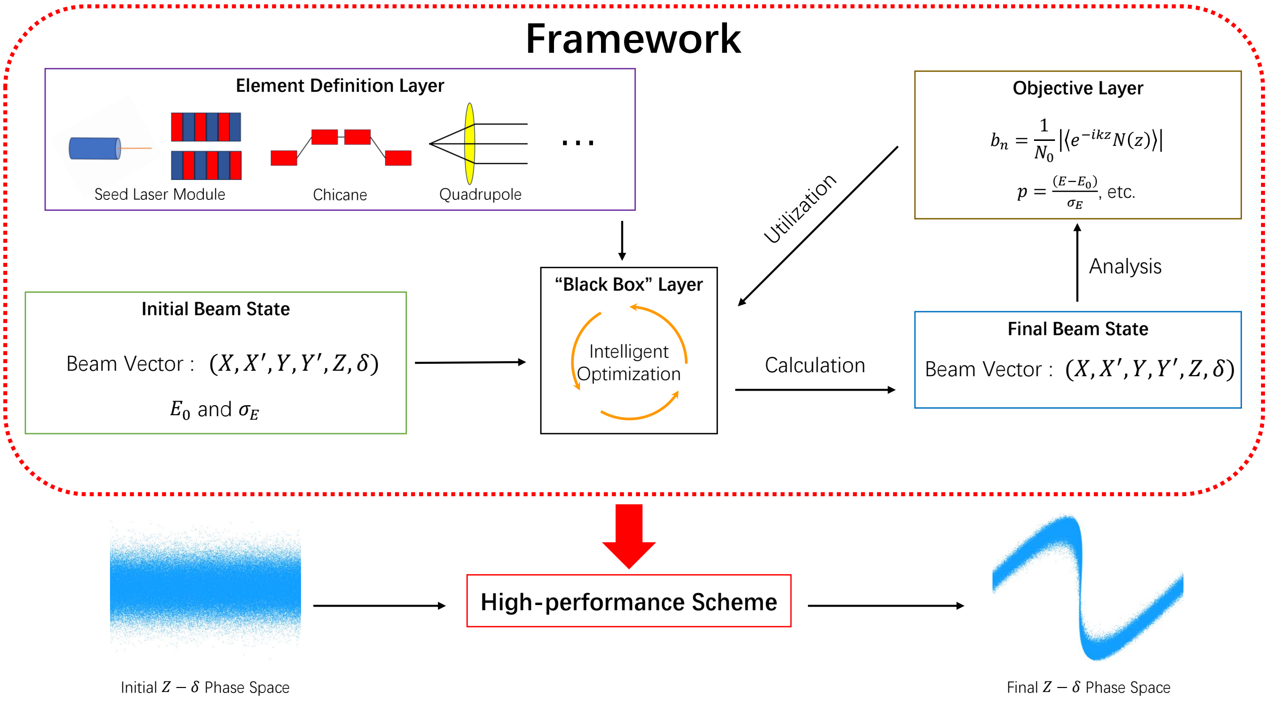

Figure 1: Description of the framework for identifying schemes of seeded FELs.

three seed laser modules and three chicanes. The seed laser module provides standard sine energy modulation. We adopt standard FEL parameters for the initial beam state, characterized by an initial Gaussian energy distribution with an average energy of 1.2 GeV and an energy spread of 0.15 MeV.

In this example, the NSGA-II algorithm [5] is employed, with the characteristic harmonic number and characteristic bunching factor designated as optimization targets. For each scheme, the maximum harmonic number at which the bunching factor exceeds 0.02 is designated as its characteristic harmonic number. The characteristic bunching factor is defined as that corresponding to the characteristic harmonic number. Table 1 lists the ranges of key parameters for both the seed lasers and chicanes.

Table 1: Ranges of Key Parameters

Parameter	**Min. value**	**Max. value**
Wavelength (Laser)	160 nm	360 nm
Energy modulation strength (Laser)	7.5 keV	1.5 MeV
Dispersive strength (Chicane)	0	0.1 m

For better comparison of different schemes, we impose an additional rule: when two schemes share the same characteristic harmonic numbers and their characteristic bunching factors are not significantly distinct, the scheme with fewer elements is considered superior. To achieve this, we propose a modified characteristic bunching factor. The expression for this modified characteristic bunching factor at the h-th harmonic can be expanded as:

$$\tilde{B}(h) = B(h) - N_{\mathrm{e}} \cdot f(h) \tag{1}$$

where $B(h)$ is the characteristic bunching factor for the h-th harmonic, N_{e} is the number of physical elements, and $f(h)$ is a pre-defined evaluation function that is always positive and decreases as h increases.

The optimization result for this example is shown in Fig. 2. Six distinct schemes were identified under the constraint of limiting the harmonic number to ≤ 200. The "LC" scheme corresponds to HGHG, which achieves high bunching factors only at low harmonic numbers. In contrast, the "LCLC" scheme (corresponding to EEHG) outperforms HGHG for harmonic numbers above 10. The "LLC" scheme employs two lasers of different wavelengths to achieve high bunching factors at the sixth and seventh harmonics; its physical mechanism differs from both HGHG and EEHG. For harmonic numbers exceeding 50, the other three schemes utilizing three lasers can also achieve significantly larger bunching factors through precise configurations of lasers and chicanes.

This optimization framework successfully reproduces established results for HGHG and EEHG while revealing that several other schemes also achieve high bunching factors. The corresponding longitudinal phase spaces are shown in Fig. 3. However, in the above optimization, the energy modulation strength was only treated as a constraint. This "LLC" scheme requires significantly higher energy modulation strength than the EEHG scheme. This results in substantial energy spread within the radiator, which is detrimental to the subsequent lasing process. By comparison, the three

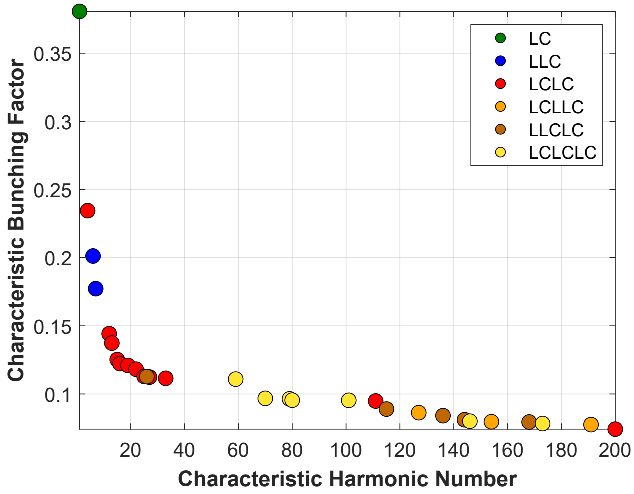

Figure 2: Characteristic harmonic numbers and characteristic bunching factors of different schemes from the optimization framework, where the evaluation function is defined as $f(h) = 0.1/\sqrt[3]{h}$. The "LC" scheme denotes a configuration where the first element is a laser and the second is a chicane; this naming convention applies analogously to other schemes.

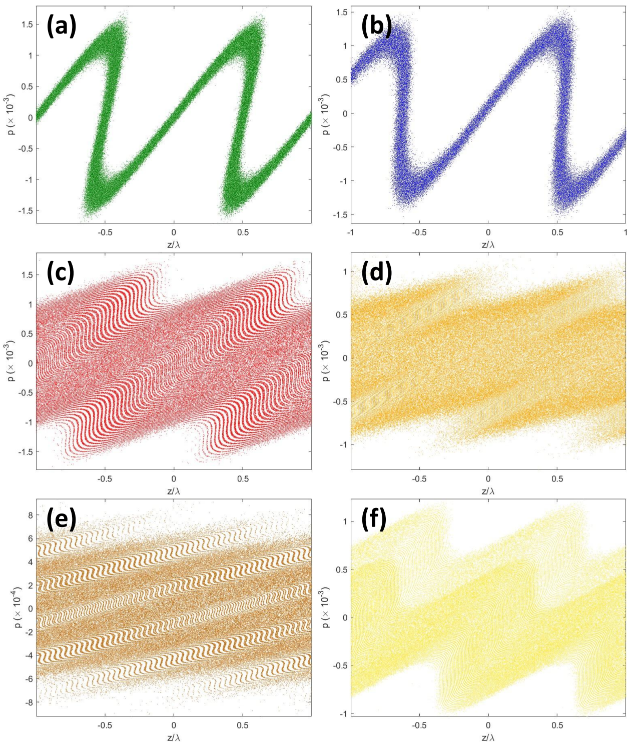

Figure 3: Longitudinal phase spaces in different schemes: (a) the "LC" scheme, (b) the "LLC" scheme, (c) the "LCLC" scheme, (d) the "LCLLC" scheme, (e) the "LLCLC" scheme, and (f) the "LCLCLC" scheme.

schemes utilizing three lasers can achieve comparable or better performance with less energy modulation strength than EEHG. However, their configurations are inherently more complex. Furthermore, their physical mechanism closely resembles that of EEHG, differing primarily in the addition of an extra pre-bunching stage, thus enhancing the bunching factors at specific harmonic numbers.

CONCLUSION

In this work, we proposed a universal numerical optimization framework for automated design and discovery of seeded free-electron laser schemes. Using this framework, we reproduced established results for HGHG and EEHG. Although other schemes were discovered simultaneously, their radiation performance failed to demonstrate significant improvement over EEHG and were found to exhibit disadvantages upon analysis. Consequently, we conclude that only HGHG and EEHG emerge as high-performance schemes implementable using standard laser modules and chicanes alone.

This optimization framework enables the discovery of novel seeded FEL configurations. Future work will enhance the framework by incorporating additional physical elements and modifying the initial beam state, with the goal of considering other physical mechanisms. Our research revealed that relying solely on harmonic number and bunching factor is insufficient to fully characterize the performance differences between schemes. This limitation can be addressed by refining the objective layer and constraints of the framework, such as incorporating energy modulation strength as an objective function under fixed harmonic numbers or bunching factors.

REFERENCES

[1] C. Pellegrini, A. Marinelli, and S. Reiche, "The physics of x-ray free-electron lasers", *Rev. Mod. Phys.*, vol. 88, p. 015006, 2016. `doi:10.1103/RevModPhys.88.015006`

[2] E.L. Saldin, E.A. Schneidmiller, and M.V. Yurkov, "Influence of nonlinear effects on statistical properties of the radiation from SASE FEL", *Nucl. Instrum. Methods A*, vol. 407, pp. 285–290, 1998. `doi:10.1016/S0168-9002(98)00036-9`

[3] L.H. Yu, "Generation of intense uv radiation by subharmonically seeded single-pass free-electron lasers", *Phys. Rev. A*, vol. 44, pp. 5178–5193, 1991. `doi:10.1103/PhysRevA.44.5178`

[4] Gennady Stupakov, "Using the Beam-Echo Effect for Generation of Short-Wavelength Radiation", *Phys. Rev. Lett.*, vol. 102, p. 074801, 2009. `doi:10.1103/PhysRevLett.102.074801`

[5] K. Deb, A. Pratap, S. Agarwal, and T. Meyarivan, "A fast and elitist multiobjective genetic algorithm: NSGA-II", *IEEE Trans. Evol. Comput.*, vol. 6, pp. 182–197, 2002. `doi:10.1109/4235.996017`

ISBN: 978-3-95450-279-0 ISSN: 3043-0208 doi: 10.18429/JACoW-SAP2025-THP04

MINIMIZING THE FLUCTUATION OF STORAGE RING RESONANCE DRIVING TERMS USING THE STEP-BY-STEP CHROMATICITY COMPENSATION METHOD

Wanbin Li*, Yuejing Huang, Zihan Wang, Bingfeng Wei†, Penghui Yang, Zhenghe Bai‡
NSRL, University of Science and Technology of China, Hefei, China

Abstract

Our recent studies showed that reducing the fluctuation of resonance driving terms (RDTs) can enlarge the dynamic aperture (DA) of a storage ring very effectively. In this paper, we use the step-by-step chromaticity compensation method to minimize RDT fluctuations for DA optimization. For the minimization of third-order RDT fluctuations, this method yields the same optimization result as the differential evolution (DE) algorithm. Crucially, however, this method exhibits much faster convergence than the DE algorithm.

INTRODUCTION

Achieving a large dynamic aperture (DA) is a critical objective in the lattice design of a low-emittance storage ring. The numerical approach based on particle tracking is highly powerful for DA optimization but comes at the expense of high computational cost. The analytical approach based on the minimization of resonance driving terms (RDTs) was recently further developed; reducing the variation or fluctuation of RDTs along the longitudinal position is significantly more effective in increasing DA than reducing the commonly-used one-turn RDTs [1, 2]. Therefore, minimizing RDT fluctuations enables highly efficient DA optimization with substantially reduced computational cost. Instead of using evolutionary algorithms, this paper employs the step-by-step chromaticity compensation (SCC) method [3] to minimize RDT fluctuations.

THE SCC METHOD REVISITED AND MODIFICATION

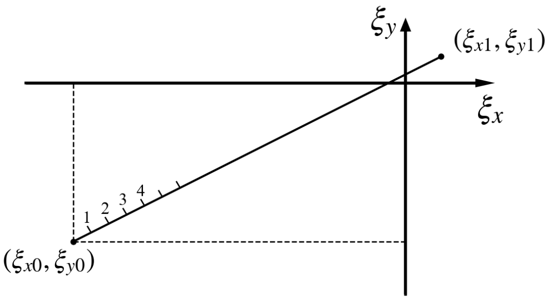

Figure 1: Schematic of the step-by-step chromaticity compensation method.

In the SCC method [3], shown in Fig. 1, the horizontal and vertical chromaticities are corrected by taking N small steps from the natural chromaticity point (ξ_{x0}, ξ_{y0}) to the desired chromaticity point (ξ_{x1}, ξ_{y1}). At each step, one pair of focusing and defocusing sextupoles (SF_i, SD_j), which provides the greatest increase in the DA area, is selected from all possible sextupole pairs to compensate for a fraction of chromaticities. The largest final DA is achieved at a reasonably large number of steps N. If N is too large, the individual contribution of each sextupole pair to the DA area becomes indistinguishable, making it hard to identify the best pair for chromaticity correction at each step. Consequently, this causes the effectiveness of the SCC method to break down.

Our recent studies found a very strong correlation between reducing RDT fluctuations and enlarging DA. Based on this correlation, the fluctuation of RDTs is used in this paper as the evaluation function to select the best sextupole pair at each step. Compared with the DA area, this evaluation function can distinguish the effects of different sextupole pairs, regardless of the number of steps N. Moreover, it significantly reduces the computational cost.

MINIMIZING RDT FLUCTUATIONS USING THE SCC METHOD

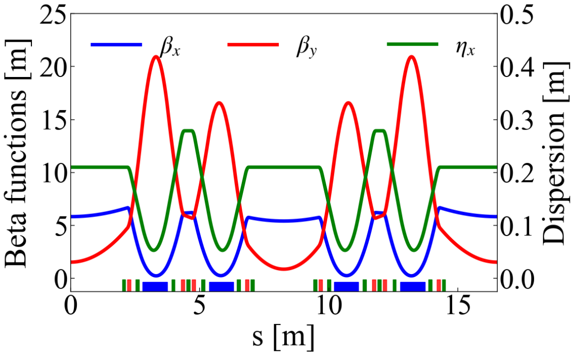

Figure 2: Linear optical functions and magnet layout of one lattice period of the HLS-III storage ring.

The HLS-III storage ring lattice [4] was used to apply and validate the SCC method. The optical functions and magnet layout of the lattice are presented in Fig. 2. The lattice has seven families of sextupoles used for chromaticity correction and nonlinear dynamics optimization. To facilitate a comparison between the SCC method with RDT fluctuations

---

* wanbin_li@mail.ustc.edu.cn
† weibf@ustc.edu.cn
‡ baizhe@ustc.edu.cn

being minimized and the scanning method based on particle tracking, the seven families of sextupoles were regrouped into five, including two focusing (SF_1, SF_2) and three defocusing (SD_1, SD_2, SD_3) families. This makes six sextupole pairs for evaluation: (SF_1, SD_1), (SF_1, SD_2), (SF_1, SD_3), (SF_2, SD_1), (SF_2, SD_2), and (SF_2, SD_3).

Minimizing Third-order RDT Fluctuations

The fluctuation of third-order RDTs, represented by the RMS value of third-order RDTs along the longitudinal position (denoted as $f_{3,\mathrm{rms}}$), was firstly used as the evaluation function. Then, we investigated the performance of the SCC method for three different chromaticity compensation paths (with the same number of steps $N = 900$): (i) the straight path from (ξ_{x0}, ξ_{y0}) to (ξ_{x1}, ξ_{y1}), (ii) an arbitrary curved path from (ξ_{x0}, ξ_{y0}) to (ξ_{x1}, ξ_{y1}), and (iii) the straight path from an arbitrary chromaticity point (ξ_{x2}, ξ_{y2}) to (ξ_{x1}, ξ_{y1}), as shown in Fig. 3. The changes of $f_{3,\mathrm{rms}}$ along the three paths are shown in Fig. 4. Figures 3 and 4 demonstrate that the final value of $f_{3,\mathrm{rms}}$ is essentially identical for a fixed endpoint (ξ_{x1}, ξ_{y1}), independent of the chromaticity compensation path.

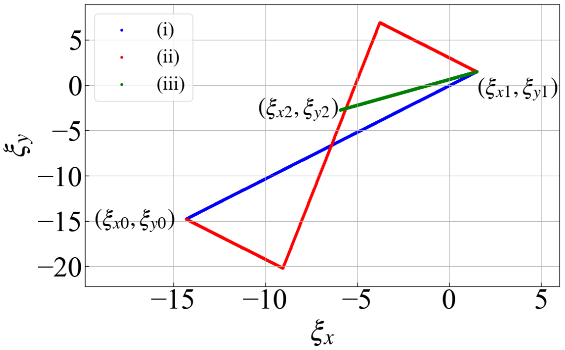

Figure 3: Three different chromaticity compensation paths.

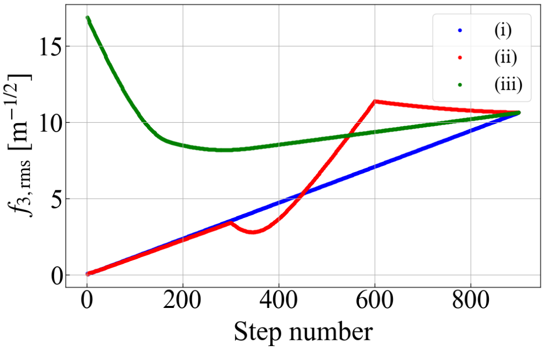

Figure 4: Changes of $f_{3,\mathrm{rms}}$ along the three paths.

We studied the influence of the number of steps N on the optimization results for the straight path from (ξ_{x0}, ξ_{y0}) to (ξ_{x1}, ξ_{y1}). Figure 5 shows the values of final $f_{3,\mathrm{rms}}$ for $N =$ 10, 50, 200 and 1000, and the usage proportions of the six sextupole pairs for these four numbers of steps are shown in Fig. 6. Notably, unlike the original SCC method that maximizes the DA area, our SCC method that minimizes RDT fluctuations avoids convergence degradation even as N increases to a very large value. The fast convergence of the SCC method is evident from a comparison between N=10 and N=1000, showing that the overall usage proportions of sextupole pairs is achieved with relatively few steps.

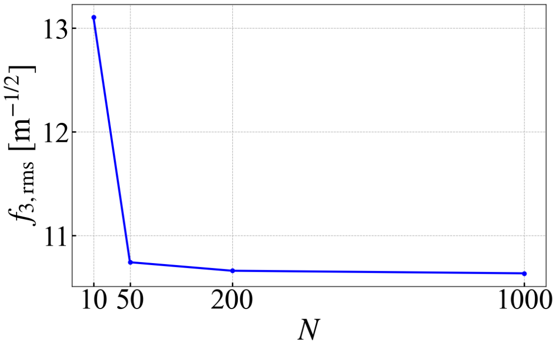

Figure 5: Convergence of final $f_{3,\mathrm{rms}}$ for N = 10, 50, 200 and 1000.

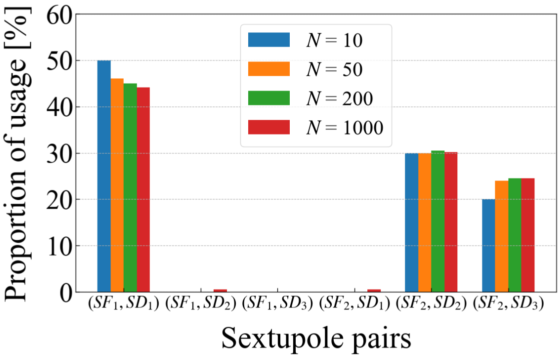

Figure 6: The usage proportions of sextupole pairs for the four numbers of steps N.

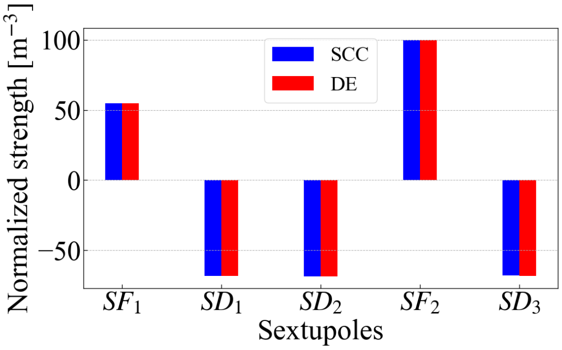

Figure 7: Normalized sextupole strengths obtained using the SCC method and the DE algorithm.

To further evaluate the performance of the SCC method, we compared it with the differential evolution (DE) algorithm. The DE algorithm was parameterized with the sextupole strengths as variables, $f_{3,\mathrm{rms}}$ as the objective function, a population size of 100 and a maximum iteration of 60. Figure 7 presents a comparison of the sextupole strengths obtained using the SCC method (N = 1000) and the DE algorithm (after 60 generations), both with a total of 6000 computation counts. It is clearly seen that the SCC method and the DE algorithm yield the same results. This agreement is non-coincidental; our recent work demonstrates that minimizing $f_{3,\mathrm{rms}}$ constitutes a special convex optimization problem, which also explains why the distinct chromaticity compensation paths presented in Fig. 4 converge to the same value.

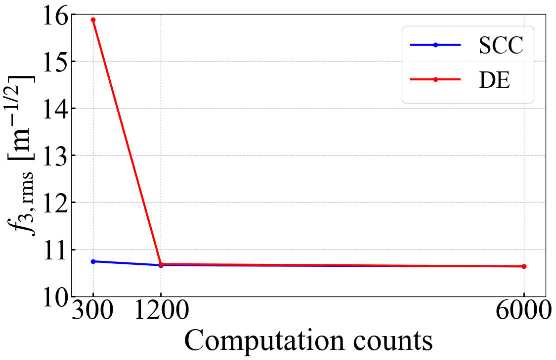

Figure 8: The $f_{3,\mathrm{rms}}$ values obtained using the SCC method and the DE algorithm for computation counts of 300, 1200, and 6000.

Figure 8 shows the $f_{3,\mathrm{rms}}$ values obtained using the SCC method and the DE algorithm for computation counts of 300 (corresponding to N = 50 and 3 generations), 1200 (N = 200 and 12 generations), and 6000 (N = 1000 and 60 generations). A clear observation is that the SCC method converges markedly faster than the DE algorithm, which also explains why the usage proportions of sextupole pairs can be approximated with a relatively small number of steps N as shown in Fig. 6.

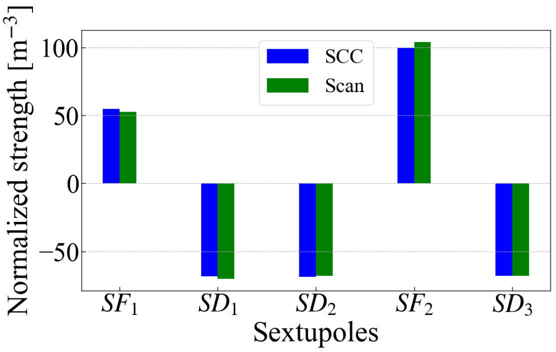

Figure 9: Normalized sextupole strengths optimized using the SCC method with $f_{3,\mathrm{rms}}$ being minimized and the scanning method based on particle tracking.

We used the scanning method based on particle tracking to obtain the best DA, with its sextupole strengths presented in Fig. 9. For comparison, the sextupole strengths obtained previously using the SCC method with N=1000 are also displayed in the figure. It is seen that the results from the two methods are in close agreement, indicating that the SCC method with RDT fluctuations being minimized can rapidly find solution regions with large DAs.

Minimizing Third- and Fourth-order RDT Fluctuations

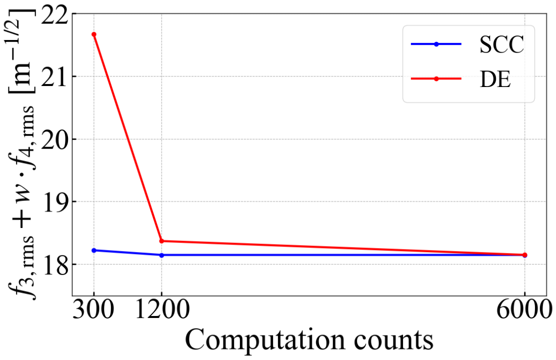

Figure 10: The $f_{3,\mathrm{rms}} + w \cdot f_{4,\mathrm{rms}}$ (w = 0.01 m^{-1}) values obtained using the SCC method and the DE algorithm.

Although the fluctuation of third-order RDTs is significantly important, further consideration of fourth-order RDT fluctuations is generally beneficial for nonlinear optimization. We used the SCC method and DE algorithm to minimize third- and fourth-order RDT fluctuations, $f_{3,\mathrm{rms}} + w \cdot f_{4,\mathrm{rms}}$, where w is a weight factor and $f_{4,\mathrm{rms}}$ is the RMS value of fourth-order RDTs. The parameter settings in both methods remained the same as before, and the optimization results are presented in Fig. 10. It is seen that when applied to minimize $f_{3,\mathrm{rms}} + w \cdot f_{4,\mathrm{rms}}$, both the SCC method and the DE algorithm achieve comparable final results and the SCC method still converges faster.

CONCLUSION AND OUTLOOK

This study combines the SCC method with minimization of RDT fluctuations for DA optimization. In contrast to the original SCC method, our method avoids convergence failure at a large number of steps and reduces computational cost. It has much faster convergence than the DE algorithm. In the nonlinear dynamics optimization, we can first use the SCC method to quickly minimize RDT fluctuations, and then around the solution regions obtained, evolutionary algorithms can be used to achieve the best results. Owing to the fast convergence, the SCC method can be used for online DA optimization.

ACKNOWLEDGEMENTS

This work was supported by the National Natural Science Foundation of China under Grants No. 12205299 and No. 12375325.

REFERENCES

[1] B. Wei *et al.*, “Minimizing the fluctuation of resonance driving terms in dynamic aperture optimization”, *Phys. Rev. Accel. Beams*, vol. 26, p. 084001, Aug. 2023. `doi:10.1103/PhysRevAccelBeams.26.084001`

[2] B. Wei, Z. Bai, G, Feng, “Analysis of off-momentum nonlinear driving terms for enlarging off-momentum dynamic apertures”, *Phys. Rev. Accel. Beams*, vol. 27, p. 104001, Oct. 2024. `doi:doi:10.1103/PhysRevAccelBeams.27.104001`

[3] E. Levichev and P. A. Piminov, “Algorithms for Chromatic Sextupole Optimization and Dynamic Aperture Increase”, in *Proc. EPAC’06*, Edinburgh, UK, Jun. 2006, paper WEPCH085, pp. 2116–2118.

[4] W. Li *et al.*, “Symmetric double-double bend lattice for a potential EUV diffraction limited upgrade of the HLS”, in *Proc. IPAC’25*, Taipei, Taiwan, Jun. 2025, pp. 2113–2116. `doi:10.18429/JACoW-IPAC25-WEPM063`

ISBN: 978-3-95450-279-0 ISSN: 3043-0208 doi: 10.18429/JACoW-SAP2025-THP05

GPU-ACCELERATED SIMULATION OF LONGITUDINAL SINGLE-BUNCH INSTABILITY IN ELECTRON STORAGE RINGS

Tianlong He*, Weiwei Li, Weimin Li, Zhenghe Bai
National Synchrotron Radiation Laboratory, USTC, Hefei, China

Abstract

Longitudinal single-bunch instability driven by high-frequency impedance is a major challenge for achieving optimal performance in fourth-generation synchrotron light sources and future electron-positron colliders. Accurate simulations of this instability are critical, yet computationally intensive, often requiring millions of macro-particles and fine slicing to resolve bunch density distributions. To address this, we have developed a GPU-accelerated tracking code that enables efficient simulations of longitudinal single-bunch instability. Our solution is specifically designed to run on a desktop computer equipped with a high-performance GPU, providing an accessible and cost-effective alternative to computing clusters.

INTRODUCTION

For storage-ring light sources and electron-positron colliders, the longitudinal high-frequency dominant impedance, e.g., coherent synchrotron radiation (CSR) impedance and NEG-coating resistive wall (RW) impedance, can lead to a relatively low microwave instability (MWI) threshold current, which becomes a key factor limiting the machine performance. As a consequence, accurately computing the MWI threshold is essential for optimizing the design of a machine. Currently, there are two main types of methods that can accurately predict the MWI threshold. One is based on the Vlasov-Fokker-Planck solver, typically like the code developed by Warnock and Ellison [1], and the GPU-accelerated code of Inovesa [2]. The other is based on the macro-particle tracking, such as ELEGANT [3], its parallel version PELEGANT [4], MBTRACK [5], and its Python version MBTRACK2 [6]. This paper focuses on the tracking method. To improve the accuracy of tracking simulation, it is commonly necessary to have a sufficient number of particles and slices to accurately count the bunch density distribution and reduce numerical noise. However, this requirement undoubtedly and significantly increases the computational load, making the tracking simulation very time-consuming. To address this issue, we have developed a GPU-accelerated tracking code to significantly improve the computational efficiency of tracking simulation for MWI. We expect that this tracking code will become a useful tool for the accelerator community.

SINGLE BUNCH TRACKING WITH THE STABLE CODE

The STABLE code [7] is developed specifically for multi-bunch, multi-particle tracking simualtion for longitudinal beam dynamics. It is implemented in a MATLAB environment with the use of state-of-the-art GPU acceleration techniques, which significantly improve the tracking efficiency.

From Multi-Bunch to Single Bunch

For the original version of STABLE, the macro-particle's coordinates are stored in a 2D matrix, where each column corresponds to one bunch. In order to accurately simulate the single-bunch dynamics, which usually requires millions or even tens of millions of macro-particles, we need only modify the STABLE code by dividing the macro-particles of a single bunch into multiple parts and storing them in each column of the 2D matrix. We can separately count the bin distribution of each column and then summarize them to obtain the total bunch distribution. In addition, a fixed bin width is set by default instead of the number of bins. Therefore, the bin number will increase as the bunch lengthens. The remaining operations, such as convolution of the bunch distribution and the short-range wake (or short-bunch wake potential), and interpolation to obtain the short-range wake kick of each macro-particle, can be kept the same as those in the original version of STABLE.

Operations for Longitudinal Tracking

The longitudinal tracking in STABLE is executed to update the coordinates of macro-particles turn by turn. For convenience, the normalized quantities $q = \tau/\sigma_{\tau 0}$ and $p = \delta/\sigma_{\delta 0}$ are used. Here, τ and δ are the arrival time and relative energy deviation with respect to the reference particle, respectively. $\sigma_{\tau 0}$ and $\sigma_{\delta 0}$ are the initially given rms values of bunch length and energy spread used for normalization, which do not necessarily have to be equal to the natural rms values determined by the equilibrium between radiation damping and quantum excitation. The quantity q is updated simply with the following equation:

$$q_{i+1} = q_i + \frac{\alpha_c T_0 \sigma_{\delta_0}}{\sigma_{\tau_0}} p_i, \tag{1}$$

where α_c is the momentum compaction factor, T_0 is the revolution time, and the subscript "i" denotes the turn number. The change of p should take into account the kick factors from RF voltage, short-range wakefield, radiation damping and quantum excitation, which can be simply expressed as:

$$\Delta p = p_{i+1} - p_i = p_{RF} + p_{wake} + p_{rad.+quan.}. \tag{2}$$

---

* htlong@ustc.edu.cn

ISBN: 978-3-95450-279-0 ISSN: 3043-0208 doi: 10.18429/JACoW-SAP2025-THP05

where

$$p_{RF} = \Sigma_j V_j \sin(\omega_j \sigma_{\tau 0} q + \phi_j)$$
$$p_{rad.+quan.} = -2\frac{T_0}{\tau_z} p_i + 2\sqrt{\frac{T_0}{\tau_z}} R, \tag{3}$$

V_j, ϕ_j, and ω_j refer to the RF voltage amplitude, phase, and angular frequency, respectively. τ_z is the radiation damping time. R is a random number from the standard normal distribution. Please note that, except for the calculation of p_{wake} in Eq. (2), all other computations are performed in parallel for each particle, which facilitates efficient implementation on GPUs. However, to implement the calculation of p_{wake}, it generally requires three steps:

1) Binning of the particle distribution.
2) Convolution of the particle distribution and the short-range wake potential (a pseudo-Green wakefield).
3) Linear interpolation to get p_{wake} for each particle.

The third-step linear interpolation generally has a very high execution efficiency, and the second-step convolution can be sped up using the fast Fourier transform. In the case of a bunch being very long compared to the wakefield variations, we utilize the techniques of Gaussian filtering and finer-bin interpolation to improve the convolution convergence and accuracy. Compared to these two steps, the first step is usually the most time-consuming and often the bottleneck in improving tracking efficiency.

Breaking the Efficiency Bottleneck

The binning of particle distribution can be computed using MATLAB's built-in function of "histcounts", which also supports GPU computing. Instead of using this function, a CUDA kernel named "BinNumCalZ" is programmed to speed up the binning calculation. This kernel accepts a 2D matrix as input. By default, the number of columns in this 2D matrix is equal to the value of "blocksPerGrid", and each block uses two threads to count the sub-distribution for each-column particles. Finally, the sum of the sub-distributions is exactly the total distribution.

Figure 1 shows the efficiency test results for the built-in function "histcounts" and the self-made kernel "BinNumCalZ". This test was conducted on a desktop computer equipped with a "13th Gen Intel(R) Core(TM) i9-13900K" CPU and an "NVIDIA Geforce RTX 4090" GPU. It can be seen that the efficiency of "histcounts" is almost unaffected by the number of rows in a 2D matrix. In contrast, the efficiency of "BinNumCalZ" depends on the number of rows. This kernel achieves its best efficiency for the case of 2,000 columns (blocksPerGrid=2,000). Compared to "histcounts@GPU" and "histcounts@CPU", it can increase the efficiency by a factor of ~8 and ~40, respectively.

Overall Tracking Performance

For 10 million particles and more than 4800 bins, it takes about 5 millisecond to track one turn when using the above-mentioned desktop computer configuration. A tracking simulation with a typical number of 50,000 turns will therefore take about 4-5 minutes.

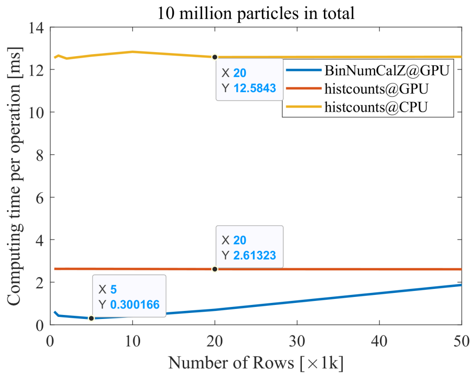

Figure 1: Efficiency test for binning of particle distribution.

Benchmark

We have utilized the STABLE code to study the longitudinal single-bunch dynamics induced by the NEG-coating resistive wall impedance for the Hefei Advanced Light Facility (HALF) storage ring [8]. Some of the tracking results were verified using the PELEGANT code, and a good agreement was observed. Details can be found in Ref. [9].

APPLICATION

The HALF Storage Ring

The HALF, a fourth-generation synchrotron light source, is under construction in Hefei, China, and the storage ring is scheduled to start commissioning in spring 2027. Figure 2 shows the latest longitudinal RW wake potential (considering a NEG-coating thickness of 1 µm and a resistivity of $1 \times 10^{-5}\ \Omega\cdot\text{m}$) according to the current vacuum layout.

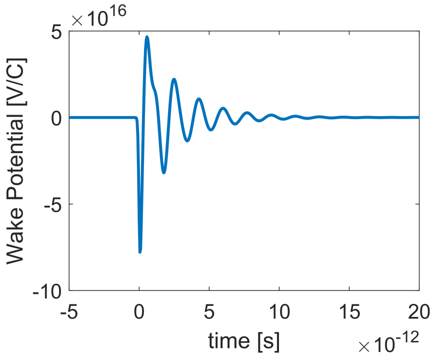

Figure 2: Longitudinal RW wake potential of 0.02 mm rms bunch length.

Figure 3 presents tracking simulation results. Without harmonic cavity-induced bunch lengthening (blue curve), the MWI threshold is approximately 0.25 mA — half of the target bunch current (~0.5 mA). When the bunch is triply lengthened by the harmonic cavity (red curve), the MWI threshold increases to ~0.75 mA, demonstrating an approximately linear proportionality between the MWI threshold and bunch length.

Figure 4 shows the bunch phase-space distribution at 0.5 mA when MWI occurs, revealing distinct microbunching structures whose dimensions match the oscillation period length of the wake potential in Fig. 2. This highlights unique instability features. Notably, each simulation run takes ~2.5 minutes, with the total simulation completed in 52 minutes. Our code achieves rapid computation while dynamically visualizing bunch phase-space evolution, providing intuitive and comprehensive insights into beam dynamics.

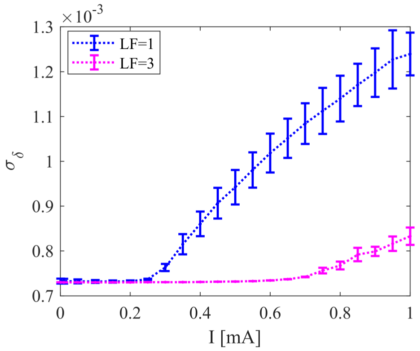

Figure 3: Bunch energy spread as a function of bunch current.

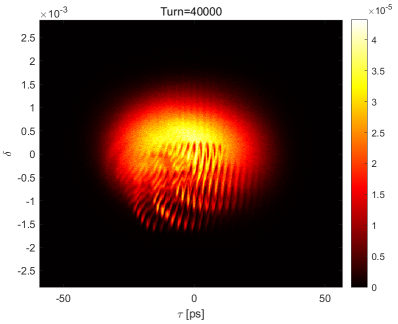

Figure 4: Normalized phase space distribution at bunch current of 0.5 mA, obtained at the 40,000 th tracking turn.

The Super Tau-Charm Facility Storage Ring

The STCF is being designed as a symmetric electron-positron collider in Hefei, China, with a centre-of-mass energy ranging from 2 to 7 GeV. For a minimum energy of 1 GeV and a nominal beam current of 1.1 A (1.6 mA per bunch at 48 % filling rate), the STCF storage ring is likely to encounter the CSR instability. As illustrated in Fig. 5, the CSR wake potential from bending magnets and the CWR wake potential from the latest designed damping wigglers are computed using impedance data obtained from the steady-state parallel-plates model [10] and the CSRZ code [11], respectively.

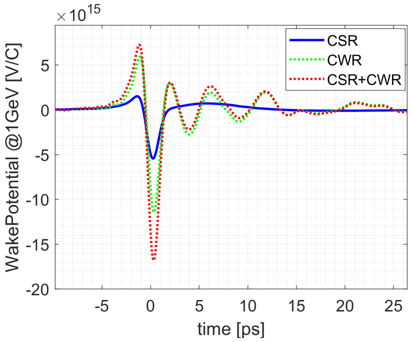

Figure 5: CSR and CWR wake potentials at rms bunch length of 0.2 mm.

Figure 6 presents STABLE tracking results using the wake potential data shown in Fig. 5. The MWI threshold current is observed at ~0.9 mA, well below the target value of 1.6 mA. These simulations informed the optimization of the wiggler scheme to mitigate CSR effects. Notably, the full tracking process—simulating 10 million macroparticles over 40,000 turns—was completed in ~1 hour across 27 bunch current points, demonstrating high computational efficiency.

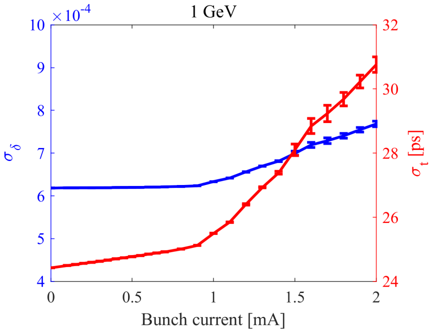

Figure 6: Bunch energy spread (blue) and rms length (red) as a function of bunch current.

CONCLUSION

This work presents the algorithmic details of the STABLE code for single-bunch longitudinal dynamics tracking simulations, with applications to two common high-frequency impedance sources: RW (for HALF) and CSR (for STCF) instabilities. We demonstrate its high computational efficiency, establishing STABLE as a powerful tool for investigating microwave instabilities in electron storage rings. The code is publicly accessible at: *https://github.com/hetianlong-afk/STABLE-SingleBunch*.

ACKNOWLEDGEMENTS

This work was supported by National Natural Science Foundation of China (No. 12375324 and 12105284), and the Fundamental Research Funds for the Central Universities (No. WK2310000127).

ISBN: 978-3-95450-279-0 ISSN: 3043-0208 doi: 10.18429/JACoW-SAP2025-THP05

REFERENCES

[1] R. Warnock and J. A. Ellison, “A general method for propagation of the phase space distribution, with application to the sawtooth instability”, in *Proceedings of 2nd ICFA Advanced Accelerator Workshop on the Physics of High Brightness Beams*, UCLA, 1999.

[2] P. Schönfeldt, M. Brosi, M. Schwarz, J. L. Steinmann, and A.-S. Müller, “Parallelized Vlasov-Fokker-Planck solver for desktop personal computers”, *Phys. Rev. Accel. Beams*, vol. 20, p. 030704, 2017. `doi:10.1103/PhysRevAccelBeams.20.030704`

[3] User’s manual for ELEGANT, `http://ops.aps.anl.gov/manuals/elegant_latest/elegant.html`

[4] I. V. Pogorelov, K. M. Amyx, J. R. King, M. Borland, and R. Soliday, “Current Status of the GPU-Accelerated ELEGANT”, in *Proc. IPAC’14*, Dresden, Germany, Jun. 2014, pp. 454–456. `doi:10.18429/JACoW-IPAC2014-MOPME035`

[5] G. Skripka, R. Nagaoka, M. Klein, F. Cullinan, and P. F. Tavares, “Simultaneous computation of intrabunch and interbunch collective beam motions in storage rings”, *Nucl. Instrum. Methods Phys. Res., Sect. A*, vol. 806, p. 221, 2016. `doi:10.1016/j.nima.2015.10.029`

[6] A. Gamelin, W. Foosang, and R. Nagaoka, “mbtrack2, a Collective Effect Library in Python”, in *Proc. IPAC’21*, Campinas, Brazil, May 2021, pp. 282–285. `doi:10.18429/JACoW-IPAC2021-MOPAB070`

[7] T. He, and Z. Bai, “Graphics-processing-unit-accelerated simulation for longitudinal beam dynamics of arbitrary bunch trains in electron storage rings”, *Phys. Rev. Accel. Beams*, vol. 24, p. 104401, 2021. `doi:10.1103/PhysRevAccelBeams.24.104401`

[8] Z. Bai *et al.*, “Progress on the storage ring physics design of Hefei Advanced Light Facility (HALF)”, in *Proc. IPAC’23*, Venice, Italy, May 2023, pp. 1075–1078. `doi:10.18429/JACoW-IPAC2023-MOPM038`

[9] W. Li, T. He, and Z. Bai, “Terahertz scale microbunching instability driven by high resistivity nonevaporable getter coating resistive-wall impedance”, *Phys. Rev. Accel. Beams*, vol. 27, p. 034401, 2024. `doi:10.1103/PhysRevAccelBeams.27.034401`

[10] K. L. F. Bane, Y. Cai, and G. Stupakov, “Threshold studies of the microwave instability in electron storage rings”, *Phys. Rev. ST Accel. Beams*, vol. 13, p. 104402, 2010. `doi:10.1103/PhysRevSTAB.13.104402`

[11] D. Zhou, “Coherent Synchrotron Radiation and Microwave Instability in Electron Storage Rings”, Ph.D. thesis, SOKENDAI and KEK, 2011.

ISBN: 978-3-95450-279-0 ISSN: 3043-0208 doi: 10.18429/JACoW-SAP2025-THP06

PRELIMINARY SCHEME FOR ELECTRON COOLING USING LONGITUDINAL HOLLOW ELECTRON BEAM*

X. D. Yang[†], He Zhao, Institute of Modern Physics, CAS, Lanzhou, China

Abstract

The intra-beam scattering in high charge state intense heavy ion beams is a problem worth considering. By controlling the longitudinal distribution of the ion beam, it may be possible to alleviate the ion beam loss and improve the lifetime of the ion beam caused by intra-beam scattering. Unlike the traditional cooling process of direct current electron beams or longitudinal uniform distribution electron bunch beams, a longitudinal hollow electron beam is used to cool heavy ion beams. Ions at the edge of the ion beam will receive stronger cooling, while ions at the center of the ion beam will receive weaker cooling, avoiding overcooling at the center of the ion beam. This paper discusses the generation, measurement, and related issues of longitudinal hollow electron beams. Corresponding solutions and suggestions have been proposed for the problems and challenges that may be encountered in the research. The cooling process of longitudinal hollow electron beams will be simulated and experimentally studied in the future, with the hope of obtaining beneficial effects.

INTRODUCTION

Intra-beam scattering is one of the main reasons of reduction of the beam intensity and shortening of stored lifetime in the collider, light source and storage ring, especially in the case of the high energy high intensity heavy ion beam with high charge state. The intra-beam scattering presents dissimilar influence in the different facilities. It can be counteracted partially by the synchrotron radiation damping in the lepton machine. It also can be suppressed by the wiggler. But there is no similar damping in the hadron machine.

The intensity and quality of ion beam in an accelerator are the most important parameters, and they are often asked to increase and improve according to the requirements of various physics experiments. High intensity beam of heavy ion with high charge state and short bunch length was expected to store in a storage ring with long lifetime and less loss.

Intra-beam scattering has become a bottleneck for maintaining the optimal performance of the accelerator. In this case, intra-beam scattering becomes the primary cause of emittance growth in the six-dimensional phase space. Particles with large amplitudes will escape the bucket and be lost in the ring. As a result, the lifetime of the ion beam in the storage ring decreases.

In order to increase the lifetime of ion beam and decrease the loss, the behavior of intra-beam scattering in the high intensity heavy ion storage ring with short bunch should be investigated completely and systemically. Electron cooling was chosen to suppress the effect of intra-beam scattering, another unexpected effect happened during the cooling.

From the perspective of beam dynamics, and based on understanding the mechanism of intra-beam scattering in high-density beams in heavy ion storage rings, more effective methods to suppress intra-beam scattering should be explored and attempted.

Under electron cooling, the distribution of ion beams quickly deviates from the initial Gaussian type, forming a denser core and a longer tail. The ions standing in the tail of the beam will be lost soon due to large amplitude [1].

A new idea was introduced in this paper. A novel solution was proposed. This novel method will be attempted to suppress intra-beam scattering. The feasibility and validity of this method was verified in this study. This idea will focus on the investigation on the suppression of intra-beam scattering in the high intensity heavy ion beam in the storage ring with the help of longitudinal hollow electron beam.

The traditional DC electron beam in the electron cooler was modulated into an electron bunch with different longitudinal distributions. The stronger cooling was expected in the tail of the ion beam and the weaker cooling was performed in the tail of the ion beam. The particle on the outside will experience stronger cooling and will be driven back into the center of the ion beam. The ion loss will be decreased and the lifetime will be increased. The intensity of the ion beam in the storage ring will be maintained for a longer period. Two functions will be combined into one electron cooler. The shorter the pulse, the higher intensity and lower emittance heavy ion beam was expected in the cooler storage ring. In the future, the results of this project will be constructive to the upgrade and improvement of existing machines and also be helpful to the design and operation of future storage and high-energy electron coolers.

MOTIVATION

From the previous experimental results [2] indicated that the partially transverse hollow electron beam has an advantage in beam accumulation. The optimal ratio Ugrid/Uanode is near 0.2 in the electron gun of electron cooling device. In this case, the centre density is 2 times less than the edge density in the electron beam.

The transverse hollow electron beam is beneficial for accumulating ion beams with higher current intensity.

The electron cooling will be expected to serve as a knob to control the longitudinal distribution of the ion beam in the storage ring.

The longitudinal hollow electron beam is expected to obtain benefits in the following aspects.

- Suppress intra-beam scattering.
- Control the longitudinal distribution of the ion beam.

---

* Work supported by NSFC No. 12275325, 12275323, 12205346.

† yangxd@impcas.ac.cn.

ISBN: 978-3-95450-279-0 ISSN: 3043-0208 doi: 10.18429/JACoW-SAP2025-THP06

- Make the beam bunch contain as many particles as possible.
- Increase the lifetime of ion beams in the storage ring.

GENERATION SCHEME OF LONGITUDINAL HOLLOW ELECTRON BEAM

The high voltage pulse required for the generation of the longitudinal hollow electron beam can be generated by three schemes.

The first scheme is to use two adjacent pulses and chopping techniques, the falling edge of first pulse and the rising edge of second pulse are utilized to obtain a beam bunch with higher electron density at the beginning and end sections, and lower electron density in the middle section. The waveform looks like an inverted triangle shape.

The second solution is to use the method of combining DC high voltage with sine wave and utilizing chopper technology. From the output of high-voltage power supplies with sinusoidal wave, chopper technology will cut only the required phase range from the output of high voltage. A voltage output similar to a cosine wave is generated. The voltage varies continuously, resulting in a longitudinal hollow electron beam.

The third proposal is generated by a high-voltage power supply array, where each high-voltage power supply produces a different amplitude output value of high-voltage, which is combined into the required high voltage output waveform according to the required sequence. Multiple independent pulses with different amplitudes form an inverted Gaussian distribution electron beam bunch in a certain sequence [3]. On this basis, the longitudinal hollow electron beam will be created.

MEASUREMENT OF LONGITUDINAL HOLLOW ELECTRON BEAM PARAMETERS

The waveform of the output voltage of the power supply will be measured offline by the oscilloscope and high-voltage dividers in the test platform. From the results, the parameters such as repetition rate, rising edge, plateau, descending edge, and other pulse parameters will be derived. The longitudinal distribution of the electron beam will be measured by the BPM system in the electron cooling device. The Response time of the electron gun and the transition time of the electron bunch will be acquired with the help of two BPMs as the method of time of flight. In addition, an AC transformer was installed in the collector circuit of the electron cooling device, the electron beam bunch information will be obtained from these signals.

SYNCHRONIZATION OF ELECTRON BEAM AND ION BEAM

The basic requirement for electron cooling is that the electron beam can overlap the ion beam, and in the longitudinal direction, the length of the electron beam bunch should be greater than that of the ion beam bunch. The length of the ion beam bunch will gradually decrease with the cooling process, which requires the longitudinal center of the ion beam and the electron beam to always remain consistent. That is to say, the ions at the edge of the ion beam are always subjected to a stronger cooling effect than the ions at the center of the ion beam.

The synchronization problem between ion beam and electron beam will be the key issue. It can be solved with the help of relevant technologies accumulated from beam injection and extraction in the storage ring.

The electron cooling device is equipped with beam position detectors BPM at both ends, which can measure both the positions of the electron beam and the ion beam in the cooling section of the electron cooling device. The BPM at the entrance can be used to measure the time it takes for the electron beam bunch to reach the electron cooling section, and the BPM at the exit can be used to measure the time for the electron beam bunch to leave the electron cooling section. Two measurement results can be used to calibrate and check each other.

Due to the electron gun being a capacitive load, the response time and possible time delay of the electron gun relative to the high voltage power supply. The response time from the triggering of the high voltage power supply to the generation of the control electrode voltage waveform and the generation of the electron beam pulse waveform should be measured in advance. In addition, there is a certain distance from the cathode surface of the electron gun to the entrance of the electron cooling section where the electron beam encounters and overlaps the ion beam. The transmission of the electron beam also needs time in this region.

There are several beam position detectors BPM installed in the storage ring to measure the position of the ion beam. When the ion beam passes through BPM, the signal of the ion beam is induced on BPM, which serves as a reference signal for measurement and triggering.

Through repetitious measurements, the measurement results are calibrated and mutually verified to determine the time for the ion and electron beam bunches to reach and leave the electron cooling section, as well as the trigger delay time and response time of the high-voltage pulse power supply. These two parameters are set in the synchronous control system.

The revolution frequency of the ion beam can be accurately measured. The repetition frequency of the electron beam has the ability to be finely tuning, and the output frequency of the corresponding signal generator can be adjusted. The relational components in the power supply should be selected with a certain range with adjustment capabilities.

ALIGNMENT AND MATCH OF ELECTRON BEAM AND ION BEAM

Beam position detectors are installed at both ends of the cooling section of the electron cooling device, which can measure the position of both the electron beam bunch and the ion beam bunch. The positions and angles of the electron beam and ion beam in the cooling section were measured separately. With the help of correct coils in the electron cooling device and dipoles in the storage ring, the positions and angles of the electron beam and ion beam in the cooling section were adjusted respectively. After repeated measurement and adjustment, the alignment of the ion beam and electron beam can be ensured.

REPETITIVE FREQUENCY OF PULSE OUTPUT IN HIGH-VOLTAGE SYSTEM

Reduce the repetition frequency of the electron beam bunch output, using the repetition frequency of the electron beam bunch to be half, one fourth, or one eighth of the rotation frequency of the ion beam in the storage ring. That is to say, ions rotate two, four, or eight times in the storage ring and encounter the electron beam once.

In order to reduce the repetition frequency of high-voltage output, a half, one fourth, or one eighth of revolution frequency will be used as output frequency of high-voltage pulses. The ion beam bunch meets the electron beam bunch every two, four, or eight revolutions.

By using multiple high-voltage power supplies to form an array and continuously triggering pulse trains that generate electron beam bunch trains, the output repetition frequency of a single high-voltage power supply can be greatly reduced.

CONTROL AND ADJUSTMENT OF ELECTRON BEAM BUNCH LENGTH

As mentioned above, the voltage applied to the control electrode of the electron gun determines the current intensity of the extracted electron beam. A continuous sine wave voltage with a maximum peak value of 2kV and a minimum value of zero, centered around the minimum value, can obtain electron beam bunches of different lengths by chopping in different phase intervals. However, due to the same frequency sine wave, the voltage values at different phases are different, and the maximum output voltage after chopping is different, resulting in different values of the electron beam current extracted. In order to obtain electron beam bunches with the same current intensity but different beam lengths, it is proposed to use frequency doubling, four frequency doubling, or eight frequency doubling schemes. When doubling, chop once every other cycle; At four times the frequency, chop every three cycles. In this way, the maximum output voltage value obtained by chopping is the same, the pulse length is half or a quarter of the original, and the beam length becomes shorter.

The above-mentioned frequency conversion method can generate electron beam bunch of different lengths. As the ion beam is cooled, the length of the ion beam bunch gradually becomes shorter, and the ions at the edge of the ion beam gradually leave the edge region with the highest electron beam bunch density. In order to achieve the same cooling effect, a staged cooling scheme can be used during the cooling process. At the beginning of the cooling stage, a longer electron beam bunch is used; Then use electron beam bunch of intermediate length; Finally, a shorter length electron beam bunch is used. According to the total cooling time, the entire cooling process is divided into three parts, and the electron beam bunches of the three lengths are switched sequentially.

SIMULATION CALCULATION OF COOLING PROCESS

A numerical simulation code TRACKIT [4] based on multi-particle tracking was developed to calculate the bunched ion beam cooling process, in which the electron cooling, intra-beam scattering (IBS), ion beam space-charge field, transverse and synchrotron motion are taken into account. This code can set the longitudinal distribution of the electron beam in the input file.

The DC electron beam cooling was set as reference. From the simulation results, the parameters such as the longitudinal distribution of ion beam, lifetime of ion beam, length of ion beam bunch, upper limit of ion number were derived [5-7]. The attention will be placed on the differences of cooling process by the longitudinal hollow electron beam cooling comparing with the cooling of longitudinal uniform distribution electron beams.

EXPERIMENTAL STUDY ON COOLING PROCESS

As mentioned above, the electron gun in the electron cooling device can provide three kinds of electron beams.

- Traditional DC electron beam.
- Longitudinal uniform distribution electron beam.
- Longitudinal hollow electron beam.

There are some beam diagnostics systems in the storage ring CSR. The ion beam current is monitored by a DCCT in the storage ring. The lifetime of ion beam was derived from the DCCT signal. A Schottky pickup can monitor the longitudinal information of ion beam. The longitudinal cooling process is observed by measuring the temporal bunch profile using a beam position monitor (BPM) [8, 9].

From the experiments, the longitudinal distribution of the ion beam, the lifetime of the ion beam, the length of the ion beam bunch, and the upper limit of the number of ions were obtained. These results will be compared with the case of DC electron beam cooling process. The difference of longitudinal hollow electron beam comparing with the cooling of longitudinal uniform distribution electron beams will be revealed [10-12].

SUMMARY AND PROSPECT

The ion beam was cooled by the different longitudinal distribution electron beams in the storage ring. Using electron cooling as a knob, a longitudinal hollow electron beam is used to adjust the cooling effect in different regions, applying different cooling effects in various areas to control the longitudinal distribution of the ion beam and avoid rapid cooling at the center of the ion beam. This method will become a new attempt, and it is expected to achieve the expected results in subsequent simulation calculations and experimental research. Especially, in high-energy electron cooling, the electron beam bunch will be generated by the photocathode, and microwave electron gun and accelerated by the RF cavity.

REFERENCES

[1] A.V. Fedotov, I. Ben-Zvi, Yu. Eidelman, *et al*. “IBS for ion distribution under electron cooling”, in *Proc. PAC’05*, Knoxville, TN, USA, May 2005, paper TPAT091, pp. 4263-4265.

[2] X.D. Yang, V.V. Parkhomchuk, W.L. Zhan, *et al.* “Commissioning of electron cooling in CSRm”, in *Proc. COOL’07*, Bad Kreuznach, Germany, Sep. 2007, paper TUM1I02, pp. 59-63.

[3] X. D. Yang, L. J. Mao, J. Li, *et al.* “Investigation on the suppression of intrabeam scattering in the high intensity heavy ion beam with the help of longitudinal multi-bunch chain of electron”, in *Proc. COOL’17*, Bonn, Germany, Sep. 2017. `doi:10.18429/JACoW-COOL2017-TUP14`

[4] `https://github.com/hezhao1670/ECool-TRACKIT`

[5] He Zhao, Lijun Mao, Jiancheng Yang, *et al.*,“Electron cooling of a bunched ion beam in a storage ring”, *Phys. Rev. Accel. Beams*, vol. 21, p. 023501, Feb. 2018. `doi: 10.1103/PhysRevAccelBeams.21.023501`

[6] He Zhao and Lijun Mao, “Longitudinal stacking of ion beams with pulsed electron beam cooling”, *Phys. Rev. Accel. Beams*, vol. 26, p. 030101, Mar. 2023. `doi: 10.1103/PhysRevAccelBeams.26.030101`

[7] He Zhao, Lijun Mao, Meitang Tang, *et al.* “Theoretical and simulation study of dispersive electron cooling”, *Phys. Rev. Accel. Beams*, vol. 27, p.033501, Mar. 2024. `doi: 10.1103/PhysRevAccelBeams.27.033501`

[8] H. Wang, A. Hutton, K. Jordan, *et al.* “Experimental demonstration of ion beam cooling with pulsed electron beam”, in *Proc. IPAC2018*, Vancouver, BC, Canada, Apr. – May 2018. pp. 1174-1177. `doi:10.18429/JACoW-IPAC2018-TUPAL069`

[9] M. W. Bruker, S. Benson, A. Hutton, *et al.*, “Demonstration of electron cooling using a pulsed beam from an electrostatic electron cooler”, *Phys. Rev. Accel. Beams*, vol. 24, p. 012801, Jan. 2021. `doi: 10.1103/PhysRevAccelBeams.24.012801`

[10] A. V. Fedotov, Z. Altinbas, S. Belomestnykh, *et al.*, “Experimental Demonstration of Hadron Beam Cooling Using Radio-Frequency Accelerated Electron Bunches”, *Phy. Rev. Lett.*, vol. 124, p. 084801, Feb. 2020. `doi: 10.1103/PhysRevLett.124.084801`

[11] D. Kayran, Z. Altinbas, D. Bruno, *et al.*, “High-brightness electron beams for linac-based bunched beam electron cooling”, *Phys. Rev. Accel. Beams*, vol. 23, p. 021003, Feb. 2020. `doi: 10.1103/PhysRevAccelBeams.23.021003`

[12] N. Banerjee, B. Cathey, G. Stancari, *et al.*, “Incoherent dynamics of intense proton beams under electron cooling”, in Proc. of IPAC2023, Venice, Italy, May, 2023. `doi:10.18429/JACoW-IPAC2023-TUPM026`

ISBN: 978-3-95450-279-0 ISSN: 3043-0208 doi: 10.18429/JACoW-SAP2025-THP07

LONGITUDINAL COLLECTIVE DYNAMICS IN LASER MODULATORS OF A STEADY-STATE MICROBUNCHING STORAGE RING BASED ON THE MACROPARTICLE MODEL

Cheng-Ying Tsai*, School of Electrical and Electronic Engineering,
Huazhong University of Science and Technology, Wuhan, China

Abstract

The mechanism of the steady-state microbunching (SSMB) storage ring is being actively investigated. In the conceptual design, a laser modulator used to modulate the electron beam include the co-propagating laser beam, undulator magnets and potential cavity mirrors, forming a laser modulator cavity. In this work the longitudinal single-bunch and multi-bunch collective dynamics are studied that may arise due to coherent undulator radiation, based on the macroparticle model. For multi-bunch multi-turn case, the dispersion equation is derived, and a detuning parameter is introduced to characterize the frequency deviation between the external laser and the resonant undulator radiation, and solve for the instability growth rates of different multibunch modes. When the detuning approaches a specific multibunch mode divided by the number of total microbunches, this instability mechanism tends to amplify that mode. Furthermore, possible mitigation effect of the potential well on the instability is discussed. This work may shed light on the underlying physical mechanisms of longitudinal collective beam dynamics in the laser cavity modulators of an SSMB storage ring.

INTRODUCTION

The mechanism of the steady-state microbunching (SSMB) storage ring is being actively investigated in recent years [1–20]. A distinctive feature of this mechanism is replacement of the RF cavity by a laser modulator for longitudinal focusing/modulation. The laser modulator can be implemented by a co-propagating laser along a common axis with the electron beam in an undulator. To reuse the laser beam and accumulate sufficient intensity while relaxing laser requirements, we can confine the laser beam in a closed path and configure the laser modulator as an optical cavity, called a laser modulator cavity. The existing literature for studies of electron dynamics in the laser modulators mainly focuses on single-particle effects [1–12]. The collective dynamics occurred in the laser modulators, as the next step in evaluating SSMB feasibility, has only recently been in detail studied [13–20]. In this paper we outline the main progress of longitudinal collective instability studies in laser modulators of an SSMB storage ring using the macroparticle model. An alternative approach using the beam matrix can be found in Ref. [17–19].

UNDULATOR RADIATION WAKE

The undulator radiation (UR) impedance per unit length can be derived from its radiation energy spectrum $W_{UR}(\omega)$, i.e., $\mathrm{Re}\, Z_{\parallel}(\omega) = \frac{\pi}{e^2}\frac{dW_{UR}}{d\omega}$. The corresponding wake function is $W_{\parallel}(z > 0) = \frac{2c}{\pi}\int_0^{\infty} \mathrm{Re}\, Z_{\parallel}(k) \cos kz \; dk$ with $\omega = kc$. Figure 1 shows a typical undulator wake function.

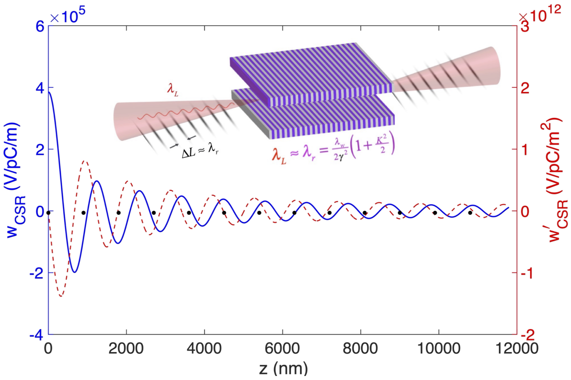

Figure 1: Undulator radiation wake function per unit length (blue solid line) and its slope (red dashed line).

SINGLE-PASS MULTI-BUNCH CASE [13]

When a microbunch train traverses the modulator undulator, every individual microbunches emit undulator radiation. On each undulator period, the wiggling motion of electron microbunches make the radiation wake advance over one resonant wavelength λ_r, affecting the leading microbunches. Denoting the index of the most trailing microbunch be 0 and that of the most leading microbunch be (N_b-1), we have the macroparticle equation of motion for the n-th microbunch

$$\frac{d^2 z_n}{ds^2} + k_{s0}^2 z_n = \frac{4\pi\epsilon_0 r_e N\eta}{\gamma}\times \sum_{j=0}^{N_b-1} W_{\parallel}\left[z_n - z_j + (n-j)\Delta L\right]\Theta\left(s - \lambda_w \sum_{k=j}^{n-1} N_{k+1}\right), \tag{1}$$

with $\Delta L \approx \lambda_L$, N_b the number of microbunches, k_{s0} the modulation strength characterizing the longitudinal oscillation wavenumber, $\eta = -\frac{1+\frac{K^2}{2}}{\gamma^2}$, Θ the Heaviside unit step function, and N_{k+1} the distance between the $(k+1)$-th and k-th microbunches in terms of the resonant wavelength. The set of total of n coupled differential equations can in general

---

* Email: jcytsai@hust.edu.cn. This work is supported by the Fundamental Research Funds for the Central Universities (HUST) under Project No. 2021GCRC006 and National Natural Science Foundation of China under project No. 12275094.

ISBN: 978-3-95450-279-0 ISSN: 3043-0208 doi: 10.18429/JACoW-SAP2025-THP07

be solved numerically. When the wake function is linearized, the set of equations can have analytical solutions. Here we skip the detailed derivations and refer interested readers to Ref. [13]. Here we note that, besides the external modulation laser, the radiation wake may provide additional longitudinal focusing to stabilize the electron beam, i.e., effect of potential well distortion (PWD) [13]. Under the present nominal SSMB design parameters, i.e., $10^4 \sim 10^5$ electrons per microbunch, such coherent UR driven single-pass multi-bunch beam breakup instability is not a concern [13].

SINGLE-BUNCH MULTI-TURN CASE [14, 15]

When the laser modulator forms a cavity, the radiation wake can be confined in a closed path among the mirrors, particularly the spectral resonant components. In this situation, in addition to the external modulation laser, when circulating microbunches come back to the laser modulator. they see the radiation wake accumulated on previous turns. For the single microbunch circulating in the storage ring, on the m-th turn, from n-th to $(n+1)$-th undulator period, the macroparticle equation of motion can be formulated as

$$\begin{aligned} z_m^{(n+1)} &= z_m^{(n)} - \eta_w \lambda_w \delta_m^{(n+1)} \\ \delta_m^{(n+1)} &= \delta_m^{(n)} + \frac{k_{s0}^2 \lambda_w}{\eta_w k_L} \sin k_L z_m^{(n)} \\ &\quad - \frac{4\pi\epsilon_0 N r_e \lambda_w}{\gamma} \sum_{k=0}^{m-1} W_\parallel \left[(N_w - n)\,\lambda_r + z_m^{(n)} - z_k^{(0)} \right], \end{aligned} \tag{2}$$

where the driving wake is originated from the previous $(m-1)$ turns at the corresponding undulator period. The above equations of motion can be period-by-period and turn-by-turn tracked numerically. Analytically we may solve the equations by first linearizing the wake function and taking Z-transform to obtain the dispersion equation [14, 15]. We find that such multi-turn instability is intrinsically different from conventional Robinson instability. This is because the radiation wake in the laser cavity can slip, while the conventional wake in RF cavity is localized. Such a type of instability appears similar to the free-electron laser (FEL) instability. For more detailed discussions, see Ref. [15].

MULTI-BUNCH MULTI-TURN CASE [20]

The above single-bunch multi-turn case can be generalized to multi-bunch case, corresponding to a more realistic SSMB scenario. The radiation driving term can be deduced from Fig. 2: the wake function experienced by the n-th microbunch on the m-th turn at the q-th undulator period is

$$\begin{aligned} &\sum_{k=0}^{m-1} \sum_{j=0}^{N_b-1} \sum_{p=0}^{q-1} (\sqrt{R})^{N_m(m-k)} \times \\ &W_\parallel \left[(N_{w1} - p)\,\lambda_{r,k,j} + (n-j)\lambda_L + z_{m,n}^{(p)} - z_{k,j}^{(0)} \right], \end{aligned} \tag{3}$$

with R the single mirror reflectivity and N_m the number of mirrors that radiation wake traverses in the cavity.

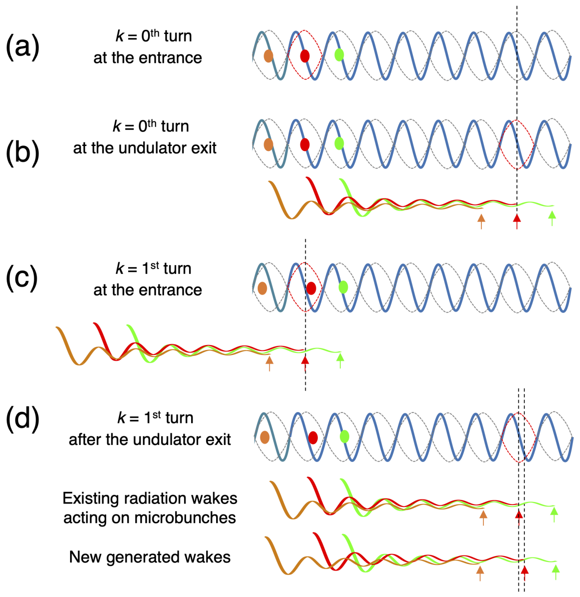

Figure 2: Illustration of the relative positions of the microbunches to the phase space buckets and the undulator radiation wakes for the case of $N_w = 6$.

For the case of uniform filling, there will be a total of $N_b = C_0/\Delta L = C_0/\lambda_L$ microbunches circulating in the storage ring with the circumference C_0. We remind that $N_b = C_0/\lambda_L \sim \mathcal{O}(10^7)$ is a huge number! This number is about 10^5 larger than that of a conventional storage ring. Tracking every individual SSMB microbunches on each turn and on each undulator period becomes almost impossible. Such order of magnitude difference may make it computationally prohibitive to achieve satisfactory turn-by-turn tracking simulations within a short time frame. Thus we need to derive the dispersion equation for the multi-turn multi-bunch case, which becomes a necessary tool from a practical viewpoint. The stability can then be determined by finding the corresponding dispersion or secular equation of the following tracking equations for the n-th microbunch at the p-th period in the modulator undulator on the m-th turn

$$\begin{aligned} z_{m,n}^{(p+1)} &= z_{m,n}^{(p)} - \eta_w \lambda_w \delta_{m,n}^{(p+1)} \\ \delta_{m,n}^{(p+1)} &= \delta_{m,n}^{(p)} + \frac{k_{s0}^2 \lambda_w}{\eta_w} z_{m,n}^{(p)} - \sum_{k=0}^{m-1} \sum_{j=0}^{N_b-1} \left(\sqrt{R}\right)^{N_m(m-k)} \\ &\quad \times \mathcal{W}_\parallel \left[(N_w - p)\,\lambda_{r,k,j} + (n-j)\lambda_L + z_{m,n}^{(p)} - z_{k,j}^{(0)} \right], \end{aligned} \tag{4}$$

where $\mathcal{W}_\parallel = \frac{4\pi\epsilon_0 r_e N \lambda_w}{\gamma} \times W_\parallel$, and in the remaining storage ring from m-th turn to $(m+1)$-th turn

$$\begin{pmatrix} z \\ \delta \end{pmatrix}_{m+1,n}^{(0)} = e^{-\frac{T_0}{2\tau_{\mathrm{SR}}}} \begin{pmatrix} \cos\psi_s & \beta_z \sin\psi_s \\ -\frac{1}{\beta_z}\sin\psi_s & \cos\psi_s \end{pmatrix} \begin{pmatrix} z \\ \delta \end{pmatrix}_{m,n}^{(N_w)}, \tag{5}$$

with T_0 the revolution time, τ_{SR} the synchrotron radiation damping time, the synchrotron phase advance $\psi_s = 2\pi\nu_s$ and $\beta_z \approx -\eta_w/k_{s0}$. Here we assume the longitudinal damping partition number $J_s = 2$. To find the dispersion equation,

ISBN: 978-3-95450-279-0 ISSN: 3043-0208 doi: 10.18429/JACoW-SAP2025-THP07

we define the undulator-averaged phase space coordinates

$$\bar{z}_{m,n} = \frac{1}{N_w}\sum_{p=0}^{N_w-1} z_{m,n}^{(p)}, \quad \bar{\delta}_{m,n} = \frac{1}{N_w}\sum_{p=0}^{N_w-1} \delta_{m,n}^{(p)} \tag{6}$$

after linearizing the above tracking equations for the wake function, the two sets of equations can be simplified to

$$\begin{aligned}
\bar{z}_{m+1,n} &= \bar{z}_{m,n} - \bar{\eta} C_0 \bar{\delta}_{m,n} \\
\bar{\delta}_{m+1,n} &= \frac{k_{s0}^2 L_w}{\eta_w}\bar{z}_{m,n} + \bar{\delta}_{m,n} + \sum_{k=0}^{m-1}\sum_{j=0}^{N_b-1}\left(\sqrt{R}\right)^{N_m(m-k)} \\
&\quad \times \sum_{p=0}^{N_w-1} \mathcal{W}_\parallel' \left[\left(N_w - p\right)\lambda_{r,k,j} + (n-j)\lambda_L\right]\bar{z}_{k,j},
\end{aligned} \tag{7}$$

with $\bar{\eta} = \frac{\eta_w L_w + \eta_{\text{ring}} C_{\text{ring}}}{C_0}$. Let z denote the complex transform-variable corresponding to the discrete time-like index m. Now we apply Z-transform to obtain the dispersion equation, giving

$$(\mathrm{z}-1)^2 + \bar{\eta} C_{\text{tot}}\left(\frac{k_{s0}^2 L_w}{\eta_w}\right) + \frac{\bar{\eta} C_{\text{tot}}\left(\sqrt{R_1}\right)^{N_m}}{\mathrm{z} - \left(\sqrt{R_1}\right)^{N_m}}\mathcal{F}_{\text{LM}}(\mu;\nu) = 0, \tag{8}$$

$$\begin{aligned}
\mathcal{F}_{\text{LM}}(\mu;\nu) &\approx \frac{4\pi\epsilon_0 r_e N N_b L_{w1}}{\gamma_0}\frac{ik_{r1}^2 c}{2\pi}\times \\
&\int_{-H}^{H} d\tilde{k}\,\tilde{k}\,Z_{\parallel,\text{CUR}}(\tilde{k})e^{i2\pi\tilde{k}\left(\frac{N_{w1}+1}{2}\right)}\left(\frac{\sin N_{w1}\pi\tilde{k}}{\sin\pi\tilde{k}}\right)\Pi(\mu;\nu)
\end{aligned} \tag{9}$$

where μ is the multi-bunch mode index, $\Pi(\mu;\nu)$ is the detuning function and $\nu = \frac{\lambda_L - \lambda_r}{\lambda_r}$ is the the detuning parameter between the external laser and the resonant undulator radiation. The cubic dispersion equation can now be solved numerically for z. For general dynamical systems exhibiting exponential growth or decay with time, we assume $\mathrm{z} \propto e^{-i\Omega T_0}$, and the corresponding growth rate per turn can be evaluated by taking the logarithm, i.e., $\tau^{-1} = \operatorname{Im}\Omega/2\pi T_0$ with $\Omega = i/T_0 \cdot \ln \mathrm{z}$.

Now we apply the above theoretical model to estimate the multi-bunch multi-turn instability based on a set of preliminary SSMB design parameters. Assume the electron bunch charge $N = 10^5$ (here we make a slightly more aggressive setting), beam energy 400 MeV, modulator voltage 70 kV, corresponding modulation laser power 500 kW at 1064 nm, modulator undulator $K = 2.6$, $\lambda_w = 30$ cm, $N_w = 11$ and total mirror reflectivity 0.999. The storage ring circumference is assumed 100 m, with $\bar{\eta} \approx 10^{-7}$. For uniform filling, the total number of microbunches is approximately 10^8, which indeed increases by almost five orders of magnitude compared to conventional storage rings, making turn-by-turn tracking of individual microbunches nearly impossible. Figure 3 presents the multi-bunch growth rate per turn as a function of the detune parameter ν (left) and the multi-bunch index μ (right). For the left panel, the initial multibunch mode is set $\mu = N_b - 10^4$, where $-10^4/N_b \approx -1.064\times10^{-4}$. It is found that when the detune happens to be close to this ratio, this multi-bunch mode may potentially be excited. Near the "excitation" detune, the growth rate per turn $\tau^{-1} \approx 0.65$ or $1.95\times10^6\ \mathrm{s}^{-1}$. Since the total number of multibunch modes N_b is too large to display in the figure, we only present the modes near the ones with significantly non-zero growth rates, while the growth rates of most other modes not shown in the figure approach zero. In the right panel we set the initial detune to $+1.064\times10^{-4}$. As anticipated, the excited mode is $\mu = 10^4$.

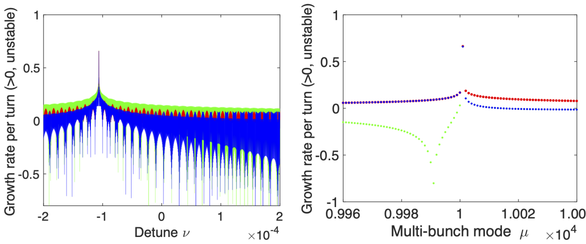

Figure 3: Growth rate per turn as a function of the frequency detune ν (left) and the multi-bunch mode index μ (right).

According to the current preliminary design, for the nominal case the microbunch charge is 10^4. From the above calculation results, it can be inferred that the growth rate would be reduced by roughly one order of magnitude. Such a growth rate may still be somewhat larger than that typically estimated for coupled-bunch instabilities in conventional storage rings. While we do not address mitigation schemes for this type of instability here, we note that, under favorable conditions in the laser modulator cavity, the coherent undulator radiation may enhance synchrotron oscillations, as discussed in Ref. [13]. Therefore, the growth rates inferred based on the present calculation may still fall within an acceptable range. It is also worth noting that this inference seems consistent with the conclusions reached when applying an alternative approach to the study of multibunch multiturn beam dynamics in the SSMB storage ring [16–18].

SUMMARY

In the above analysis we find that under the present nominal design parameters, the undulator radiation driven single-pass multi-bunch beam breakup instability is not a concern. For multi-bunch multi-turn case, we have derived and numerically solved the corresponding dispersion equation for the instability growth rate. We find that when the detuning parameter approaches a specific multi-bunch mode divided by the number of total microbunches, this instability mechanism tends to amplify that mode. We discuss possible mitigation effect of the potential well on the instability and find that based on the nominal SSMB beam and undulator parameters, the undulator radiation driven multi-bunch instability remains within an acceptable range or roughly at the stability margin. The present theoretical analysis is constructed based on the macroparticle model and assumes uniform fill around the storage ring. For practical scenarios involving uneven fill or partial uniform fill, this analysis requires further generalization.

REFERENCES

[1] D. F. Ratner and A. W. Chao, "Steady-state microbunching in a storage ring for generating coherent radiation", *Phys. Rev. Lett.*, vol. 105, p. 154801, 2010. `doi:10.1103/PhysRevLett.105.154801`

[2] Y. Jiao, D. F. Ratner, and A. W. Chao, "Terahertz coherent radiation from steady-state microbunching in storage rings with x-band radio-frequency system", *Phys. Rev. Spec. Top.-Accel. Beams*, vol. 14, p. 110702, 2011. `doi:10.1103/PhysRevSTAB.14.110702`

[3] D. F. Ratner and A. Chao, "Reversible Seeding in Storage Rings", in *Proc. FEL'11*, Shanghai, China, Aug. 2011, paper MOPB23, pp. 57–60.

[4] A. Chao, E. Granados, X. Huang, D. F. Ratner, and H. W. Luo, "High Power Radiation Sources using the Steady-state Microbunching Mechanism", in *Proc. IPAC'16*, Busan, Korea, May 2016, pp. 1048–1053. `doi:10.18429/JACoW-IPAC2016-TUXB01`

[5] X. J. Deng *et al.*, "Widening and distortion of the particle energy distribution by chromaticity in quasi-isochronous rings", *Phys. Rev. Accel. Beams*, vol. 23, p. 044001, 2020. `doi:10.1103/PhysRevAccelBeams.23.044001`

[6] X. J. Deng, A. W. Chao, J. Feikes, W. H. Huang, M. Ries, and C. X. Tang. "Single-particle dynamics of microbunching", *Phys. Rev. Accel. Beams*, vol. 23, p. 044002, 2020. `doi:10.1103/PhysRevAccelBeams.23.044002`

[7] X. J. Deng *et al.*, "Experimental demonstration of the mechanism of steady-state microbunching", *Nature*, vol. 590, pp. 576–579, 2021. `doi:10.1038/s41586-021-03203-0`

[8] X. J. Deng, A. W. Chao, W. H. Huang, and C. X. Tang, "Courant-Snyder formalism of longitudinal dynamics", *Phys. Rev. Accel. Beams*, vol. 24, p. 094001, 2021. `doi:10.1103/PhysRevAccelBeams.24.094001`

[9] Z. Li, X. Deng, Z. Pan, C. Tang, and A. Chao, "Generalized longitudinal strong focusing in a steady-state microbunching storage ring", *Phys. Rev. Accel. Beams*, vol. 26, p. 110701, 2023. `doi:10.1103/PhysRevAccelBeams.26.110701`

[10] Y. Zhang, X. J. Deng, Z. L. Pan, Z. Z. Li, K. S. Zhou, W. H. Huang, R. K. Li, C. X. Tang, and A. W. Chao, "Ultralow longitudinal emittance storage rings", *Phys. Rev. Accel. Beams*, vol. 24, p. 090701, 2021. `doi:10.1103/PhysRevAccelBeams.24.090701`

[11] X. J. Deng, Y. Zhang, Z. L. Pan, Z. Z. Li, J. H. Bian, C.-Y. Tsai, R. K. Li, A. W. Chao, W. H. Huang, and C. X. Tang, "Average and statistical properties of coherent radiation from steady-state microbunching", *J. Synchrotron Radiat.*, vol. 30, pp. 35–50, 2023. `doi:10.1107/S1600577522009973`

[12] X. J. Deng, Theoretical and experimental studies on steady-state microbunching. Singapore: Springer, 2024. `doi:10.1007/978-981-99-5800-9`

[13] C.-Y. Tsai, A. W. Chao, Y. Jiao, H.-W. Luo, M. Ying, and Q. Zhou, "Coherent-radiation-induced longitudinal single-pass beam breakup instability of a steady-state microbunch train in an undulator", *Phys. Rev. Accel. Beams*, vol. 24, p. 114401, 2021. `doi:10.1103/PhysRevAccelBeams.24.114401`

[14] C.-Y. Tsai, "Longitudinal single-bunch instabilities driven by coherent undulator radiation in the cavity modulator of a steady-state microbunching storage ring", *Nucl. Instrum. Methods Phys. Res. A: Accel. Spectrom. Detect. Assoc. Equip. A*, vol. 1042, p. 167454, 2022. `doi:10.1016/j.nima.2022.167454`

[15] C.-Y. Tsai. "Theoretical formulation of multiturn collective dynamics in a laser cavity modulator with comparison to Robinson and high-gain free-electron laser instability", *Phys. Rev. Accel. Beams*, vol. 25, p. 064401, 2022. `doi:10.1103/PhysRevAccelBeams.25.064401`

[16] C.-Y. Tsai and X. J. Deng. "A recursive model for laser-electron-radiation interaction in insertion section of SSMB storage rings based on the transverse-longitudinal coupling scheme", in *Proc. 67th ICFA Adv. Beam Dyn. Workshop Future Light Sources (FLS'23)*, Luzern, Switzerland, Aug.-Sep. 2023, pp. 147–150. `doi:10.18429/JACoW-FLS2023-TU4P31`

[17] C.-Y. Tsai and X. J. Deng, "Analysis of laser-electron-radiation interaction in laser modulators for three SSMB scenarios", presented at the IPAC'25, Taipei, Taiwan, Jun. 2025, paper TUPM030, to be published.

[18] C.-Y. Tsai and X. J. Deng, "Simple model for electron beam dynamics in laser modulators and radiation characteristics of steady-state microbunching storage ring", *Phys. Rev. Accel. Beams*, vol. 28, p. 074402, 2025. `doi:10.1103/kwxj-4bff`

[19] C.-Y. Tsai, "Mechanism to generate continuous kilowatt coherent THz radiation based on self-sustained laser modulation in a steady-state microbunching storage ring", *Opt. Lett.*, vol. 50, pp. 5198–5201, 2025. `doi:10.1364/OL.568233`

[20] C.-Y. Tsai, "Study of the longitudinal multibunch multiturn collective dynamics in the laser modulators of a steady-state microbunching storage ring: A macroparticle model", *Nucl. Instrum. Methods Phys. Res. A: Accel. Spectrom. Detect. Assoc. Equip. A*, vol. 1083, p. 171127, 2025. `doi:10.1016/j.nima.2025.171127`

ISBN: 978-3-95450-279-0 ISSN: 3043-0208 doi: 10.18429/JACoW-SAP2025-THP08

COHERENT kW THz RADIATION FROM AN SSMB STORAGE RING VIA SELF-SUSTAINED LASER MODULATION*

Cheng-Ying Tsai†, School of Electrical and Electronic Engineering,
Huazhong University of Science and Technology, Wuhan, China

Abstract

Due to the unique role of terahertz (THz) radiation in the electromagnetic spectrum, it possesses significant scientific value and potential applications in fundamental science, biomedical research, spectroscopy, and etc. This paper proposes a novel mechanism for generating continuous kilowatt-level coherent terahertz radiation in steady-state microbunching storage rings, based on self-sustaining laser modulation processes. The analysis employs the transfer matrix method from accelerator physics, considering the dynamical evolution of electron beams during multiple passes through the laser modulator, as well as radiation damping and quantum excitation effects in the storage ring. Numerical tracking results demonstrate the feasibility of this mechanism. In a demonstrative case, we show that 1 kW continuous coherent radiation can be achieved at 5 THz frequency, corresponding to electric field strengths on the order of MV/m. Since this scheme is based on free electrons, its radiation output characteristics can be tuned over a broad frequency range of 1–10 THz, offering extremely high application value in scientific research.

INTRODUCTION

Terahertz (THz) radiation holds significant scientific value and broad potential for applications across both fundamental and applied sciences. In the most demanded frequency range of 1–10 THz, existing electronic and opto-electronic systems struggle to generate high-average-power, narrowband, tunable terahertz radiation, leading to the so-called “THz gap” [1]. Currently, numerous methods exist for generating THz radiation. In this paper we propose a novel mechanism capable of generating continuous, high-average-power coherent THz radiation. As illustrated in Fig. 1, based on the steady-state microbunching (SSMB) mechanism [2, 3], this electron storage ring primarily comprises a laser modulator (LM) with laser wavelength λ_L that modulates the traversing electron beam to produce a microbunch train with bunch spacing $\approx \lambda_L$, and a radiator downstream (with target radiation wavelength λ_{THz}), where the electron beam emits the desired coherent radiation. The microbunches in the storage ring receive energy modulation from the two modulator undulators with slightly different undulator parameters. Then the microbunches with frequency-beating component will emit coherent radiation at the beating frequency in the downstream radiator. This innovative storage ring differs from conventional RF-based ones, as the electron bunch length is now determined by the phase space bucket formed by the LM, with a bucket width approximately equal to the laser modulation wavelength — at least five orders of magnitude shorter than the RF wavelength of conventional microwave cavities. To provide stable and effective energy modulation in the LM, an optical enhancement cavity (OEC) is designed to store sufficient laser power while external laser injection is typically required to compensate for cavity losses. This novel scheme significantly reduces the dependence on the external modulation laser by directly utilizing the resonant undulator radiation generated by the traversing electron beam in the LM. The proposed scheme requires the external laser modulation only very briefly during the initial stage to form a microbunch train, eliminating the need for long-term stable maintenance of external laser injection. The analysis employs transfer matrices incorporating the dynamics as the electron beam traverses the LM in successive passes, along with radiation damping and quantum excitation in the storage ring. In the demonstrated example, continuous 1 kW of coherent radiation at 5 THz can be generated.

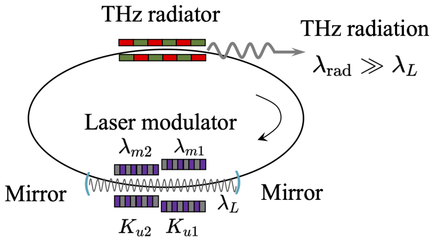

Figure 1: Schematic layout of the self-sustained infrared laser modulator (LM) based on an SSMB storage ring.

THEORETICAL MODEL

Here we summarize the basic ingredients of the theoretical model. Due to page limit, we refer the interested readers to Refs. [4–7] for more details.

- The transfer matrix of a laser modulator (LM) is described as a thick longitudinal quadrupole, in which the modulation or chirp strength $h = k_L \frac{\Delta\mathscr{E}}{\gamma mc^2}$ is evaluated from Lorentz equation for the energy exchange $\Delta\mathscr{E} = \int (d\mathscr{E}/ds)ds$ in the two modulator undulators.
- The turn-by-turn variation of modulation power in the LM is expressed as the sum of accumulated external injection laser power $P_{L,n}^{\mathrm{ext}}$ and the resonant undulator radiation power, i.e., $P_{L,n} = P_{L,n}^{\mathrm{ext}} + \delta P^{(n)}$, where the latter is evaluated according to Ref. [8].

---

* This work is supported by the Fundamental Research Funds for the Central Universities (HUST) under Project No. 2021GCRC006 and National Natural Science Foundation of China under project No. 12275094.

† jcytsai@hust.edu.cn

ISBN: 978-3-95450-279-0 ISSN: 3043-0208 doi: 10.18429/JACoW-SAP2025-THP08

- In the LM cavity, the evolution of modulation power can be described by $P_{L,n+1} = R \cdot P_{L,n}$, where $R < 1$ is total mirror reflectivity.
- The longitudinal transport for the remaining half a storage ring $\mathbf{R}_{1/2}$ is expressed as the familiar 2×2 transfer matrix. The turn-by-turn tracking for the beam sigma matrix Σ_n follows $\Sigma_{n+1} = \mathscr{O}_n \Sigma_n \mathscr{O}_n^T$ with one-turn matrix $\mathscr{O}_n = \mathbf{R}_{1/2}\mathbf{M}_{LM,n}\mathbf{R}_{1/2}$.
- Radiation damping and quantum excitation are included respectively in $\mathbf{R}_{1/2}$ and Σ_n, as described in Ref. [6]. Intrabeam scattering (IBS) is added following Ref. [7].

EXAMPLE

Now we present a preliminary design for generating THz radiation using a self-sustained LM. The parameters of the electron beam, the laser modulator, and the radiator are summarized in Table 1. According to the resonance condition of the LM, an appropriate choice can be made for $\lambda_{u,\mathrm{mod}}$ and $K_{u,\mathrm{mod}}$, where $K_u \approx 0.934 B_0[\mathrm{T}]\lambda_u[\mathrm{cm}]$. The choice is not unique; as shown in Fig. 2(a), we select those marked by red arrows. The total length of modulator undulators should not be excessively long to prevent the occurrence of FEL gain process [9]. The parameters for the radiator undulator can be determined through the resonance relations between $\lambda_{\mathrm{THz}} = \frac{\lambda_{u,\mathrm{rad}}}{2\gamma^2}\left(1 + \frac{K_{u,\mathrm{rad}}^2}{2}\right) = \frac{\lambda_L}{2\Delta}$ and λ_L in the LM, which gives $\frac{\lambda_{u,\mathrm{mod}}}{2\Delta}\left(1 + \frac{K_{u,\mathrm{mod}}^2}{2}\right) = \lambda_{u,\mathrm{rad}}\left(1 + \frac{K_{u,\mathrm{rad}}^2}{2}\right)$. Here $\Delta = (K_{u2} - K_{u1})/K_{u,\,\mathrm{mod}}$. Combining the relation $K_{u,\mathrm{rad}} \approx 0.934 B_{0,\mathrm{rad}}[\mathrm{T}]\lambda_{u,\mathrm{rad}}[\mathrm{cm}]$, Fig. 2(b) gives possible choices of $\lambda_{u,\mathrm{rad}}$ and $K_{u,\mathrm{rad}}$.

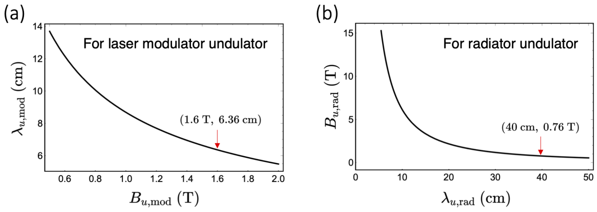

Figure 2: (a) Modulator undulator period and the on-axis magnetic field for $\lambda_L = 1064$ nm; (b) radiator undulator period and the on-axis magnetic field for the case of 5 THz central frequency. Assume beam energy is 600 MeV.

Table 1: Preliminary Design Parameters of the Electron Beam, the Laser Modulator, and the Radiator for THz Radiation

Name	Value	Unit
Beam energy γmc^2	600	MeV
Average bunch current I_b	0.55	A
Initial rms energy spread $\sigma_{\delta 0}$	4.28×10^{-4}	
Initial rms bunch length σ_{z0}	0.195	μm
Initial rms beam size σ_x	100	μm
Transverse beam emittance ϵ_x	4.8	nm
Laser mod. wavelength λ_L	1064	nm
Rayleigh length z_R	0.424	m
Initial energy chirp strength h	958	m^{-1}
Modulator undu. period $\lambda_{u1,u2}$	6.36, 6.36	cm
Modulator undu. length $L_{u1,u2}$	0.636, 0.636	m
Modulator undu. param. $K_{u1,u2}$	9.46, 9.54	
Ave. mod. und. mag. field B_0	1.6	T
Target radiation frequency f_{THz}	5	THz
Radiator undu. period $\lambda_{u,\mathrm{rad}}$	40	cm
Radiator undu. length $L_{u,\mathrm{rad}}$	16	m
Radiator undu. param. $K_{u,\mathrm{rad}}$	28.62	
Radiator undu. $B_{0,\mathrm{rad}}$	0.76	T
Storage ring circumference C_0	50	m
Storage ring slippage factor η_{tot}	4×10^{-6}	
Synchrotron tune ν_s	0.06	
Radiation damping time τ_{RD}	0.125	ms

The laser power stored in the LM is used to provide sufficient energy modulation to stabilize the electron beam through successive turns in the storage ring. During the first passage, a modulation laser power ≈ 500 kW is required to provide the initial equilibrium energy modulation strength $h \approx 958\,\mathrm{m}^{-1}$; however, once the microbunch is formed, our analysis below demonstrates that an external injection laser is no longer needed. Based on the given parameters, we track the beam over 10^5 turns. Figure 3 illustrates the dependence of the microbunch length, the bunching factor, the modulation laser power, and the average radiation power at the radiator on cavity mirror reflectivities at 600 MeV. The coherent radiation power at the radiator can be calculated using the following formula [8]

$$P_{\mathrm{rad}}^{(n)} = \frac{\pi}{\epsilon_0 c} N_{u,\mathrm{rad}} \left(\frac{K_{u,\mathrm{rad}}^2}{4 + 2K_{u,\mathrm{rad}}^2}\right) [\mathrm{JJ}]^2 FF_\perp(S) |b_n|^2 I_b^2, \quad (1)$$

where the relevant physical quantities are now evaluated at the radiator. Here the bunching factor b_n can be evaluated from beam sigma matrix as $|b_n| = e^{-\frac{1}{2}\left(\frac{2\pi}{\lambda_L}\right)^2 \sigma_{z,n}^2}$, $[\mathrm{JJ}] = J_0\left(\frac{K_u^2}{4+2K_u^2}\right) - J_1\left(\frac{K_u^2}{4+2K_u^2}\right)$ and $FF_\perp(S) = \frac{2}{\pi}\left[\tan^{-1}\left(\frac{1}{2S}\right) + S \ln\left(\frac{(2S)^2}{(2S)^2+1}\right)\right]$ with $S = \sigma_x^2 \omega_L / c L_u$. For the turn-by-turn evolution of the modulation laser in the LM, we consider three scenarios:

1. Neglecting the gain process in the LM, i.e., neglecting resonant undulator radiation $\delta P^{(n)} = 0$, where the cavity reflectivity loss is compensated by externally injected laser power $P_{\mathrm{inj}} = P_{L,n}(1 - R)$. Equilibrium is reached when the cavity loss is precisely compensated by the external laser input. This scenario corresponds to the blue lines in Fig. 3 and aligns with the initial design parameters;
2. With external laser compensation as above, we further consider the gain process from resonant undulator radiation of the electron beam in the LM. This scenario corresponds to the red lines in Fig. 3;
3. Without external laser injection, we consider only the gain process in the LM. This scenario corresponds to

ISBN: 978-3-95450-279-0 ISSN: 3043-0208 doi: 10.18429/JACoW-SAP2025-THP08

the black lines in Fig. 3, representing the self-sustained LM scheme.

For scenario 2), since the radiation generated by the electron beam on each pass is captured and trapped within the cavity, the increasingly powerful modulation laser provides stronger energy modulation than the design value. This incremental mismatch leads to shorter microbunch lengths and higher bunching factors in the LM. When the dynamics forms a positive feedback, the power in the LM cavity continues to grow. However, according to the present laser technology, the maximum sustainable power level in an enhancement cavity is limited to below 1 MW, with the state-of-the-art stable storage power reaching approximately 710 kW [10]. Thus the situations where $P_L > 1$ MW will not be physically realistic. In contrast, when the reflectivity is too small, the cavity loss becomes excessive and the LM will not be self-sustainable. Thus, for scenario 3), the gain process from resonant undulator radiation alone cannot compensate to restore equilibrium if the reflectivity is too low. Fortunately, there exists a range of reflectivity values where a portion of resonant undulator radiation can compensate for cavity losses, while in the first few turns, the remaining radiation can effectively accumulate and stably provide the necessary energy modulation for the electron beam passing through the LM.

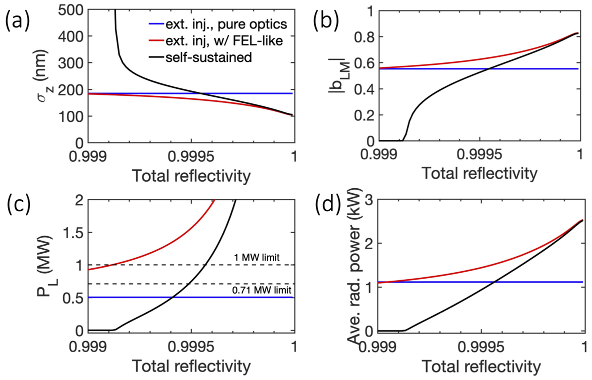

Figure 3: Dependence of the microbunch length at the LM (a); the bunching factor at the LM (b); storage power at the LM (c) and the radiation power at the radiator undulator (d) on the total cavity reflectivity for different physics settings.

Figure 3 illustrates the dependence of the radiator power on different cavity reflectivities at 600 MeV. Within the present laser technology, i.e., 0.7 MW to 1 MW limit, corresponding to $R \approx 0.9995 \sim 0.9996$, approximately 1 kW of continuous coherent radiation at 5 THz can be generated. Intra-cavity powers exceeding 1 MW can induce thermal distortions in enhancement cavity mirrors, affecting mode quality and stability; practical mitigation involves optimized cavity design, efficient heat removal, and thermally robust optical components. As for beam stability, we find that the IBS effect at 600 MeV can be negligible. Our calculations indicate that for lower electron energies, such as 400 MeV, IBS effects would become significant. Unlike ERL-based FELs, the proposed scheme benefits from synchrotron radiation damping in the storage ring, providing enhanced stability and improved control of the circulating electron beam. The selection of beam current needs to consider both single-bunch and multi-bunch instabilities. Our previous analysis [11] suggests that multi-bunch beam breakup instability is not a significant concern. According to Ref. [12], space-charge-induced single-bunch tune shift is negligibly small and multibunch space-charge tune shift is also not a critical issue. We estimate the coherent synchrotron radiation (CSR) induced single-bunch instability threshold in the storage ring to be approximately 0.77 A. In the design parameters, we have selected a bunch current of 0.55 A. Figure 4 presents the calculated results for modulation laser power P_L and radiator power P_{rad} after scanning a range of currents; we believe that achieving 1 kW radiation output using a self-sustained LM is feasible.

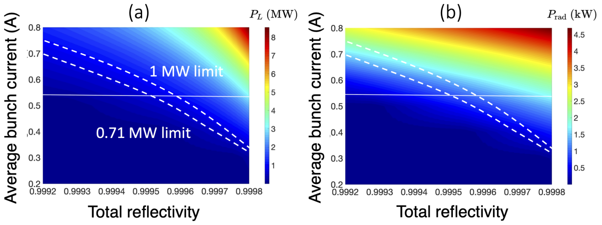

Figure 4: Dependence of the laser power P_L in the LM (a) and that of the radiation power in the radiator (b) on the average bunch current and the total cavity reflectivity.

SUMMARY AND DISCUSSION

In this paper we propose a scheme to generate continuous kilowatt coherent THz radiation based on self-sustained laser modulation in an SSMB storage ring. Using the developed transfer matrix formulation, we evaluate the feasibility of this mechanism for a 600 MeV electron beam energy. The key advantage of this scheme is that, apart from briefly requiring external laser modulation during the initial stage, it subsequently can operate without external injection, relying instead on the resonant undulator radiation generated by the microbunch for stable operation. Under the present limits of storage power in optical enhancement cavities, our scheme can produce continuous 1 kW of coherent radiation at 5 THz. Since this scheme is based on free electrons, similar radiation output characteristics can be tuned across a wide central frequency range of 1–10 THz, rendering it an valuable tool for scientific explorations.

It deserves here to emphasize that using macroparticle model to analyze the multi-bunch multi-turn beam dynamics in the SSMB storage ring provides an alternative approach to the problem. While the two approaches are not equivalent, the macroparticle results seem consistent with the conclusions reached here. The interested readers are referred to Refs. [13–15] for more discussions.

REFERENCES

[1] R.A. Lewis, "A review of terahertz sources", *J. Phys. D: Appl. Phys.*, vol. 47, p. 374001, 2014. doi:10.1088/0022-3727/47/37/374001

[2] D.F. Ratner and A.W. Chao, "Steady-state microbunching in a storage ring for generating coherent radiation", *Phys. Rev. Lett.*, vol. 105, no. 15, p. 154801, 2010. doi:10.1103/PhysRevLett.105.154801

[3] Y. Jiao, D.F. Ratner, and A.W. Chao, "Terahertz coherent radiation from steady-state microbunching in storage rings with x-band radio-frequency system", *Phys. Rev. Spec. Top. Accel. Beams*, vol. 14, no. 11, p. 110702, 2011. doi:10.1103/PhysRevSTAB.14.110702

[4] C.-Y. Tsai and X.J. Deng, "A recursive model for laser-electron-radiation interaction in insertion section of SSMB storage rings based on the transverse-longitudinal coupling scheme", in *Proc. FLS'23*, Luzern, Switzerland, Aug.-Sep. 2023, pp. 147–150. doi:10.18429/JACoW-FLS2023-TU4P31

[5] C.-Y. Tsai and X.J. Deng, "Analysis of laser-electron-radiation interaction in laser modulators for three SSMB scenarios", presented at IPAC'25, Taipei, Taiwan, Jun. 2025, paper TUPM030, to be published.

[6] C.-Y. Tsai and X.J. Deng, "Simple model for electron beam dynamics in laser modulators and radiation characteristics of steady-state microbunching storage ring", *Phys. Rev. Accel. Beams*, vol. 28, p. 074402, 2025. doi:10.1103/kwxj-4bff

[7] C.-Y. Tsai, "Mechanism to generate continuous kilowatt coherent THz radiation based on self-sustained laser modulation in a steady-state microbunching storage ring", *Opt. Lett.*, vol. 50, no. 17, pp. 5198–5201, 2025. doi:10.1364/OL.568233

[8] X.J. Deng, *Theoretical and experimental studies on steady-state microbunching*. Singapore: Springer Nature, 2024. doi:10.1007/978-981-99-5800-9

[9] K.-J. Kim, Z. Huang, and R. Lindberg, *Synchrotron radiation and free-electron lasers*. Cambridge, UK: Cambridge University Press, 2017.

[10] X.-Y. Lu, R. Chiche, K. Dupraz, *et al.*, "710 kw stable average power in a 45,000 finesse two-mirror optical cavity", *Opt. Lett.*, vol. 49, pp. 6884–6887, 2024. doi:10.1364/OL.543388

[11] C.-Y. Tsai, A.W. Chao, Y. Jiao, H.-W. Luo, M. Ying, and Q. Zhou, "Coherent-radiation-induced longitudinal single-pass beam breakup instability of a steady-state microbunch train in an undulator", *Phys. Rev. Accel. Beams*, vol. 24, no. 11, p. 114401, 2021. doi:10.1103/PhysRevAccelBeams.24.114401

[12] Z. Zhao, N. Wang, H. Xu, and Z. Pan, "Calculations of space-charge tune shifts in storage rings with extremely short bunches and small bunch spacing", *Phys. Rev. Accel. Beams*, vol. 27, p. 094201, 2024. doi:10.1103/PhysRevAccelBeams.27.094201

[13] C.-Y. Tsai, "Longitudinal single-bunch instabilities driven by coherent undulator radiation in the cavity modulator of a steady-state microbunching storage ring", *Nucl. Instrum. Methods Phys. Res. A*, vol. 1042, p. 167454, 2022. doi:10.1016/j.nima.2022.167454

[14] C.-Y. Tsai, "Theoretical formulation of multiturn collective dynamics in a laser cavity modulator with comparison to Robinson and high-gain free-electron laser instability", *Phys. Rev. Accel. Beams*, vol. 25, no. 6, p. 064401, 2022. doi:10.1103/PhysRevAccelBeams.25.064401

[15] C.-Y. Tsai, "Study of the longitudinal multibunch multiturn collective dynamics in the laser modulators of a steady-state microbunching storage ring: a macroparticle model", submitted for publication.

QUASI-LINEAR THEORY OF SINGLE-PASS MICROBUNCHING INSTABILITY

Cheng-Ying Tsai*, School of Electrical and Electronic Engineering,
Huazhong University of Science and Technology, Wuhan, China

Abstract

The existing theoretical treatment of single-pass microbunching instability (MBI) typically assumes a coasting beam and adopts a linear framework, within which the microbunching gain may grow without bound. While the inclusion of intrabeam scattering (IBS) introduces damping effects that may suppress excessive gain, these models remain fundamentally linear and do not capture saturation behavior. In this work, we develop a quasi-linear theory of MBI based on the Vlasov equation, incorporating the evolution of beam energy spread induced by the instability itself. The quasi-linear formulation yields a set of coupled equations describing the evolution of the bunching factor and energy spread, still under the coasting beam approximation where different modulation wavelengths evolve independently. This approach provides a more realistic description of the nonlinear evolution of MBI and offers insight into its natural saturation mechanism.

INTRODUCTION

Microbunching instability (MBI) in a single-pass high-brightness electron beam transport has been an active research topic in the past two decades (see, for example, Refs. [1–13]). The existing theoretical treatment of single-pass MBI typically assumes a coasting beam and adopts a linear framework, within which the microbunching gain may grow without bound, i.e., there is no saturation mechanism. MBI with inclusion of intrabeam scattering (IBS) or incoherent synchrotron radiation (ISR) may cause the gain not grow too high, but still a linear theory [9–12]. Here in this paper we formulate a quasi-linear theory, which, although not including IBS/ISR, can lead to saturation when the intrinsic energy spread increases due to the instability mechanism itself. It is found that the quasi-linear theory gives a set of coupled equations for bunching factor and energy spread. Here we remark that our developed quasi-linear theory still assumes a coasting beam, i.e., the modulation wavelength is much shorter compared to the total electron duration. This implies that different modulation wavelengths do not couple in the governing integral equations.

QUASI-LINEAR THEORY

For simplicity, the following analysis assumes only the longitudinal 2-D phase space (z, δ). It is straightforward to extend the theoretical formulation to 4-D or 6-D including transverse dimensions. We start from the single particle equations of motion

$$\begin{aligned} \frac{dz}{ds} &= -\eta\delta = R'_{56}\delta \\ \frac{d\delta}{ds} &= \frac{k_{s0}^2}{\eta}z - \frac{4\pi\epsilon_0 r_e c N}{\gamma}\int_{-\infty}^{\infty}\frac{dk}{2\pi}Z_\parallel(k;s)b(k;s)e^{ikz} \end{aligned} \tag{1}$$

where η or R_{56} is the momentum compaction function, k_{s0} is the longitudinal oscillation wavenumber (under coasting beam approximation, $k_{s0} \to 0$), r_e is the classical electron radius, c is the speed of light, N is the number of electrons, γ is the beam reference energy in unit of rest-mass energy, and $k = 2\pi/\lambda = \omega/c$ is the modulation wavenumber. Here $b(k; s)$ is the bunching factor defined as the Fourier transform of the perturbed line density distribution (see later) and $Z_\parallel(k; s)$ is the high-frequency impedance per unit length. Note that $b^*(k) = b(-k)$ and $Z^*_\parallel(k) = Z_\parallel(-k)$.

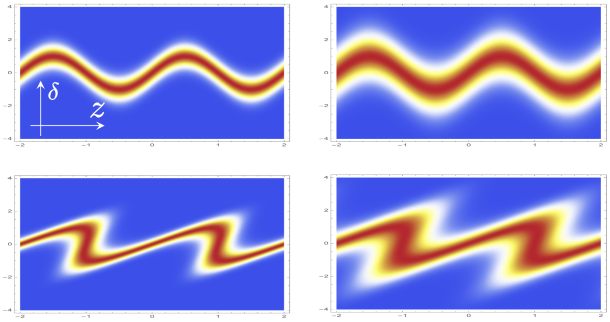

Figure 1: Illustration of intrinsic energy spread increase in the longitudinal phase space distribution.

The phase space distribution $f(z, \delta; s)$, with normalization condition $\iint f(z, \delta) = N$, follows the Vlasov equation

$$\frac{\partial f}{\partial s} + \left(\frac{dz}{ds}\right)\frac{\partial f}{\partial z} + \left(\frac{d\delta}{ds}\right)\frac{\partial f}{\partial \delta} = 0. \tag{2}$$

To simplify, we assume $f(z, \delta; s) = f_0(\delta; s) + f_1(z, \delta; s)$ with $|f_1| \ll f_0$. Now we can split the Vlasov equation into two parts: the slow equation

$$\frac{\partial f_0}{\partial s} + \left(\frac{dz}{ds}\right)\frac{\partial f_0}{\partial z} + \left(\frac{d\delta}{ds}\right)_1\frac{\partial f_1}{\partial \delta} = 0 \tag{3}$$

and the fast equation

$$\frac{\partial f_1}{\partial s} + \left(\frac{dz}{ds}\right)\frac{\partial f_1}{\partial z} + \left(\frac{d\delta}{ds}\right)_1\frac{\partial f_0}{\partial \delta} = 0, \tag{4}$$

where we keep the last term on LHS of Eq. (3). We note that it is this term that plays a role in the quasi-linear theory; see

---

[*] Email: jcytsai@hust.edu.cn. This work is supported by the Fundamental Research Funds for the Central Universities (HUST) under Project No. 2021GCRC006 and National Natural Science Foundation of China under project No. 12275094.

Fig. 1. This treatment is similar to that applied in the quasi-linear theory of FEL [14]. An equivalent integral equation of Eq. (4) can be written as

$$f_1(s) = f_1(s=0) - \int_0^s \frac{d\delta}{d\tau}\frac{\partial f_0}{\partial \delta_\tau} d\tau, \tag{5}$$

which we will solve. Before proceeding, let us define the bunching function below

$$\mathcal{B}(k,\delta;s) = \frac{1}{2\pi}\int_{-\infty}^{\infty} f_1(z,\delta;s) e^{-ikz} dz, \tag{6}$$

then the familiar bunching factor becomes

$$\begin{aligned} b(k;s) &= \frac{1}{N}\iint_{-\infty}^{\infty} d\delta dz f_1(z,\delta;s) e^{-ikz} \\ &= \frac{2\pi}{N}\int_{-\infty}^{\infty} d\delta \mathcal{B}(k,\delta;s). \end{aligned} \tag{7}$$

Moreover, we define the energy distribution $V(\delta;s) = \int_{-\infty}^{\infty} f_0(z,\delta;s)dz$. Now, Integrating the slow equation over z on both sides gives

$$\frac{\partial V}{\partial s} - \alpha \int_{-\infty}^{\infty} dk Z_\parallel^*(k;s) b^*(k;s) \frac{\partial}{\partial \delta}\mathcal{B}(k,\delta;s) = 0 \tag{8}$$

with $\alpha = \frac{4\pi\epsilon_0 r_e c N}{\gamma} = \frac{4\pi}{Z_0}\frac{I_b}{\gamma I_A}$. Note that without the second term, which is the usual linearized Vlasov theory, the energy distribution remains unchanged, as expected. Let us further define the following notations associated with the m-th moment, denoted by square bracket $[m]$

$$\begin{aligned} \mathcal{V}_{[m]}(s) &= \int_{-\infty}^{\infty} V(\delta;s)\delta^m d\delta \\ b_{[m]}(k;s) &= \frac{2\pi}{N}\int_{-\infty}^{\infty} \mathcal{B}(k,\delta;s)\delta^m d\delta. \end{aligned} \tag{9}$$

For $m=0$ case, we have

$$\mathcal{V}_{[0]} = \int_{-\infty}^{\infty} V(\delta;s)d\delta = \int_{-\infty}^{\infty}\int_{-\infty}^{\infty} f_0(z,\delta;s)dzd\delta = N, \tag{10}$$

which indicates the conservation of particles. The usual bunching factor becomes $b_{[0]}(k;s)$. With the definition of $\mathcal{B}$, the fast equation can be cast into the following form

$$\begin{aligned} \mathcal{B}(k,\delta;s) &= \mathcal{B}^{(0)}(k,\delta;s) + \\ &\frac{\alpha}{2\pi}\int_0^s d\tau \frac{\partial f_0}{\partial \delta_\tau} Z_\parallel(k;\tau) b_{[0]}(k;\tau) e^{-ikR_{56}(\tau\to s)\delta_\tau} \end{aligned} \tag{11}$$

here for 2-D case, $R_{56}(\tau \to s) = R_{56}(s) - R_{56}(\tau)$. Now we integrate the slow equation over energy deviation δ to obtain a set of recursive equations. Skipping the detailed derivations, we obtain

$$\begin{aligned} &\frac{\partial}{\partial s}\mathcal{V}_{[m]} + \\ &m\frac{\alpha N}{2\pi}\int_{-\infty}^{\infty} dk Z_\parallel^*(k;s) b_{[0]}^*(k;s) b_{[m-1]}(k;s) = 0. \end{aligned} \tag{12}$$

Some observations from the equation:

- for $m=0$ case, from Eq. (12) we have

$$\begin{aligned} &\frac{\partial}{\partial s}\mathcal{V}_{[0]} - \\ &\frac{\alpha N}{2\pi}\int_{-\infty}^{\infty} dk Z_\parallel^*(k;s) b_{[0]}^*(k;s) \int \frac{\partial}{\partial \delta}\mathcal{B}(k,\delta;s)d\delta = 0, \end{aligned} \tag{13}$$

  since the term $\int \frac{\partial}{\partial \delta}\mathcal{B}(k,\delta;s)d\delta$ vanishes, thus $\mathcal{V}_{[0]} = N$ (constant), indicating the conservation of particle numbers;

- for $m=1$ case, from Eq. (12) we have

$$\begin{aligned} \frac{\partial \mathcal{V}_{[1]}}{\partial s} &= \frac{\partial}{\partial s}\int d\delta(\delta\cdot V) = \int d\delta\left(\delta\cdot\frac{\partial V}{\partial s}\right) \\ &= \alpha\int d\delta\delta\cdot\int dk Z_\parallel^*(k;s) b^*(k;s)\frac{\partial}{\partial \delta}\mathcal{B}(k,\delta;s) \\ &= -\frac{\alpha N}{2\pi}\int_{-\infty}^{\infty} dk Z_\parallel^*(k;s)|b(k;s)|^2, \end{aligned} \tag{14}$$

  the physical picture refers to energy loss (or energy conservation);

- for $m=2$ case, the physical picture will, as we anticipate, be the energy spread increase. This is what we want and the existing linear theory does not have this term. The governing equation for the energy spread becomes

$$\frac{\partial}{\partial s}\mathcal{V}_{[2]} + 2\frac{\alpha N}{2\pi}\int_{-\infty}^{\infty} dk Z_\parallel^*(k;s) b_{[0]}^*(k;s) b_{[1]}(k;s) = 0. \tag{15}$$

- for $m=3$ case, the physical picture will correspond to the beam skewness.

Our next step is to integrate the fast equation over energy deviation δ to obtain a set of recursive equations. For $m=0$ case,

$$\begin{aligned} b_{[0]}(k;s) &= b_{[0]}^{(0)}(k;s) + \int_0^s i\frac{4\pi\epsilon_0 r_e c N}{\gamma} k R_{56}(\tau\to s)\times \\ &\qquad Z_\parallel(k;\tau) b_{[0]}(k;\tau)\{L, D; ; \tau\to s\}d\tau \\ &= b_{[0]}^{(0)}(k;s) + \int_0^s K_{[0]}(\tau,s) b_{[0]}(k;\tau)d\tau, \end{aligned} \tag{16}$$

where the kernel function $K_{[0]}(\tau,s)$ is the familiar one, which can also be derived from existing linear theory. For $m=1$ case,

$$\begin{aligned} b_{[1]}(k;s) &= b_{[1]}^{(0)}(k;s) + \int_0^s \frac{I_b(\tau)}{\gamma I_A}\frac{4\pi}{Z_0} Z_\parallel(k;\tau) b_{[0]}(k;\tau)\times \\ &\qquad \left(k^2 R_{56}^2(\tau\to s)\sigma_{\delta\tau}^2 - 1\right)\{L, D;\tau\to s\}d\tau \\ &= b_{[1]}^{(0)}(k;s) + \int_0^s K_{[1]}(\tau,s) b_{[0]}(k;\tau)d\tau, \end{aligned} \tag{17}$$

ISBN: 978-3-95450-279-0 ISSN: 3043-0208 doi: 10.18429/JACoW-SAP2025-THP09

which requires the zeroth-order bunching factor. Similarly, we can obtain for the $m = 2$ case. In general, by principle of mathematical induction, we have

$$b_{[m]}(k;s) = b^{(0)}_{[m]}(k;s) + \int_0^s K_{[m]}(\tau,s) b_{[0]}(k;\tau) d\tau. \quad (18)$$

So far we have obtained the slow and fast equations in terms of $\mathcal{V}_{[m]}$ and $b_{[m]}$. To complete the theory, we still need to find analytical expressions for the pure-optics bunching factors at the m-th moment, i.e.,

$$\begin{aligned} b^{(0)}_{[m]}(k;s) &\equiv \frac{2\pi}{N} \int_{-\infty}^{\infty} \mathcal{B}^{(0)}(k,\delta;s)\delta^m d\delta \\ &= \frac{1}{N} \int_{-\infty}^{\infty} d\delta \delta^m \int_{-\infty}^{\infty} dz f_1(z,\delta;s) e^{-ikz}. \end{aligned} \quad (19)$$

For the $m = 0$ case, we have

$$\begin{aligned} b^{(0)}_{[0]}(k;s) &= \frac{1}{N} \int_{-\infty}^{\infty} d\delta_s \int_{-\infty}^{\infty} dz_s f_1(z,\delta;s) e^{-ikz_s} \\ &= \frac{1}{N} \int_{-\infty}^{\infty} d\delta_0 \int_{-\infty}^{\infty} dz_0 \frac{\Delta n\left(z_0\right)}{n_0} \times \\ &\quad f_0(\delta;0) e^{-ik(z_0 + R_{56}(s)\delta_0)} \\ &= b^{(0)}_{[0]}(k;0)\{L.D.;s\}, \end{aligned} \quad (20)$$

with

$$b^{(0)}_{[0]}(k;0) = \frac{1}{N} \int dz_0 \frac{\Delta n\left(z_0\right)}{n_0} e^{-ikz_0} \approx \frac{1}{\sqrt{N}} \quad (21)$$

and $\{L.D.;s\} = e^{-\frac{1}{2}k^2(s)R^2_{56}(s)\sigma^2_{\delta 0}}$.

For the $m = 1$ case, we have

$$\begin{aligned} b^{(0)}_{[1]}(k;s) &= b^{(0)}_{[0]}(k;0) \int_{-\infty}^{\infty} d\delta_0 \delta_0 f_0(\delta;0) e^{-ik(s)R_{56}(s)\delta_0} \\ &= -ik(s)R_{56}(s)\sigma^2_{\delta 0} b^{(0)}_{[0]}(k;0)\{L.D.;s\}. \end{aligned} \quad (22)$$

For the $m = 2$ case, we have

$$b^{(0)}_{[2]}(k;s) = \sigma^2_{\delta 0}\left[1 - k^2(s)R^2_{56}(s)\sigma^2_{\delta 0}\right] b^{(0)}_{[0]}(k;0)\{L.D.;s\}. \quad (23)$$

For the $m = 3$ case and other higher order moments, they all have analytical expressions.

SUMMARY AND OUTLOOK

In this paper we have formulated a quasi-linear theory, which can lead to saturation when the intrinsic energy spread increases due to the instability mechanism itself. The quasi-linear theory gives a set of coupled equations for bunching factor and energy spread. To sum, we have the coupled recursive equations Eqs. (12) and (18), together with the pure-optics bunching factors Eqs. (20)-(23). Numerical procedures to solve the recursive equations are sketched in Fig. 2. Our next step is to implement and incorporate the numerical solutions to the semi-analytical Vlasov solver [10].

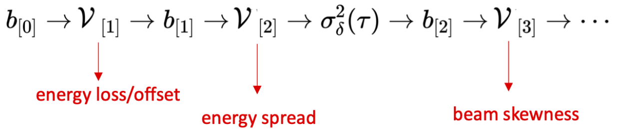

$$b_{[0]} \rightarrow \mathcal{V}_{[1]} \rightarrow b_{[1]} \rightarrow \mathcal{V}_{[2]} \rightarrow \sigma^2_{\delta}(\tau) \rightarrow b_{[2]} \rightarrow \mathcal{V}_{[3]} \rightarrow \cdots$$

Figure 2: Sketch of solving the coupled recursive equations.

Here we add a side note to remind that in Ref. [11, 12] the energy spread increase due to collective effects is expressed as

$$\sigma^2_{\delta,\text{coll}} = \frac{8}{n_b} C_{\text{tot}} \int_0^{\lambda^*} \frac{d\lambda}{\lambda^2} \left| \int_0^{s_f} d\tau \frac{I_b(\tau)}{\gamma I_A} Z_\parallel(\lambda;\tau) \tilde{G}(\lambda;\tau) \right|^2, \quad (24)$$

where n_b is line density, C_{tot} is the total compression factor, λ^* is the cutoff wavelength, I_b is the bunch current, I_A is the Alfven current, and the complex quantity $\tilde{G} = b(k;\tau)/b(k;0)$ is the MBI gain. In the above expression the derivation is somewhat empirical and intuitive. It will be worth to compare the existing expression with that obtained from our derived recursive equations in quasi-linear theory.

REFERENCES

[1] S. Heifets, G. Stupakov, and S. Krinsky, "Coherent synchrotron radiation instability in a bunch compressor", *Phys. Rev. ST Accel. Beams*, vol. 5, p. 064401, 2002. `doi:10.1103/PhysRevSTAB.5.064401`

[2] Z. Huang and K.-J. Kim, "Formulas for coherent synchrotron radiation microbunching in a bunch compressor chicane", *Phys. Rev. ST Accel. Beams*, vol. 5, p. 074401, 2002. `doi:10.1103/PhysRevSTAB.5.074401`

[3] M. Venturini, "Microbunching instability in a single-pass system using a direct two-dimensional Vlasov solver", *Phys. Rev. ST Accel. Beams*, vol. 10, p. 104401, 2007. `doi:10.1103/PhysRevSTAB.10.104401`

[4] C.-Y. Tsai *et al.*, "Linear microbunching analysis for recirculation machines", *Phys. Rev. Accel. Beams*, vol. 19, p. 114401, 2016. `doi:10.1103/PhysRevAccelBeams.19.114401`

[5] C.-Y. Tsai *et al.*, "Conditions for coherent-synchrotron-radiation-induced microbunching suppression in multibend beam transport or recirculation arcs", *Phys. Rev. Accel. Beams*, vol. 20, p. 024401, 2017. `doi:10.1103/PhysRevAccelBeams.20.024401`

[6] C.-Y. Tsai *et al.*, "Vlasov analysis of microbunching instability for magnetized beams", *Phys. Rev. Accel. Beams*, vol. 20, p. 054401, 2017. `doi:10.1103/PhysRevAccelBeams.20.054401`

[7] C.-Y. Tsai, "Concatenated analyses of phase space microbunching in high brightness electron beam transport", *Nucl. Instrum. Methods A*, vol. 940, pp. 462–474, 2019. `doi:10.1016/j.nima.2019.06.061`

[8] C.-Y. Tsai, "An alternative view of coherent synchrotron radiation induced microbunching development in multibend recirculation arcs", *Nucl. Instrum. Methods A*, vol. 943, p. 162499, 2019. `doi:10.1016/j.nima.2019.162499`

[9] S. Di Mitri *et al.*, "Experimental evidence of intrabeam scattering in a free-electron laser driver", *New J. Phys.*, vol. 22, p. 083053, 2020. `doi:10.1088/1367-2630/aba572`

[10] C.-Y. Tsai *et al.*, "Theoretical formulation of phase space microbunching instability in the presence of intrabeam scattering for single-pass or recirculation accelerators", *Phys. Rev. Accel. Beams*, vol. 23, p. 124401, 2020. `doi:10.1103/PhysRevAccelBeams.23.124401`

[11] C.-Y. Tsai and W. Qin, "Semi-analytical analysis of high-brightness microbunched beam dynamics with collective and intrabeam scattering effects", *Phys. Plasmas*, vol. 28, p. 013112, 2021. `doi:10.1063/5.0038246`

[12] G. Perosa and S. Di Mitri, "Matrix model for collective phenomena in electron beam's longitudinal phase space", *Sci. Rep.*, vol. 11, p. 7895, 2021. `doi:10.1038/s41598-021-87041-0`

[13] B. Liu, C.-Y. Tsai, Y. Jiao, W. Liu, F. Zeng, and W. Qin, "Analytical formulas of coherent-synchrotron-radiation induced microbunching gain and emittance growth in an arbitrary achromatic four-bend chicane", *Nucl. Instrum. Methods A*, vol. 1067, p. 169703, 2024. `doi:10.1016/j.nima.2024.169703`

[14] K.-J. Kim, Z. Huang, and R. Lindberg, *Synchrotron Radiation and Free-Electron Lasers*, Cambridge University Press, Cambridge, England, 2017.

QUICK ESTIMATE OF CSR-INDUCED MICROBUNCHING INSTABILITY IN A MULTIBEND TRANSPORT BEAMLINE

Cheng-Ying Tsai[*], School of Electrical and Electronic Engineering,
Huazhong University of Science and Technology, Wuhan, China

Abstract

Microbunching instability (MBI) driven by short-range wakefields in high-brightness electron beams has been an active area of research over the past decade. While most existing studies focus on single-pass or linear accelerators — particularly few-dipole bunch compressor chicanes — MBI studies in multi-bend transport lines has relied predominantly on time-consuming numerical simulations. In this work, we present a quick estimate for evaluating MBI gain in generic multi-bend beamlines, thereby avoiding computational costs. Starting from Volterra integral equation governing the bunching factor, we first find the optimal wavelength and introduce physically motivated simplifications to derive the maximum gain. A gain spectrum is then constructed based on physical insights into MBI amplification mechanisms. The results show good agreement with detailed numerical calculations from Vlasov solver. The developed approach enables quick and reasonably accurate estimates of the MBI gain using only the lattice optics functions and the initial beam parameters, offering a practical tool for beamline design and mitigation of MBI.

INTRODUCTION

Microbunching instability (MBI) driven by short-range wakefields in high-brightness electron beams has been an active area of research over the past decade for linear accelerators (linac) [1–6] and for recirculating accelerators or energy-recovery linacs [7–15]. For a multi-bend transport line, coherent synchrotron radiation (CSR) [16–19] plays a dominant role and may lead to transverse emittance growth (see, e.g., Refs [20–22]) and/or longitudinal MBI. For a brief review, see Ref. [23]. Study of MBI can be computationally intensive through particle tracking simulations because of sensitivity to the numerical noise. Existing linearized theory is formulated based on Volterra integral equation of the second kind. Only few cases have analytical solution (based on iterative method), e.g., symmetric 3-dipole C-shape chicane [2], recently extended to arbitrary non-symmetric 4-dipole chicane [6]. For multi-bend transport lattices, there is not available quick-to-use solution; this is primarily because the MBI gain depends on lattice properties. For a generic multi-bend lattice, it is not easy to give a general formula. Therefore we need to solve the integral equation; otherwise, intense time-consuming particle tracking simulations will be performed. This work is of practical importance: instead of solving the integral equation or performing particle tracking, we give a quick estimate of maximal MBI gain and, based on knowledge of the kernel behavior, construct the gain spectrum. The required inputs are beam parameters, lattice optics, including $R_{56}(s)$ and curly-H function $\mathcal{H}_x(s)$.

THEORETICAL FORMULATION: REVIEW

Based on the linearized Vlasov analysis, the governing equation for the bunching factor $b(k;s)$ can be formulated as a linear Volterra-type integral equation of the second kind,

$$b(k;s) = b^{(0)}(k;s) + \int_0^s K(\tau,s) b(k;\tau) d\tau, \qquad (1)$$

where $k = 2\pi/\lambda$ being the modulation wavenumber, $b^{(0)}(k;s) = b^{(0)}(k;0)\{L.D.;0,s\}$, the kernel function

$$K(\tau,s) = ik(s) R_{56}(\tau \to s) \frac{4\pi}{Z_0} \frac{I_b(\tau)}{\gamma I_A} Z_{\parallel}(k;\tau)\{L.D.;\tau,s\}, \qquad (2)$$

with Z_0 the free-space impedance, I_b the bunch current, γ the electron energy in unit of rest-mass energy, I_A the Alfven current, and Landau-damping {L.D.} factor

$$\{L.D.;\tau,s\} = \exp\left[-\frac{k^2}{2}U^2(s,\tau)\sigma_{\delta 0}^2 - \frac{k^2 \epsilon_{x0}\beta_{x0}}{2} \times \left(V(s,\tau) - \frac{\alpha_{x0}}{\beta_{x0}}W(s,\tau)\right)^2 - \frac{k^2\epsilon_{x0}}{2\beta_{x0}}W^2(s,\tau)\right] \qquad (3)$$

with $U(s,\tau) = R_{56}(s) - R_{56}(\tau)$, $V(s,\tau) = R_{51}(s) - R_{51}(\tau)$, $W(s,\tau) = R_{52}(s) - R_{52}(\tau)$ and $R_{56}(\tau \to s) = R_{56}(s) - R_{56}(\tau) + R_{51}(\tau)R_{52}(s) - R_{51}(s)R_{52}(\tau)$. Here $\sigma_{\delta 0}$ is the initial slice energy spread, ϵ_{x0} the initial transverse geometric emittance, and β_{x0}, α_{x0} the initial Courant-Snyder parameters. The microbunching gain is defined as

$$G_c(k;s) = \frac{b(k;s)}{b(k;0)}, \quad G(k;s) = \left|G_c(k;s)\right|. \qquad (4)$$

For high-brightness electron beam, reduction of pure-optics bunching due to Landau damping may be neglected, i.e., Eq. (1) can be approximately written as

$$G_c(k;s) \approx 1 + \int_0^s K(\tau,s) G_c(k;\tau) d\tau. \qquad (5)$$

THEORETICAL FORMULATION: SERIES EXPANSION

Now we want to solve Eq. (5) via series expansion by writing $G_c\left(k_{opt};s\right) = \sum_{m=0}^{M} d_m s^m \Lambda^m$ with $\Lambda = \frac{I_b}{\gamma I_A}$ and

---

[*] Email: jcytsai@hust.edu.cn. This work is supported by the Fundamental Research Funds for the Central Universities (HUST) under Project No. 2021GCRC006 and National Natural Science Foundation of China under project No. 12275094.

$d_0 = 1$. Our strategy consists three steps: first, we identify the optimal wavelength corresponding to the maximum gain; second, we derive approximate expression for the maximum gain ignoring Landau damping effect; third, we include Landau damping. In what follows we consider 1-D free-space steady-state CSR [16–19] with

$$Z_{\parallel,\mathrm{CSR}}(k) = -iA\frac{Z_0}{4\pi}\frac{k^{1/3}}{\rho^{2/3}}, \quad A = -0.94 + 1.63i \quad (6)$$

with ρ the instantaneous bending radius. As the first step, assuming the gain spectrum behaves like

$$G_c(k) \propto kR_{56}e^{-\frac{k^2}{2}R_{56}^2\sigma_{\delta 0}^2 - \frac{k^2}{2}\mathcal{H}_x\epsilon_{x0}}. \quad (7)$$

The maximum gain occurs when $\partial G_c(k)/\partial k = 0$. The corresponding optimal wavenumber becomes

$$k_{opt} = \frac{1}{\sqrt{R_{56,\,\mathrm{eff}}^2\sigma_{\delta 0}^2 + \mathcal{H}_{x,\,\mathrm{eff}}\,\epsilon_{x0}}} = \frac{2\pi}{\lambda_{opt}} \quad (8)$$

with the corresponding rms values of R_{56} and $\mathcal{H}_x$

$$\begin{aligned} R_{56,\,\mathrm{eff}} &\equiv \left[\frac{1}{s_f - s_0}\int_{s_0}^{s_f}\left[R_{56}(s) - \bar{R}_{56}\right]^2 ds\right]^{\frac{1}{2}} \\ \mathcal{H}_{x,\,\mathrm{eff}} &\equiv \left[\frac{1}{s_f - s_0}\int_{s_0}^{s_f}\left[\mathcal{H}_x(s) - \overline{\mathcal{H}}_x\right]^2 ds\right]^{\frac{1}{2}}, \end{aligned} \quad (9)$$

with s_0 and s_f the initial and final location of the beamline.

As the second step, substituting the series expansion $G_c(k_{opt}; s)$ into Eq. (5) gives (assume isochronous line)

$$\sum_{m=0}^{M} d_m s_f^m \Lambda^m \approx 1 - k_{opt}\mathbb{Z}_{\mathrm{CSR}}\sum_{m=0}^{M} d_m\Lambda^{m+1}\left(\Sigma_{56}^m\right), \quad (10)$$

where $\mathbb{Z}_{\mathrm{CSR}} = A\frac{k_{opt}^{1/3}}{\rho^{2/3}}$ and

$$\Sigma_{56}^m \equiv \sum_{j=1}^{N_d}\int_B R_{56}\left(\tau_j\right)\tau_j^m d\tau \approx L_B\sum_{j=1}^{N_d} R_{56}\left(s_j\right)s_j^m \quad (11)$$

comparing order by order in Λ gives

$$d_m = -\frac{k_{opt}\mathbb{Z}_{\mathrm{CSR}}d_{m-1}\Sigma_{56}^{m-1}}{s_f^m}. \quad (12)$$

The maximal gain can then be written as

$$\begin{aligned} G_c\left(k_{opt}; s_f\right) &= \sum_{m=0}^{M} d_m s_f^m \Lambda^m \\ &= 1 + \sum_{q=1}^{M}(-1)^q\frac{\left(k_{opt}\mathbb{Z}_{\mathrm{CSR}}\Lambda\right)^q}{s_f^{q(q-1)/2}}\prod_{r=0}^{q-1}\Sigma_{56}^r. \end{aligned} \quad (13)$$

As the final step, we include Landau damping for the maximum gain in the following way

$$\begin{aligned} &G_c\left(k_{opt}; s_f\right) \to G_c\left(k_{opt}; s_f\right) \times \\ &\exp\left[-\frac{k_{opt}^2}{2}\sigma_{\delta 0}^2\left|\max\left(R_{56}\right)\right|^2 - \frac{k_{opt}^2}{2}\epsilon_{x0}\left|\max\left(\mathcal{H}_x\right)\right|\right] \end{aligned} \quad (14)$$

with

$$\mathcal{H}_x(s) = \beta_x(s)\left[R_{51}(s) - \frac{\alpha_x(s)}{\beta_x(s)}R_{52}(s)\right]^2 + \frac{1}{\beta_x(s)}R_{52}^2(s). \quad (15)$$

Here we assume significant damping occurs at largest R_{56} via energy spread and largest $\mathcal{H}_x$ via transverse emittance. Having completed the three steps, from Eq. (5) we construct MBI gain spectrum as

$$\begin{aligned} &G_c\left(k; s_f\right) \approx 1 + \\ &\qquad G_c\left(k_{opt}; s_f\right)\frac{k}{k_{opt}}e^{\frac{1}{2} - \frac{k^2}{2}\left(R_{56,\,\mathrm{eff}}^2\sigma_{\delta 0}^2 + \mathcal{H}_{x,\,\mathrm{eff}}\,\epsilon_{x0}\right)}. \end{aligned} \quad (16)$$

If finite bunch length effect is to be included, we may multiply $G_c\left(k; s_f\right)$ with a reduction factor $\mathscr{R}$

$$\begin{aligned} &G_c\left(k; s_f\right) \approx 1 + \\ &\qquad \mathscr{R}\cdot G_c\left(k_{opt}; s_f\right)\frac{k}{k_{opt}}e^{\frac{1}{2} - \frac{k^2}{2}\left(R_{56,\,\mathrm{eff}}^2\sigma_{\delta 0}^2 + \mathcal{H}_{x,\,\mathrm{eff}}\,\epsilon_{x0}\right)} \end{aligned} \quad (17)$$

where

$$\mathscr{R} \approx \sqrt{\frac{1}{\chi^2 + 1}}e^{-\frac{1}{2}\left(\frac{1}{\chi^2+1}\right)}, \quad \chi = \Sigma_z/\sigma_z \quad (18)$$

with $\Sigma_z^2 \approx R_{56,\,\mathrm{eff}}^2\sigma_{\delta 0}^2 + \mathcal{H}_{x,\,\mathrm{eff}}\,\epsilon_{x_0}$.

EXAMPLE: 180° ISOCHRONOUS ARC

In this section we apply the above quick estimate for MBI for one 180° isochronous arc. For the initial beam parameters used in our calculations, we set the beam energy 1.3 GeV, the bunch peak current to 65 A, the initial transverse normalized emittance is 0.3 µm for both horizontal and vertical directions, and the relative energy spread to $\sigma_{\delta 0} = 1.23 \times 10^{-5}$ with no chirp. The initial Courant-Snyder parameters of the beam are matched to the lattice: $\beta_{x0} = 35.81$ m, $\beta_{y0} = 3$ m, $\alpha_{x0} = 0, \alpha_{y0} = 0$. The total length of the arc is about 240 m. Description of the lattice layout and relevant beam parameters can be found in Refs. [7, 9–11]. Figure 1 shows the basic optics functions and transport functions along the beamline. From the lattice, $\mathrm{rms}(R_{56}) \approx 0.12$ m, $\mathrm{rms}(\mathcal{H}x) \approx 0.246$ m. Provided the beam parameters, we have

$$\begin{aligned} \left(R_{56,\,\mathrm{eff}}\,\sigma_{\delta 0}\right)^2 &\sim 2\times 10^{-12}\ \mathrm{m}^2, \\ \epsilon_{x0}\mathcal{H}_{x,\,\mathrm{eff}} &\sim 3\times 10^{-11}\ \mathrm{m}^2, \\ \epsilon_{x0}\mathcal{H}_{x,\,\mathrm{eff}} &\sim 10\left(R_{56,\,\mathrm{eff}}\,\sigma_{\delta 0}\right)^2. \end{aligned} \quad (19)$$

Using Eq. (8) we estimate the optimal wavenumber k_{opt}. From the lattice information Fig. 1(c), we can evaluate Σ_{56}^{m} and the coefficients d_m for different orders m. With all these prepared, we can construct the MBI gain spectrum shown in Fig. 1(b).

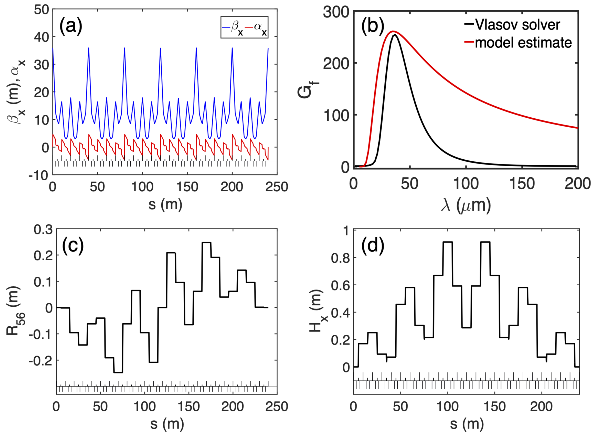

Figure 1: (a) Courant-Snyder optics functions; (b) MBI gain spectrum; (c,d) transport functions $R_{56}(s)$ and $\mathcal{H}_x(s)$.

To ensure that the series expansion converges, we perform convergence test over m and find that up to $M = 14$ is sufficient. The result is shown in Fig. 2. It deserves here to comment that this calculation is almost immediate because we do not solve integral equation; instead, we only evaluate Σ_{56}^{m} and the coefficients d_m for different orders m and sum them up!

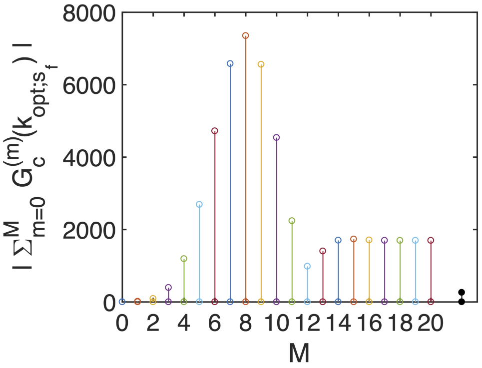

Figure 2: Convergence of sum of the expansion coefficients.

Once the coefficients $G_c\left(k_{opt}; s\right) = \sum_{m=0}^{M} d_m s^m \Lambda^m$ are obtained, it is interesting to plot MBI gain $G(s)$ along the beamline. Figure 3 shows the comparison from Vlasov solver and our model estimate. A good agreement is found.

SUMMARY AND OUTLOOK

In this paper we have developed a quick estimate to evaluate MBI gain in generic multi-bend beamlines. Starting from Volterra integral equation, we first find the optimal wavelength and introduce physically motivated simplifications to derive the maximum gain. Then Landau damping effect is included. A gain spectrum is then constructed based on physical insights into MBI amplification mechanisms. The results show good agreement with detailed numerical calculations from Vlasov solver. Here we comment that although only the 1-D free-space steady-state CSR is included and the same radius of curvature for all bending magnets are assumed, the present formulation is straightforward to extend to include other relevant impedance models and with different bending radii along the beamline. The quick estimate does not really solve the equation; thereby avoiding or minimizing computational costs. The required inputs are only beam parameters, and lattice optics, including $R_{56}(s)$ and curly-H function $\mathcal{H}_x(s)$. It is believed that this quick estimate will offer a practical tool for beamline design and mitigation of MBI.

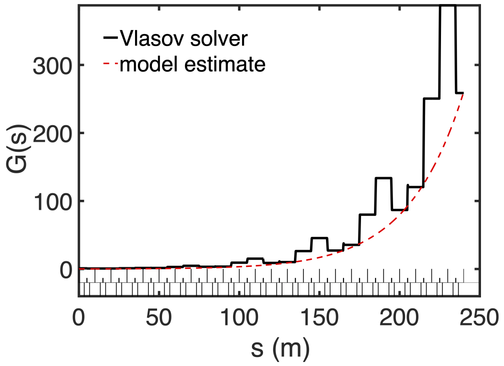

Figure 3: MBI gain function $G(s)$ along the beamline. Here the initial modulation wavelength $\lambda = 36$ μm.

REFERENCES

[1] S. Heifets, G. Stupakov, and S. Krinsky, "Coherent synchrotron radiation instability in a bunch compressor", *Phys. Rev. ST Accel. Beams*, vol. 5, p. 064401, 2002. `doi:10.1103/PhysRevSTAB.5.064401`

[2] Z. Huang and K.-J. Kim, "Formulas for coherent synchrotron radiation microbunching in a bunch compressor chicane", *Phys. Rev. ST Accel. Beams*, vol. 5, vol. 074401, 2002. `doi:10.1103/PhysRevSTAB.5.074401`

[3] M. Venturini, "Microbunching instability in a single-pass system using a direct two-dimensional Vlasov solver", *Phys. Rev. ST Accel. Beams*, vol. 10, p. 104401, 2007. `doi:10.1103/PhysRevSTAB.10.104401`

[4] C.-Y. Tsai and W. Qin, "Semi-analytical analysis of high-brightness microbunched beam dynamics with collective and intrabeam scattering effects", *Phys. Plasmas*, vol. 28, p. 013112, 2021. `doi:10.1063/5.0038246`

[5] A. D. Brynes *et al.*, "Mitigation of the Microbunching Instability Through Transverse Landau Damping", *Phys. Rev. Accel. Beams*, vol. 27, p. 074402, 2024. `doi:10.1103/PhysRevAccelBeams.27.074402`

[6] B. Liu, C.-Y. Tsai, Y. Jiao, W. Liu, F. Zeng, and W. Qin, "Analytical formulas of coherent-synchrotron-radiation induced microbunching gain and emittance growth in an arbitrary

achromatic four-bend chicane", *Nucl. Instrum. Methods A*, vol. 1067, p. 169703, 2024. `doi:10.1016/j.nima.2024.169703`

[7] Douglas *et al.*, "Control of Coherent Synchrotron Radiation and Micro-Bunching Effects During Transport of High Brightness Electron Beams", 2014. `arxiv:1403.2318`

[8] D. Douglas *et al.*, "Control of Synchrotron Radiation Effects During Recirculation with Bunch Compression", in *Proc. IPAC'15*, Richmond, VA, USA, May 2015, pp. 1910–1912. `doi:10.18429/JACoW-IPAC2015-TUPMA034`

[9] D. Douglas *et al.*, "Control of Synchrotron Radiation Effects during Recirculation", in *Proc. IPAC'15*, Richmond, VA, USA, May 2015, pp. 1913–1915. `doi:10.18429/JACoW-IPAC2015-TUPMA035`

[10] C.-Y. Tsai *et al.*, "Linear microbunching analysis for recirculation machines", *Phys. Rev. Accel. Beams*, vol. 19, p. 114401, 2016. `doi:10.1103/PhysRevAccelBeams.19.114401`

[11] C.-Y. Tsai *et al.*, "Conditions for coherent-synchrotron-radiation-induced microbunching suppression in multibend beam transport or recirculation arcs", *Phys. Rev. Accel. Beams*, vol. 20, p. 024401, 2017. `doi:10.1103/PhysRevAccelBeams.20.024401`

[12] C.-Y. Tsai *et al.*, "Vlasov analysis of microbunching instability for magnetized beams", *Phys. Rev. Accel. Beams*, vol. 20, p. 054401, 2017. `doi:10.1103/PhysRevAccelBeams.20.054401`

[13] C.-Y. Tsai, "Concatenated analyses of phase space microbunching in high brightness electron beam transport", *Nucl. Instrum. Methods A*, vol. 940, pp. 462–474, 2019. `doi:10.1016/j.nima.2019.06.061`

[14] C.-Y. Tsai, "An alternative view of coherent synchrotron radiation induced microbunching development in multibend recirculation arcs", *Nucl. Instrum. Methods A*, vol. 943, p. 162499, 2019. `doi:10.1016/j.nima.2019.162499`

[15] C.-Y. Tsai *et al.*, "Theoretical formulation of phase space microbunching instability in the presence of intrabeam scattering for single-pass or recirculation accelerators", *Phys. Rev. Accel. Beams*, vol. 23, p. 124401, 2020. `doi:10.1103/PhysRevAccelBeams.23.124401`

[16] Ya. S. Derbenev, J. Rossbach, E. L. Saldin, and V. D. Shiltsev, "Microbunch radiative tailhead interaction", TESLA-FEL Report No. 1995–05. `http://cds.cern.ch/record/291102?ln=en`

[17] E. L. Saldin, E. A. Schneidmiller, and M. V. Yurkov, "On the coherent radiation of an electron bunch moving in an arc of a circle", *Nucl. Instrum. Methods A*, vol. 398, p. 373, 1997. `doi:10.1016/S0168-9002(97)00822-X`

[18] R. Li and C.-Y. Tsai, "CSR Impedance for Non-Ultrarelativistic Beams", in *Proc. IPAC'15*, Richmond, VA, USA, May 2015, pp. 709–712. `doi:10.18429/JACoW-IPAC2015-MOPMN004`

[19] R. Li and C.-Y. Tsai, "Entrance and Exit CSR Impedance for Non-Ultrarelativistic Beam", in *Proc. IPAC'17*, Copenhagen, Denmark, May 2017, pp. 3214–3217. `doi:10.18429/JACoW-IPAC2017-WEPIK113`

[20] C. Zhang, Y. Jiao, and C.-Y. Tsai, "Theoretical Analysis of the Conditions for an Isochronous and CSR-Immune Triple-Bend Achromat with Stable Optics", in *Proc. IPAC'21*, Campinas, Brazil, May 2021, pp. 786–789. `doi:10.18429/JACoW-IPAC2021-MOPAB245`

[21] F. Zeng, Y. Jiao, W. Liu, and C.-Y. Tsai, "Solvable model of the coherent synchrotron radiation effects in a four-bend chicane compressor", *New J. Phys.*, vol. 27, p. 063801, 2025. `doi:10.1088/1367-2630/addde2`

[22] F. Zeng, Y. Jiao, W. Liu, and C.-Y. Tsai, "Cancelation of coherent synchrotron radiation kicks in chicane bunch compressors", *Phys. Rev. Accel. Beam*, vol. 28, p. 070701, 2025. `doi:10.1103/2vjn-t4qb`

[23] C.-Y. Tsai, "Suppressing CSR Microbunching in Recirculation Arcs", in *Proc. IPAC'18*, Vancouver, Canada, Apr.-May 2018, pp. 1784–1789. `doi:10.18429/JACoW-IPAC2018-WEYGBE1`

ISBN: 978-3-95450-279-0 ISSN: 3043-0208 doi: 10.18429/JACoW-SAP2025-THP11

BUNCHED-BEAM THEORY OF OF MICROBUNCHING INSTABILITY

Cheng-Ying Tsai*, School of Electrical and Electronic Engineering,
Huazhong University of Science and Technology, Wuhan, China

Abstract

Conventional theory of single-pass microbunching instability (MBI) is primarily based on the coasting-beam approximation, which assumes that the modulation wavelength is much shorter than the bunch length. However, in isochronous beamlines, the characteristic modulation wavelength may sometimes become comparable to the bunch length, rendering the coasting-beam assumption invalid. In this paper we develop a bunched-beam theory of MBI, starting from the linearized Vlasov equation, aiming to quantify the impact of finite bunch length on the evolution of density modulations. Our analysis reveals that the final MBI gain, or the amplified bunching factor, exhibits a dependence on the initial modulation phase, a feature absent in the existing coasting-beam model. The proposed bunched-beam formulation may offer additional physical insights into the underlying mechanism of MBI, particularly in regimes where the finite extent of the bunch plays a non-negligible role.

INTRODUCTION

Microbunching instability (MBI) in a single-pass high-brightness electron beam transport has been an active research topic in the past two decades (see, for example, Refs. [1–13]). The existing theoretical treatment of single-pass MBI typically assumes a coasting beam, where the modulation wavelength is much smaller compared with the total bunch duration. The coasting beam approximation significantly simplifies the Vlasov analysis and the derivation of the governing equation for the bunching factor. When the total bunch length is comparable to the modulation wavelength, the existing theory is no longer valid. An intuitive way to estimate the bunched-beam MBI gain is to convolute the MBI gain with finite-bunch spectrum. However this method may be lack of theoretical foundation. In this paper we formulate this problem starting from the linearized Vlasov equation, providing a self-consistent formulation. As demonstrated below, we find that the initial modulation phase and the finite modulation amplitude will be relevant to the final MBI gain.

VLASOV FORMULATION

Considering the only longitudinal phase space $\mathbf{Z} = [z\ \delta]^T$ and assuming that the initial phase space distribution

$$f(z,\delta;0) = \bar{f}_0(z,\delta;0) + f_1(z,\delta;0), \tag{1}$$

with $|f_1| \ll \bar{f}_0$ and the normalization condition $\int_{-\infty}^{\infty}\int_{-\infty}^{\infty} f(z,\delta)dzd\delta = N$ (here N is the number of electrons). Note that the unperturbed term has z dependence, different from the conventional MBI theory which has only δ dependence. Start from the integral form of the linearized Vlasov equation

$$f(z,\delta;s) = f(z,\delta;0) - \int_0^s \frac{\partial f_0(z,\delta;\tau)}{\partial\delta}\left(\frac{d\delta}{d\tau}\right)d\tau \tag{2}$$

where

$$\begin{aligned}\frac{d\delta}{ds} &\approx -\frac{4\pi\epsilon_0 r_e}{\gamma}\int_{-\infty}^{\infty} d\zeta W_{\parallel}(z-\zeta;s)n(\zeta;s)\\ &= -\frac{4\pi\epsilon_0 r_e c}{\gamma}\int_{-\infty}^{\infty}\frac{dk}{2\pi}Z_{\parallel}(k;s)Nb(k;s)e^{ikz}\end{aligned} \tag{3}$$

with r_e the classical electron radius, c the speed of light, γ the electron beam reference energy in unit of rest-mass energy, $W_{\parallel}$ or $Z_{\parallel}$ the wake function or impedance per unit length, n the line density, $k = 2\pi/\lambda$ the modulation wavelength and $b(k;s)$ the bunching factor defined as Fourier transform of the line density function. We define the beam sigma matrix as $\Sigma = \begin{pmatrix}\sigma_z^2 & \sigma_{z\delta}\\ \sigma_{z\delta} & \sigma_\delta^2\end{pmatrix}$, in which the chirp parameter $h = \frac{\partial\delta}{\partial z} = \frac{\sigma_{z\delta}}{\sigma_z^2}$. The Gaussian phase space distribution can be described as

$$\begin{aligned}\bar{f}_0(z,\delta;0) &= \frac{N}{2\pi\sqrt{\det\Sigma}}e^{-\frac{1}{2}\mathbf{Z}^T\Sigma^{-1}\mathbf{Z}}\\ &= \frac{N}{2\pi\sqrt{\sigma_{z0}^2\sigma_{\delta0}^2 - h^2\sigma_{z0}^4}}e^{-\frac{1}{2}\frac{1}{\det\Sigma}\left(z^2\sigma_{\delta0}^2+\delta^2\sigma_{z0}^2-2h\sigma_{z0}^2 z\delta\right)}\end{aligned} \tag{4}$$

Under coasting approximation, we have $\sigma_{z0} \to \infty$ with $\frac{N}{\sqrt{2\pi}\sigma_{z0}} = n_0$. In such a situation, the prefactor becomes

$$\begin{aligned}\frac{n_0}{\sqrt{2\pi}\sigma_{\delta0}}\frac{1}{\sqrt{1-h^2\frac{\sigma_{z0}^2}{\sigma_{\delta0}^2}}} &= \frac{n_0}{\sqrt{2\pi}\sigma_{\delta0}}\frac{1}{\sqrt{1-\frac{\sigma_{z\delta}^2}{\sigma_{z0}^2\sigma_{\delta0}^2}}}\\ &\to \frac{n_0}{\sqrt{2\pi}\sigma_{\delta0}}\end{aligned} \tag{5}$$

and the exponent becomes

$$\begin{aligned}&-\frac{1}{2}\frac{1}{\sigma_{\delta0}^2\sigma_{z0}^2}\left(z^2\sigma_{\delta0}^2+\delta^2\sigma_{z0}^2-2h\sigma_{z0}^2 z\delta\right)\\ &= -\frac{1}{2}\left(\frac{z^2}{\sigma_{z0}^2}+\frac{\delta^2}{\sigma_{\delta0}^2}-\frac{2h}{\sigma_{\delta0}^2}z\delta\right)\\ &\to -\frac{1}{2\sigma_{\delta0}^2}\left(\delta^2-2hz\delta\right) \approx -\frac{1}{2\sigma_{\delta0}^2}(\delta-hz)^2.\end{aligned} \tag{6}$$

---

* Email: jcytsai@hust.edu.cn. This work is supported by the Fundamental Research Funds for the Central Universities (HUST) under Project No. 2021GCRC006 and National Natural Science Foundation of China under project No. 12275094.

ISBN: 978-3-95450-279-0 ISSN: 3043-0208 doi: 10.18429/JACoW-SAP2025-THP11

For finite-bunch-length case, a simplified expression of $\bar{f}_0$ can be written as

$$\bar{f}_0(z,\delta;0) = \frac{N}{2\pi\sigma_{\delta 0}\sigma_{z0}} e^{-\frac{(\delta - hz)^2}{2\sigma_{\delta 0}^2} - \frac{z^2}{2\sigma_{z0}^2}} \tag{7}$$

and the perturbed part can be formulated as

$$f_1(z,\delta;0) = 2\Delta\cos\left(k_0 z_0 + \varphi\right) \cdot \bar{f}_0(z,\delta;0) \tag{8}$$

with Δ the modulation amplitude, $k_0 = 2\pi/\lambda_0$ the modulation wavenumber and φ the modulation phase (Fig. 1).

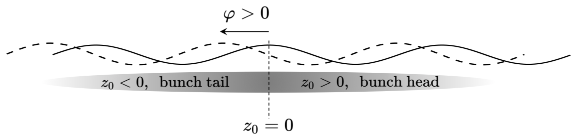

Figure 1: Illustration of the density modulation on top of the finite bunched beam. Phase of density modulation in a finite-bunch beam matters when the bunch length becomes shorter.

Multiplying Eq. (2) with e^{-ikz_s} on both sides and integrating over the phase space at s gives

$$b(k;s) = b^{(0)}(k;s) - \int_0^s \left[\int_{-\infty}^{\infty}\int_{-\infty}^{\infty} \frac{\partial f_0(z,\delta;\tau)}{\partial \delta_\tau} e^{-ikz_s}\left(\frac{d\delta}{d\tau}\right) dz_s d\delta_s\right] d\tau \tag{9}$$

In what follows we will derive the expressions for the two terms on RHS.

Pure-Optics Term

Let us start from the first term on RHS

$$\begin{aligned} b^{(0)}(k;s) &= \frac{1}{N}\iint f(z,\delta;0) e^{-ikz_s} dz_s d\delta_s \\ &= \iint \frac{1}{2\pi\sigma_{z0}\sigma_{\delta 0}}\left[1 + 2\Delta\cos\left(k_0 z_0 + \varphi\right)\right] \times \\ &\quad e^{-\frac{\delta_0^2}{2\sigma_{\delta 0}^2} - \frac{z_0^2}{2\sigma_{z0}^2} - ikz_s} dz_s d\delta_s \\ &= \frac{1}{2\pi\sigma_{z0}\sigma_{\delta 0}}\iint \left[1 + 2\Delta\cos\left(k_0 z_0 + \varphi\right)\right] \times \\ &\quad e^{-\frac{\delta_0^2}{2\sigma_{\delta 0}^2} - \frac{z_0^2}{2\sigma_{z0}^2} - ik(z_0 + R_{56}\delta_0)} dz_0 d\delta_0 \\ &= \frac{1}{\sqrt{2\pi}\sigma_{z0}} e^{-\frac{k^2}{2}R_{56}^2\sigma_{\delta 0}^2}\left[(*) + 2\Delta\cdot(**)\right], \end{aligned} \tag{10}$$

where

$$\begin{aligned} (*) &= \sqrt{2\pi}\sigma_{z0} e^{-\frac{k^2}{2}\sigma_{z0}^2} \\ (**) &= \sqrt{2\pi}\sigma_{z0} e^{-\frac{k^2}{2}\sigma_{z0}^2 - \frac{k_0^2}{2}\sigma_{z0}^2}\left[\cos\varphi\cosh\left(kk_0\sigma_{z0}^2\right)\right. \\ &\qquad \left. + i\sin\varphi\sinh\left(kk_0\sigma_{z0}^2\right)\right] \\ &= \sqrt{2\pi}\sigma_{z0} e^{-\frac{k^2}{2}\sigma_{z0}^2 - \frac{k_0^2}{2}\sigma_{z0}^2}\cosh\left(kk_0\sigma_{z0}^2 + i\varphi\right). \end{aligned} \tag{11}$$

Note that k is arbitrary wavenumber at s and k_0 is the initial wavenumber. Note also that $(*)$ is real and $(**)$ is complex. For coasting beam case, $(*) \to 0$ and $(**) \to \sqrt{\frac{\pi}{2}}\sigma_{z0}e^{i\varphi}$. In general, the pure-optics bunched-beam bunching factor becomes

$$\begin{aligned} b^{(0)}(k;s) &= e^{-\frac{k^2}{2}R_{56}^2(s)\sigma_{\delta 0}^2}\left[e^{-\frac{K^2\zeta^2}{2}} + \Delta\cdot\mathcal{R}(K,\zeta,\varphi)\right] \\ &= e^{-\frac{k^2}{2}R_{56}^2(s)\sigma_{\delta 0}^2}\,\Xi(K,\zeta,\varphi), \quad K = \frac{k}{k_0}, \zeta = k_0\sigma_{z0} \end{aligned} \tag{12}$$

Here the complex function $\mathcal{R}(K,\zeta,\varphi)$ is

$$\mathcal{R}(K,\zeta,\varphi) = 2e^{-\frac{1}{2}(1+K^2)\zeta^2}\cosh\left(K\zeta^2 + i\varphi\right). \tag{13}$$

The function $\Xi(K,\zeta,\varphi)$ is

$$\Xi(K,\zeta,\varphi) = e^{-\frac{K^2\zeta^2}{2}} + \Delta\cdot\mathcal{R}(K,\zeta,\varphi), \tag{14}$$

with its amplitude and phase shown in Figs. 2 and 3.

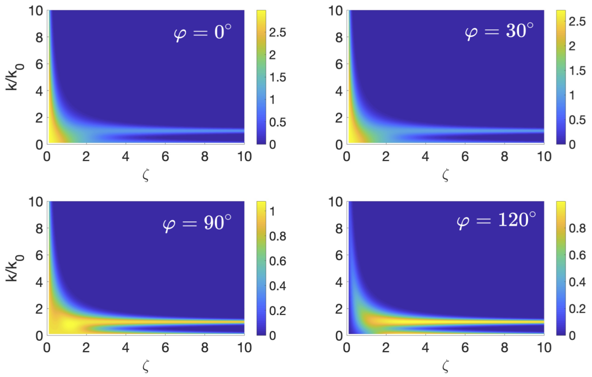

Figure 2: Amplitude of the function $\Xi(K,\zeta,\varphi)$.

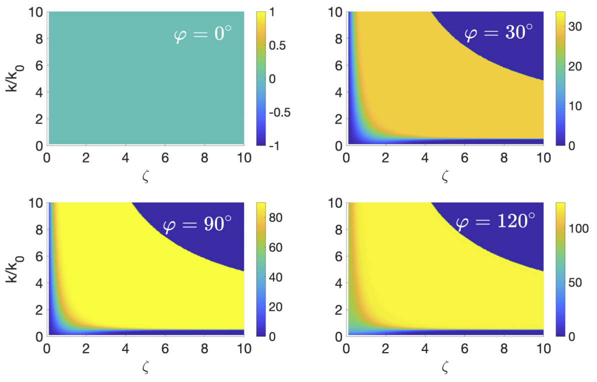

Figure 3: Phase of the function $\Xi(K,\zeta,\varphi)$ in degree.

A few remarks about the pure-optics bunched-beam bunching factor:

- In most situations $\Xi(1,\zeta,\varphi)$ takes appreciable value at the wavenumber equal to the initial one (i.e., at $K \approx 1$);

ISBN: 978-3-95450-279-0 ISSN: 3043-0208 doi: 10.18429/JACoW-SAP2025-THP11

- Under coasting beam approximation ($\zeta \gg 1$), nonzero value only exits when $k = k_0$;
- For finite bunch beam, nonzero value may exist for $K \neq 1$ and this becomes evident for smaller ζ or shorter bunches;
- For $\zeta < 2$, i.e., a bunch only takes half modulation wavelength, the bunching factor can be larger than 1;
- For short bunch case, dependence on K become less evident, as expected;
- For finite bunch case, Ξ depends on phase φ.

Collective Term

Now we move onto the second term on RHS of Eq. (9). Integration by parts gives

$$\iint \frac{\partial f_0}{\partial \delta_\tau}\left(\frac{d\delta}{d\tau}\right) e^{-ik(z_\tau + R_{56}(\tau\to s)\delta_\tau)} dz_s d\delta_s \\ = ikR_{56}(\tau \to s) \iint dz_\tau d\delta_\tau f_0(z,\delta;\tau) e^{-ikz_s}\left(\frac{d\delta}{d\tau}\right) \tag{15}$$

Substitution of Eq. (3) into the above equation gives

$$\iint \frac{\partial f_0}{\partial \delta_\tau}\left(\frac{d\delta}{d\tau}\right) e^{-ikz_s} dz_s d\delta_s \\ = -\left(\frac{4\pi\epsilon_0 r_e c N}{\gamma}\right) ikR_{56}(\tau\to s)\times \\ \int_{-\infty}^{\infty} \frac{d\kappa}{2\pi} Z_\parallel(\kappa;\tau) b(\kappa;\tau) e^{-\frac{\sigma_{\delta 0}^2}{2}[kR_{56}(s)-\kappa R_{56}(\tau)]^2 - \frac{\sigma_{z0}^2}{2}(k-\kappa)} \tag{16}$$

Putting altogether, we have the generalized Volterra integral equation for the bunching factor

$$b(k;s) = b^{(0)}(k;s) + \int_0^s \mathcal{K}[s;\tau, b(k,\kappa)] d\tau \tag{17}$$

where the kernel function becomes

$$\mathcal{K}[s;\tau,b(k,\kappa)] = i\frac{4\pi}{Z_0}\frac{I_b(\tau)}{\gamma I_A} k(s) R_{56}(\tau\to s)\times \\ \int_{-\infty}^{\infty} \frac{d\kappa}{2\pi} Z_\parallel(\kappa;\tau) b(\kappa;\tau) e^{-\frac{\sigma_{\delta 0}^2}{2}[kR_{56}(s)-\kappa R_{56}(\tau)]^2 - \frac{\sigma_{z0}^2}{2}(k-\kappa)^2} \tag{18}$$

For the coasting beam case, $\sigma_{z0} \to \infty$, only $\kappa(\tau) = k(\tau)$ can survive the integral. Significant Landau damping due to finite bunch length occurs when $\sigma_{z0}(k-\kappa) \leq 1$ or $|\kappa - k| \leq \sigma_{z0}^{-1}$. For finite bunched beam case, $\sigma_{z0} < \infty$, those $\kappa(\tau)$ near $k(\tau)$ will contribute to the integral. More specifically, those components with $k(\tau) \pm \sigma_z^{-1}(\tau)$ can be relevant.

Extension with Inclusion of Transverse Terms

The kernel function will be multiplied by the transverse Landau damping factor

$$\{\,\text{L.D.}; s,\tau\}_\perp = \\ \exp\left\{-\frac{1}{2}\left[\epsilon_{x0}\beta_{x0}\left(\mathfrak{R}_{51}(s,\tau) - \frac{\alpha_{x0}}{\beta_{x0}}\mathfrak{R}_{52}(s,\tau)\right)^2 \right.\right. \\ \left.\left. + \frac{\epsilon_{x0}}{\beta_{x0}}\mathfrak{R}_{52}^2(s,\tau)\right]\right\} \tag{19}$$

with $\mathfrak{R}_{5j}(s,\tau) = k(s)R_{5j}(s) - \kappa(\tau)R_{5j}(\tau), j = 1,2.$

INTUITIVE CONVOLUTION APPROACH

Once the coasting-beam (CB) bunching factor is obtained, to estimate the bunched-beam case, a basic idea is to convolute the coasting-beam bunching factor to bunched-beam form factor. Here we remind that the convolution operator itself is dimensional. Assuming Gaussian distribution, we define

$$\Xi_{\text{Gaussian}}(k) = \frac{\sigma_z(s)}{\sqrt{2\pi}} e^{-\frac{k^2(s)}{2}\sigma_z^2(s)}. \tag{20}$$

Note that $\Xi_{\text{Gaussian}}(k)$ has the dimension of length.

Then the bunched-beam (BB) bunching factor can be evaluated as

$$\begin{aligned} b_{0,\text{BB}}(k) &= b_{0,\text{CB}}(k) * \Xi_{\text{Gaussian}}(k) \\ &= \int_{-\infty}^{\infty} b_{0,\text{CB}}(k)\Xi_{\text{Gaussian}}(k-\kappa) d\kappa \\ &= b_{0,\text{CB}}(k;0)\frac{\sigma_z}{\sqrt{2\pi}}\int_{-\infty}^{\infty} e^{-\frac{k^2}{2}\Sigma_z^2 - \frac{(k-\kappa)^2}{2}\sigma_z^2} d\kappa \\ &= b_{0,\text{CB}}(k;0)\frac{\sigma_z}{\sqrt{2\pi}}\sqrt{\frac{2\pi}{\Sigma_z^2+\sigma_z^2}} e^{-\frac{k^2}{2}\left(\frac{\Sigma_z^2\cdot\sigma_z^2}{\Sigma_z^2+\sigma_z^2}\right)} \end{aligned} \tag{21}$$

where $\Sigma_z^2(s) = \epsilon_{x0}\mathcal{H}_x(s) + \sigma_{\delta 0}^2 R_{56}^2(s)$. When $\sigma_z \to \infty$, the above expression is reduced to the familiar one. While this convolution approach may appear intuitive, it does not take into account the effect of bunched beam on the kernel function. Therefore it is believed that this expression Eq. (21) may not be valid for a general case. As an ongoing work, it will be worth comparing the solution of Eq. (17) with Eq. (21) obtained from intuitive approach.

SUMMARY

In this paper we have derived the generalized integral equation for the bunching factor of single-pass MBI. Preliminary results regarding the key factors of the bunched-beam model are summarized in Figs. 2 and 3. Although the theory is formulated in 2-D case, the formulation can be extended to 4-D or 6-D case in a straightforward way. As an ongoing work, after numerically implementing the solution procedures, the results will be compared with that using convolution. From the present analysis we get some idea that the bunched-beam MBI gain will include a reduction factor because it seems that the denominator is larger than before. This observation is consistent with that based on convolution.

ISBN: 978-3-95450-279-0 ISSN: 3043-0208 doi: 10.18429/JACoW-SAP2025-THP11

REFERENCES

[1] S. Heifets, G. Stupakov, and S. Krinsky, "Coherent synchrotron radiation instability in a bunch compressor", *Phys. Rev. ST Accel. Beams*, vol. 5, p. 064401, 2002. `doi:10.1103/PhysRevSTAB.5.064401`

[2] Z. Huang and K.-J. Kim, "Formulas for coherent synchrotron radiation microbunching in a bunch compressor chicane", *Phys. Rev. ST Accel. Beams*, vol. 5, p. 074401, 2002. `doi:10.1103/PhysRevSTAB.5.074401`

[3] M. Venturini, "Microbunching instability in a single-pass system using a direct two-dimensional Vlasov solver", *Phys. Rev. ST Accel. Beams*, vol. 10, p. 104401, 2007. `doi:10.1103/PhysRevSTAB.10.104401`

[4] C.-Y. Tsai *et al.*, "Linear microbunching analysis for recirculation machines", *Phys. Rev. Accel. Beams*, vol. 19, p. 114401, 2016. `doi:10.1103/PhysRevAccelBeams.19.114401`

[5] C.-Y. Tsai *et al.*, "Conditions for coherent-synchrotron-radiation-induced microbunching suppression in multibend beam transport or recirculation arcs", *Phys. Rev. Accel. Beams*, vol. 20, p. 024401, 2017. `doi:10.1103/PhysRevAccelBeams.20.024401`

[6] C.-Y. Tsai *et al.*, "Vlasov analysis of microbunching instability for magnetized beams", *Phys. Rev. Accel. Beams*, vol. 20, p. 054401, 2017. `doi:10.1103/PhysRevAccelBeams.20.054401`

[7] C.-Y. Tsai, "Concatenated analyses of phase space microbunching in high brightness electron beam transport", *Nucl. Instrum. Methods A*, vol. 940, pp. 462–474, 2019. `doi:10.1016/j.nima.2019.06.061`

[8] C.-Y. Tsai, "An alternative view of coherent synchrotron radiation induced microbunching development in multibend recirculation arcs", *Nucl. Instrum. Methods A*, vol. 943, p. 162499, 2019. `doi:10.1016/j.nima.2019.162499`

[9] S. Di Mitri *et al.*, "Experimental evidence of intrabeam scattering in a free-electron laser driver", *New J. Phys.*, vol. 22, p. 083053, 2020. `doi:10.1088/1367-2630/aba572`

[10] C.-Y. Tsai *et al.*, "Theoretical formulation of phase space microbunching instability in the presence of intrabeam scattering for single-pass or recirculation accelerators", *Phys. Rev. Accel. Beams*, vol. 23, p. 124401, 2020. `doi:10.1103/PhysRevAccelBeams.23.124401`

[11] C.-Y. Tsai and W. Qin, "Semi-analytical analysis of high-brightness microbunched beam dynamics with collective and intrabeam scattering effects", *Phys. Plasmas*, vol. 28, p. 013112, 2021. `doi:10.1063/5.0038246`

[12] G. Perosa and S. Di Mitri, "Matrix model for collective phenomena in electron beam's longitudinal phase space", *Sci. Rep.*, vol. 11, p. 7895, 2021. `doi:10.1038/s41598-021-87041-0`

[13] B. Liu, C.-Y. Tsai, Y. Jiao, W. Liu, F. Zeng, and W. Qin, "Analytical formulas of coherent-synchrotron-radiation induced microbunching gain and emittance growth in an arbitrary achromatic four-bend chicane", *Nucl. Instrum. Methods A*, vol. 1067, p. 169703, 2024. `doi:10.1016/j.nima.2024.169703`

ISBN: 978-3-95450-279-0 ISSN: 3043-0208 doi: 10.18429/JACoW-SAP2025-THP12

SUPPRESSION OF EMITTANCE VARIATION FOR THE HALF STORAGE RING

Xiaoyu Liu, Zhenghe Bai*, Penghui Yang, Gangwen Liu, Zhouyu Zhao, Guangyao Feng
National Synchrotron Radiation Laboratory, USTC, Hefei, China

Abstract

The Hefei Advanced Light Facility (HALF) is a diffraction-limited storage ring light source. The HALF storage ring lattice has relatively long damping times, and the adjustment of insertion device gaps can result in substantial variations in beam emittance. This paper investigates multiple methods to suppress the emittance variation of the HALF storage ring, including the usage of damping wigglers in long straight sections, wigglers in short dispersive straight sections and leaked dispersion in long straight sections.

INTRODUCTION

The Hefei Advanced Light Facility (HALF), currently under construction and scheduled to commence trial operation in 2028, is a diffraction-limited storage ring light source operating in the soft X-ray and VUV spectral range [1]. To achieve a natural emittance below 100 pm · rad, enhanced nonlinear dynamics performance and more straight sections, the HALF storage ring design adopts a modified hybrid six-bend achromat (H6BA) lattice as its baseline configuration. The lattice optics and main storage ring parameters are shown in Fig. 1 and Table 1 [2].

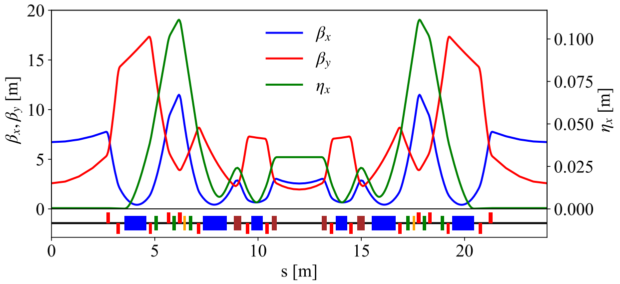

Figure 1: Linear optical functions and magnet layout of the HALF lattice. In the lower layout, bends are in blue, reverse bends in brown, quadrupoles in red, sextupoles in green and octupole in orange.

The HALF storage ring has 20 long straight sections and 20 middle straight sections, and all the experimental stations in Phase-I will employ undulators as radiation sources [3]. The Phase-I insertion devices (IDs) of HALF include 2 damping wigglers, 1 helical undulator (HU), 2 linearly polarized undulators (LPU), 6 elliptically polarized undulators (EPU) and 2 in-vacuum undulators (IVU). One short IVU will be installed in a middle straight section and the others are all in long straight sections. Table 2 shows the main parameters of the IDs at HALF.

Table 1: Main Parameters of the HALF Storage Ring

Parameter	**Value**
Energy	2.2 GeV
Circumference	479.86 m
Number of cells	20
Natural emittance	85.8 pm · rad
Natural energy spread	0.61×10^{-3}
Betatron tunes (H/V)	48.19 / 17.19
Natural chromaticities (H/V)	$-81.6/-56.6$
Momentum compaction factor	0.94×10^{-4}
Damping partitions (H/V/L)	1.36 / 1.0 / 1.64
Natural damping times (H/V/L)	28.5 / 38.8 / 23.7 ms
Energy loss per turn	181.4 keV

Table 2: Main Parameters of the HALF Insertion Devices

ID Type	λ_w **[mm]**	N_w	**Max. K**	**Number**
HU	115	35	8.97	1
EPU	120	33	11.26	1
EPU	63	65	5.77	1
EPU	43.5	36	2.94	2
EPU	46	90	3.29	1
EPU	41.5	99	2.67	1
IVU	20.7	182	2.10	1
IVU	20.7	52	2.10	1
LPU	38.2	108	2.83	1
LPU	38.5	108	3.36	1
Wiggler	100	42	16.00	2

In the HALF storage ring, the energy radiated in the bending magnets becomes comparable to the usually much less energy radiated in IDs. Consequently, the independent adjustment of ID gaps controlled by users can generate large random variations of emittance [4]. Several methods have been developed to suppress the emittance variation. The most common method is using compensation wigglers in long dispersion-free straight sections [5, 6], which is based on the radiation damping effect. A passive method from SPring-8-II is to leak a small amount of dispersion into each ID-equipped straight sections [7], which is based on the balance of radiation damping and quantum excitation. Other methods such as variable dispersion bump, beam momentum variation or using intra-beam scattering effect are also introduced in Ref. [4].

This paper presents a novel method based on quantum excitation effect that can suppress the emittance variation for the H6BA lattice of the HALF storage ring, and the effective-

---

* baizhe@ustc.edu.cn

ness of various emittance variation suppression techniques is comparatively analyzed.

EFFECT OF INSERTION DEVICES ON BEAM EMITTANCE

The natural emittance of the electron beam in a storage ring can be calculated using synchrotron radiation integrals when it reaches equilibrium between radiation damping and quantum excitation. The natural emittance and energy spread can be written as

$$\epsilon_x = C_q\gamma^2\frac{I_5}{I_2 - I_4}, \quad \sigma_\delta = \sqrt{C_q\gamma^2\frac{I_3}{2I_2 + I_4}}, \qquad (1)$$

where γ is the relativistic energy, C_q is 3.382×10^{-13}m, I_2, I_3, I_4 and I_5 are the radiation integrals, I_2 and I_4 represent the radiation damping effect, and I_5 represents the quantum excitation effect. The contribution of IDs on the radiation integrals is shown in the following formulas [5, 8]

$$\begin{aligned}
\Delta I_{2,ID} &= \frac{L_{ID}}{2\rho_{ID}^2}, \\
\Delta I_{3,ID} &= \frac{4L_{ID}}{3\pi\rho_{ID}^3}, \\
\Delta I_{4,ID} &\approx 0, \\
\Delta I_{5,ID} &= \frac{4\eta_x^2 L_{ID}}{3\pi\beta_x\rho_{ID}^3} + \frac{\beta_x\lambda_{ID}^2 L_{ID}}{15\pi^3\rho_{ID}^5}.
\end{aligned} \qquad (2)$$

To suppress the emittance variation induced by IDs, damping wigglers in long dispersion-free straight sections can be used to compensate for the energy loss variation based on the radiation damping effect, which can significantly change I_2 while maintaining I_4 and I_5 almost constant. When introducing a small amount of dispersion in each straight section, the four radiation integrals will be changed simultaneously, and the beam size can be represented by an effective emittance $\epsilon_{\text{eff}} = \left[\epsilon_x^2 + \gamma_x\eta_x^2\epsilon_x\sigma_\delta^2\right]^{1/2}$ (assuming $\eta_x' = 0$). An optimal leaked dispersion can reach the balance of radiation damping and quantum excitation and therefore minimize the effective emittance variation induced by IDs. Besides these two methods, taking full advantage of the relative large dispersion in the middle straight section, a novel suppression method can be used for the HALF storage ring based on the quantum excitation effect. When a short wiggler is installed in the middle straight section of the HALF storage ring, its gap variations induce a significant change in I_5 and relative small change in I_2 and I_4, which collectively compensate for emittance variations by effecting a slight net increase in emittance.

SUPPRESSION EMITTANCE VARIATION FOR THE HALF STORAGE RING

In this section, we will discuss the effectiveness of the three methods mentioned above based on the HALF storage ring. Statistical analysis indicates that the ID-induced energy loss per turn, $U_{0,ID}$, ranges from 25 % to 55 % of the maximum ID-induced energy loss per turn, $U_{0,ID,max}$, for approximately 90 % of ID operation cases, and the natural emittance variation during this operation ranges from 72 pm · rad to 84 pm · rad.

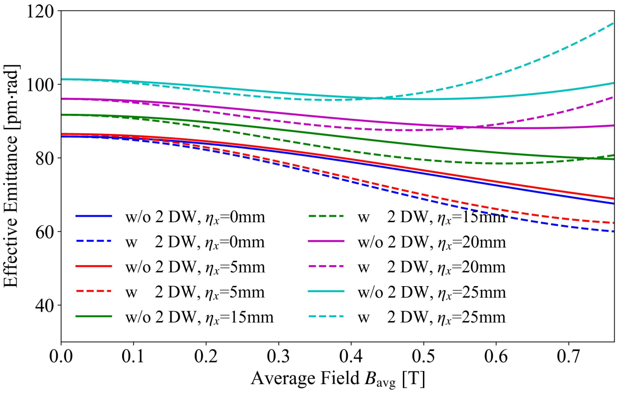

Figure 2: Compensation with leaked dispersion in each long straight section.

Compensation with Leaked Dispersion in Each Long Straight Sections

Inspired by the SPring-8-II method, we introduced controlled dispersion leakage into each long straight section, and quantified effective emittance variations at multiple dispersion values. Our analysis demonstrates that dispersion values in the 20~25 mm range minimize emittance variations induced by IDs, as shown in Fig. 2. However, this relatively high dispersion deteriorates nonlinear beam dynamics. Consequently, this method is not suitable for the HALF storage ring configuration.

Compensation Wigglers in Long Dispersion-Free Straight Sections

Two 4.2 m-long damping wigglers can be used as compensation wigglers to suppress the emittance variation. Successful implementation requires synchronous operation of both wigglers. The required magnetic field for each wiggler ranges from 0.28 T to 1.68 T, which is achievable for the HALF storage ring. The primary advantage of this method is the low compensation emittance (71 pm · rad), as shown in Fig. 3 and there is no need for additional devices. However, the disadvantage is that the strong magnetic attraction between wiggler poles creates substantial mechanical challenges for gap control precision. Additionally, the energy spread variation is relatively large.

Short Compensation Wiggler in Middle Straight Sections

The HALF storage ring features significant dispersion in its middle straight sections. Leveraging this characteristic, a wiggler installed in such a non-zero dispersion region enhances quantum excitation effects, thereby increasing emittance proportionally with wiggler field strength, which can

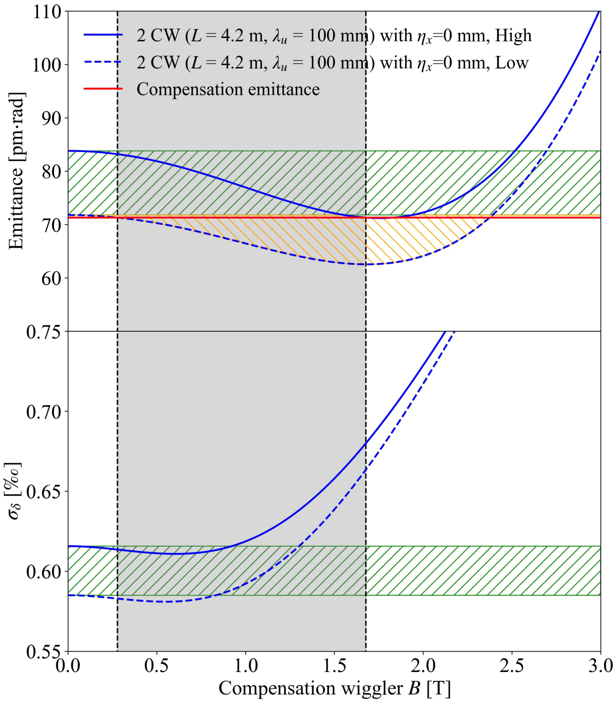

Figure 3: Compensation with variable-gap wigglers in long dispersion-free straight sections. The green shaded area denotes the fluctuation range of beam emittance and energy spread induced by random variations of the ID gaps, and the orange shaded area is the available compensation emittance, the gray area representing the required magnetic field range of the compensation wigglers.

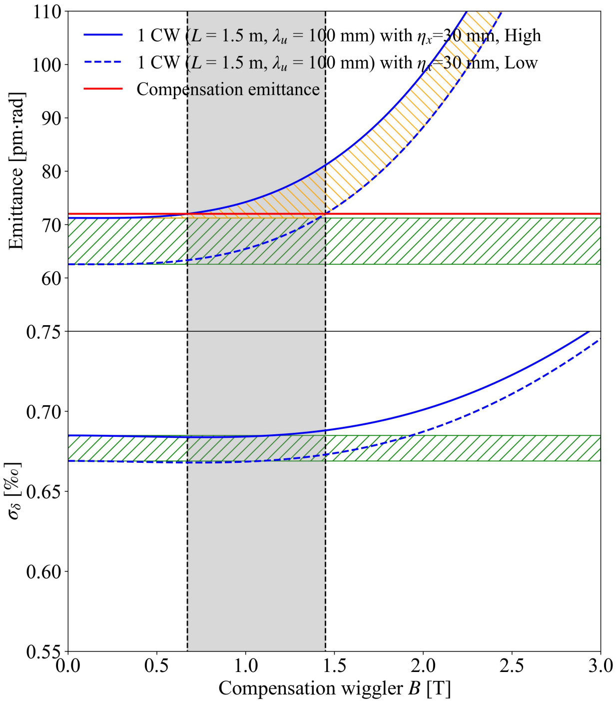

Figure 4: Compensation with one variable-gap wiggler in a middle straight section when the gaps of 2 damping wigglers in dispersion-free straight sections are closed. The green shaded area denotes the fluctuation range of beam emittance and energy spread induced by random variations of the ID gaps, and the orange shaded area is the available compensation emittance, the gray area representing the required magnetic field range of the compensation wigglers.

also be used to suppress the emittance variation. Notably, the middle straight section adjacent to the injection region cannot be used for user beamlines due to the space constraint, presenting an ideal location for a short compensation wiggler. In this study, the length and period length of this short wiggler is chosen as 1.5 m and 100 mm. Without 2 damping wigglers, this configuration achieves 84 pm · rad compensated emittance at 0.46∼1.48 T magnetic fields, and the maximum magnetic field is lower than the dispersion-free section case. When the gaps of 2 damping wigglers located in dispersion-free straight sections are closed, emittance further reduces to 72 pm · rad for the magnetic field range of 0.67∼1.45 T, as shown in Fig. 4.

This method demonstrates multiple advantages over the dispersion-free section case. (1) Fixed-gap damping wigglers can provide two additional experimental beamlines for users. (2) The closed damping wigglers can reduce the damping times, which is helpful to suppress collective effects. (3) The compensation emittance is near-equivalent compared with the dispersion-free section case. (4) A shorter wiggler results in weaker magnetic attraction in wiggler poles. (5) The energy spread variation is reduced during compensation. Consequently, a short compensation wiggler in a middle straight section is a better choice for HALF.

CONCLUSION

The HALF storage ring lattice has relatively long damping times, and the adjustment of ID gaps can result in substantial variations in beam emittance. This paper investigates multiple methods to suppress the emittance variation of the HALF storage ring, including the usage of damping wigglers in long straight sections, wigglers in short dispersive straight sections and leaked dispersion in long straight sections. Comparative analysis demonstrates that employing a short compensation wiggler in a middle straight section presents substantial advantages for emittance stabilization of the HALF lattice.

ACKNOWLEDGEMENTS

This work was supported by the National Natural Science Foundation of China under Grants No. 12375325 and No. 12205299.

REFERENCES

[1] Z. H. Sun, G. Y. Feng, and X. S. Liu, "Construction of Hefei Advanced Light Facility Begins", *Innovation*, vol. 4, no. 6, 100514. `doi:10.1016/j.xinn.2023.100514`

[2] Z. H. Bai, G. Y. Feng, T. L. He, *et al*, "Progress on the storage ring physics design of Hefei Advanced Light Facility (HALF)",

in *Proc. IPAC'23*, Venice, Italy, May 2023, pp. 1075–1078. doi:10.18429/JACoW-IPAC2023-MOPM038

[3] Z. Zhao, Y. Xu, and H. Li, "Preliminary design of insertion devices at Hefei Advanced Light Facility", in *Proc. IPAC'23*, Venice, Italy, May 2023, pp. 1247–1249. doi:10.18429/JACoW-IPAC2023-MOPM115

[4] F. Sannibale, S. C. Leemann, H. Nishimura, *et al*, "Compensation of Insertion Device Induced Emittance Variations in Ultralow Emittance Storage Rings", in *Proc. IPAC'18*, Vancouver, Canada, Apr.-May 2018, pp. 1751–1754. doi:10.18429/JACoW-IPAC2018-WEXGBE2

[5] D. Hidas, T. Shaftan, and T. Tanabe, "Emittance and energy spread compensation for current and future low emittance synchrotron light sources", *Phys. Rev. Accel. Beams*, vol. 24, p. 081601, 2021. doi:10.1103/PhysRevAccelBeams.24.081601

[6] L. Tan, S. Tian, X. Liu, *et al*, "Emittance and energy spread compensation in future synchrotron light sources", *Nucl. Instrum. Methods Phys. Res. A*, vol. 1052, p. 168278, 2023. doi:10.1016/j.nima.2023.168278

[7] T. Hiraiwa, K. Soutome, and H. Tanaka, "Suppression of emittance variation in extremely low emittance light source storage rings", *Phys. Rev. Accel. Beams*, vol. 25, p. 040703, 2022. doi:10.1103/PhysRevAccelBeams.25.040703

[8] X. Deng, J. Li, and Y. Lu, "Contribution of wiggler to radiation integral in an electron storage ring", *arXiv*, 2024. doi:10.48550/arXiv.2410.12863

ISBN: 978-3-95450-279-0 ISSN: 3043-0208 doi: 10.18429/JACoW-SAP2025-THP21

MODELING AND OPTIMIZATION OF TRANSVERSE TRAPPED-MODE IMPEDANCE FOR IN-VACUUM UNDULATORS OF HALF

Haiyan Yao, Xin Huang, Tianlong He*, Xiaoyu Liu, Weiwei Li, Zhenghe Bai†
National Synchrotron Radiation Laboratory, USTC, Hefei, China

Abstract

The in-vacuum undulator (IVU) exhibits exceptionally strong trapped-mode impedance due to its distinctive ridge-loaded waveguide structure and narrow magnetic gap design, which may lead to beam instability issues. This study primarily use the CST wakefield solver to investigate the trapped-mode impedance of the IVUs of the Hefei Advanced Light Facility (HALF). The trapped-mode impedance in the vertical direction is evaluated for both structures, with and without pump ports. Based on the impedance results, two mitigation strategies are proposed: ferrite damping and transition section optimization. Simulation results demonstrate that both strategies effectively reduce the impedance, with the transition section optimization strategy showing superior suppression performance.

INTRODUCTION

Modern storage-ring light sources typically employ IVUs, which consist of magnet arrays with very narrow gaps. These devices can generate photon beams with superior characteristics: higher photon energy, higher flux, and greater brightness. However, the combination of the ridged waveguide structure and the millimeter-scale magnet gaps induces strong electromagnetic interactions between the electron beam and its surroundings, creating particularly strong trapped-mode impedance in the vertical plane. This can lead to issues such as coupled-bunch instabilities. Several facilities, including Australia Light Source [1], SPEAR3 [2], BESSY II [3], PETRA-IV [4], CLS [5] and HEPS [6] have conducted relevant studies on the trapped modes of IVU.

The HALF storage ring incorporates one short and one long IVU with longitudinal lengths of approximately 1.5 meters and 4.2 meters, respectively. This paper models and simulates the short IVU under two configurations—with and without pump ports—to calculate the vertical trapped-mode impedance. Additionally, two mitigation strategies are proposed: installing ferrite damping blocks and optimizing the transition section geometry. These approaches are crucial for reducing coupling impedance and ensuring beam stability.

MODEL WITHOUT PUMP PORTS

To reduce the computational load, this study appropriately simplified the IVU model by omitting components such as cooling water pipes during the modeling process. The y–z cross-section of the simplified CST model is illustrated in Fig. 1.

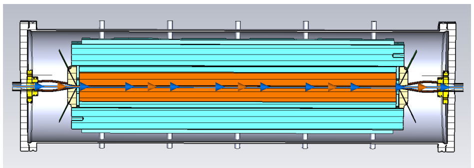

Figure 1: Model without pump ports.

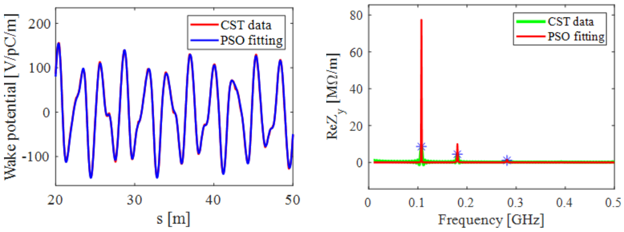

Figure 2: Results of wake potential (left) and impedance (right).

Table 1: Characteristic Parameters of the Primary Trapped Modes for the IVU Model Without Pump Ports

f_W | f_E **[MHz]**	R/Q_W | R/Q_E **[kΩ/m]**	Q_W | Q_E
107.2 | 106.6	154.8 | 154.0	500.1 | 547.9
180.4 | 180.3	56.6 | 52.4	176.2 | 322.0
281.4 | 281.9	9.2 | 8.4	149.2 | 313.4

The subscripts W and E denote the results from the wakefield solver and eigenmode solver, respectively.

The CST wakefield solver was primarily employed, with the bunch RMS length set to 50 mm and the offset to 1 mm. Due to partialy decay of the wakefield at 50 m, direct calculation would underestimate the impedance values. To obtain more accurate trapped-mode impedance data, the particle swarm optimization (PSO) algorithm was used to fit the wake potential and extract the characteristic parameters of the trapped modes. A comparison between the wake potential and impedance directly computed by CST and that obtained via PSO fitting is shown in Fig. 2. Three prominent impedance peaks are observed, with the strongest near 100 MHz exceeding 75 MΩ/m.

To validate the wakefield solver results, we also evaluated the impedance values of the aforementioned three modes using the CST eigenmode solver. As the simulation of the IVU model with realistic material settings required a prohibitively large mesh count and excessively long computation time, eigenmode simulations were conducted using a vacuum model (background material conductivity: 1.35×10^6 S/m). Table 1 presents the results obtained from both solvers. It can be observed that the frequencies and R/Q values of the three modes show good agreement, while certain discrepancies

---

* htlong@ustc.edu.cn
† baizhe@ustc.edu.cn

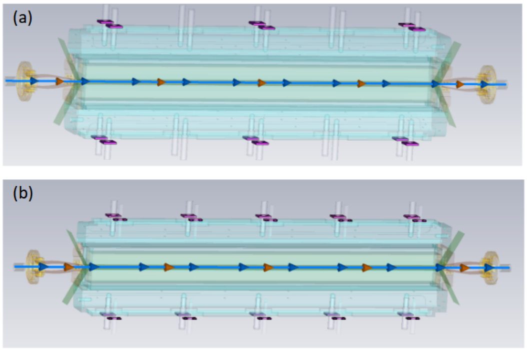

Figure 3: Installation schematics: (a) 12 ferrite blocks and (b) 20 ferrite blocks.

exist in the Q-values (computed by the eigenmode solver are slightly higher than those from the wakefield solver). This differences can be primarily attributed to the high sensitivity of the Q-value in the eigenmode solver to the background material settings: the actual IVU structure comprises multiple material layers, whereas the air model allows for only a single background material parameter, leading to deviations between the computed and actual values.

According to the results, the impedance values considerably exceed the synchrotron radiation damping threshold, thereby posing a significant risk of coupled-bunch instability. Therefore, the implementation of effective mitigation strategies is essential.

MITIGATION STRATEGIES

Ferrite Damping

Ferrite damping has been studied by facilities such as Australia Light Source [1], SPEAR3 [2], and HEPS [6] for impedance suppression in strong field regions. Based on this approach, this study designed two ferrite configuration schemes for the IVUs of HALF: one with 12 ferrite blocks on 6 pairs of support pillars and the other with 20 ferrite blocks on all 10 pairs of support pillars, as shown in Fig. 3. The ferrite blocks have specifications of 36 mm × 36 mm × 5 mm with a central installation hole of 11 mm diameter.

Figure 4 presents the wake potential computed by CST wakefield solver and the impedance obtained through PSO fitting, including the initial model, the model with 12 ferrite blocks, and the model with 20 ferrite blocks. The results demonstrate that with ferrite damping, the wake potential amplitude decays significantly and rapidly. Correspondingly, the impedance peaks are reduced from approximately 75 MΩ/m to 1.6 MΩ/m and 0.5 MΩ/m, respectively.

Transition Section Optimization

To further reduce the impedance fundamentally, this paper proposes a three-stage transition optimization design, consisting of a first tapered transition section, a rectangular section, and a second tapered transition section. The cross-sectional view in the Y-Z plane is shown in Fig. 5.

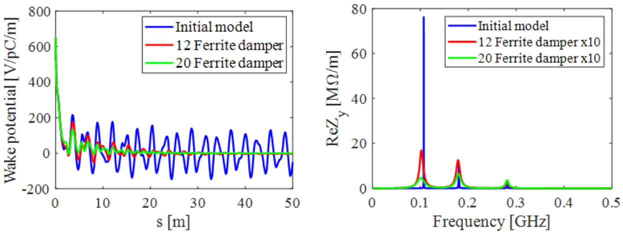

Figure 4: Results of wake potential (left) and impedance (right). For ease of comparison, the impedance values for ferrite damping are scaled by a factor of 10.

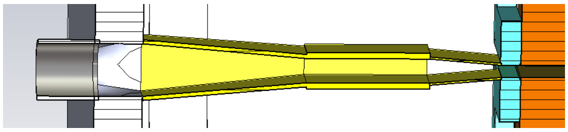

Figure 5: Cutaway view of the optimized transition section.

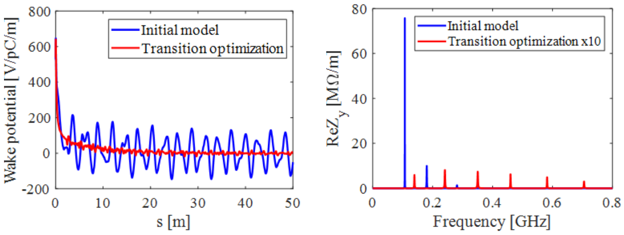

Figure 6: Results of wake potential (left) and impedance (right), including the initial model and transition optimization. The impedance values for transition optimization is scaled by a factor of 10.

Figure 6 shows the wake potential and impedance of the optimized transition section model. This design alters the trapped-mode frequencies. Although new modes emerge, the impedance of all modes remains significantly lower than that of the original design—reduced by approximately two orders of magnitude. This suppression effect slightly outperforms the ferrite damping scheme (with 20 ferrite blocks).

The characteristic parameters of the primary trapped modes, obtained through PSO fitting, are summarized in Table 2. Compared to the initial transition section structure, the proposed design has a minor effect on the quality factor (Q) but reduces the shunt impedance by approximately two orders of magnitude and significantly lowers the R/Q value. This result aligns with the findings in Ref. [6], where the quality factors remained largely unchanged while the R/Q values decreased due to the interruption of the resonant structure of the field distribution.

MODEL WITH PUMP PORTS

To better approximate realistic conditions, this study considers a detailed structural model that includes pump ports, with simulation parameters consistent with the previous model. The corresponding CST model is shown in Fig. 7.

The characteristic parameters of the primary trapped modes for the structure with pump ports are summarized in Table 3. The pump port configuration alters the trapped-

Table 2: Characteristic Parameters of the Primary Trapped Modes for the Optimized Transition Section Model

f [MHz]	R_s [MΩ/m]	$R/Q\perp$ [kΩ/m]	Q
139.2	0.6	5.6	105.3
240.9	0.8	5.5	147.8
350.6	0.7	4.1	180.1
459.8	0.6	1.6	380.3
581.9	0.5	1.1	437.5
705.2	0.3	0.8	372.2

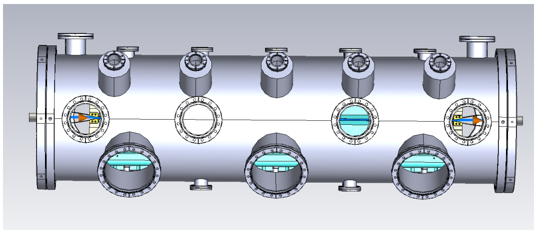

Figure 7: Model with pump ports.

Table 3: Characteristic Parameters of the Primary Trapped Modes for the Initial Model

f [MHz]	R_s [MΩ/m]	$R/Q\perp$ [kΩ/m]	Q
60.1	38.4	187.8	204.2
178.8	2.6	12.4	209.9
220.6	21.7	38.9	559.1
296.9	5.0	14.2	349.8

mode frequencies and yields lower impedance compared to the case without pump ports. Nevertheless, the impedance remains considerably high, thus necessitating the implementation of trapped-mode suppression measures.

Figure 8 shows the wake potential and impedance results for three configurations: the initial model, the model with 20 ferrite blocks, and the model with optimized transition sections. Compared with the initial model, the ferrite damping effectively suppresses the impedance peaks near 179 MHz, 221 MHz, and 297 MHz. However, it provides only limited suppression of the trapped-mode peak at 60 MHz. In contrast, the transition-section optimization significantly suppresses all trapped-mode impedance.

CONCLUSION

This study comprehensively investigates the transverse trapped-mode impedance of the IVUs in the HALF storage ring. The effectiveness of two mitigation strategies—ferrite damping and transition section optimization—is evaluated by assessing their impedance suppression performance on models both with and without pump ports. The results demonstrate that the impedance level of the IVU models without pump ports is significantly higher than the model with pump ports. Several distinct trapped-mode impedance peaks were observed in the vertical direction in both models, with impedance values substantially exceeding the threshold determined by synchrotron radiation damping, posing a risk of coupled-bunch instability. For the structure without pump ports, both impedance mitigation measures prove effective. However, for the structure with pump ports, ferrite damping is not effective in suppressing all modes. In contrast, the optimized transition section design fundamentally alters the impedance characteristics. It reduces the impedance peaks by approximately two orders of magnitude and exhibits excellent suppression capability for all trapped modes, thereby providing a more effective solution for overall IVU impedance suppression and beam stability assurance.

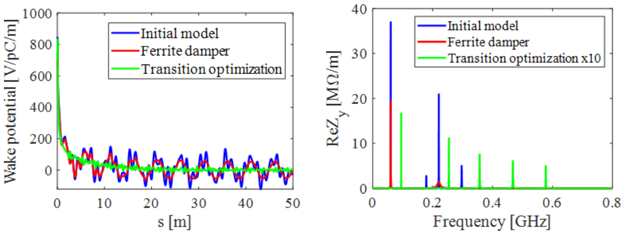

Figure 8: Results of wake potential (left) and impedance (right). The impedance values for transition optimization are scaled by a factor of 10.

ACKNOWLEDGEMENTS

This work was supported by National Natural Science Foundation of China (No. 12375324 and 12105284), and the Fundamental Research Funds for the Central Universities (No. WK2310000127).

REFERENCES

[1] R. T. Dowd, W. J. Chi, and D. Pelz, “Investigation of option for damping trapped IVU resonances”, in *Proc. IPAC’18*, Vancouver, Canada, Apr.–May 2018, pp. 1296–1299. `doi:10.18429/JACoW-IPAC2018-TUPMF021`

[2] K. Tian, J. J. Sebek, A. D. Ringwall, and Z. Li, “Damping trapped modes in an in-vacuum undulator at a synchrotron radiation light source”, *Phys. Rev. Accel. Beams*, vol. 22, no. 5, p. 050702, 2019. `doi:10.1103/PhysRevAccelBeams.22.050702`

[3] P. Volz, S. Grimmer, M. Huck, A. Meseck, *et al.*, “Goubau-line set up for bench testing impedance of in-vacuum undulator components”, in *Proc. IPAC’21*, Campinas, Brazil, May 2021, pp. 3883–3885. `doi:10.18429/JACoW-IPAC2021-THPAB057`

[4] F. Quetscher, E. Gjonaj, and H. D. Gersem, “Shunt impedance calculations for an in-vacuum undulator at PETRA IV”, in *Proc. IPAC’23*, Venice, Italy, May 2023, pp. 1064–1067. `doi:10.18429/JACoW-IPAC2023-MOPM034`

[5] E. Ericson, D. Bertwistle, M. J. Boland, and D. Pelz, “Analysis of RF modes in an in-vacuum undulator”, *Nucl. Instrum. Methods Phys. Res. A*, vol. 1070, p. 170027, 2025. `doi:10.1016/j.nima.2024.170027`

[6] N. Wang *et al.*, “Impedance characterization and optimization of the High Energy Photon Source in-vacuum undulator”, *Phys. Rev. Accel. Beams*, vol. 28, no. 9, p. 094401, 2025. `doi:10.1103/PhysRevAccelBeams.28.094401`

EXPONENTIAL SUM FITTING OF THE LONG-RANGE TRANSVERSE RESISTIVE-WALL WAKEFIELD

Xin Huang, Haiyan Yao, Tianlong He[*], Weiwei Li, Xiaoyu Liu, Zhenghe Bai, Hongliang Xu[†]
National Synchrotron Radiation Laboratory, USTC, Hefei, China

Abstract

In high-intensity storage rings, long-range transverse resistive-wall (RW) wakefield is a dominant source of coupled-bunch instability. Conventional particle tracking algorithms handling this wakefield require storing bunch-by-bunch and turn-by-turn centroid position histories, resulting in excessive memory consumption, which leads to computational inefficiency. This study proposes fitting the long-range transverse RW wakefield through a sum of exponentials. This method eliminates the need for bunch centroid histories during tracking computations while facilitating GPU-based parallel implementation, thereby significantly enhancing computational efficiency. This work demonstrates the dependence of the fitting performance on the number of exponential functions and the fitting interval.

INTRODUCTION

When a charged beam passes through a vacuum chamber with finite conductivity, it interacts with the chamber walls and excites electromagnetic fields, known as the resistive-wall (RW) wakefield. The RW wakefield can be categorized into the longitudinal and transverse wakefield. Among these, the long-range transverse wakefield can cause coupled bunch instability (CBI) [1, 2], which leads to beam quality degradation and, ultimately, to beam loss. Several codes, such as ELEGANT [3, 4] and MBTRACK2 [5], can simulate this effect. However, they require storing the bunch-by-bunch and turn-by-turn centroid histories, which consumes substantial memory and leads to low computational efficiency.

To address this issue, a wakefield approximation method known as resonator fitting can be employed. For instance, in the MUSIC code, M. Migliorati et al. successfully fitted the longitudinal RW impedance of the CERN Proton Synchrotron using 18 resonator functions [6]. However, as the long-range transverse RW wakefield decreases monotonically, resonator fitting is not effective. This study proposes a method to approximate the long-range transverse RW wakefield with a sum of exponentials.

Under the long-range approximation, the transverse RW wakefield of a single-layer, infinitely thick cylindrical chamber can be expressed as [7]:

$$W_{RW}^{\perp}(\tau) \approx C\frac{1}{\sqrt{\tau}}, \tag{1}$$

where C is a constant of $\frac{L}{\pi b^3}\sqrt{\frac{Z_0 c}{\pi \sigma}}$, L is the vacuum chamber length, b is the chamber radius, Z_0 is the free space impedance, c is the speed of light, and σ is the chamber material conductivity.

The long-range transverse RW wakefield is fitted using a sum of exponentials and is defined as follows:

$$\frac{1}{\sqrt{\tau}} \approx \sum_k A_k e^{-\alpha_k \tau}, \tag{2}$$

where A_k and α_k are the fitting coefficients, representing the weights and the decay factors, respectively.

Applying Eq. (2) in tracking simulations allows the wakefield kick calculation to avoid convolution with historical centroid positions. Similar to the resonator fitting method [8], this approach is well-suited for implementation on GPU parallel computing architectures, thus significantly improving computational efficiency for long-range RW wakefield induced instability simulations.

THEORY AND ALGORITHM

In the following section, we introduce two algorithms for calculating the fitting coefficients: one based on the Particle Swarm Optimization (PSO) and the other, an analytical algorithm.

PSO-Based Algorithm

Determining a set of coefficients $[A_1, \alpha_1, A_2, \alpha_2, \ldots]$ satisfying Eq. (2) can be translated into a single-objective, multi-variable optimization problem. Here, the fitting coefficients serve as the variables, and the objective function is defined by:

$$f_{\text{obj}} = \int_a^b \left(f(\tau) - \frac{1}{\sqrt{\tau}}\right)^2 d\tau, \tag{3}$$

where $f(\tau) = \sum_{k=1}^{N} A_k e^{-\alpha_k \tau}$ and N denotes the number of exponential terms. This least-squares objective function quantifies the closeness of the fitted curve to the target. Minimizing it yields the optimal coefficients for approximating the long-range RW wakefield.

Commonly used optimization algorithms include the Genetic Algorithm (GA) [9], Simulated Annealing (SA) [10], and Particle Swarm Optimization (PSO) [11, 12]. In comparison to GA and SA, PSO offers distinct advantages, including fewer adjustable parameters, conceptual simplicity, and ease of implementation. Considering both its convergence speed and capability to locate the global optimum, we prioritize the use of PSO for the fitting procedure in this study.

PSO is a population-based stochastic optimization technique inspired by collective biological behavior. The configuration in this study comprised a population of 50 particles, where each particle represented a candidate coefficient set $[A_{1,i}, \alpha_{1,i}, A_{2,i}, \alpha_{2,i}, \ldots]$. The optimization was run

---

[*] htlong@ustc.edu.cn

[†] hlxu@ustc.edu.cn

ISBN: 978-3-95450-279-0 ISSN: 3043-0208 doi: 10.18429/JACoW-SAP2025-THP22

for a maximum of 4000 iterations. Parameter bounds, determined through preliminary scanning, were set to $A_k \in [0, 4.72 \times 10^4]$ and $\alpha_k \in [1 \times 10^3, 5 \times 10^{10}]$.

Analytical Algorithm

This algorithm, proposed by W. McLean [13], enables the direct computation of weights and decay factors for given intervals and exponents, offering high computational efficiency. The underlying principle begins with the integral identity:

$$\frac{1}{\tau^\beta} = \frac{1}{\Gamma(\beta)} \int_0^\infty e^{-p\tau} p^\beta \frac{dp}{p} \quad \text{for } \tau > 0 \text{ and } \beta > 0. \tag{4}$$

A variable substitution is applied to p:

$$p = e^{x - e^{-x}}. \tag{5}$$

Substituting Eq. (5) into Eq. (4) yields:

$$\frac{1}{\tau^\beta} = \frac{1}{\Gamma(\beta)} \int_{-\infty}^\infty e^{-\tau e^{x-e^{-x}}} e^{\beta(x - e^{-x})} (1 + e^{-x})\, dx. \tag{6}$$

For τ in $[a, b]$, the integration interval is truncated to $[-M\delta_x, N\delta_x]$ based on the asymptotic behavior of the integrand. Then, the continuous integral is discretized to yield:

$$\frac{1}{\tau^\beta} = \sum_{k=-M}^{N} A_k e^{-\alpha_k \tau}, \tag{7}$$

where M and N are natural numbers satisfying $N + M + 1$ equal to the number of functions, δ_x is the step size used in the discretized integral. The corresponding weights and decay factors are given by:

$$A_k = \frac{\delta_x}{b^\beta \Gamma(\beta)} e^{\beta(k\delta_x - e^{-k\delta_x})} (1 + e^{-k\delta_x}), \tag{8}$$

and

$$\alpha_k = \frac{1}{b} e^{k\delta_x - e^{-k\delta_x}}, \tag{9}$$

where $\Gamma(z)$ is gamma function. Owing to the complexity of the original method by W. McLean for estimating δ_x, M, and N, the parameter scanning method was used to determine their values. Finally, setting $\beta = 1/2$ yields the values of the fitting coefficients for the case of long-range transverse RW wakefield.

RESULTS AND DISCUSSION

For the long-range transverse RW wakefield, this study adopts the wakefield truncation strategy used in ELEGANT [3, 4] and MBTRACK2 [5, 14]. Specifically, only the wakefield within a finite range (e.g., up to 50 turns) is considered. This is justified because the wakefield strength decays over time; beyond a certain number of turns, it becomes negligible. Neglecting these distant wakefields does not compromise the accuracy of the results but significantly improves computational efficiency. The fitting performance can be evaluated using two quantitative metrics:

$$e_R(\tau) = \sqrt{\tau} f(\tau) - 1, \tag{10}$$

and

$$e_W = \frac{\int_a^b \left| f(\tau) - \tau^{-1/2} \right| d\tau}{\int_a^b \tau^{-1/2} d\tau}. \tag{11}$$

where $e_R(\tau)$ is the relative error, and e_W is the normalized relative error weighted by the wakefield strength. The objective is to minimize $|e_R(\tau)|$ within the fitting interval.

Figure 1 presents a comparative analysis of the fitting results obtained from the PSO-based and analytical algorithms, using the Hefei Advanced Light Facility storage ring parameters as a case study. The time interval of one turn corresponds to a revolution period of 1.6 µs. The fitting was performed over the interval [1/800, 50] using a set of 9 fitting functions. As shown in Fig. 1(a), the relative error within the fitting interval remains within ±1 % for the analytical algorithm and ±2 % for the PSO-based algorithm. Figure 1(b) shows the results extended to the 200th turn. It can be observed that outside the fitting interval, the PSO error becomes negative and decreases rapidly with increasing turns, indicating that the PSO-fitted RW wakefield beyond this interval can be neglected without affecting the accuracy.

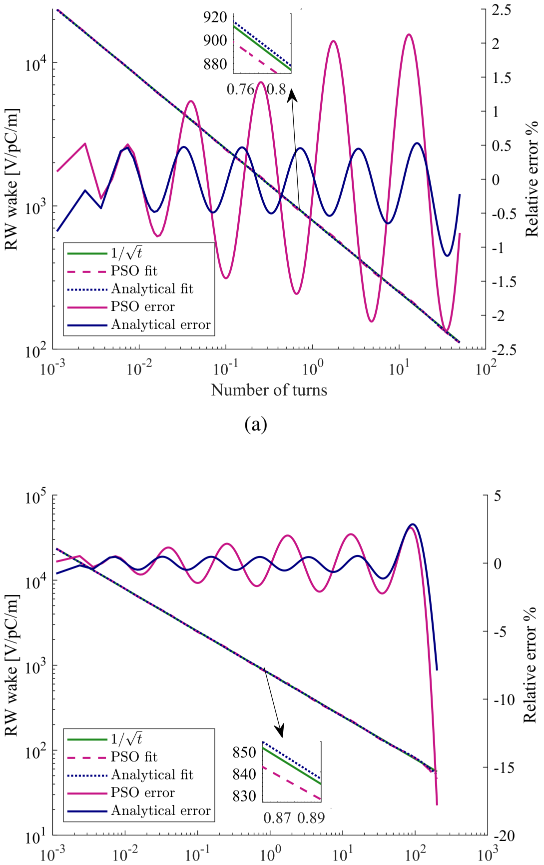

(a)

(b)

Figure 1: Comparison of PSO-based and analytical fitting using a ten-exponential model: (a) results for 1/800 to 50 turns; (b) results extended to 200 turns.

Figure 2 compares the fitting performance of the PSO-based and analytical algorithms across different number of function and fitting intervals, using the weighted error metric e_W. As the number of functions increases and the fitting interval narrows, the performance of both algorithms improves, reflected in the decreasing e_W values. Observably, the PSO results exhibit minor variations due to the stochastic nature of the PSO algorithm. Furthermore, a sharp decrease in the e_W is uniquely observed in the six-function analytical model, which is attributed to the improved fitting accuracy in the high-amplitude wakefield region when the fitting upper limit is increased from 175 to 200 turns. Between the two factors, the number of functions has a far greater impact on the fitting quality than the fitting interval. The PSO algorithm outperforms the analytical method with a small number of basis functions, while the analytical algorithm becomes superior when more than nine are used. In summary, when the number of fitting functions is set to 9, both algorithms achieve high accuracy ($e_W < 2.1$ %) over intervals of up to 250 turns.

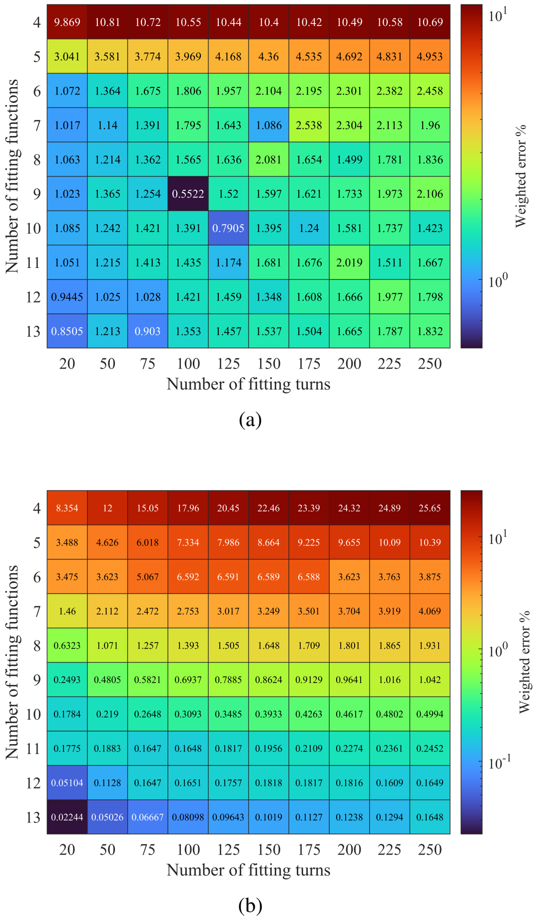

(a)

	20	50	75	100	125	150	175	200	225	250
4	9.869	10.81	10.72	10.55	10.44	10.4	10.42	10.49	10.58	10.69
5	3.041	3.581	3.774	3.969	4.168	4.36	4.535	4.692	4.831	4.953
6	1.072	1.364	1.675	1.806	1.957	2.104	2.195	2.301	2.382	2.458
7	1.017	1.14	1.391	1.795	1.643	1.086	2.538	2.304	2.113	1.96
8	1.063	1.214	1.362	1.565	1.636	2.081	1.654	1.499	1.781	1.836
9	1.023	1.365	1.254	0.5522	1.52	1.597	1.621	1.733	1.973	2.106
10	1.085	1.242	1.421	1.391	0.7905	1.395	1.24	1.581	1.737	1.423
11	1.051	1.215	1.413	1.435	1.174	1.681	1.676	2.019	1.511	1.667
12	0.9445	1.025	1.028	1.421	1.459	1.348	1.608	1.666	1.977	1.798
13	0.8505	1.213	0.903	1.353	1.457	1.537	1.504	1.665	1.787	1.832

(b)

	20	50	75	100	125	150	175	200	225	250
4	8.354	12	15.05	17.96	20.45	22.46	23.39	24.32	24.89	25.65
5	3.488	4.626	6.018	7.334	7.986	8.664	9.225	9.655	10.09	10.39
6	3.475	3.623	5.067	6.592	6.591	6.589	6.588	3.623	3.763	3.875
7	1.46	2.112	2.472	2.753	3.017	3.249	3.501	3.704	3.919	4.069
8	0.6323	1.071	1.257	1.393	1.505	1.648	1.709	1.801	1.865	1.931
9	0.2493	0.4805	0.5821	0.6937	0.7885	0.8624	0.9129	0.9641	1.016	1.042
10	0.1784	0.219	0.2648	0.3093	0.3485	0.3933	0.4263	0.4617	0.4802	0.4994
11	0.1775	0.1883	0.1647	0.1648	0.1817	0.1956	0.2109	0.2274	0.2361	0.2452
12	0.05104	0.1128	0.1647	0.1651	0.1757	0.1818	0.1817	0.1816	0.1609	0.1649
13	0.02244	0.05026	0.06667	0.08098	0.09643	0.1019	0.1127	0.1238	0.1294	0.1648

Figure 2: Fitting performance of the (a) PSO-based and (b) analytical algorithms with varying numbers of fitting intervals and exponentials.

The analytical algorithm offers two principal advantages: high computational efficiency, achieved through the direct calculation of coefficients with minimal resource consumption, and high accuracy when the RW wakefield adheres to the $\propto 1/\sqrt{\tau}$ scaling. Despite these advantages, its applicability is limited. In practice, the long-range transverse RW wakefield deviates from this theoretical $\propto 1/\sqrt{\tau}$ dependence due to effects such as multilayer material composition and finite wall thickness, which renders the analytical method invalid. Under these conditions, the PSO algorithm serves as a robust alternative. It should be noted, however, that the convergence of PSO becomes progressively more challenging as the number of basis functions increases, owing to the linear growth in the number of degrees of freedom.

Table 1 lists the fitting coefficients obtained from the PSO-based and analytical algorithms. A specific optimal PSO result, obtained using 9 functions over 100 turns, is presented here to illustrate the algorithm's performance.

Table 1: Fitting Coefficients from the Analytical (e_W = 0.69 %) and PSO-Based (e_W = 0.55 %) Algorithms

k	$A_{k,\text{analytical}}$	$\alpha_{k,\text{analytical}}$	$A_{k,\text{PSO}}$	$\alpha_{k,\text{PSO}}$
1	1.53×10^1	7.56	1.77×10^2	5.43×10^3
2	8.80×10^1	2.30×10^3	3.50×10^2	8.31×10^4
3	1.78×10^2	2.61×10^4	9.26×10^2	6.52×10^5
4	3.76×10^2	1.56×10^5	2.49×10^3	4.94×10^6
5	8.36×10^2	8.17×10^5	5.96×10^3	3.33×10^7
6	1.88×10^3	4.19×10^6	1.31×10^3	1.90×10^8
7	4.24×10^3	2.13×10^7	2.90×10^4	1.01×10^9
8	9.57×10^3	1.09×10^8	4.71×10^4	4.84×10^9
9	2.16×10^4	5.53×10^8	3.43×10^4	1.12×10^{10}

SUMMARY AND OUTLOOK

This study presents a method for approximating the long-range transverse RW wakefield by a sum of exponentials. Two algorithms for computing the fitting coefficients are introduced, and their performance is systematically evaluated across varying numbers of basis functions and fitting intervals. The proposed approximation method is designed for integration into particle tracking algorithms to enable GPU-accelerated simulation of the impact of long-range transverse RW wakefield on coupled-bunch instabilities.

ACKNOWLEDGEMENTS

This work was supported by National Natural Science Foundation of China (No. 12375324 and 12105284), and the Fundamental Research Funds for the Central Universities (No. WK2310000127).

REFERENCES

[1] M. Migliorati, L. Palumbo, C. Zannini, N. Biancacci, and V. Vaccaro, "Resistive wall impedance in elliptical multilayer vacuum chambers", *Phys. Rev. Accel. Beams*, vol. 22, no. 12, p. 121001, 2019. `doi:10.1103/PhysRevAccelBeams.22.121001`

[2] N. Mounet, “The LHC transverse coupled-bunch instability”, Ph.D. thesis, École Polytechnique Fédérale de Lausanne, Lausanne, Switzerland, 2012.

[3] *User’s manual for ELEGANT*, Advanced Photon Source, 1993.

[4] M. Borland, R. Lindberg, and A. Xiao, “Improvements in modeling of collective effects in ELEGANT”, in *Proc. IPAC’15*, Richmond, VA, USA, May 2015, pp. 549–552. doi:10.18429/JACoW-IPAC2015-MOPMA009

[5] A. Gamelin, W. Foosang, R. Nagaoka, *et al.*, “mbtrack2, a collective effect library in Python”, in *Proc. IPAC’21*, Campinas, Brazil, May 2021, pp. 282–285. doi:10.18429/JACoW-IPAC2021-MOPAB070

[6] M. Migliorati and L. Palumbo, “Multibunch and multiparticle simulation code with an alternative approach to wakefield effects”, *Phys. Rev. Spec. Top. Accel. Beams*, vol. 18, no. 3, p. 031001, 2015. doi:10.1103/PhysRevSTAB.18.031001

[7] A. W. Chao, *Physics of collective beam instabilities in high energy accelerators*. NJ, USA: John Wiley & Sons, 1993.

[8] T. He and Z. Bai, “Graphics-processing-unit-accelerated simulation for longitudinal beam dynamics of arbitrary bunch trains in electron storage rings”, *Phys. Rev. Accel. Beams*, vol. 24, no. 10, p. 104401, 2021. doi:10.1103/PhysRevAccelBeams.24.104401

[9] S. Katoch, S. S. Chauhan, and V. Kumar, “A review on genetic algorithm: past, present, and future”, *Multimedia tools and applications*, vol. 80, no. 5, pp. 8091–8126, 2021. doi:10.1007/s11042-020-10139-6

[10] S. Jajodia, I. Minis, G. Harhalakis, and J.-M. Proth, “CLASS: Computerized LAyout Solutions using Simulated annealing”, *Int. J. Prod. Res.*, vol. 30, no. 1, pp. 95–108, 1992. doi:10.1080/00207549208942880

[11] F. Marini and B. Walczak, “Particle swarm optimization (PSO). A tutorial”, *Chemom. Intell. Lab. Syst.*, vol. 149, pp. 153–165, 2015. doi:10.1016/j.chemolab.2015.08.020

[12] J. Blank and K. Deb, “Pymoo: multi-objective optimization in Python”, *IEEE Access*, vol. 8, pp. 89497–89509, 2020. doi:10.1109/ACCESS.2020.2990567

[13] W. McLean, “Exponential sum approximations for $t^{-\beta}$”, in *Contemporary computational mathematics-a Celebration of the 80th birthday of Ian Sloan*. Cham, Switzerland: Springer, 2018, pp. 911–930. doi:10.1007/978-3-319-72456-0_40

[14] W. Foosang, A. Gamelin, M. Tordeux, and P. Alexandre, “Resistive-wall instability evaluation along the ramp in the SOLEIL II booster”, *J. Phys.: Conf. Ser.*, vol. 2687, no. 6, p. 062017, 2024. doi:10.1088/1742-6596/2687/6/062017

ISBN: 978-3-95450-279-0 ISSN: 3043-0208 doi: 10.18429/JACoW-SAP2025-THP24

STUDY OF BUNCH LENGTHENING WITH HARMONIC CAVITIES FOR HLS-III

Wenshu Liang, Tianlong He[*], Weiwei Li, Xiaoyu Liu, Zhenghe Bai[†], Qing Luo[‡]
National Synchrotron Radiation Laboratory, USTC, Hefei, China

Abstract

NSRL recently proposed a future plan to further upgrade the HLS to an EUV diffraction-limited storage ring, named HLS-III. To improve the Touschek lifetime and suppress beam instabilities, HLS-III will employ a bunch-lengthening harmonic cavity system. Based on theoretical analysis, this work evaluates the bunch lengthening performance under five distinct double RF configurations involving different frequencies and harmonic orders, identifies the required harmonic cavity voltage to achieve the target bunch lengthening, and quantifies the corresponding improvement factor in Touschek lifetime. These findings provide valuable guidance for the selection of RF frequencies and the design of harmonic cavity parameters for HLS-III.

INTRODUCTION

The HLS-III upgrade proposal of HLS-II aims to achieve lower emittance and higher beam brightness. Key design parameters of HLS-III are summarized in Table 1, including a beam energy of 800 MeV, a circumference of approximately 66 m, and a natural emittance of 2.82 nm · rad—representing an order-of-magnitude reduction compared to HLS-II [1]. Similar to modern diffraction-limited storage ring light sources, HLS-III will employ harmonic cavities (HCs) for bunch lengthening to enhance beam quality by improving beam lifetime, suppressing emittance growth due to intra-beam scattering (IBS), and mitigating beam instabilities.

Table 1: Main Parameters of the HLS-III Storage Ring

Energy	800 MeV
Circumference	66.1308 m
Number of cells	4
Natural emittance	2.82 nm·rad
Momentum compaction factor	6.74×10^{-3}
Natural energy spread	4.99×10^{-4}
Natural damping times (x/y/z)	16.3 / 23.6 / 15.1 ms
Energy loss per turn	20 keV

This paper presents a theoretical analysis of bunch lengthening with harmonic cavities in HLS-III. By solving the Haïssinski equation for a double-RF system [2], we evaluate the bunch lengthening performance and corresponding cavity voltage requirements for several harmonic orders at two RF frequencies (204 MHz and 500 MHz). It should be noted that the two RF frequencies are considered for distinct reasons: the 204 MHz option is retained due to the availability of existing main cavities (MCs), though their higher-order modes (HOMs) remain undamped, posing a risk of coupled-bunch instabilities; the 500 MHz option represents a mature, commercially available technology with well-damped HOMs, aligning with current state-of-the-art practices.

THEORY AND METHOD

For the double-RF system, the total cavity voltage can be expressed as:

$$V_T(\tau) = V_1 \sin(\omega_{rf}\tau + \varphi_1) + kV_1 \sin(n\omega_{rf}\tau + \varphi_n), \quad (1)$$

where V_1 denotes the MC voltage amplitude, $k = V_n/V_1$ represents the voltage ratio of the HC to the MC, φ_1 and φ_n are the synchrotron phases of MC and HC, ω_{rf} is the angular radio-frequency, and n is the harmonic order of HC [3].

The value of V_1 can be determined based on the momentum acceptance requirement. For a single-RF system, the momentum acceptance is given by:

$$\delta_{\text{acc}} = \sqrt{\frac{2eV_1}{\pi h \alpha_c E_0} \times \left| \cos\varphi_s + \left(\varphi_s - \frac{\pi}{2}\right) \sin\varphi_s \right|}, \quad (2)$$

where e is the electron charge, φ_s is the synchronous phase ignoring HC, α_c denotes the momentum compaction factor, E_0 is the electron energy, and h is the harmonic number.

By setting the first and second derivatives of the total cavity voltage to zero, the well-known optimal-lengthening condition is obtained [4]:

$$\sin(\varphi_{1,fp}) = \frac{n^2}{n^2-1}\frac{U_0}{eV_1}, \quad (3)$$

$$k_{fp} = \sqrt{\frac{1}{n^2} - \frac{1}{n^2-1}\left(\frac{U_0}{eV_1}\right)^2}, \quad (4)$$

$$\tan(\varphi_{n,fp}) = -\frac{nU_0}{eV_1}\frac{1}{\sqrt{(n^2-1)^2 - \left(\frac{n^2U_0}{eV_1}\right)^2}}, \quad (5)$$

where k_{fp}, $\varphi_{1,fp}$, and $\varphi_{n,fp}$ denote the voltage ratio between HC and MC, synchronous phases for MC and HC under the optimal-lengthening condition, respectively.

The longitudinal RF potential, which determines the equilibrium density distribution, is given by [5]:

$$\begin{aligned}\Phi_{\text{RF}}(\tau) = \frac{eV_1}{2\pi h E_0 \alpha_c \sigma_\delta^2}\{ &\cos(\varphi_1) - \cos(\omega_{\text{rf}}\tau + \varphi_1) \\ &+ \frac{k}{n}\left[\cos(\varphi_n) - \cos(n\omega_{\text{rf}}\tau + \varphi_n)\right] - \frac{U_0\omega_{\text{rf}}\tau}{eV_1}\},\end{aligned} \quad (6)$$

---

[*] htlong@ustc.edu.cn
[†] baizhe@ustc.edu.cn
[‡] luoqing@ustc.edu.cn

ISBN: 978-3-95450-279-0 ISSN: 3043-0208 doi: 10.18429/JACoW-SAP2025-THP24

where σ_δ is the RMS energy spread, and U_0 the energy loss per turn.

The normalized equilibrium bunch distribution can be obtained from the Haïssinski equation:

$$\rho(\tau) = \frac{e^{\Phi_{\mathrm{RF}}(\tau)}}{\int_{-\infty}^{+\infty} e^{\Phi_{\mathrm{RF}}(\tau)}\, d\tau}\,. \tag{7}$$

The main purpose of employing HCs to lengthen bunches is to improve the Touschek beam lifetime. This improvement is typically quantified using the following expression:

$$\mathscr{R} = \frac{\int_{-\infty}^{+\infty} \rho_0^2(\tau)\, d\tau}{\int_{-\infty}^{+\infty} \rho^2(\tau)\, d\tau}\,. \tag{8}$$

where $\rho_0(\tau)$ denotes the zero-current longitudinal bunch density distribution in the absence of HC.

This paper intentionally focuses on head-tail symmetric bunch distributions. For arbitrary distributions, a skewness factor is introduced to quantify the degree of asymmetry, defined as follows:

$$\gamma_1 = \frac{\mu_3}{\sigma^3} = \frac{\int (\tau - \bar{\tau})^3 \rho(\tau) d\tau}{\left[\int (\tau - \bar{\tau})^2 \rho(\tau) d\tau\right]^{3/2}}, \tag{9}$$

where μ_3 is the third central moment, and σ is the standard deviation. A distribution becomes fully symmetric when $|\gamma_1| = 0$.

For the subsequent analysis, we introduce two scaling factors of K_V and K_φ to parameterize the HC settings:

$$V_n = K_V \cdot V_{n,\mathrm{fp}}, \quad \varphi_n = K_\varphi \cdot \varphi_{n,\mathrm{fp}}, \tag{10}$$

where $V_{n,\mathrm{fp}}$ is the voltage amplitude under the optimal-lengthening condition. Following the theoretical framework in Ref. [6], we adopt the constraint $K_V + K_\varphi \approx 2$. The optimization begins by determining K_V such that $\mathscr{L}(K_V, 2 - K_V) = \mathscr{L}_{\mathrm{target}}$, where $\mathscr{L}$ is the bunch lengthening factor, defined as the length ratio of lengthened bunch to natural bunch, and $\mathscr{L}_{target}$ denotes the target lengthening ratio.

With K_V fixed, we then employ the golden section search algorithm to optimize K_φ within the interval $[0.6(2 - K_V), 1.2(2-K_V)]$, minimizing the $|\gamma_1|$. This iterative method systematically narrows the search interval using points determined by the golden ratio $\psi = (1 + \sqrt{5})/2$, ensuring rapid convergence to the global minimum with proven efficiency [7].

The optimization problem is formally stated as:

$$\min_{K_\varphi} |\gamma_1(K_V, K_\varphi)|, \tag{11}$$

subject to:

$$\mathscr{L}(K_V, K_\varphi) = \mathscr{L}_{\mathrm{target}}, \tag{12}$$

$$K_\varphi \in [0.6(2 - K_V),\ 1.2(2 - K_V)]. \tag{13}$$

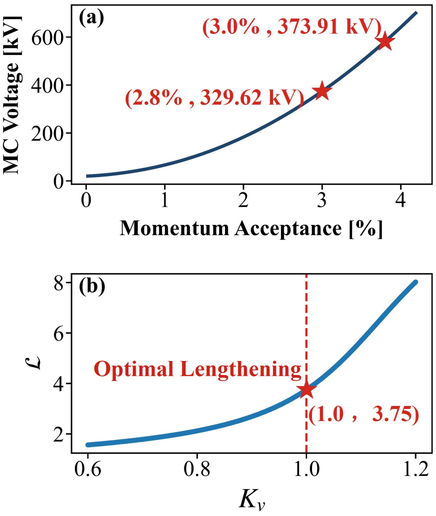

Figure 1: (a) MC voltage as a function of momentum acceptance. (b) Bunch lengthening factor $\mathscr{L}$ versus HC voltage scaling factor K_V.

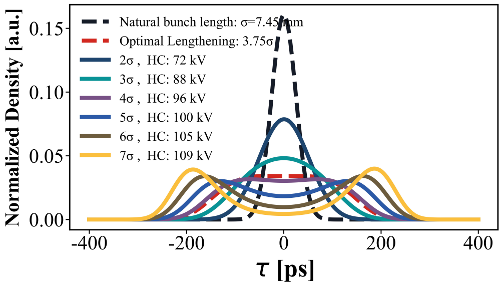

Figure 2: Equilibrium bunch distributions at different lengthening factors for the case of 204 MHz with a 4th order HC.

RESULTS AND DISCUSSION

Next, we first use the 204 MHz case as an example to elaborate on our computational methodology, and then proceed to compare the bunch lengthening performance, cavity voltage requirements, and Touschek lifetime improvement factors between the 204 MHz and 500 MHz configurations.

Case of 204 MHz with a 4th-Harmonic Cavity

Figure 1(a) shows the MC voltage required as a function of momentum acceptance, computed from Eq. (2). For HLS-III, a minimum MC voltage of 374 kV is needed to achieve a momentum acceptance of 3.0 %. Figure 1(b) presents $\mathscr{L}$ as a function of the HC voltage scaling factor, as defined in Eq. (10). The $\mathscr{L}$ increases monotonically with the HC voltage.

For the double-RF system, the parameter setting for optimal-lengthening condition is determined using Eqs. (3)-(5). Figure 2 shows the natural and optimally lengthened bunch distributions, obtained with an MC voltage of 375 kV and an HC voltage of 94 kV, corresponding to a lengthening factor of 3.75. Using the search method described in Eqs. (10)–(12), various symmetrical distributions with a

ISBN: 978-3-95450-279-0 ISSN: 3043-0208 doi: 10.18429/JACoW-SAP2025-THP24

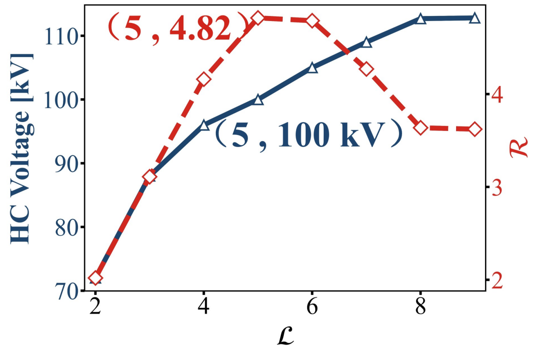

Figure 3: HC voltage and Touschek lifetime improvement factor $\mathscr{R}$ versus $\mathscr{L}$.

lengthening factor of 2-7 can be obtained, as also shown in Fig. 2.

Figure 3 shows the Touschek lifetime improvement factor $\mathscr{R}$ and the HC voltage as functions of $\mathscr{L}$. The improvement factor reaches its maximum value of 4.82 at a lengthening factor of 5, corresponding to an HC voltage of 100 kV.

Comparison of the 204 MHz and 500 MHz RF Options

We evaluated five RF configurations: a 204 MHz system with 2nd-, 3rd-, and 4th-order HCs, and a 500 MHz system with 2nd- and 3rd-order HCs. To achieve a momentum acceptance of 3 %, the MC voltages are set to 870 kV for the 500 MHz system and 375 kV for the 204 MHz system.

Figure 4 shows the corresponding HC voltage and $\mathscr{R}$ versus $\mathscr{L}$. The results reveal a monotonic increase in the required HC voltage with $\mathscr{L}$. In contrast, $\mathscr{R}$ generally increases but eventually reaches a maximum, indicating that moderate over-lengthening can further improve beam lifetime. Furthermore, for a given $\mathscr{L}$, a higher RF frequency (500 MHz) demands a greater HC voltage than a lower frequency (204 MHz). Additionally, for a given frequency, a lower harmonic number corresponds to a higher voltage requirement.

Based on the aforementioned analysis and with reference to existing cavity parameters, the estimated numbers of main and harmonic cavities required for HLS-III are summarized in Table 2. For the 204 MHz option, utilizing existing MCs of HLS-III with a maximum design voltage of 250 kV would require two units. However, a newly designed 204 MHz cavity could theoretically achieve the target voltage with a single cavity. As for the harmonic system, a single cavity readily meets the requirements, as the necessary voltages remain below 200 kV and the operating frequencies do not exceed 1 GHz.

For the 500 MHz option, referring to existing cavities, such as the 500 MHz EU-HOM damped cavity at the ALBA light source [8], typically two MCs are required. For the HC design, at least 435 kV and 290 kV are necessary for the cases of $n = 2$ and $n = 3$, respectively. In these cases, the requirements can be met using either two single-cell TM020 cavities [9] or a two-cell TM020 cavity [10].

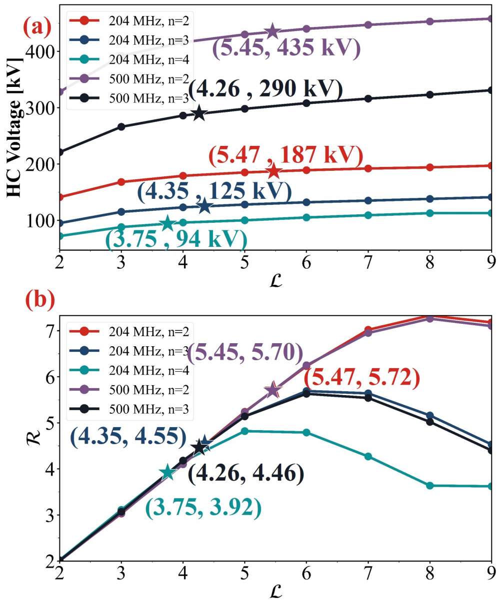

Figure 4: HC voltages and Touschek lifetime improvement factors $\mathscr{R}$ as functions of $\mathscr{L}$. The asterisk symbol indicates the optimal bunch lengthening setpoint.

Table 2: Estimated Requirements of Main and Harmonic Cavities for HLS-III

RF (MHz)	V_1 (kV)	N_{MC}	n	V_{hc} (kV)	N_{HC}
204	375	1	2	187	1
204	375	1	3	125	1
204	375	1	4	94	1
500	870	2	2	435	≥ 2
500	870	2	3	290	≥ 2

CONCLUSION

We investigated bunch lengthening for HLS-III across five RF configurations: 204 MHz with 2nd–4th HCs, and 500 MHz with 2nd–3rd HCs. Using a golden section search to optimize bunch symmetry, we determined the required cavity parameters for each bunch lengthening factor $\mathscr{L}$. The results reveal a consistent increase in the required HC voltage with $\mathscr{L}$, while the lifetime improvement reaches a maximum under moderate over-bunch lengthening. Furthermore, the analysis confirms that higher RF frequencies require greater voltages. These findings directly inform the cavity selection and implementation strategy for HLS-III and establish a foundation for future studies on beam dynamics stability.

ACKNOWLEDGMENT

This research was supported by the National Natural Science Foundation of China (No. 12375324 and No. 12105284) and the Fundamental Research Funds for the Central Universities (No. WK2310000127).

REFERENCES

[1] W. Li, B. Wei, X. Liu, M. Hosaka, Z. Ren, and Z. Bai, "Symmetric double-double bend lattice for a potential EUV diffraction limited upgrade of the HLS", presented at IPAC'25, Taipei, Taiwan, Jun. 2025, paper WEPM063, unpublished.

[2] J. Haissinski, "Exact longitudinal equilibrium distribution of stored electrons in the presence of self-fields", *Nuovo Cimento B*, vol. 18, no. 1, pp. 72–82, 1973. doi:10.1007/BF02832640

[3] T. He, W. Li, Z. Bai, and L. Wang, "Longitudinal equilibrium density distribution of arbitrary filled bunches in presence of a passive harmonic cavity and the short range wakefield", *Phys. Rev. Accel. Beams*, vol. 24, no. 4, p. 044401, Apr. 2021. doi:10.1103/PhysRevAccelBeams.24.044401

[4] J. Byrd and M. Georgsson, "Lifetime increase using passive harmonic cavities in synchrotron light sources", *Phys. Rev. Spec. Top. Accel. Beams*, vol. 4, no. 3, p. 030701, 2001. doi:10.1103/PhysRevSTAB.4.030701

[5] T. He, J. Xiao, W. Li, Z. Bai, and W. Li, "Impact of short-range wakefields from radio-frequency cavity resonant modes on bunch lengthening", *Nucl. Instrum. Methods Phys. Res. A*, vol. 1080, p. 170672, 2025. doi:10.1016/j.nima.2025.170672

[6] J. Xiao, T. He, and W. Li, "Periodic transient beam loading effect in triple radio-frequency systems", *Phys. Rev. Accel. Beams*, vol. 28, no. 10, p. 104401, Oct. 2025. doi:10.1103/PhysRevAccelBeams.28.104401

[7] Y.-C. Chang, "N-dimension golden section search: its variants and limitations", in *2009 2nd International Conference on Biomedical Engineering and Informatics*, Tianjin, China, Oct. 2009, pp. 1–6. doi:10.1109/BMEI.2009.5304779

[8] P. Solans *et al.*, "Active 3rd harmonic RF system for ALBA", presented at IPAC'25, Taipei, Taiwan, Jun. 2025, paper WEBD2, unpublished.

[9] T. Yamaguchi, N. Yamamoto, D. Naito, T. Takahashi, and S. Sakanaka, "Design and low-power measurement of 1.5 GHz TM020-type harmonic cavity for KEK future synchrotron light source", *Nucl. Instrum. Methods Phys. Res. A*, vol. 1053, p. 168362, 2023. doi:10.1016/j.nima.2023.168362

[10] A. D'Elia, J. Jacob, V. Serrière, X. Zhu, *et al.*, "Design of 4th harmonic RF cavities for ESRF-EBS", in *Proc. IPAC'21*, Campinas, Brazil, May 2021, pp. 1031–1033. doi:10.18429/JACoW-IPAC2021-MOPAB332

ISBN: 978-3-95450-279-0 ISSN: 3043-0208 doi: 10.18429/JACoW-SAP2025-THP34

ANALYTICAL STUDY OF FRINGE FIELDS AND NONLINEAR TRANSPORT IN A SECTOR-BASED ENERGY ANALYSIS SYSTEM*

Y. Wang†, Y. Zeng†, D. Xiao†, H. Hu, K. Liu, T. Hu‡
Huazhong University of Science and Technology, Wuhan, China
Y. Lu, G. Feng, University of Science and Technology of China, Hefei, China

Abstract

Energy Analysis (EA) systems based on sector magnets are widely applied in accelerators. Nevertheless, for low-energy electron beams below 15 MeV, extra measurement errors introduced by fringe fields of the sector magnet cannot be neglected. Moreover, initial beams with large momentum spread will encounter system errors arising from nonlinear transport. Such fringe-field-induced aberrations and their impact on momentum spectrum are studied analytically and a compensation scheme considering high-order momentum spread terms is proposed. Further, the theoretical derivation is validated with simulations, and correction of second-order aberration errors is explored via data processing. These methods and conclusions improve the accuracy of built/operational EA systems without extra costs.

INTRODUCTION

Injectors are regarded as core components of various electron accelerator–based facilities [1, 2]. Accurate measurement of the momentum distribution for the beam injectors is vital for the necessary facility. The energy analysis method based on magnetic deflection is widely applied in various domestic and international accelerator facilities [3–5], owing to its simple structure, high resolution, and ease of implementation.

This method is implemented by combining the dispersion effect of the sector magnet with beam transport theory, through which the momentum spectrum of the electron beam is obtained by measuring the bunch size at the downstream end of the EA system [6, 7]. When a electron with initial transverse offset x_0, angular deviation x_0', and momentum deviation δ passes through a system characterized by a transfer matrix M, the horizontal displacement at the the system end can be expressed as $x_1 = m_{11}x_0 + m_{12}x_0' + m_{13}\delta$ [8], where m_{11}, m_{12} and m_{13} are the corresponding elements of M.

However, in the measurement of low-energy beams with large momentum spread, the momentum spectrum errors caused by fringe fields and nonlinear transport effects are often neglected in conventional magnetic deflection methods [9–11]. The analytical expression for the longitudinal beam transport in the sector magnets is derived through the analysis of its fringe fields and the nonlinear transport process, and the sources of momentum dispersion measurement errors and their correction methods are further explored in this study.

ANALYTICAL STUDY OF FRINGE-FIELD-INDUCED ERRORS

For convenience, the magnet is divided into three sections along the s direction: the entrance and exit fringe field regions and the bending region. Only the main magnetic field is typically considered in conventional sector-magnets analysis. Momentum spectrum errors are caused by the neglected fringe fields [12], necessitating in-depth analysis of dynamical effects [13, 14].

To focus on the effect of the fringe fields, assuming $\delta = 0$. Starting from the Hamiltonian equation, the magnetic field components of the fringe fields are substituted into the equations of motion and integrated within the fringe regions [15, 16]. Neglecting high-order terms, the expression for a electron with the initial state $(x_0, p_{x_0}, y_0, p_{y_0})$ after passing through the entrance fringe field region is obtained as follows, where x_0 and y_0 denote the position offsets in the x and y, p_{x_0} and p_{y_0} represent the angular deviations, ρ denotes the bending radius, and p_z denotes the longitudinal momentum of the electron:

$$\begin{cases} x_1 = x_0 + \dfrac{y_0^2}{2\rho p_z}, \\ p_{x_1} = p_{x_0}, \\ y_1 = y_0, \\ p_{y_1} = p_{y_0} - \dfrac{y_0 p_{x_0}}{\rho p_z}. \end{cases} \tag{1}$$

The effect of the bending region is described directly by the first-order linear transfer matrix, and the expression of the electron after traversing the bending region is thereby obtained as follows:

$$\begin{cases} x_2 = \dfrac{\cos\theta}{2\rho p_z} y_0^2 + x_0\cos\theta + \rho p_{x_0}\sin\theta, \\ p_{x_2} = -\dfrac{\sin\theta}{2\rho^2 p_z} y_0^2 - \dfrac{\sin\theta}{\rho} x_0 + p_{x_0}\cos\theta, \\ y_2 = \left(1 - \dfrac{p_{x_0}\theta}{p_z}\right) y_0 + \rho\theta p_{y_0}, \\ p_{y_2} = -\dfrac{p_{x_0}}{\rho p_z} y_0 + p_{y_0}. \end{cases} \tag{2}$$

Then the electron motion through the exit fringe field region is integrated by the same analytical method as the entrance

---

[*] Work supported by the National Natural Science Foundation of China (No.1257051916 and No.12341501) and the National Key R & D Program of China (No.2024YFA1612200)

[†] Equal contribution

[‡] TongningHu@hust.edu.cn

ISBN: 978-3-95450-279-0 ISSN: 3043-0208 doi: 10.18429/JACoW-SAP2025-THP34

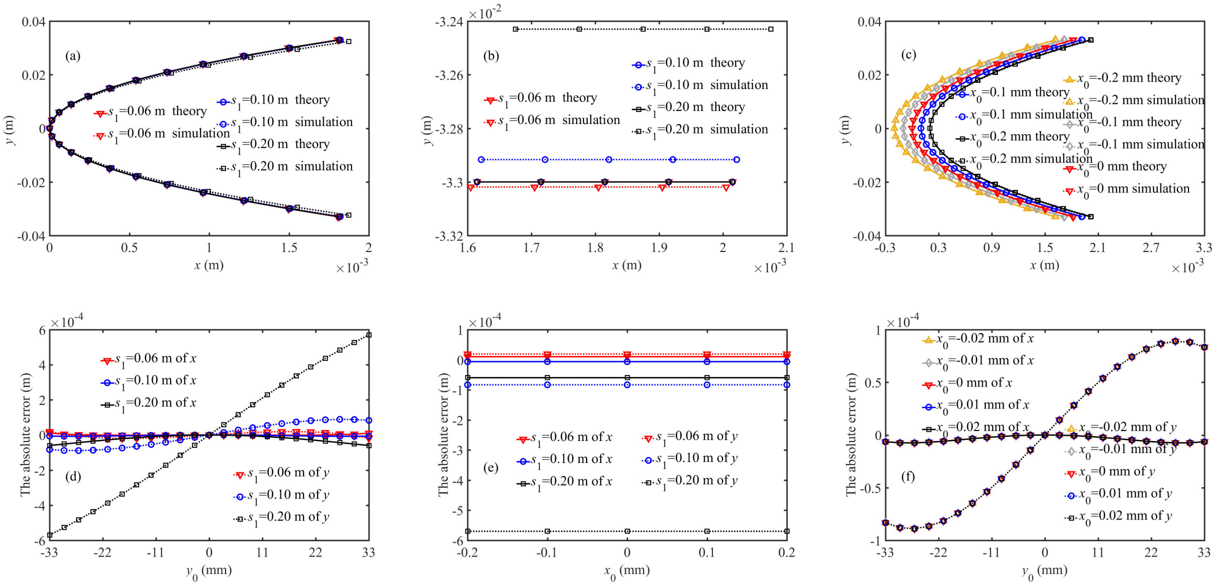

Figure 1: Comparison between theory and simulation of the bunch phase space: (a)-(c): $x - y$ for $x_0 = 0$ mm, $y_0 = -33$ mm and fringe field region $s_1 = 0.1$ m, respectively; (d)-(f): absolute errors in x and y for the same cases.

fringe field region, yielding the final electron state:

$$\begin{cases} x_3 = \dfrac{\cos\theta}{2\rho p_z} y_0^2 + x_0\cos\theta + \rho p_{x_0}\sin\theta - \dfrac{{y_2}^2}{2\rho p_z}, \\ p_{x_3} = -\dfrac{\sin\theta}{2\rho^2 p_z} y_0^2 - \dfrac{\sin\theta}{\rho} x_0 + p_{x_0}\cos\theta, \\ y_3 = \left(1 - \dfrac{p_{x_0}\theta}{p_z}\right) y_0 + \rho\theta p_{y_0}, \\ p_{y_3} = -\dfrac{p_{x_0}}{\rho p_z} y_0 + p_{y_0} + \dfrac{y_2 p_{x_2}}{\rho p_z}. \end{cases} \tag{3}$$

It is observed from the Eqs. (1)–(3) that y_0 will contribute to x. As previously mentioned, momentum dispersion is calculated from the exit x, and y_0 inevitably leads to an additional offset in x, thereby affecting the measurement of momentum spectrum.

FURTHER ANALYSIS CONTAINING NONLINEAR-TRANSPORT UNDER LARGE MOMENTUM SPREAD

Within the sector magnets, the deflection trajectory of electrons is determined by their momentum. When momentum spectrum is measured with the EA system, it is practice to rely on the linear transport theory.This approach can lead to an increase in nonlinear transmission errors during the measurement of beams with large momentum spreads. Therefore, higher-order compensation, which incorporates the momentum dispersion term, is proposed for the hard-edge model.

Consistent with the entrance fringe field region, the electron trajectory within the bending section is analyzed using a geometric approach. For the reference electron with $\delta = 0$, the corresponding bending radius and angle are denoted as ρ_0 and θ_0, respectively. For electron with δ, the bending radius and angle can be expressed as $\rho(\delta)$ and $\theta(\delta)$. Accordingly, the horizontal displacement of the electron relative to the reference one at the exit of the bending section can be obtained through geometric relations.

$$x = \rho(\delta)\frac{\sin\theta(\delta)}{\sin\theta_0} - \rho_0. \tag{4}$$

Then a Taylor expansion of x around $\delta = 0$ is performed:

$$x = k_1\delta + k_2\delta^2 + k_3\delta^3 + o(3), \tag{5}$$

where, k_i represents the coefficient of the ith-order term, $o(3)$ denotes the sum of all other higher-order terms.

Based on the previous analysis, the electron position at the exit of the sector magnet can be expressed as:

$$\begin{cases} x = \left(\dfrac{\cos\theta}{2\rho P} - \dfrac{(P - p_{x_0}\theta)^2}{2\rho P^3}\right) y_0^2 - \dfrac{(P - p_{x_0}\theta)\theta p_{y_0}}{P^2} y_0 + k_1\delta + k_2\delta^2 + k_3\delta^3 + x_0\cos\theta + \rho p_{x_0}\sin\theta - \dfrac{(\rho\theta p_{y_0})^2}{2\rho P}, \\ y = \left(1 - \dfrac{p_{x_0}\theta}{P}\right) y_0 + \rho\theta p_{y_0}, \end{cases} \tag{6}$$

where $P = p_z(1+\delta)$. Therefore, based on the analytical trajectory (x, y, δ) derived from the initial state (x_0, y_0, δ), and combined with the measured data of x and y on the fluorescent screen, the measurement result of the electron momentum deviation can be obtained.

The actual fringe field is more complex and does not vanish abruptly. To better reflect reality, an analytical model including quadrupole components is developed.

With the main magnetic field B_0 and fringe field length s_1, the expression of the electron horizontal position after passing through the entrance fringe field is:

$$\begin{cases} x_1 = x_0 + \dfrac{p_{x_0} s_1}{p_z} - \dfrac{3y_0^2 - s_1^2}{6\rho p_z}, \\ y_1 = y_0 + \dfrac{p_{y_0} s_1}{p_z} - \dfrac{y_0 p_{x_0} s_1}{2\rho p_z^2} - \dfrac{y_0(6y_0^2 - s_1^2)}{24\rho^2 p_z^2}. \end{cases} \tag{7}$$

The accuracy and feasibility of the theoretical derivation are verified by the simulation software COSY [17], with initial conditions set by engineering parameters. When the beam has an initial offset in the y-direction, as shown in Fig. 1(a), the maximum displacement obtained from the theoretical model is 6×10^{-4} m. If the beam bunch has offsets in both x and y, the maximum deviation is 1×10^{-4} m, as shown in Fig. 1(b). Furthermore, when fringe fields with quadrupole components are considered, as shown in Fig. 1(c), the maximum displacement is approximately 1×10^{-4} m. Extending the analysis to the phase space at the exit fringe field region, the maximum absolute deviations in x and y are 1.2×10^{-3} m and 8×10^{-3} m. These results indicate the relative difference between the theoretical and simulation remains within an acceptable range, confirming the validity of the theoretical model. Therefore, the derivation presented above provides a reliable theoretical basis for analyzing more complex effects using the COSY.

CONCLUSION

The influences of fringe fields and nonlinear transport within the EA system are analyzed, leading to improved accuracy and reliability of momentum dispersion measurements in systems without additional cost. Future research will refine the compensation mechanism for complex fringe fields using simulation tools, providing a theoretical and practical foundation for performance optimization of existing accelerator facilities.

REFERENCES

[1] P. Musumeci, J.G. Navarro, J.B. Rosenzweig, *et al.*, “Advances in bright electron sources”, *Nucl. Instrum. Methods Phys. Res. A*, vol. 907, pp. 209–220, 2018. doi:10.1016/j.nima.2018.03.019

[2] S. Di Mitri, “On the importance of electron beam brightness in high gain free electron lasers”, *Photonics*, vol. 2, no. 2, pp. 317341, 2015. doi:10.3390/photonics2020317

[3] Y. Wang, X. Jiang, G. Yang, *et al.*, “Time-resolved energy spectrum measurement of a linear induction accelerator with the magnetic analyzer” , *Chin. Phys. C*, vol. 39, no. 1, p. 017004, 2015. doi:10.1088/1674-1137/39/1/017004

[4] L. Yao, J. Yang, J. Xia, *et al.*, “A 60 MeV ultra-compact proton accelerator for proton radiation effects in China”, *Nucl. Instrum. Methods Phys. Res. A*, vol. 1064, p. 169341, 2024. doi:10.1016/j.nima.2024.169341

[5] S. DiDona, Z. Russell, J. Glass, *et al.*, “A high resolution miniature electron energy spectrometer”, *Nucl. Instrum. Methods Phys. Res. A*, vol. 1064, p. 169391, 2024. doi:10.1016/j.nima.2024.169391

[6] T. Hu, Y. Zeng, and K. Liu, “Design considerations of a magnet-based diagnosis system with compact layout for typical beam injector”, *IEEE Trans. Appl. Supercond.*, 2024. doi:10.1109/TASC.2024.1234567

[7] S. Zhang, C. Meng, Z. Zhou, *et al.*, “Design of 10 MeV electron linear accelerator for space environment simulation”, *Nucl. Sci. Tech.*, vol. 35, p. 177, 2024. doi:10.1007/s41365-024-0177-x

[8] Y. Wang, H. Hu, Y. Zeng, *et al.*, “Analysis and correction of intrinsic measurement errors for the dipole-magnet-based energy analysis system on HuTeX”, *Nucl. Eng. Technol.*, to be published.

[9] H. A. Enge, “Effect of extended fringing fields on ion-focusing properties of deflecting magnets”, *Rev. Sci. Instrum.*, vol. 35, pp. 278-287, 1964. doi:10.1063/1.1718806

[10] K. L. Brown, “A first- and second-order matrix theory for the design of beam transport systems and charged particle spectrometers”, *SLAC, Menlo Park, CA (United States)*, 1967. doi:10.2172/4496097

[11] S. Blitz and R. Molloy, “Fringe field effects on bending magnets, derived for TRANSPORT/TURTLE”, *arXiv*, 2013. doi:10.48550/arXiv.1310.8630

[12] H. Zeng, Y. Xiong, and Y. Pei, “The effects of magnetic fringe fields on beam dynamics in a beam transport line of a terahertz FEL source”, *Nucl. Instrum. Methods Phys. Res. A*, vol. 764, pp. 284-290, 2014. doi:10.1016/j.nima.2014.07.042

[13] M. Yoon, D. S. Robin, “Method of computing first-, second-, and third-order transfer coefficients for arbitrary fields”, *IEEE Trans. Nucl. Sci.*, vol. 60, no. 5, pp. 3837–3842, 2013. doi:10.1109/TNS.2013.2277726

[14] A. Brez, “Differential algebraic description of beam dynamics to very high orders”, *Part. Accel.*, vol. 24, pp. 109–124, 1988.

[15] G. E. Lee-Whiting, “First- and second-order motion through the fringing field of a bending magnet”, *Nucl. Instrum. Methods Phys. Res. A*, vol. 294, pp. 31–71, 1990. doi:10.1016/0168-9002(90)91825-V

[16] B. Hartmann, M. Berz, and H. Wollnik, “The computation of aberrations of fringing fields of magnetic multipoles and sector magnets using differential algebra”, *Nucl. Instrum. Methods Phys. Res. A*, vol. 297, no. 3, pp. 343-353, 1990. doi:10.1016/0168-9002(90)91317-5

[17] M. Berz and K. Makino, “COSY INFINITY Version 8.1 – User’s Guide and Reference Manual”, Department of Physics and Astronomy, Michigan State University, Rep. MSUHEP-20704, 2002.

ISBN: 978-3-95450-279-0 ISSN: 3043-0208 doi: 10.18429/JACoW-SAP2025-THP37

PHYSICAL DESIGN OF MICROWAVE ELECTRON GUN OPTIMIZED FOR CARBON NANOTUBE CATHODES*

Tianhui He[†]
Institute of Applied Electronics, Chinese Academy of Engineering Physics, Mianyang, China

Abstract

Since the maximum electric field strength that a carbon nanotube field-emission cathode can withstand is less than 13 MV/m, the optimization scheme of shortening the length of the first cavity based on the traditional 1/2+1 cavity-type microwave electron gun fails to solve the problems of electron phase slippage and back-bombardment. Therefore, in accordance with the emission characteristics of the carbon nanotube field-emission cathode, beam dynamics optimization was conducted on different cavity structures to select a more suitable cavity structure. Subsequently, the radio frequency (RF) design of the electron gun was completed through fine parameter adjustment of the cavity structure. Finally, the engineering design of the electron gun was accomplished after considering multiple aspects such as the gun's assembly, cathode structure, microwave feed-in structure, and electron beam output structure.

INTRODUCTION

Cold cathodes, as devices that can achieve electron emission without external heating, have become a research focus in the field of vacuum electronics due to their characteristics such as fast response, compact structure, and low power consumption. With the development of materials science, their material system has expanded from traditional metal tips and diamond films to carbon nanotubes (CNTs) and two-dimensional materials. Their emission performance and stability have been continuously improved, and cold cathode electron guns have also been initially applied in fields such as small vacuum devices and pulsed power systems. However, challenges remain in the generation of high-brightness and high-stability beams, especially in the practical application in the accelerator field [1, 2].

In the accelerator field, the performance of electron sources directly restricts beam quality and system efficiency. Compared with traditional hot cathodes, cold cathodes do not require preheating, which can shorten start-up time, avoid energy waste caused by heat loss, simplify structural design and reduce operating costs. Their fast-switching characteristic also enables precise regulation of pulsed beams, providing a new path for scenarios with strict requirements on time resolution, such as free-electron lasers and medical radiotherapy [3, 4]. Therefore, the development of cold cathode microwave electron guns is crucial for the miniaturization and integration of accelerators.

CNTs, with their high aspect ratio, excellent electrical conductivity, and low work function, have a low field emission threshold and high current density, making them ideal candidate cathodes for microwave electron guns [5]. However, when applied to existing platforms, due to their low electric field strength tolerance (less than 13 MV/m), while microwave electron guns require a high electric field in the cavity for strong-field acceleration, severe electron back bombardment occurs, resulting in cathode surface damage and performance degradation [6, 7].

To address this issue, this paper optimizes the physical design of the microwave electron gun based on the characteristics of CNTs cathodes: shortening the cavity length to reduce the residence time of electrons in the cavity, and introducing a nose cone structure to optimize the microwave electric field distribution. Simulation results show that after optimization, the electron back bombardment phenomenon is significantly reduced, laying a foundation for the practical application of CNTs cathodes in microwave electron guns.

RF-GUN DESIGN

In 2023, we established a cold cathode test platform based on a single-cavity 0.38-cell RF-gun, on which the field emission characteristics of a series of carbon nanotube thin-film cathodes and diamond thin-film cathodes were tested. Based on the more representative test results among them, we designed a single-cavity RF-gun using a carbon nanotube thin-film cathode.

Field Emission Characteristics of CNTs

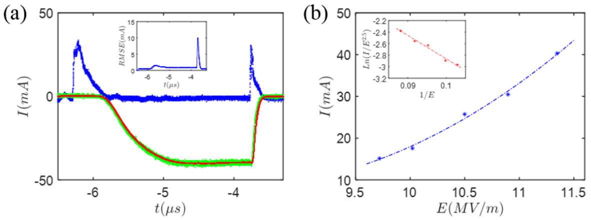

Figure 1: Test Results: (a) Field emission current waveform and reflection waveform; (b) Fitting curve of field emission characteristics.

The results of the CNTs thin-film cathode are shown in Figure 1. Among them, Figure 1(a) contains three characteristic curves: the blue curve represents the microwave reflection waveform, the green curve represents the macro-pulse current waveform, and the red curve is the smoothed curve of the macro-pulse current waveform; Figure 1(b) is the F-N fitting curve for the field emission characteristics.

The maximum field-emission current of the CNTs thin-film cathode is approximately 40 mA (with a cathode field-emission diameter of 6 mm and a current density of 0.14 A/cm²), among which the field enhancement factor is

---

* Work supported by Infrared terahertz free electron laser device project.
[†] htth111@163.com

ISBN: 978-3-95450-279-0 ISSN: 3043-0208 doi: 10.18429/JACoW-SAP2025-THP37

about 1179 and the root-mean-square (RMS) phase width is roughly 17.2°. Based on the above experimental data, the ASTRA software was used to conduct beam dynamics simulation on the RF-gun of the cold cathode test platform. The simulation parameters were set as follows: cathode field-emission diameter of 6 mm, longitudinal RMS phase width of 15°, charge quantity of 14 pC (corresponding to a macro-pulse current of approximately 40 mA), maximum electric field strength on the cathode surface of about 13 MV/m, and initial emission phase of 90°. Ultimately, the proportion of electron back-bombardment obtained from the simulation was approximately 40.51%.

Cavity Type Selection

The microwave frequency used by the RF-gun is 2856 MHz. Since the maximum electric field that the CNTs cathode can withstand is 13 MV/m (a relatively low electric field strength), the use of a conventional single-cavity Pillbox cavity will lead to severe back-bombardment. To reduce electron back-bombardment and achieve a certain beam bunching effect, a cavity structure with a nose cone added at the cathode end was adopted. Meanwhile, the distance from the cathode surface to the electron gun exit was shortened; in addition, reducing the diameter of the beam tube at the electron gun exit (to match the cathode emission area) can work with the nose cone to achieve a beam bunching effect. The basic cavity structure is shown in Figure 2.

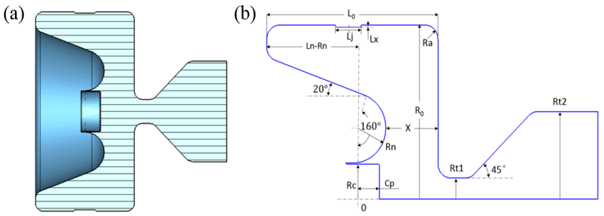

Figure 2: RF-gun cavity structure: (a) Cavity configuration; (b) Geometric structure.

The tuning of the RF-gun cavity is performed in the eigenmode by adjusting and modifying the cavity radius R₀, equatorial ridge height Lx, and chamfer radius Ra of the cavity's rear wall.

Beam Dynamics Simulation of the RF-gun

Based on the selection of the cavity structure, beam dynamics simulation and optimization of the RF-gun were conducted using the field emission parameters of a typical CNTs thin-film cathode obtained from the cold cathode test platform. The optimized results are shown in Figure 3, with the proportion of electron back-bombardment reduced to 5.6%.

Figure 3(a) shows the longitudinal distribution of the optimized electron beam transverse emittance in the electron gun. Figure 3(b) presents the longitudinal distributions of electron beam kinetic energy and energy spread: the kinetic energy at the electron gun exit exceeds 40 keV, and the energy spread of the beam bunch at the exit is less than 60%. Figure 3(c) displays the longitudinal momentum distribution of the beam bunch, from which it can be observed that the beam bunch length is within 40 mm and the distribution is approximately linear. Figure 3(d) illustrates the simulated longitudinal distribution of particles in the beam bunch. Figure 3(e) shows the statistical result of the number of beam bunch particles: among 20,000 particles, only 18,889 are emitted to the electron gun exit, 900 particles undergo back-bombardment, and 1,111 particles return to the cathode surface.

It can be concluded from the beam dynamics optimization results that reducing the gap exerts a certain effect on lowering electron back-bombardment.

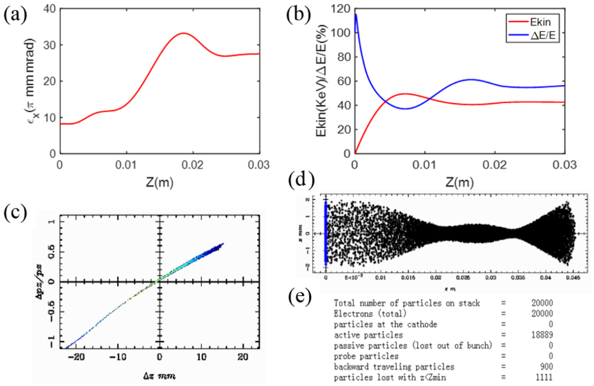

```
Total number of particles on stack          =     20000
Electrons (total)                           =     20000
particles at the cathode                    =         0
active particles                            =     18889
passive particles (lost out of bunch)       =         0
probe particles                             =         0
backward traveling particles                =       900
particles lost with z<Zmin                  =      1111
```

Figure 3: Beam dynamics optimization results of the cold cathode RF-gun: (a) Emittance optimization results; (b) Longitudinal kinetic energy distribution and energy spread distribution; (c) Longitudinal momentum distribution of the beam bunch at the electron gun exit; (d) Longitudinal particle distribution of the electron beam; (e) Statistical results of beam bunch particles.

RF Design

Based on the RF-gun cavity design results and beam dynamics optimization results, the RF-gun with a gap of 5 mm was selected as the target cavity structure. Software was used to conduct the radio frequency (RF) design of the electron gun, which mainly included the design of the RF-gun cavity and the microwave coupling structure.

The design of the RF-gun cavity primarily focused on eigenmode design. After the eigenmode optimization, the resonant frequency of the RF-gun was 2855.937 MHz, and the unloaded quality factor Q_0 was 5983.

The design of the microwave coupling structure required the use of a driven-mode design module. The main objectives of the RF-gun driven-mode design were as follows: the microwave coupling frequency should be 2856 MHz; the coupling state of the coupling hole should be over-coupling; and the coupling coefficient should be above 1.5.

On the basis of the eigenmode design and optimization, favorable driven-mode design and optimization results were obtained through the design and optimization of the microwave coupling structure, and the design results are shown in Figure 4.

As can be seen in Figure 4(a), the microwave coupling frequency is 2856.006 MHz. When a microwave power of 1 MW (at 2856 MHz) is fed into the electron gun, the

ISBN: 978-3-95450-279-0 ISSN: 3043-0208 doi: 10.18429/JACoW-SAP2025-THP37

electric field strength on the cathode surface can reach 73.76 MV/m. The coupling degree of the coupling hole at the microwave coupling frequency is approximately 1.7456, and it can be seen from the SMITH chart that the coupling state is over-coupling. The coupling degree of the probe at a frequency of 2856 MHz is approximately 50.5 dB.

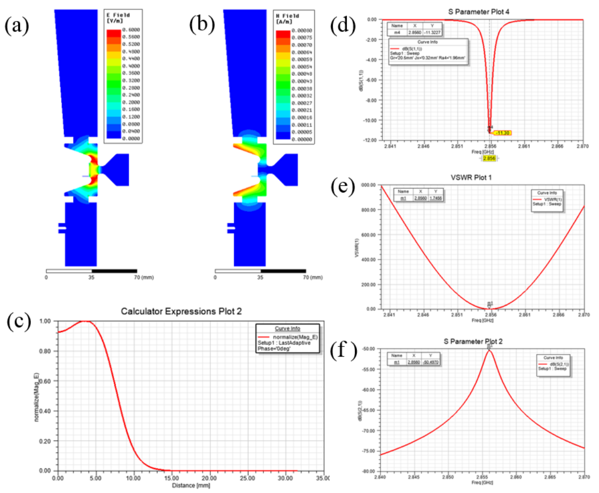

Figure 4: RF-gun optimization results: (a) Electric field distribution of the electron gun; (b) Magnetic field distribution of the electron gun; (c) Axial Electric Field Distribution of the Electron Gun; (d) S_{11} plot of the electron gun; (e) VSWR result of the coupling hole; (f) Probe coupling degree of the electron gun.

Mechanical Design

After the radio frequency (RF) design of the RF-gun was completed, the specific dimensions of its vacuum cavity were fully determined. Taking into account the mechanical strength and thermal conductivity of pure copper, a complete mechanical structure design of the electron gun was carried out. Given that the microwave pulse repetition frequency of the cold cathode test platform is relatively low, which will not cause significant heat accumulation, a separate thermal conductivity analysis of the electron gun is not performed here.

The electron gun is mainly composed of core components such as the cavity, tapered waveguide, and cathode insertion structure. Among them, the cavity body is assembled by two parts: the cavity main body and the nose cone. Water-cooled plates, water-cooled grooves, and cooling water pipes are matched on both sides of the cavity to form a complete heat dissipation system; coupling holes with consistent dimensions are symmetrically opened on the upper and lower parts of the cavity to ensure the symmetry of microwave coupling.

The upper part of the cavity is rigidly connected to the tapered waveguide, and a vacuum SNAC negative flange is welded on the top of the waveguide to realize the vacuum isolation function; the lower part of the cavity is sequentially connected to the CF25 beam tube and CF35 vacuum flange, forming the preliminary transmission channel for the electron beam. The electron beam exit end of the electron gun is directly welded with the CF35 beam tube and supporting flange to ensure the tightness and stability of beam transmission.

The cathode insertion structure assembled on the other side of the cavity adopts a modular design, integrating key parts such as the cathode holder, cathode transmission rod, bellows, and slide rail, which can realize precise positioning and flexible adjustment of the cathode. The layout and assembly relationship of all components of the electron gun are shown in the exploded view of Figure 5.

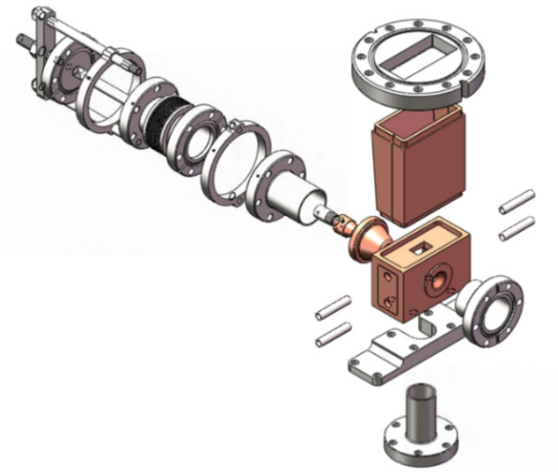

Figure 5: Exploded view of electron gun components.

CONCLUSION

After multiple rounds of discussions and design iterations, the electron gun development finally focused on optimizing the carbon nanotube field-emission cathode, culminating in the completion of both its physical and mechanical designs. The optimized electron gun achieves a significant suppression of electron back-bombardment: compared to the original electron gun on the cold cathode test platform, the proportion of electron back-bombardment is drastically reduced from 40.51% to 5.6%.

REFERENCES

[1] C. A. Spindt, I. Brodie, L. Humphrey, and E. R. Westerberg, “Physical properties of thin-film field emission cathodes with molybdenum cones”, *J. Appl. Phys.*, vol. 47, no. 12, pp. 5248–5263, Dec. 1976. doi:10.1063/1.322600

[2] J. W. Lewellen and J. Noonan, “Field-emission cathode gating for RF electron guns”, *Phys. Rev. ST Accel. Beams*, vol. 8, no. 3, p. 033502, Mar. 2005. doi:10.1103/PhysRevSTAB.8.033502

[3] K. Hu *et al.*, “A Novel Cold Cathode Design for S-Band Continuous-Wave Magnetron”, *IEEE Trans. Electron Devices*, vol. 68, no. 10, pp. 5238–5243, Oct. 2021. doi:10.1109/TED.2021.3109218

[4] M. Krysztof, “Field-emission electron gun for a MEMS electron microscope”, *Microsyst. Nanoeng.*, vol. 7, no. 1, Jun. 2021. doi:10.1038/s41378-021-00268-9

[5] Y. Saito and S. Uemura, “Field emission from cabon nanotubes and its application to electron sources”, *Carbon*,

vol. 38, no. 2, pp. 169–182, Dec. 2000. doi:10.1016/S0008-6223(99)00139-6

[6] G. S. Bocharov and A. V. Eletskii, “Degradation of a carbon nanotube-based field-emission cathode during ion sputtering”, *Tech. Phys.*, vol. 57, no. 7, pp. 1008–1012, Jul. 2012. doi:10.1134/S1063784212070055

[7] X. Li, M. Li, L. Dan, Y. Liu, and C. Tang, “Cold cathode RF guns based study on field emission”, *Phys. Rev. ST Accel. Beams*, vol. 16, no. 12, p. 23401, Dec. 2013. doi:10.1103/PhysRevSTAB.16.123401

15th Symposium on Accelerator Physics, Urumqi, China JACoW Publishing
ISBN: 978-3-95450-279-0 ISSN: 3043-0208 doi: 10.18429/JACoW-SAP2025-THP42

SPECTRAL FORM FUNCTION WITH APPLICATIONS IN BEAM PHYSICS

Xiujie Deng*, Institute for Advanced Study, Tsinghua University, Beijing, China

Abstract

To describe longitudinal fine structure like microbunching within a particle beam, a classical approach is to define a bunching factor which is the Fourier transform of the particle longitudinal density distribution. Such a 1D definition of bunching factor can be generalized to a 6D spectral form function (SFF) to describe more complicated structure in phase space. The complex SFF is another complete description of beam in spectral domain and can offer complementary and valuable insight in beam dynamics study which usually invokes the real particle density distribution. The basic property and Fokker-Planck equation of the SFF is presented, along with its solution in a general coupled linear lattice. The example applications of SFF in electron storage ring physics and laser-induced microbunching are presented.

INTRODUCTION

Microbunching enables laser-like radiation generation from charged particle beam, and is one of the main driving forces advancing accelerator light sources in the past decades. The most prominent example is free-electron laser. Usually we mainly care about the longitudinal coordinate of the particles in quantifying the degree of microbunching, since the radiation of a relativistic beam is dominantly in the forward direction. But strictly speaking the 6D particle phase space coordinates can all have an impact on coherent radiation [1]. One can even create novel 6D structures in phase space for various purposes, for example to tailor the radiation properties or to control collective beam dynamics. One example is the creation of helical microbunching for light generation with orbit angular momentum [2]. The classical 1D definition of bunching factor is clearly not sufficient in many applications. This justifies our motivation to investigate such a generalized definition of spectral form function (SFF). But we recognize the potential applications of SFF can be much broader than this original motivation.

SPECTRAL FORM FUNCTION

6D particle state vector: $\mathbf{X}\equiv\begin{pmatrix}x & x' & y & y' & z & \delta\end{pmatrix}^T$. 6D spectral vector: $\mathbf{K}\equiv\begin{pmatrix}k_x & k_{x'} & k_y & k_{y'} & k_z & k_\delta\end{pmatrix}$. Normalized charge density function: $\psi(\mathbf{X})$ satisfying $\int\psi(\mathbf{X})d\mathbf{X}=1$, $\psi(\mathbf{X})\geq 0$. Then SFF is defined as:

$$\mathcal{F}(\mathbf{K})\equiv\int\psi(\mathbf{X})e^{-i\mathbf{K}\mathbf{X}}d\mathbf{X}. \tag{1}$$

$\psi(\mathbf{X})$ and $\mathcal{F}(\mathbf{K})$ forms a Fourier transform pair

$$\psi(\mathbf{X})=\frac{1}{(2\pi)^6}\int\mathcal{F}(\mathbf{K})e^{i\mathbf{K}\mathbf{X}}d\mathbf{K}. \tag{2}$$

The linear symplectic dynamics in an accelerator is dictated by a quadratic Hamiltonian $\mathcal{H}=\frac{\mathbf{X}^T\mathbf{H}\mathbf{X}}{2}$, where $\mathbf{H}=\mathbf{H}^T$. The Hamiltonian equation in matrix form is then $\frac{d\mathbf{X}}{ds}=\mathbf{SHX}$, with $\mathbf{S}$ the symplectic form. The evolution of particle state vector from the initial point s_i to the final point s_f can be described by a symplectic transfer matrix according to $\mathbf{X}(s_f)=\mathbf{R}(s_f,s_i)\mathbf{X}(s_i)$, with $\mathbf{R}(s_f,s_i)=e^{\int_{s_i}^{s_f}\mathbf{SH}ds}$ if $\mathbf{H}$ is s-independent from s_i to s_f. Correspondingly the transfer matrix for $\mathbf{K}$ is $\mathbf{K}(s_f)=\mathbf{K}(s_i)\mathbf{R}^{-1}(s_f,s_i)$. From continuity equation $\frac{\partial\psi}{\partial s}+\nabla_{\mathbf{X}}\cdot\left(\psi\frac{d\mathbf{X}}{ds}\right)=0$ where $\nabla_{\mathbf{X}}\equiv\left(\frac{\partial}{\partial\mathbf{X}_1},\cdots,\frac{\partial}{\partial\mathbf{X}_6}\right)$ and Hamiltonian equation follows the Liouville equation

$$\frac{d\psi}{ds}=\frac{\partial\psi}{\partial s}+[\psi,\mathcal{H}]=0,\ \frac{d\mathcal{F}}{ds}=\frac{\partial\mathcal{F}}{\partial s}+[\mathcal{H}_{\mathbf{K}},\mathcal{F}]=0, \tag{3}$$

with $\mathcal{H}_{\mathbf{K}}=-\frac{\mathbf{KSHSK}^T}{2}$, from which follows $\psi(\mathbf{X},s_f)=\psi(\mathbf{R}^{-1}(s_f,s_i)\mathbf{X},s_i)$, $\mathcal{F}(\mathbf{K},s_f)=\mathcal{F}(\mathbf{KR}(s_f,s_i),s_i)$. We recognize the work presented in this section has been obtained before by Yampolsky [3].

FOKKER-PLANCK EQUATION

Now let us add non-symplectic process, like damping and diffusion. Here we simplify the discussion by assuming that the damping coefficients are independent of the particle state vector, for example that of the radiation damping. The equation of motion is now

$$\frac{d\mathbf{X}}{ds}=(\mathbf{SHX}+\mathbf{BX})+\xi(s), \tag{4}$$

with the stochastic process ξ satisfying $\int p(\xi)d\xi=1$, $\int\xi_i p(\xi_i)d\xi_i=0$, $\int\xi_i(s)\xi_j(s')p(\xi_i(s),\xi_j(s'))d\xi_i d\xi_j=D_{ij}\delta(s-s')$, where $p(\xi)$ is the probability distribution function of ξ. We have assumed that the noise is a Gaussian white noise. In the above equation, $\mathbf{B}$ is responsible for the deterministic damping or antidamping, and ξ for diffusion. Note that here we actually assume that the diffusion is a continuous-diffusion process, instead of a jump-diffusion process whose rigorous description requires the Kramers-Moyal expansion [4]. The quantum excitation for example is more accurately modeled by a jump-diffusion process. Denote $\mathbf{C}\equiv\mathbf{SH}+\mathbf{B}$, and note that $\mathrm{Tr}(\mathbf{SH})=0$, we can then derive the Fokker-Planck equation for $\psi(\mathbf{X})$

$$\frac{\partial\psi}{\partial s}+\nabla_{\mathbf{X}}(\psi\mathbf{CX})=\frac{1}{2}\sum_{i=1}^{6}\sum_{j=1}^{6}D_{ij}\frac{\partial^2\psi}{\partial\mathbf{X}_i\partial\mathbf{X}_j}. \tag{5}$$

The corresponding equation in spectral domain is

$$\frac{\partial\mathcal{F}}{\partial s}-(\mathbf{KC})(\nabla_{\mathbf{K}}\mathcal{F})=-\frac{\mathbf{KDK}^T}{2}\mathcal{F}, \tag{6}$$

---

* dengxiujie@mail.tsinghua.edu.cn

ISBN: 978-3-95450-279-0 ISSN: 3043-0208 doi: 10.18429/JACoW-SAP2025-THP42

where $\nabla_{\mathbf{K}} \equiv \left(\frac{\partial}{\partial \mathbf{K}_1}, \cdots, \frac{\partial}{\partial \mathbf{K}_6}\right)^T$. From the right hand side of Eq. (6), it is clear that diffusion has a stronger impact on high-frequency bunching, i.e., finer structures in phase space. Also note that if there is no diffusion in phase space, i.e., if $\mathbf{D} = \mathbf{0}$, we have $\frac{d\psi}{ds} = \frac{\partial\psi}{\partial s} + (\nabla_{\mathbf{X}}\psi)(\mathbf{CX}) = -\mathrm{Tr}(\mathbf{C})\psi = -\mathrm{Tr}(\mathbf{B})\psi$, and $\frac{d\mathcal{F}}{ds} = \frac{\partial\mathcal{F}}{\partial s} - (\mathbf{KC})(\nabla_{\mathbf{K}}\mathcal{F}) = 0$. So the information of fine structure in phase space in some sense can only be destroyed by diffusion or stochastic process. The deterministic linear transport with damping or anti-damping can only rotate, shrink or expand the structure.

Now we solve the Fokker-Planck equation. First we assume the accelerator lattice is a piece-wise one and we solve the equation in each piece, in which $\mathbf{C}$ is a constant matrix. First we diagonalize the matrix $\mathbf{C}$, $\mathbf{C} = \mathbf{P}^{-1}\mathbf{QP}$, with $\mathbf{Q}$ a diagonal matrix, and $\mathbf{Q}_{ii} = \lambda_i$ the eigenvalues of $\mathbf{C}$. Denote $\mathbf{K}' \equiv \mathbf{KP}^{-1}$ and $\mathbf{D}' \equiv \mathbf{PDP}^T$, then Eq. (6) can be cast as

$$\frac{\partial\mathcal{F}}{\partial s} - \sum_i \mathbf{K}'_i\lambda_i\frac{\partial\mathcal{F}}{\partial\mathbf{K}'_i} = -\frac{\mathbf{K}'\mathbf{D}'\mathbf{K}'^T}{2}\mathcal{F}, \tag{7}$$

whose general solution is [5]

$$\mathcal{F}(\mathbf{K}', s) = f(\mathbf{K}'\mathbf{\Lambda}, 0)e^{\left(\sum_{ij}\frac{1}{2}\frac{D'_{ij}}{\lambda_i+\lambda_j}\mathbf{K}'_i\mathbf{K}'_j\right)}, \tag{8}$$

where $\mathbf{\Lambda} \equiv \mathrm{diag}\left\{e^{\lambda_1 s}, \cdots, e^{\lambda_6 s}\right\}$, with $\mathrm{diag}\{\cdots\}$ means diagonal matrix. The exact form of $f(\mathbf{K}', 0)$ is determined by the initial condition.

Of special importance is the fundamental solution of Eq. (5) or (6), i.e., the solution with an initial point charge distribution in phase space $\psi(\mathbf{X}, 0) = \delta(\mathbf{X} - \mathbf{X}_0)$. The evolution of a general charge distribution can then be obtained based on this fundamental solution through superposition. With $\psi(\mathbf{X}, 0) = \delta(\mathbf{X} - \mathbf{X}_0)$, we have $\mathcal{F}(\mathbf{K}, 0) = e^{-i\mathbf{KX}_0}$ and thus $\mathcal{F}(\mathbf{K}', 0) = e^{-i\mathbf{K}'\mathbf{PX}_0}$, from which we have

$$f(\mathbf{K}', 0) = e^{-i\mathbf{K}'\mathbf{PX}_0 - \sum_{ij}\frac{1}{2}\frac{\mathbf{D}'_{ij}}{\lambda_i+\lambda_j}\mathbf{K}'_i\mathbf{K}'_j}. \tag{9}$$

Denote $\mathbf{G}_{ij} \equiv -\frac{\mathbf{D}'_{ij}}{\lambda_i+\lambda_j}\left\{1 - \exp\left[(\lambda_i + \lambda_j)s\right]\right\}$, from Eq. (8) we then have

$$\mathcal{F}(\mathbf{K}', s) = e^{-i\mathbf{K}'\mathbf{\Lambda}\mathbf{PX}_0 - \frac{1}{2}\mathbf{K}'\mathbf{GK}'^T}. \tag{10}$$

Denote $\sigma \equiv \mathbf{P}^{-1}\mathbf{G}\left(\mathbf{P}^{-1}\right)^T$, we then have

$$\mathcal{F}(\mathbf{K}, s) = e^{-i\mathbf{K}\hat{\mathbf{R}}\mathbf{X}_0 - \frac{1}{2}\mathbf{K}\sigma\mathbf{K}^T}. \tag{11}$$

Note that here $\hat{\mathbf{R}}(s, 0) = e^{\int_0^s \mathbf{C}ds'} = \mathbf{P}^{-1}\mathbf{\Lambda P}$ is the deterministic transfer matrix with damping or antidamping. The above solution of $\mathcal{F}(\mathbf{K}, s)$ is the Fourier transform of a 6D Gaussian distribution given by

$$g(\mathbf{X}, \mathbf{X}_0, s) = \frac{\exp\left[-\frac{1}{2}\left(\mathbf{X} - \hat{\mathbf{R}}\mathbf{X}_0\right)^T\sigma^{-1}\left(\mathbf{X} - \hat{\mathbf{R}}\mathbf{X}_0\right)\right]}{(2\pi)^3\sqrt{\mathrm{Det}(\sigma)}}. \tag{12}$$

The above result is the fundamental solution of Eq. (5). It means the average phase space coordinate and second moments of an initial point distribution evolve according to

$$\begin{aligned} \langle\mathbf{X}\rangle(s) &= \hat{\mathbf{R}}(s, 0)\mathbf{X}_0, \\ \Sigma(s) &= \langle(\mathbf{X} - \bar{\mathbf{X}})(\mathbf{X} - \bar{\mathbf{X}})^T\rangle(s) = \sigma(s), \end{aligned} \tag{13}$$

with

$$\sigma(s) = \int_0^s \hat{\mathbf{R}}(s, s')\mathbf{D}(s')\hat{\mathbf{R}}^{\mathbf{T}}(s, s')ds'. \tag{14}$$

Note that

$$\lim_{s\to 0^+} g(\mathbf{X}, \mathbf{X}_0, s) = \delta(\mathbf{X} - \mathbf{X}_0). \tag{15}$$

If $\mathrm{Re}(\lambda_i) < 0$ for $i = 1 \sim 6$, then $\lim_{s\to+\infty}\hat{\mathbf{R}}(s, 0) = \mathbf{0}$ and

$$\lim_{s\to+\infty} g(\mathbf{X}, \mathbf{X}_0, s) = \frac{\exp\left(-\frac{1}{2}\mathbf{X}^T\sigma_\infty^{-\mathbf{1}}\mathbf{X}\right)}{(2\pi)^3\sqrt{\mathrm{Det}(\sigma_\infty)}}, \tag{16}$$

where $\sigma_\infty \equiv \mathbf{P}^{-1}\mathbf{G}_\infty\left(\mathbf{P}^{-1}\right)^T$ with $\mathbf{G}_{ij,\infty} \equiv -\frac{\mathbf{D}'_{ij}}{\lambda_i+\lambda_j}$.

The evolution of a general beam distribution is then given by the superposition principle

$$\psi(\mathbf{X}, s) = \int \psi(\mathbf{X}_0, 0)g(\mathbf{X}, \mathbf{X}_0, s)d\mathbf{X}_0, \tag{17}$$

from which we have

$$\mathcal{F}(\mathbf{K}, s) = \mathcal{F}(\mathbf{K}\hat{\mathbf{R}}, 0)e^{-\frac{\mathbf{K}\sigma\mathbf{K}^{\mathbf{T}}}{2}}. \tag{18}$$

With the above analysis done, the beam distribution can then be transported from element to element in a general coupled lattice. Generally we have

$$\mathcal{F}(\mathbf{K}, s) = \mathcal{F}(\mathbf{K}\hat{\mathbf{R}}, 0)e^{-\frac{\mathbf{K}\left(\int_0^{\mathbf{s}}\hat{\mathbf{R}}(\mathbf{s},\mathbf{s}')\mathbf{D}(\mathbf{s}')\hat{\mathbf{R}}^{\mathbf{T}}(\mathbf{s},\mathbf{s}')\mathbf{ds}'\right)\mathbf{K}^{\mathbf{T}}}{2}}, \tag{19}$$

and

$$\psi(\mathbf{X}, s) = \\ \int \psi(\mathbf{X}_0, 0)\frac{\exp\left[-\frac{1}{2}\left(\mathbf{X} - \hat{\mathbf{R}}\mathbf{X}_0\right)^T\sigma^{-1}(s)\left(\mathbf{X} - \hat{\mathbf{R}}\mathbf{X}_0\right)\right]}{(2\pi)^3\sqrt{\mathrm{Det}(\sigma(s))}}d\mathbf{X}_0. \tag{20}$$

Equations (19) and (20) are the main results of this section. Note that the above relations are accurate and hold for a general coupled linear lattice, arbitrary beam distribution in phase space, and does not require the beam to be Gaussian.

ELECTRON STORAGE RING PHYSICS

Now we apply the above analysis in electron storage ring physics. We will study the evolution of second moment matrix from s_1 to s_2 under the impact of damping and diffusion

$$\begin{aligned} \mathbf{\Sigma}(s_2) &= \int \mathbf{XX}^T\psi(\mathbf{X}, s_2)d\mathbf{X} \\ &= \hat{\mathbf{R}}(s_2, s_1)\mathbf{\Sigma}(s_1)\hat{\mathbf{R}}^{\mathbf{T}}(\mathbf{s_2}, \mathbf{s_1}) \\ &+ \int_{s_1}^{s_2}\hat{\mathbf{R}}(s_2, s')\mathbf{D}(s')\hat{\mathbf{R}}^{\mathbf{T}}(s_2, s')ds'. \end{aligned} \tag{21}$$

This result is usually known as the beam envelope method [6]. We point out that Eqs. (19) and (20) are more general and contain more information than the above evolution of second moments. In other words, we can derive Eq. (21) from Eq. (19) or (20), but not the other way around.

In an electron storage ring, the equilibrium state repeats turn-by-turn, which means

$$\begin{aligned}\mathbf{\Sigma}(s) &= \hat{\mathbf{M}}\mathbf{\Sigma}(s)\hat{\mathbf{M}}^{\mathbf{T}}+\\ &\int_s^{s+C_0}\hat{\mathbf{R}}(s+C_0,s')\mathbf{D}(s')\hat{\mathbf{R}}^T(s+C_0,s')ds',\end{aligned}\tag{22}$$

where $\mathbf{\Sigma}$ now is the equilibrium second moments matrix, $\hat{\mathbf{M}}$ is the one-turn map evaluated at s with damping around the ring considered. From this matrix equation, the equilibrium beam distribution can be solved.

Assuming that the damped one-turn map can be diagonalized as $\hat{\mathbf{M}} = \mathbf{V}\mathbf{U}\mathbf{V}^{-1}$, with $\mathbf{U}_{ii}$ = the eigenvalues of $\hat{\mathbf{M}}$, which means $\hat{\mathbf{M}}\mathbf{V} = \mathbf{V}\mathbf{U}$. Denote

$$\mathcal{D}(s) \equiv \int_s^{s+C_0}\hat{\mathbf{R}}(s+C_0,s')\mathbf{D}(s')\hat{\mathbf{R}}^T(s+C_0,s')ds',\tag{23}$$

then

$$\left(\mathbf{V}^{-1}\mathbf{\Sigma}(\mathbf{V}^{-1})^T\right)_{ij}(s) = \frac{\left[\mathbf{V}^{-1}\mathcal{D}(s)(\mathbf{V}^{-1})^T\right]_{ij}}{1-\mathbf{U}_{ii}\mathbf{U}_{jj}}.\tag{24}$$

After getting $\mathbf{\Sigma}' \equiv \mathbf{V}^{-1}\mathbf{\Sigma}(\mathbf{V}^{-1})^T$, we only need another transformation $\mathbf{V}\mathbf{\Sigma}'\mathbf{V}^T$ to get the equilibrium $\mathbf{\Sigma}$. In a linear lattice, the equilibrium beam distribution under the influence of damping and diffusion will tend to be Gaussian. For a Gaussian beam with $\langle\mathbf{X}\rangle = 0$, we have $\mathcal{F}(\mathbf{K},s) = e^{-\frac{\mathbf{K}\mathbf{\Sigma}(s)\mathbf{K}^T}{2}}$ with $\mathbf{\Sigma}(s) = \langle\mathbf{X}(s)\mathbf{X}^T(s)\rangle$ the second moments matrix of the beam. In this case, once we get the $\mathbf{\Sigma}$ matrix, the problem is solved. Under small damping approximation, the above result is consistent with Chao's SLIM formalism [7].

STRUCTURED PARTICLE BEAM

Now we apply the SFF for the description of more structured particle beams, for example the laser-induced microbunching. We assume the initial beam distribution is Gaussian: $\psi_0(\mathbf{X}) = \frac{1}{(2\pi)^3\sqrt{\mathrm{Det}(\mathbf{\Sigma_0})}}\exp\left(-\frac{1}{2}\mathbf{X}^T\mathbf{\Sigma_0^{-1}}\mathbf{X}\right)$.

One-Stage Energy Modulation

Laser-induced energy modulation: $\delta = \delta + A\sin(k_L z)$, with $k_L = \frac{2\pi}{\lambda_L}$ the laser wavenumber. Beam evolution after modulation: $\mathbf{X} = \mathbf{R}\mathbf{X}$, where $\mathbf{R}$ is the linear transfer matrix of the magnet lattice. Denote: $\mathbf{U}_p \equiv \begin{pmatrix}0 & 0 & 0 & 0 & pk_L & 0\end{pmatrix}$, $\mathbf{M}_p \equiv \mathbf{K}\mathbf{R} - \mathbf{U}_p$, $\mathbf{R}_{i6} \equiv \begin{pmatrix}R_{16} & R_{26} & R_{36} & R_{46} & R_{56} & R_{66}\end{pmatrix}^T$, Then the SFF after laser modulation and lattice transport is

$$\mathcal{F}(\mathbf{K}) = \sum_{p=-\infty}^{\infty} J_p\left(-\mathbf{K}\mathbf{R}_{i6}A\right)\exp\left(-\frac{\mathbf{M}_p\mathbf{\Sigma}_0\mathbf{M}_p^T}{2}\right),\tag{25}$$

where J_p is the p-th order Bessel function of the first kind. Note that damping and diffusion can also be taken into account following our analysis presented in last section.

Using the generalized Twiss matrices given in Ref. [8], we can write $\mathbf{\Sigma}_0 = \sum_{\kappa=I,II,III}\epsilon_\kappa\mathbf{T}_\kappa$, where ϵ_κ and $\mathbf{T}_\kappa$ are the eigen emittance the generalized Twiss matrix of the κ-th eigenmode at the beginning. For a periodic system like a storage ring, if $\mathbf{R} = \mathbf{T}_0^m$ with $\mathbf{T}_0$ the symplectic one-turn map, which means the beam traverses the ring for m revolutions after the laser modulation, then

$$\mathbf{M}_p\mathbf{\Sigma}_0\mathbf{M}_p^T = \sum_{\kappa=I,II,III}\epsilon_\kappa\left(\mathbf{K}\mathbf{T}_\kappa\mathbf{K}^T - 2\mathbf{K}\mathbf{R}\mathbf{T}_\kappa\mathbf{U}_p^T + \mathbf{U}_p\mathbf{T}_\kappa\mathbf{U}_p^T\right).\tag{26}$$

The above analysis can be applied in the proof-of-principle experiment of steady-state microbunching (SSMB) [9–11], for example to investigate the microbunching wavefront tilt and off-axis coherent radiation generation after laser modulation arising from transverse-longitudinal coupling [1].

Double-Stage Energy Modulations

First-stage laser modulation: $\delta = \delta + A_1\sin(k_1 z)$, with k_1 the wavenumber of first laser. Beam evolution after first modulation: $\mathbf{X} = \mathbf{R}_1\mathbf{X}$. Second-stage laser modulation: $\delta = \delta + A_2\sin(k_2 z + \phi)$. Beam evolution after second modulation: $\mathbf{X} = \mathbf{R}_2\mathbf{X}$. Denote: $\mathbf{U}_2 \equiv \begin{pmatrix}0 & 0 & 0 & 0 & m_2k_2 & 0\end{pmatrix}$, $\mathbf{M}_2 \equiv \mathbf{K}\mathbf{R}_2 - \mathbf{U}_2$, $\mathbf{U}_1 \equiv \begin{pmatrix}0 & 0 & 0 & 0 & m_1k_1 & 0\end{pmatrix}$, $\mathbf{M}_1 \equiv \mathbf{M}_2\mathbf{R}_1 - \mathbf{U}_1$, $\mathbf{R}_{1i6} \equiv \begin{pmatrix}R_{1,16} & R_{1,26} & R_{1,36} & R_{1,46} & R_{1,56} & R_{1,66}\end{pmatrix}^T$, $\mathbf{R}_{2i6} \equiv \begin{pmatrix}R_{2,16} & R_{2,26} & R_{2,36} & R_{2,46} & R_{2,56} & R_{2,66}\end{pmatrix}^T$. Following steps similar to above, the final SFF is

$$\begin{aligned}\mathcal{F}(\mathbf{K}) = \sum_{p_1=-\infty}^{\infty}\sum_{p_2=-\infty}^{\infty} & J_{p_1}\left(-\mathbf{M_2}\mathbf{R}_{1i6}A_1\right)e^{ip_2\phi}\\ & J_{p_2}\left(-\mathbf{K}\mathbf{R}_{2i6}A_2\right)\exp\left\{-\frac{\mathbf{M}_1\mathbf{\Sigma}_0\mathbf{M}_1^T}{2}\right\}.\end{aligned}\tag{27}$$

For a periodic system like a storage ring, if $\mathbf{R}_1 = \mathbf{T}_0^{m_1}$, $\mathbf{R}_2 = \mathbf{T}_0^{m_2}$ with $\mathbf{T}_0$ the one-turn map, then

$$\begin{aligned}\mathbf{M}_1\mathbf{\Sigma}_0\mathbf{M}_1^T = \sum_{\kappa=I,II,III}\epsilon_\kappa & \Big(\mathbf{K}\mathbf{T}_\kappa\mathbf{K}^T + \mathbf{U}_2\mathbf{T}_\kappa\mathbf{U}_2^T + \mathbf{U}_1\mathbf{T}_\kappa\mathbf{U}_1^T\\ & -2\mathbf{K}\mathbf{R_2}\mathbf{T}_\kappa\mathbf{U}_2^T - 2\mathbf{K}\mathbf{R_2}\mathbf{R_1}\mathbf{T}_\kappa\mathbf{U}_1^T + 2\mathbf{U_2}\mathbf{R_1}\mathbf{T}_\kappa\mathbf{U}_1^T\Big).\end{aligned}\tag{28}$$

Similar procedures can be applied to derive the SFF for even more multiple-stage modulations.

Representative examples of the above single-stage and double-stage energy modulation-based laser-induced microbunching schemes are HGHG [12] and EEHG [13], respectively. Based on the above derivations and more calculations, we have proposed to do EEHG at the MLS storage ring using the SSMB proof-of-principle experiment setup [10,11]. We can use different revolution numbers to play the role of different R_{56} in the two-stage dispersions of EEHG. For example, we can fire the first-shot laser and wait for $2n+1$ revolutions, and then we fire the second-shot laser and then wait for 2 revolutions. Finally we can generate high harmonic bunching at the $m \times n$-th laser harmonic.

ISBN: 978-3-95450-279-0 ISSN: 3043-0208 doi: 10.18429/JACoW-SAP2025-THP42

SUMMARY

In this paper, spectral form function (SFF) has been presented as a tool to study beam dynamics. More interesting work on this is ongoing and will be reported in the future.

The author thanks Alex Chao for helpful discussion.

REFERENCES

[1] X. Deng, *Theoretical and experimental studies on steady-state microbunching*. Singapore: Springer Nature, 2024. `doi:10.1007/978-981-99-5800-9`

[2] E. Hemsing *et al.*, "Helical electron-beam microbunching by harmonic coupling in a helical undulator", *Phys. Rev. Lett.*, vol. 102, no. 17, p. 174801, Apr. 2009. `doi:10.1103/PhysRevLett.102.174801`

[3] N. A. Yampolsky, "Dynamics of modulated beams in spectral domain", *Nucl. Instrum. Methods Phys. Res. A*, vol. 870, pp. 163–173, Oct. 2017. `doi:10.1016/j.nima.2017.07.008`

[4] R. Tabar, *Analysis and data-based reconstruction of complex nonlinear dynamical systems*. Cham, Switzerland: Springer, 2019. `doi:10.1007/978-3-030-18472-8`

[5] M. C. Wang, and G. E. Uhlenbeck, "On the theory of the Brownian motion II", *Rev. Mod. Phys.*, vol. 17, no. 2-3, pp. 323–342, Apr. 1945. `doi:10.1103/RevModPhys.17.323`

[6] K. Ohmi, K, Hirata, and K. Oide, "From the beam-envelope matrix to synchrotron-radiation integrals", *Phys. Rev. E*, vol. 49, no. 1, pp. 751–765, Jan. 1994. `doi:10.1103/PhysRevE.49.751`

[7] A. W. Chao, "Evaluation of beam distribution parameters in an electron storage ring", *J. Appl. Phys.*, vol. 50, no. 2, pp. 595–598, 1979. `doi:10.1063/1.326070`

[8] X. Deng *et al.*, "Steady-state micro-bunching based on transverse-longitudinal coupling", *Nucl. Sci. Tech.*, to be published. `doi:10.48550/arXiv.2404.06920`

[9] D. F. Ratner and A. W. Chao. "Steady-state microbunching in a storage ring for generating coherent radiation", *Phys. Rev. Lett.*, vol. 105, no. 15, p. 154801, Oct. 2010. `doi:10.1103/PhysRevLett.105.154801`

[10] X. Deng *et al.*, "Experimental demonstration of the mechanism of steady-state microbunching", *Nature*, vol. 590, no. 7847, pp. 576–579, Feb. 2021. `doi:10.1038/s41586-021-03203-0`

[11] A. Kruschinski *et al.*, "Confirming the theoretical foundation of steady-state microbunching", *Commun. Phys.*, vol. 7, no. 1, p. 160, May 2024. `doi:10.1038/s42005-024-01657-y`

[12] L. H. Yu, "Generation of intense uv radiation by subharmonically seeded single-pass free-electron lasers", *Phys. Rev. A*, vol. 44, no. 8, pp. 5178–5193, Oct. 1991. `doi:10.1103/PhysRevA.44.5178`

[13] G. Stupakov, "Using the beam-echo effect for generation of short-wavelength radiation", *Phys. Rev. Lett.*, vol. 102, no. 7, p. 074801, Feb. 2009. `doi:10.1103/PhysRevLett.102.074801`

ISBN: 978-3-95450-279-0 ISSN: 3043-0208 doi: 10.18429/JACoW-SAP2025-THP44

PHYSICAL DESIGN STUDY OF THE MAIN MAGNET FOR THE CIAE 75 MeV CYCLOTRON*

JinRong Lu †, TianJian Bian, ShiZhong An, SuMin Wei, LuYu Ji
China Institute of Atomic Energy, Beijing, China

Abstract

A 75 MeV cyclotron is currently under development at the China Institute of Atomic Energy (CIAE). This cyclotron is designed to extract a beam with a rated power exceeding 60 kW for the production of medical radioisotopes, such as ^{68}Ge, ^{223}Ra, and ^{225}Ac, aiming to meet the growing domestic demand for diagnostic and therapeutic radionuclides. This paper addresses key challenges and solutions in the design and computational analysis of the main magnet. The magnet poles adopt a structural design scheme featuring integrated straight-edged sectors with a slight spiral angle at the trailing edges. The isochronous magnetic field distribution is achieved through an axial shimming method. Magnetic field optimization was performed using the numerical simulation software OPERA-3D, thereby enhancing the acceleration efficiency of the cyclotron. Furthermore, deformation simulation and mechanical structural optimization were carried out for the main magnet. Under the premise of ensuring overall performance, the deformation of the main magnet—which has a diameter of 4.4 meters and a weight of 130 tons—was controlled within acceptable engineering tolerances.

INTRODUCTION

CIAE has been a pioneer in the development of cyclotrons in China. Over decades of progress, it has successfully designed and constructed a series of high-intensity cyclotron facilities. Building upon the team's extensive experience and technical foundation in cyclotron technology, we propose the design and construction of a new high-intensity cyclotron capable of delivering an extracted beam of 75 MeV with a current of 800 μA.

This cyclotron will employ an external ion source for high-current beam injection. Through the implementation of high-efficiency injection and extraction systems, highly stable automated magnetic field mapping, and high-precision axial shimming techniques, the machine is designed to achieve low beam loss. Furthermore, an optimized compact structure significantly reduces the overall size and weight of the machine, improving both integration and engineering feasibility.

MAGNET DESIGN

The main magnet system constitutes one of the key subsystems of the cyclotron. Its physical design follows an iterative optimization process based on beam dynamics requirements, aiming to ensure that the magnetic field distribution satisfies fundamental beam dynamics conditions. The system adopts a four-fold symmetric structure. The magnet poles are designed as straight-sided sectors, which not only enhances the overall symmetry of the cyclotron but also facilitates the design and installation of critical components such as the central region.

At large radii, a specific spiral angle is introduced on the pole sides to strengthen the axial focusing capability in this region, thereby preventing the particle working orbit from crossing dangerous resonance lines. This design allows for an increase in the pole angular width by reducing the magnetic flutter, which in turn raises the average magnetic field strength and ultimately contributes to the compactness of the machine. The actual pole angle in this design is set to 53°. Furthermore, the influence of the Lorentz force-induced stripping effect on beam loss must be considered during the magnetic field design process, the peak magnetic field is limited to below 1.55 T. To avoid breakdown risks in the central region electrode structure and to provide sufficient space for an automated field mapping system, the hill gap in this design has been significantly enlarged compared to previous high-intensity cyclotrons. The hill gap ranges from 3.8 cm to 4.6 cm and features an elliptical profile to improve the pole utilization efficiency.

The total weight of the main magnet system (including shimming bars) for this high-intensity cyclotron is 130 tons, with overall dimensions of 4.3 m (length) × 4.3 m (width) × 1.56 m (height). The system specifically comprises 2 cover plates, 4 return yokes, 8 magnet poles, 8 shimming bars, and 2 central region core columns. The detailed structure is shown in Fig.1, and the dimensional parameters are listed in Table 1.

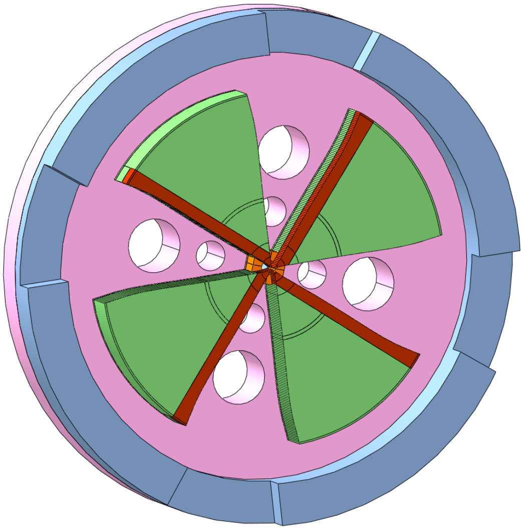

Figure 1: A top view on the 75MeV Cyclotron of CIAE.

---

* Work supported by the National Natural Science Foundation of China (Grant No.12105370)

† 359037465@qq.com.

ISBN: 978-3-95450-279-0 ISSN: 3043-0208 doi: 10.18429/JACoW-SAP2025-THP44

Table 1: Specifications of the 75 MeV Cyclotron

Parameters	**Value**	**Parameters**	**Value**
Energy	75 MeV	Current	800 µA
Pole radius	1.485 m	Hill gap	38-46 mm
Magnetic field range	0.2-1.55 T	RF frequency	53.3 MHz
RF harmonic	4rd harmonic	No. of dees	2
Ampere turns	31000 At	Weight	130 t

Electromagnetic field simulations for the main magnet of the 75 MeV cyclotron were carried out using the three-dimensional finite element analysis software OPERA-3D. To improve computational efficiency, a 1/8-scale model of the magnet was constructed leveraging the structural symmetry. Figure 2 shows the hybrid tetrahedral/hexahedral mesh and the distribution of magnetization intensity within the main magnet.

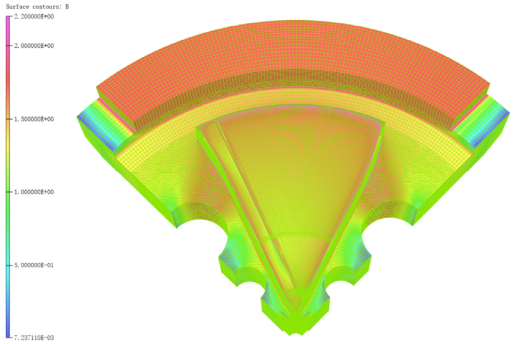

Figure 2: The hybrid tetrahedral/hexahedral mesh and the distribution of magnetization intensity.

Numerical simulations were employed to optimize the dimensional parameters of key components of the main magnet, including: the pole angular width, the offset of the poles relative to the geometric center of the machine, the pole height and radius, the thickness of the cover plates, the position and size of openings in the cover plates (for vacuum pumping, RF cavity installation, and various diagnostic and coupling devices), the ampere-turns and layout dimensions of the coils, the height and shape of the shimming bars, the profiled head structure of the shimming bars, as well as the dimensions and position of the core columns. Based on a comprehensive analysis of the influence of these components on the magnetic performance of the main magnet, a multi-objective optimization design of the magnet was completed, taking into account the integration and compatibility between the main magnet and other systems of the cyclotron [1].

After multiple iterations of optimization, the final magnetic field distribution meeting the design requirements was obtained. Figure 3 presents the magnetic field distribution in the mid-plane of the cyclotron; Fig. 4 displays the average magnetic field as a function of radius and the magnetic flutter distribution after axial shimming of the shimming bars.

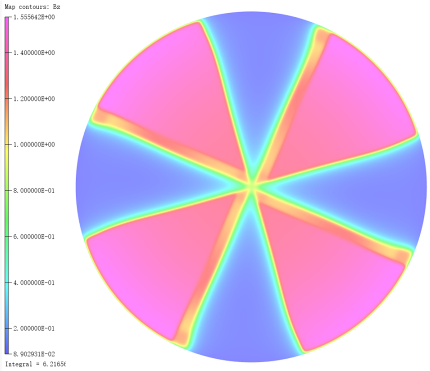

Figure 3: The magnetic field distribution in the mid-plane of the cyclotron.

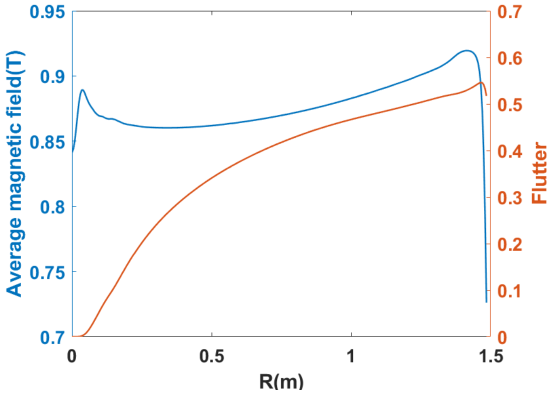

Figure 4: The average magnetic field as a function of radius and the magnetic flutter distribution.

An optimization of the deformation behavior of the main magnet for the cyclotron was carried out. The results indicate that the electromagnetic force is the primary factor contributing to the magnet deformation, while the effects of vacuum force and gravitational force are relatively minor. After optimizing the design of the magnet cover plates and return yokes, as shown in Fig. 5， the maximum deformation of the main magnet was controlled within 100 µm, the largest deformation, measuring 90 µm, was located at the pole tip region.

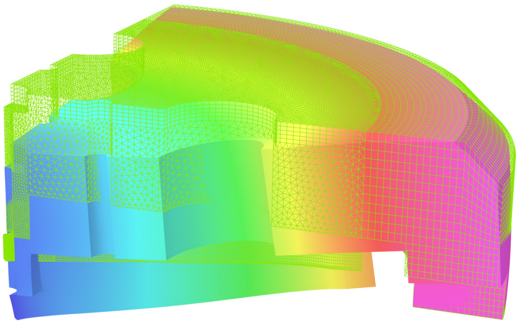

Figure 5: Deformation of cyclotron magnet.

ISBN: 978-3-95450-279-0 ISSN: 3043-0208 doi: 10.18429/JACoW-SAP2025-THP44

BEAM DYNAMICS CALCULATION

Numerical simulations of the magnetic field distribution in the cyclotron were performed using the beam dynamics code CYCLOP, yielding the static equilibrium orbits and the corresponding differential phase slip, expressed as $(\omega_0/\omega - 1) \times 1000$, where ω_0 is the reference cyclotron angular frequency and ω is the actual angular frequency at a specific energy [2]. The calculated equilibrium orbits for various energies are shown in Fig. 6.

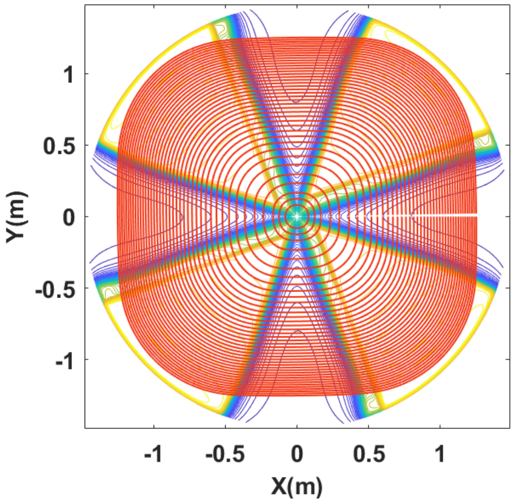

Figure 6: equilibrium orbits for various energies of the cyclotron.

Isochronism and transverse focusing properties are two key indicators for evaluating the quality of the magnetic field design in a cyclotron. During the physical design of the main magnet, the shape of the shimming bars and the angular width of the poles were optimized through iterative calculations of the equilibrium orbits, thereby satisfactorily meeting the requirements for an isochronous magnetic field. Figure 7 shows the resulting isochronism error and the static integrated phase slip distribution.

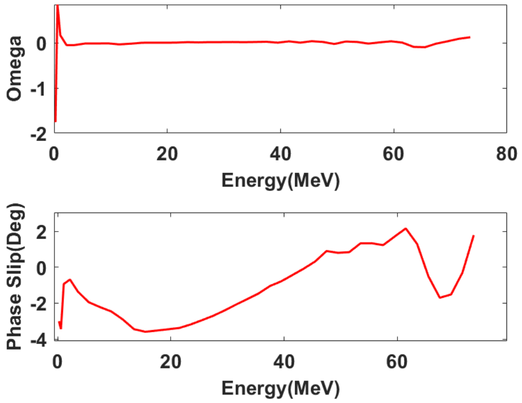

Figure 7: isochronism error and the static integrated phase slip distribution.

The transverse tune values are presented in Fig. 8, respectively. By adopting a variable-gap pole structure, the axial focusing frequency at large radii was enhanced, allowing the particle working path to cross the Walkinshaw resonance only once in the low-energy region. This effectively suppressed transverse phase-space coupling and avoided major harmful resonance lines.

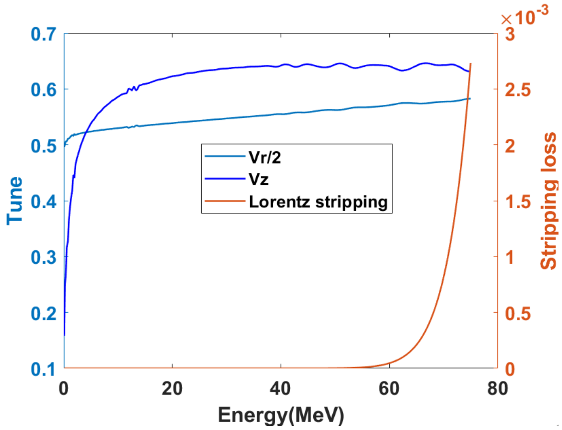

Figure 8: The transverse tune values and Lorentz stripping loss.

Negative ions such as H⁻ and D⁻, when accelerated to high energies, are susceptible to Lorentz stripping due to their low electron binding energies (0.75 eV for H⁻). Under strong magnetic fields, the equivalent electric field may strip additional electrons, converting the ions into neutral atoms and resulting in beam loss. To mitigate such losses, the peak magnetic field strength was limited, and the energy gain per turn was increased in the main magnet design. As shown in Fig. 8 calculations indicate that the beam loss rate due to Lorentz stripping at 75 MeV is approximately 0.3%, which is within an acceptable range for engineering purposes.

CONCLUSION

This paper presents a systematic study on the physical and engineering design of the main magnet for a 75 MeV high-intensity cyclotron. By optimizing the spiral angle at the pole tip, the axial focusing property of the magnetic field was effectively improved, thereby avoiding beam crossing of harmful resonances and enhancing beam stability. Integrating structural deformation simulation with magnetic saturation optimization, a lightweight magnet design was realized without compromising magnetic performance. Beam dynamics simulations demonstrate that the main magnet design meets the requirements of high-intensity and high-power operation in terms of isochronism, focusing characteristics, and mechanical stability.

REFERENCES

[1] W. Kleeven *et al.*, “Recent development and progress of IBA cyclotrons”, *Nucl. Instrum. Methods Phys. Res. B*, vol. 269, no. 24, pp. 2857–2862, Dec. 2011. `doi:10.1016/j.nimb.2011.04.031`

[2] M. M. Gordon, “Computation of closed orbits and basic focusing properties for sector-focused cyclotrons and the design of ‘cyclops’”, *Part. Accel.*, vol. 16, pp. 39-62, 1984.

REAL-TIME COMPREHENSIVE ELECTRON BEAM DIAGNOSTICS THROUGH MACHINE LEARNING IN ULTRAFAST ELECTRON DIFFRACTION SYSTEM

Jiapeng Li, Cheng-Ying Tsai[*], Kuanjun Fan, School of Electrical and Electronic Engineering,
Huazhong University of Science and Technology, Wuhan, China

Abstract

Mega-electron-volt (MeV) ultrafast electron diffraction (UED) is a powerful technique for observing atomic-scale structural dynamics in materials. Electron beam parameters, e.g., beam size, divergence, energy spread, and bunch length, determine spatio-temporal resolution. Traditional diagnostic methods require complex instrumentation that cannot be integrated into routine workflows, particularly for high-repetition-rate facilities. We present a machine learning approach enabling comprehensive, non-invasive extraction of electron beam parameters directly from diffraction patterns. Deep neural networks trained on physics-based simulations decode signatures that beam parameters imprint on diffraction images. The method exploits distinct physical mechanisms: geometric effects from beam size, angular distortions from divergence, chromatic aberrations from energy spread, and temporal convolution from bunch length. This enables bunch length measurement without dedicated temporal diagnostics — traditionally one of the most challenging parameters to access non-invasively. The trained models can be deployed across UED facilities using standard imaging detectors, democratizing access to advanced diagnostics. This approach eliminates expensive specialized equipment and enables real-time beam monitoring and optimization, enhancing experimental throughput and data quality for ultrafast materials characterization.

INTRODUCTION

MeV ultrafast electron diffraction (UED) [1–3] employs the pump-probe technique to observe atomic-scale dynamic processes with femtosecond temporal resolution. Experimental success will depend highly on electron beam quality, including beam size, divergence, energy spread, and bunch length. Existing machine learning methods only predict partial beam parameters [4–7], with bunch length measurement being particularly challenging. This work employs deep learning to directly extract all the bunch parameters from diffraction images, based on physical correlations between diffraction features and electron beam parameters, achieving the first non-invasive bunch length measurement and providing real-time diagnostic tools for UED facilities.

SETUP OF MACHINE PARAMETERS

Based on the MeV UED under construction at Huazhong University of Science and Technology [8–13], the system employs a 1.4-cell photocathode RF gun, driven by 266-nm ultraviolet laser to generate photoelectrons from a copper cathode. The 2856-MHz RF cavity provides an accelerating gradient of 76.6 MV/m, accelerating the electron beam to 3 MeV. The beam transport line features a solenoid lens positioned 0.2-m downstream of the cathode to compensate for space charge effects and control the transverse beam size at the sample position. After traversing a 1-m drift distance, the electron beam impinges on a polycrystalline aluminum sample, forming distinct diffraction ring patterns on the detector downstream. To systematically investigate the correlation between bunch parameters and diffraction images, we employed the ASTRA particle tracking simulations [14] with the diffraction utilizing the familiar polycrystalline aluminum sample. The initial bunch charge was set to 1 pC, using 5×10^4 macroparticles to adequately account for space charge effects. By adjusting key parameters including the laser spot size, RF phase, and laser pulse duration, we systematically swept the complete parameter space relevant to the experiment, including the transverse horizontal and vertical beam sizes from 0.014 to 1.28 mm, the transverse horizontal and vertical beam divergences from 0.005 to 3.33 mrad, the bunch length ranging from 96.2 to 546 fs, and the energy spread varying from 2.387 to 23 keV.

NUMERICAL METHOD

Diffraction images contain rich bunch parameter information. Transverse beam size broadens diffraction rings through geometric convolution effects; beam divergence causes the final electron momentum to be the vector sum of transverse momentum and diffraction momentum transfer, resulting in image displacement and distortion; energy spread produces radial blurring in higher-order rings through Bragg angle dispersion; bunch length measurement is based on pump-probe principles. A complete diffraction image generation workflow is developed based on kinematic diffraction theory, calculating scattering probability distributions through elastic scattering theory and determining relative intensities of diffraction rings according to structure factors. More specifically, finite bunch length modifies dynamic curves through temporal convolution, causing slower decay edges and reduced oscillation amplitudes in diffraction intensity changes. Detailed analysis of temporal evolution curve characteristics enables bunch length reconstruction and can in principle achieve the non-invasive bunch length measurement based on diffraction images.

Figure 1 illustrates our numerical methodology: impact of electron beam on the sample generates diffraction images, with neural networks extracting bunch parameters. Two spe-

---

[*] Email: jcytsai@hust.edu.cn

ISBN: 978-3-95450-279-0 ISSN: 3043-0208 doi: 10.18429/JACoW-SAP2025-FRMC6

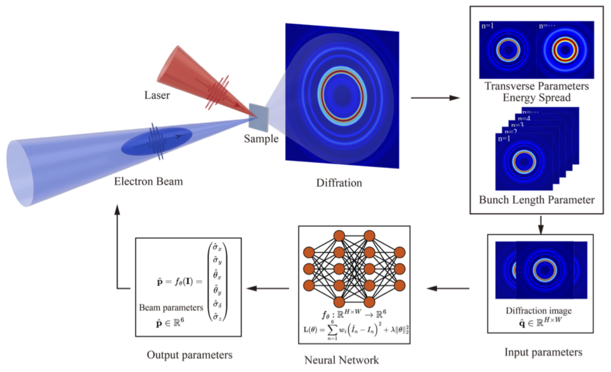

Figure 1: Schematic diagram of bunch parameter reconstruction based on diffraction images. The electron beam probes a polycrystalline aluminum sample to generate diffraction rings. A ResNet-35 network extracts transverse beam size, divergence angle, and energy spread from single-frame diffraction images. The bunch length is determined by analyzing multiple diffraction images at different pump-probe delays.

cialized ResNet-35 architectures [15] are employed: the prediction network for transverse parameters and energy spread accepts inputs from a series of normalized single-frame diffraction images, extracting features through 7 × 7 convolutional layers and residual blocks to output five parameter values; the prediction network for bunch length adopts inputs from series of diffraction images at different pump-probe time delays, analyzing image variations across multiple delay times from −200 to +2000 fs to learn how bunch length affects the dynamic curves of time-resolved diffraction.

To intuitively demonstrate the effects of bunch parameters on diffraction images, Fig. 2 presents simulation results under different conditions. Comparing Fig. 2(a) and (b), significant differences in diffraction ring width are observed when transverse parameters change, validating the physical mechanism by which transverse size affects diffraction patterns through convolution effects. Figures 2(c) and (d) demonstrate the influence of bunch length on time-resolved diffraction: under the same 500 fs pump-probe delay, the shorter bunch of 55 fs (Fig. 2(c)) and the longer bunch of 220 fs (Fig. 2(d)) produce distinctly different diffraction images, with clear changes in diffraction rings visible in the insets. The longer bunch alters response characteristics through temporal convolution effects. These simulation results validate our physical model and provide rich feature information for neural network training.

SIMULATION RESULTS

The deep learning model demonstrates excellent performance in bunch parameter prediction. Results from 7680 test samples show all parameters tightly distributed along the ideal 1:1 line (see Fig. 3). Beam size prediction achieves micrometer-level precision: x-direction MAE (mean absolute error) of 2.104 µm and y-direction MAE of 2.145 µm, with $R^2 > 0.9996$ and relative errors of 2.1–2.3 %. For transverse divergence prediction, x-direction MAE is 5.166 µrad and y-direction MAE is 4.861 µrad, with $R^2 > 0.9997$ and relative errors of 2.2–2.3 %. Energy spread prediction yields MAE of 98.5 eV, $R^2 = 0.99988$, and 1.8 % relative error, corresponding to 3.4 e−5 relative energy resolution. High-density regions concentrate in typical UED experimental operating ranges, where the model performs optimally. Training curves demonstrate stable convergence with loss functions stabilizing at the 10^{-5} level, showing no over-fitting.

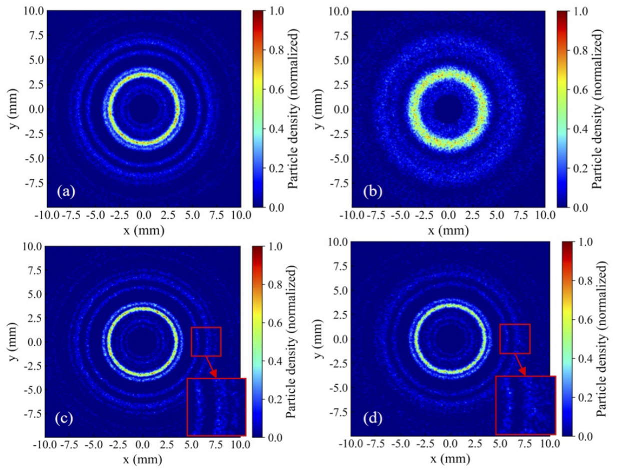

Figure 2: Effects of different bunch parameters on diffraction images. (a) $\sigma_x \approx \sigma_y \approx 0.1$ mm, $\sigma'_x \approx \sigma'_y \approx 0.05$ mrad, $\Delta E \approx 3$ keV; (b) $\sigma_x \approx \sigma_y \approx 0.1$ mm, $\sigma'_x \approx \sigma'_y \approx 0.15$ mrad, $\Delta E \approx 3$ keV; (c) time-resolved diffraction image of a 55-fs bunch at delay time 500 fs, with the inset showing distinct changes in diffraction rings; (d) diffraction image of a 220-fs bunch at the same delay time 500 fs, with the inset showing significantly smoother temporal response and changes in the center and width of diffraction rings. The color scale represents normalized particle density.

Bunch length measurement represents the innovative aspect of this work. Traditional methods such as using RF-deflecting cavities are costly and invasive, while using coherent transition radiation (CTR) or Smith-Purcell radiation (SPR) requires specialized radiation collection systems. We achieve the non-invasive measurement based on time-resolved diffraction, utilizing laser heating dynamic processes. The ResNet-35 architecture analyzes diffraction image sequences at different pump-probe delays, learning correlations between bunch length and time-resolved dynamics. This, as shown in Fig. 4, achieves a normalized MAE of 0.01480 and $R^2 = 0.99599$, with absolute error of approximately 8.7 fs in the 96.2–546 fs range, already sufficient for femtosecond experiments.

SUMMARY AND OUTLOOK

In this work we successfully develop a deep learning-based non-invasive bunch parameter diagnostic method, achieving the first simultaneous extraction of six-dimensional phase space information from electron diffraction images. The advantages of this method include: no additional hardware requirements, utilizing standard

ISBN: 978-3-95450-279-0 ISSN: 3043-0208 doi: 10.18429/JACoW-SAP2025-FRMC6

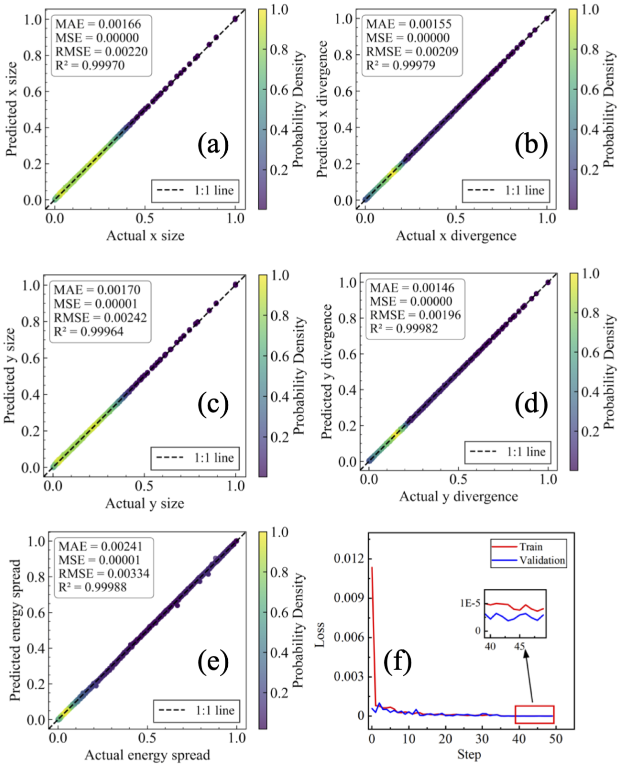

Figure 3: Prediction results of the beam transverse parameters and energy spared. (a) Beam size in x direction; (b) divergence angle in x direction; (c) beam size in y direction; (d) divergence angle in y direction; (e) energy spread. Scatter point colors represent probability density (purple-low, yellow-high), with dashed lines indicating the 1:1 ideal line. Error metrics, including MAE, mean squared error (MSE) and root mean squared error (RMSE) and coefficient of determination R^2 are annotated in each plot. (f) Training (red) and validation (blue) loss curves, with inset showing local magnification of steps 40–50, demonstrating model convergence at the 10^{-5} level. All parameters have been normalized.

MeV UED setups; simultaneous measurement with transverse parameters, enabling six-dimensional bunch characterization; reusable samples through heating rather than melting, avoiding sample damage.

To verify the sensitivity to time-of-flight jitter on the proposed method, we artificially added Gaussian-distributed temporal jitter with $\sigma = 100$ fs (simulating synchronization jitter in actual systems) in ASTRA simulations. The prediction accuracy showed no significant change, indicating that this method is insensitive to time-of-flight jitter and suitable for application in real experimental environments. It should be noted that the aforementioned precision is obtained under ideal simulation conditions; actual experimental performance may be degraded due to factors such as detector noise and mechanical vibrations. More work can be found in our subsequent publications.

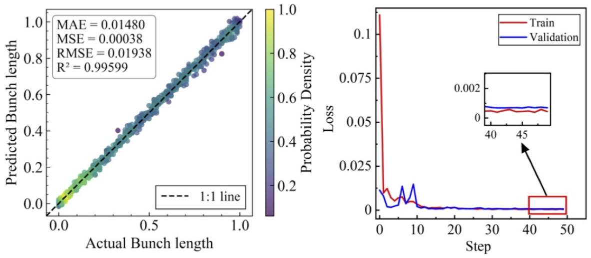

Figure 4: Prediction results of the bunch length. (Left) Comparison between predicted and actual bunch length values on the test set. Scatter point colors represent probability density distribution, with the dashed line indicating the ideal 1:1 correspondence. Normalized MAE = 0.01480, corresponding to an actual error of approximately 8.7 fs, with $R^2 = 0.99599$. (b) Loss function evolution during model training, with red line showing training loss and blue line showing validation loss. The inset displays local magnification of steps 40–50, with loss stabilizing around 0.002, indicating good model convergence. Bunch length parameters have been normalized to the 0–1 range (actual range 96.2–546 fs).

As future considerations, to enhance the model's capability, we will consider adopting transfer learning strategies, utilizing small amounts of experimental data to fine-tune pre-trained models for adaptation to specific characteristics of different facilities. At the algorithmic level, uncertainty quantification methods will be introduced to provide confidence intervals for each predicted parameter, enhancing the interpretability of diagnostic results. Moreover through integration with accelerator control systems, this intelligent diagnostic tool may enable adaptive beam optimization, automatically adjusting key parameters, such as RF phase based on real-time diagnostic results, ultimately establishing a closed-loop control system of "measurement-analysis-optimization." This diagnostic approach, integrating physical mechanisms with artificial intelligence, will provide more stable and efficient beam quality assurance for UED experiments, promoting its greater role in frontier research areas such as material dynamics and chemical reaction mechanisms.

ACKNOWLEDGMENT

This work is supported by the Fundamental Research Funds for the Central Universities (HUST) under Project No. 2021GCRC006 and National Natural Science Foundation of China under project No. 12275094.

REFERENCES

[1] S.P. Weathersby *et al.*, "Mega-electron-volt ultrafast electron diffraction at SLAC National Accelerator Laboratory", *Rev. Sci. Instrum.*, vol. 86, p. 073702, 2015. doi:10.1063/1.4926994

[2] J.B. Hastings *et al.*, "Ultrafast time-resolved electron diffraction with megavolt electron beams", *App. Phys. Lett.*, vol. 89, p. 184109, 2006. doi:10.1063/1.2372697

[3] D. Filippetto *et al.*, "Ultrafast electron diffraction: Visualizing dynamic states of matter", *Rev. Mod. Phys.*, vol. 94, p. 045004,

2022. doi:10.1103/RevModPhys.94.045004

[4] Z. Zhang *et al.*, “Accurate prediction of mega-electron-volt electron beam properties from UED using machine learning”, *Sci. Rep.*, vol. 11, p. 13890, 2021. doi:10.1038/s41598-021-93341-2

[5] Z. Zhang *et al.*, “Toward fully automated UED operation using two-stage machine learning model”, *Sci. Rep.*, vol. 12, p. 4240, 2022. doi:10.1038/s41598-022-08260-7

[6] F. Ji *et al.*, “Multi-objective Bayesian active learning for MeV-ultrafast electron diffraction”, *Nat. Comm.*, vol. 15, p. 4726, 2024. doi:10.1038/s41467-024-48923-9

[7] Z. Chen *et al.*, “Panoramic Mapping of Phonon Transport from Ultrafast Electron Diffraction and Scientific Machine Learning”, *Adv. Mater.*, vol. 35, p. 2206997, 2023. doi:10.1002/adma.202206997

[8] C.-Y. Tsai *et al.*, “Low-energy high-brightness electron beam dynamics based on slice beam matrix method”, *Nucl. Instrum. Methods Phys. Res. A*, vol. 937, pp. 1–20, 2019. doi:10.1016/j.nima.2019.05.035

[9] Y. Song *et al.*, “Development of a 1.4-cell RF photocathode gun for single-shot MeV ultrafast electron diffraction devices with femtosecond resolution”, *Nucl. Instrum. Methods Phys. Res. A*, vol. 1031, p. 166602, 2022. doi:10.1016/j.nima.2022.166602

[10] Y. Xu *et al.*, “Manipulation and diagnosis of femtosecond relativistic electron bunch using terahertz-driven resonators”, *Nucl. Eng. Technol.*, vol. 56, no. 10, pp. 4237–4246, 2024. doi:10.1016/j.net.2024.05.029

[11] H. Qi *et al.*, “Observation of THz surface waves escaping from metal gratings through a dielectric substrate”, *Opt. Express*, vol. 32, pp. 23180–23192, 2024. doi:10.1364/OE.525614

[12] H. Qi *et al.*, “Self-synchronized ultrafast electron beam diagnostics using a split-ring resonator driven by multicycle THz pulses”, *Nucl. Eng. Technol.*, vol. 57, p. 103434, 2025. doi:10.1016/j.net.2025.103434

[13] Y. Xu *et al.*, “Towards precise diagnosis time profile of ultrafast electron bunch trains using orthogonal terahertz streak camera”, *Opt. Express*, vol. 31, pp. 19777–19793, 2023. doi:10.1364/OE.488132

[14] ASTRA: a space charge tracking algorithm, `https://www.desy.de/~mpyflo/`

[15] K. He *et al.*, “Deep residual learning for image recognition”, in *2016 Conference on Computer Vision and Pattern Recognition (CVPR)*, Las Vegas, NV, USA, Jun. 2016, pp. 770–778. doi:10.1109/CVPR.2016.90

THE START-TO-END BEAM DYNAMICS SIMULATION STUDY AND ITS APPLICATION IN THE HIGH-INTENSITY CYCLOTRON OF CIAE*

Tianjian Bian†, Fengping Guan, Shizhong An, Sumin Wei, Luyu Ji, Jinrong Lu, Lin Dai, Ruijin Liu, Yuzhuo Huang, Peng Huang, China Institute of Atomic Energy, Beijing, China

Abstract

The beam dynamics simulation technology for cyclotrons is relatively mature, however, it is typically implemented independently in each subsystem and assumed initial conditions are introduced multiple times, making it difficult to obtain quantitative results and carry out a global optimized design. Precise and quantitative start-to-end beam dynamics simulations facilitate a better understanding of the complex beam dynamics behaviours, which is one of the key technologies for high-intensity accelerators. In this paper, start-to-end (S2E) beam-dynamics simulations are performed for an 18 MeV/1 mA high-intensity cyclotron. Every subsystem, the injection line, spiral inflector, central region, acceleration region, extraction region and uniform beam-transport line, is modelled quantitatively. Furthermore, the central region is optimized by S2E method and the resulting gain in beam performance is evaluated.

INTRODUCTION

The neutron yield of the neutron source based on the 18 MeV/1 mA high-intensity cyclotron developed by the China Institute of Atomic Energy (CYCIAE-18) has reached 7×10^{13} n/s and has been successfully applied in high-resolution neutron imaging and Boron Neutron Capture Therapy (BNCT) experiments. In high-intensity cyclotrons, global optimisation of beam dynamics and minimisation of beam loss are essential. Traditionally, cyclotron beam-dynamics simulations are usually performed section-by-section with assumed initial conditions. Although efficient, this approach introduces cumulative errors that prevent quantitative analysis in high-intensity, beam-loss-sensitive machines.

Start-to-end (S2E) simulations provide high-fidelity predictions of accelerator performance and enable global optimisation [1]. The S2E method are used to simulate the beam dynamics of CYCIAE-18, includes injection line, spiral inflector, central region, acceleration and extraction region, uniform beamline, etc. Based on S2E method, the radial-phase space as a metric is proposed to optimise the central region for higher beam quality and the corresponding improvement in beam performance is evaluated. Furthermore, this paper proposes a uniform beamline based on combined-function quadrupole-octupole magnets, and experimental results show 83% uniformity.

INJECTION LINE

The injection beamline focuses and bunches the 35 keV beam from the H^- ion source. The CYCIAE-18 employs two solenoids with a buncher positioned between them. For high-intensity beams, the space-charge effect is significant in the injection line, so solenoid fields of more than 2000 Gs is required to counteract it. The normalized emittance at the ion source is 0.240 π mm·mrad. With increasing the current, nonlinear space-charge forces drive emittance growth at the injection line exit, as shown in Figure 1. At 5 mA, the emittance reaches 0.274 π mm·mrad.

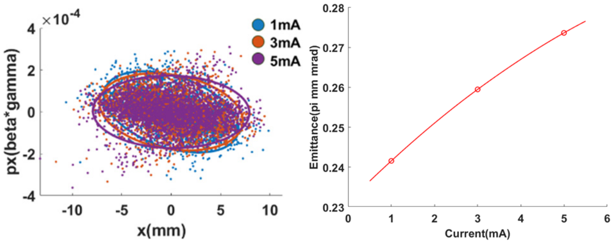

Figure 1: Phase space (left plot) and the emittance growth as function of current (right plot).

Six-dimensional phase space coordinates at the injection-line exit provide the initial conditions for the spiral inflector simulation.

SPIRAL INFLECTOR

The spiral inflector bends the axially injected beam into the median plane. The axial defocusing and longitudinal stretching inside it cause beam loss and quality degradation. Figure 2 illustrates the longitudinal defocusing effect: (a) shows the longitudinal phase space at the inflector inlet and outlet, and (b) the particle-density distribution in phase. The inflector electric field increases the energy spread and flattens the particle-density peak, thereby reducing the beam capture efficiency in central region.

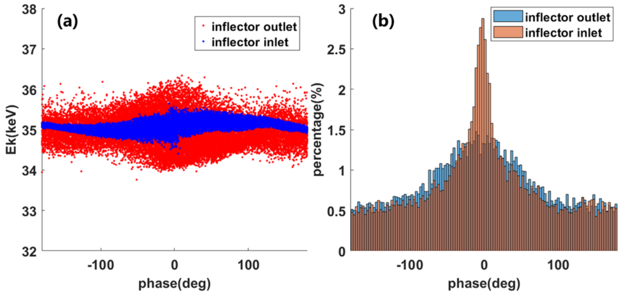

Figure 2: The longitudinal phase space (a) and the particle-density distribution (b).

---

* Work supported by Sustained Support Research Project (Grant No. BJ040261224908), the National Natural Science Foundation of China (Grant No. 12375156), China National Nuclear Corporation Fundamental Research Project (Grant No. CNNC-JCYJ-202404) and Nuclear technology research and development (Grant No.HJSYF2025(11)).

† biantianjian@foxmail.com or biantianjian@ciae.ac.cn

ISBN: 978-3-95450-279-0 ISSN: 3043-0208 doi: 10.18429/JACoW-SAP2025-FRNC2

Figure 3 illustrates the axial-defocusing effect of the spiral inflector. At the inflector exit, the beam extends to approximately ±10 mm, causing approximately 10% losses in the first acceleration gap. This axial mismatch subsequently drives further beam loss in the central region.

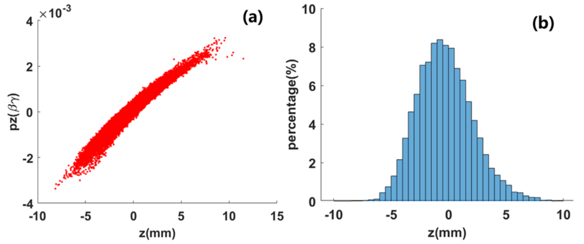

Figure 3: (a) The axial phase space; (b) the particle-density distribution along the axial direction.

CENTRAL REGION

In the cyclotron center, the magnetic flutter is almost zero, so the RF electric field must provide both acceleration and vertical focusing. Beam transmission efficiency and vertical focusing strength are frequently emphasized, however, beam quality is also critical. In the first few turns, radial-phase coupling is the main source of beam-quality degradation.

Starting from the original design, we optimized the crossing phases of the four acceleration gaps (gap 1-4). Figure 4 shows the radial-phase space of the fourth turn, where the RF phase and radial position are recorded as the particles cross the gaps. A 40° phase-width beam is injected into the first accelerating gap and tracked for four turns. The phase width grows to over 90°, the radial width increases, and the core charge density falls (top row of Figure 4). For comparison, the bottom row shows the optimized central-region results: phase width is kept within 60° and radial width within 15 mm.

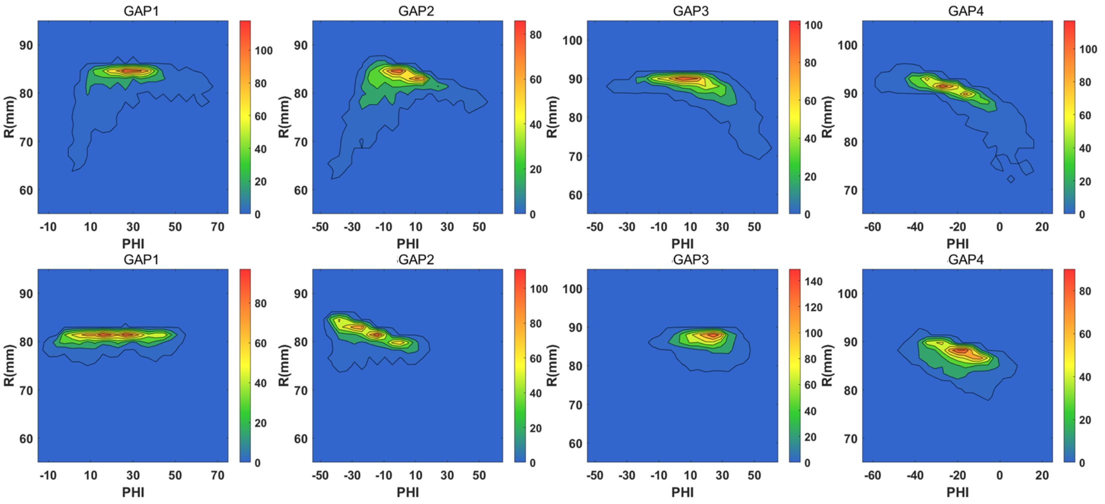

Figure 4: The first row: radial-phase space at the 4th turn of original design. The second row: radial-phase space at the 4th turn of optimized design.

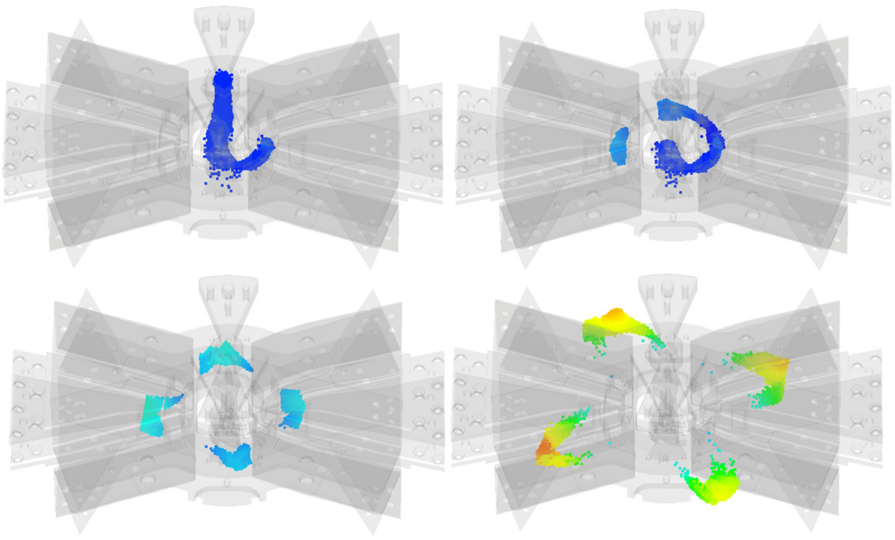

Figure 5: The formation of the banana-shaped beam in central region.

Figure 5 visualises the beam in the spiral inflector and central region, where the formation of the banana-shaped profile is clearly observed. Particle coordinates from both the original and optimised central region designs are used for comparison in subsequent simulations.

ACCELERATION REGION

The Walkinshaw resonance is the one of the dominant resonances in acceleration region, which coupling the radial oscillations to the axial direction. Conventionally, it is assessed by offsetting a perfectly matched beam of narrow phase width and monitoring the axial beam envelopes [2]. This approach is reasonable but lacks precision. The banana-shaped beam contains numerous off-centered particles and spans more than 90 degrees in phase. Particles with poor phase gain little energy and cross slowly through the resonance are more likely to be lost.

Figure 6 compares the axial beam envelopes obtained with the original and the optimized central-region designs. Owing to the removal of large-phase-width particles, the optimized case shows weaker envelope oscillations and the axial envelope is approximately 25% smaller than the original.

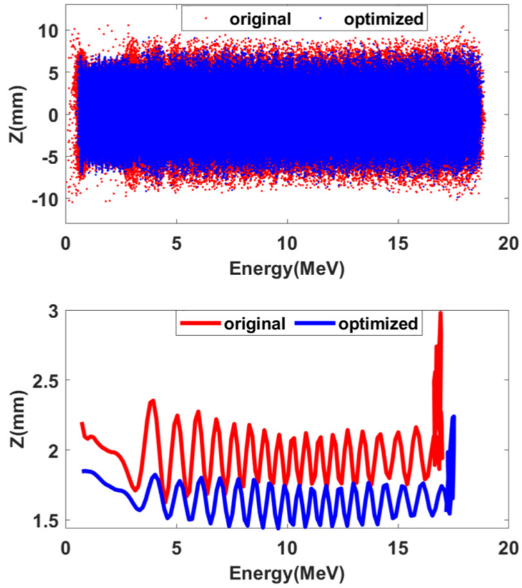

Figure 6: (a) Beam spots on the radial probe; (b) its root-mean-square beam envelopes.

EXTRACTION REGION

A stripper foil is used for negative hydrogen stripping to proton. Particle distribution on stripper foil is show in Figure 7. By reducing the fraction of poorly phased particles with the optimized central region, the maximum number of extraction turns falls from more than 130 to less than 80 turns, lowering the risk of beam loss from residual-gas stripping and improving extraction efficiency. Furthermore, relative to the original design, the optimized central region produces a more compact distribution and a narrower energy spread in the extracted beam, as shown in Figure 8. This improves beam quality and reduces the risk of losses at the foil frame and along the transport line.

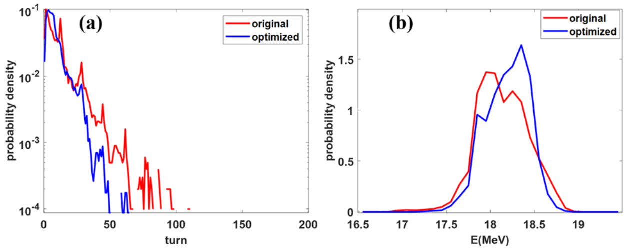

Figure 7: (a) Extraction turns distribution; (b) Extracted beam energy distribution.

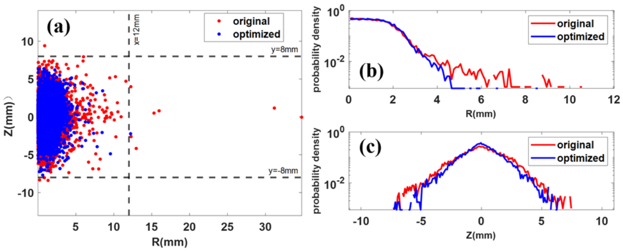

Figure 8: (a) The beam spot on the stripper foil; (b) The particle-density distribution.

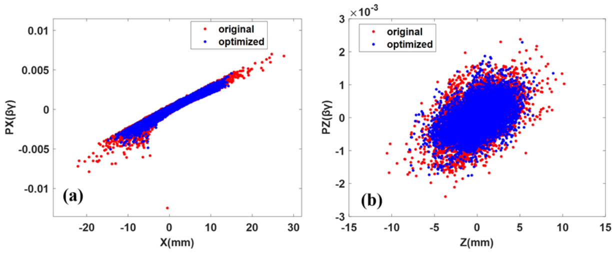

Figure 9: The horizontal (a) and (b) the axial phase space at the cyclotron and transport line interface.

The phase space plots at the cyclotron and transport line interface are shown in Figure 9, and the corresponding normalized emittances are listed in Table 1.

Table 1: The Emittances at the Cyclotron and Beamline Interface

	Normalized ε_x (π mm·mrad)	**Normalized ε_z (π mm·mrad)**
Original	1.7999	0.88742
Optimized	1.0314	0.61256

UNIFORM BEAMLINE

A high-power proton beam from a cyclotron bombards a fixed target to generate an intense neutron flux or to produce radioisotopes. Local power hotspots overload the cooling system and shorten target life, so a uniform beam spot on the target is essential [3, 4]. We use combined

ISBN: 978-3-95450-279-0 ISSN: 3043-0208 doi: 10.18429/JACoW-SAP2025-FRNC2

function multipole magnets to reshape the Gaussian beam into a rectangular profile with almost uniform distribution.

Uniform beamlines based on multipole magnets are seldom used in compact accelerators (to the best of our knowledge, no such uniform beamline exists), because the beta function at the magnets and the phase advance to the target must be tuned precisely, which inevitably lengthens and complicates the beamline. To solve this problem, we use combined function Quadrupole-Octupole Magnets (QOMs) to let the maximum and minimum beam envelopes form naturally near the QOMs. As shown in Figure 10, the beamline consists of one quadrupole and two QOMs, giving a short, simple and easily tuned system.

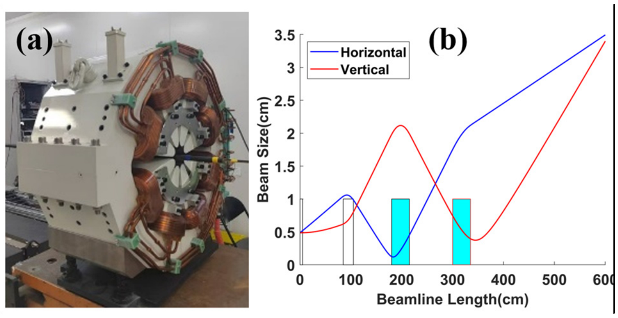

Figure 10: (a) QOM and (b) the beam envelopes in uniform beamline.

Owing to limited space in the accelerator hall, the 18 MeV cyclotron is equipped with two beamlines, a straight one and a bent one, that share a common segment and deliver the beam to neutron targets 1 and 2, respectively, as shown in Figure 11. The neutron target 1 is used for BNCT experiment and the target 2 for neutron imaging.

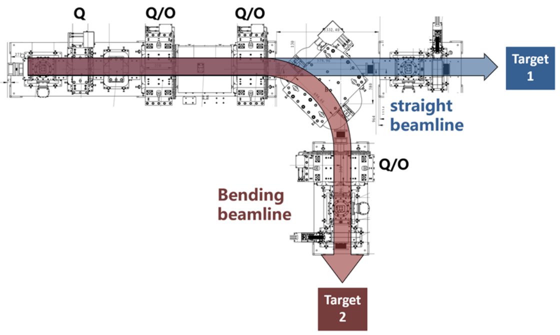

Figure 11: Layout of the uniform beamlines.

Figure 12(a) shows the particle-density distribution on neutron target 1 and the uniformity measured with a fluorescent screen is about 83%. The corresponding S2E simulation result is given in Figure 12(b) and correctly reproduces the high- and low-density regions, demonstrating high fidelity. Despite 83% uniformity, a 600 µA beam bombarded the neutron target 1 for one hour without observable surface damage. Throughout the run the vacuum remained below 5×10^{-7} mbar, confirming that beam loss was low and insufficient to degrade the vacuum.

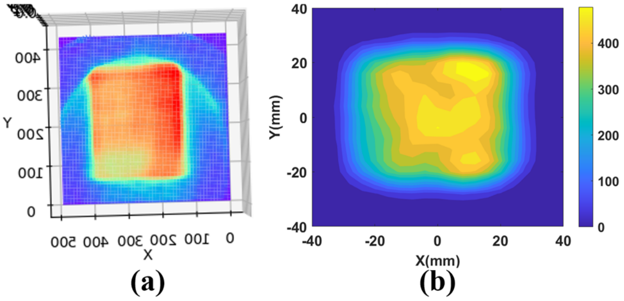

Figure 12: (a) Measured and (b) simulated particle-density distributions on neutron target 1.

SUMMARY

During the development of the 18 MeV/1 mA high-intensity cyclotron, S2E beam-dynamics simulations served as an efficient tool for design, optimization and interpretation of beam-tuning phenomena. The future plan is to improve the S2E simulation results and enhance long-term operational stability through two aspects: (1) Beam loss caused by residual-gas stripping is not yet included in the simulation, but it is essential for a quantitative description of beam loss. (2) The beamline's uniformity requires further improvement and needs fine-tuning to achieve a more homogeneous beam distribution.

REFERENCES

[1] A. Adelmann, A. Alba, and A. Fallahi, “OPAL for Self-Consistent Start-to-End Simulation of Undulator-Based Facilities”, presented at North American Particle Accelerator Conference, Albuquerque, New Mexico, USA, Aug. 2022. `https://conference.sns.gov/event/335/contributions/509/attachments/895/8202/opal-fel.pdf`

[2] T. Zhang *et al.*, “Physics design of a 70 MeV high intensity cyclotron, CYCIAE-70”, *Nucl. Instrum. Methods Phys. Res., Sect. B*, vol. 269, no. 24, pp. 2959–2963, Dec. 2011. `doi:10.1016/j.nimb.2011.04.052`

[3] Y. Y. Guo and G. Xu, “Design of transport lines for uniforming beam distribution with octupoles”, *Phys. Rev. Spec. Top. Accel Beams*, vol. 16, no. 2, Feb. 2013. `doi:10.1103/physrevstab.16.023501`

[4] Y. Yuri, N. Miyawaki, T. Kamiya, W. Yokota, K. Arakawa, and M. Fukuda, “Uniformization of the transverse beam profile by means of nonlinear focusing method,” *Phys. Rev. Spec. Top. Accel Beams*, vol. 10, no. 10, Oct. 2007. `doi:10.1103/physrevstab.10.104001`